Solar spectropolarimetry in orbit: from raw data to physical parameters

Von der Fakultät für Elektrotechnik, Informationstechnik, Physik
der Technischen Universität Carolo-Wilhelmina zu Braunschweig

zur Erlangung des Grades einer Doktorin
der Ingenieurwissenschaften (Dr.-Ing.)

Kumulative Arbeit

von **Kinga Albert**
aus Csíkszereda, Rumänien

eingereicht am:	31.05.2024
mündliche Prüfung am:	30.08.2024

1. Referent:	Prof. Dr.-Ing. Harald Michalik
2. Referent:	Prof. Dr. Sami Solanki

Druckjahr: 2024

Dissertation an der Technischen Universität Braunschweig,
Fakultät für Elektrotechnik, Informationstechnik, Physik

To Arne, Astrid and Patrik,
in no particular order.

Abstract

For space missions, especially those in deep space, communication bandwidth plays a pivotal role. Information is not transmitted instantaneously across vast distances, and the rate at which the spacecraft communicates with Earth is influenced by the distance, antenna diameter and the available power for the communication. These factors collectively determine the available communication bandwidth. This constraint in the data bandwidth has significant implications. Not only does it affect the speed at which transmitted data becomes available, but it also restricts the volume of data that can be communicated to Earth from remote spacecraft.

In this thesis, we design, implement, and validate a system, that addresses this communication problem by reducing the necessity of transmitting extensive data in the first place. This system processes the data on board the spacecraft, and as a result, we are able to transmit representations of physical properties to Earth rather than raw measurements. It is implemented for the Polarimetric and Helioseismic Imager on the Solar Orbiter mission (SO/PHI), the first solar spectropolarimeter that orbits the Sun in deep space. This approach is novel for solar spectropolarimetry, successfully maximising the scientific potential of the instrument by reducing the amount of data that must be transmitted by nearly 80%.

Zusammenfassung

Bei Weltraummissionen, insbesondere bei solchen im tiefen Weltraum, spielt die Kommunikationsbandbreite eine entscheidende Rolle. Informationen werden über große Entfernungen nicht sofort übertragen und die Geschwindigkeit, mit der das Raumfahrzeug mit der Erde kommuniziert, hängt von der Entfernung, dem Antennendurchmesser und der verfügbaren Leistung für die Kommunikation ab. Diese Faktoren bestimmen zusammen die verfügbare Kommunikationsbandbreite, wobei die Einschränkung der Datenbandbreite erhebliche Auswirkungen hat. Sie beschränkt nicht nur die Geschwindigkeit, mit der die übertragenen Daten zur Verfügung stehen, sondern limitiert auch das Datenvolumen, das von entfernten Raumfahrzeugen an die Erde übermittelt werden kann.
In dieser Arbeit planen, implementieren und validieren wir ein System, das dieses Kommunikationsproblem umgeht, indem es die Notwendigkeit der Übermittlung umfangreicher Daten von vornherein reduziert. Das System verarbeitet die Daten an Bord der Raumsonde, so dass wir in der Lage sind, anstatt der Rohdaten, direkt die berechneten physikalischen Eigenschaften an die Erde zu übermitteln. Diese Technik wird für den Polarimetric and Helioseismic Imager auf der Solar Orbiter Mission (SO/PHI) eingesetzt, dem ersten Sonnenspektropolarimeter, das die Sonne im tiefen Weltraum umkreist. Dieser Ansatz ist ein Novum in der Sonnenspektropolarimetrie und maximiert das wissenschaftliche Potenzial des Instruments, indem die zu übertragende Datenmenge erfolgreich um fast 80% reduziert wird.

Contents

List of Figures

List of Tables

1. Introduction

Humanity's innate urge to explore not only advances our understanding of the world but also pushes our technological boundaries. From ancient times, we have been striving to explain what we see around us. Our fascination with the cosmos has persisted throughout our history, gazing at the sky, pondering the nature of what we observed above us. Among our most captivating cosmic neighbours is the one that governs life on Earth: the Sun. It's no surprise that evidence of solar eclipse observations dates back to before 1200 BC, and of sunspots records to as early as 800 BC.

Our quest for answers has led us to expand our horizons in various ways. We have improved our observational capabilities through technological advancements. Galileo directed his telescope at the Sun already in 1609, and we have not stopped ever since. Today, we build observatories that enable us to capture unprecedented high-resolution images of our closest star, one image pixel equivalent to as little as 25 km on its surface (such as the SuFi instrument on the Sunrise balloon-borne observatory, Barthol et al., 2011; Gandorfer et al., 2011; Solanki et al., 2010). Through spectrometry and polarimetry, we extract every known piece of information encoded in the Sun's light. We even journey into space to observe what lies beyond the reach of earthbound observers. Here we can intercept and analyse the particles that it emits, we avoid Earth's atmosphere, as well as we can observe it from new angles.

The presence in space, that we built up purely in the name of scientific exploration of our planet and skies, is remarkable. We have constructed a vast fleet of spacecraft dedicated to studying our neighbours in the solar system and to looking into the depths of space. As an illustration of a fraction of our advances, Figures 1.1 and 1.2 showcases the space missions launched or planned by the European Space Agency (ESA), all dedicated to scientific ventures.

In our tireless quest to push the boundaries of space exploration, we confront a formidable challenge: communication with our robotic explorers becomes increasingly difficult as we journey deeper into space. The farther we are from Earth, the greater is the demand for power to transmit and receive information, as we build our antennas already as large as practical. This swiftly transforms missions to the most extraordinary and unique places into data-starved endeavours. Furthermore, we struggle with severe constraints on time-critical operations: the further we venture, the longer

it takes for the signals to arrive, and at many captivating vantage points, our spacecraft becomes temporarily silent to us.

Given these substantial limitations to communication, it becomes evident that, in our pursuit of further expanding the horizons of space exploration, we must tackle this challenge. One potential approach involves enhancing the capabilities of our systems to operate autonomously, without the need for frequent or extensive human intervention. This approach has long been employed for time-sensitive operations in spacecraft, an imperative for the success of our space missions. However, the realm of scientific data analysis has seen less exploration in this regard. Several factors contribute to this shortfall: scientific observations are often exploratory, leading to diverse and intricate analyses; trade-offs such as simplified instrument designs or alternate orbit design are often preferred solutions; and finally, the loss of unexplored potential in the data through automation is often unattractive.

In the present research landscape, equipping our scientific instruments with autonomy in both operations and data analysis opens up unprecedented avenues. Our efforts in autonomous operations and scientific data analysis for astronomy and space science are still in their infancy, both in ground-based observations (see Reardon et al., 2009) and for space-based observatories (see Curtis et al., 1989; Scherrer et al., 1995). This work represents a new effort in this direction, enabling the Polarimetric and Helioseismic Imager (Solanki et al., 2020) on board the ESA-NASA Solar Orbiter mission (Müller et al., 2020) to autonomously perform instrument characterisation and process scientific data on board the spacecraft. The calculations carried out on board include instrument characterisation, scientific data calibration, and the inversion of the radiative transfer equation, which transforms spectropolarimetric data (measurements of light spectrum and polarisation) into physical parameters (magnetic field vector and line-of-sight velocity). This project marks a pioneering effort to achieve autonomous, on-board data reduction for solar spectropolarimetry.

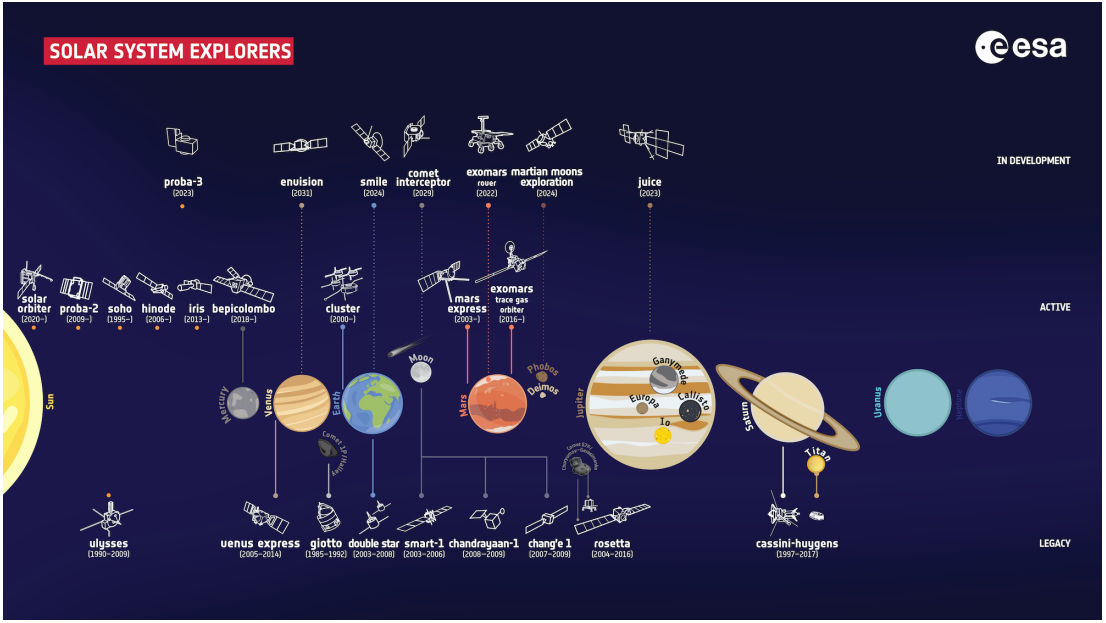

Figure 1.1. Past, present, and future science missions studying the Solar System, led by, or with contribution from the European Space Agency (ESA), from Nov. 2021. Image credit: ESA.

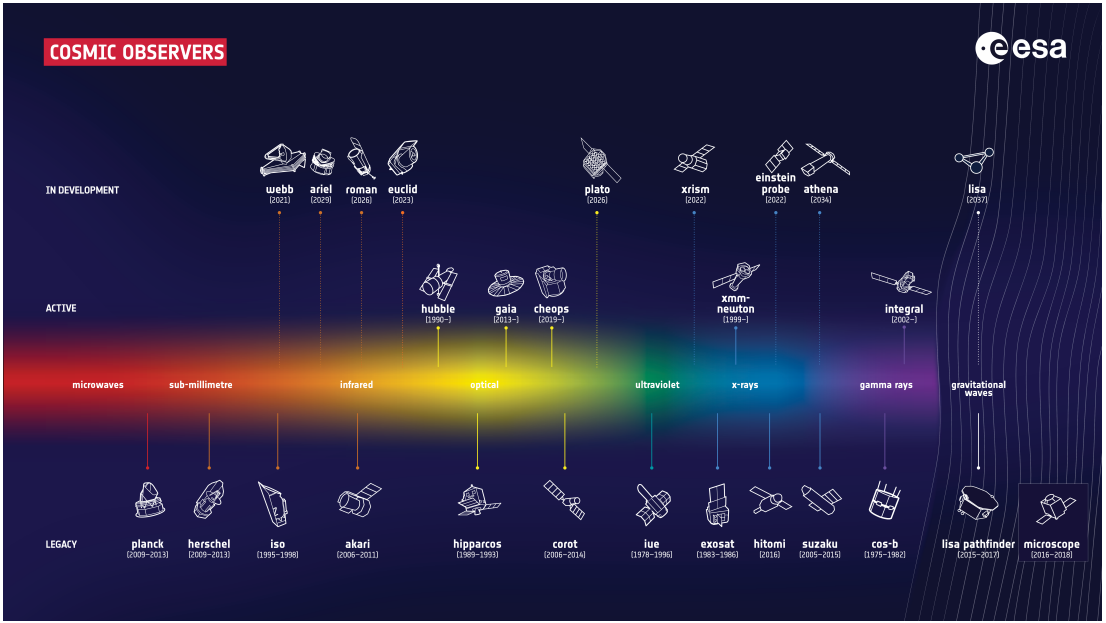

Figure 1.2. Past, present, and future science missions studying the Universe, led by, or with contribution from the European Space Agency (ESA), from Nov. 2021. Image credit: ESA.

2. About this work

The main objective of this project was to establish onboard processing capabilities for the Polarimetric and Helioseismic Imager instrument on board the Solar Orbiter spacecraft (SO/PHI, see Solanki et al., 2020). As a result, SO/PHI is capable of autonomously performing three tasks: (1) determining the optimal operation parameters, such as the optimal focus position, (2) determining instrumental effects, including instrumental response to uniform illumination (referred to as the flat field), and (3) applying the results of the instrument characterisation to calibrate science data, demodulate the polarisation states, which then enables us to estimate the components of the magnetic field vector and the line-of-sight velocity through the inversion of the polarised radiative transfer equation. Executing this last step on-board is a novel approach. The inversion of the radiative transfer equation is a non-linear step, meaning that the data prior to executing it cannot be recovered, and therefore its accuracy is critical. However, it effectively reduces the data volume encapsulating the information from 24 images to 5, that is, by a factor of 4.8. Additionally, it is important to note that the execution of all these steps requires minimal interaction from the ground.

To attain this objective, we carried out a series of tasks, which collectively make up the work presented in this thesis (see also fig. 2.1).

(1) We started by studying methods used on the ground for calibrating and analysing solar spectropolarimetric data. In this process, we simulated data from certain (more complex) operational steps, to understand how much we can simplify the methods, and to adapt them to our specific needs. We also created an inventory of the necessary mathematical operations for each of the methods, and of the necessary parameters that the methods must receive.

(2) Mostly parallel to step (1), we initiated the design of the framework in which the necessary methods could be seamlessly integrated. Within this framework, we defined various organisation levels for the processing software, considering the desired abstraction levels and paying special attention to information hiding (that is, defining a clear purpose and scope for each organisational level, and making sure that they encapsulate all necessary information with minimal interfaces). In the process, we established well-defined interfaces with lower-level software components and articulated the requirements

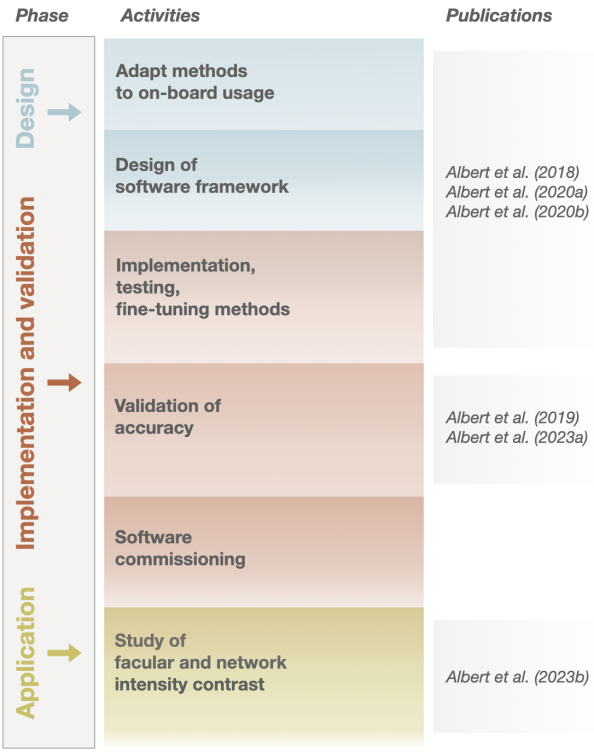

Figure 2.1. Summary of the main activities that form the work presented in this thesis, and the corresponding publications.

for functions that necessitated hardware implementation in field programmable gate arrays (FPGAs). Simultaneously, we designed robust error-handling mechanisms, and we defined the information that must be embedded into the data to trace all executed steps and their parameters, to which we refer to as metadata. The metadata management system emerged as the central pillar of the data processing framework, facilitating information transmission, thus ensuring synchronisation among all processing steps. Furthermore, it assumes a crucial role in recording essential information that enables troubleshooting on the ground, and ensure the traceability of on-board processes. Throughout this phase we prioritised considerations such as the simplicity and adaptability of instrument operation. This work is presented in the conference proceedings Albert et al., 2018 and Albert et al., 2020a, as well as in the peer-reviewed publication Albert et al., 2020b.

(3) The validation of the data reduction system has been a high priority, due to the many constraints encountered during the design and implementation phases. We began evaluating the achieved accuracy as soon as critical data processing steps became available. Initially, we used data from the Helioseismic and Magnetic Imager on-board the Solar Dynamics Observatory (SDO/HMI, see Schou et al., 2012), which is presented in the conference proceeding Albert et al., 2019. As the data processing system reached a more complete implementation and some existing steps were revised, we conducted a more thorough accuracy assessment. To distinguish processing inaccuracies from observational effects, we used artificial data from magnetohydrodynamics (MHD) simulations. This study is reported in Albert et al., 2023a.

(4) Shortly after the launch of the Solar Orbiter, we initiated the commissioning of the onboard data processing system. This undertaking, to ensure the instrument's capability to autonomously generate science-ready data, has required extensive collaboration from the entire SO/PHI team, as well as from the operations team at ESA. In its current state, SO/PHI autonomously determines operational parameters for each telescope and supporting subsystem, such as focus position and exposure time. It also conducts instrument characterisation, including the measurements of flat and dark fields. These calibration data are then applied to the science observations, which consequently can undergo the radiative transfer equation inversion. Our ongoing efforts involve continuous assessment of data quality received from orbit. In combination with on-ground simulations, we continue to

refine the existing processes to maximise data quality.

(5) Concluding the work presented in this thesis, we applied SO/PHI data processed on board the spacecraft in a study. We utilised the unique vantage point provided by the instrument and, in conjunction with SDO/HMI data, conducted observations of facular and network contrast near the solar limb. The relationship between intensity, magnetic field, and observation angle of bright features, such as faculae and network, is important in understanding and modelling them. Additionally, it contributes to the study and modelling of variations in solar irradiance across various time scales. Previous research encountered challenges when exploring regions near the solar limb due to measurement uncertainties in these areas. In our study, detailed in Albert et al., 2023b, we demonstrated that a multi-angle approach can improve our understanding of facular and network contrast near the limb, yielding valuable preliminary results.

In summary, activities (1) and (2) encompass the design phase of the onboard data processing system, in which SO/PHI's data processing pipelines are described. Tasks (3) to (5) comprise the implementation, validation, and commissioning of the system. Finally, task (6) concerns the application of the data generated by the system in a scientific project. These six steps are presented in six publications: three of these are first-authored, peer reviewed works, and the remaining three are first-authored conference proceedings. See their reprints in the appendices. Figure 2.1 illustrates the different steps of the project, and the corresponding publications.

The research conducted in this thesis enabled the SO/PHI instrument to deliver science data to the scientific community. Consequently, it contributed to numerous studies and publications, with various leading authors. As of the current date, these include: Bailén et al., 2024; Calchetti et al., 2023; Janvier et al., 2023; Kahil et al., 2023, 2022b, 2022a; Loeschl et al., 2024; Nölke et al., 2023; Schou et al., 2023; Sinjan et al., 2023; Valori et al., 2023; Yang et al., 2023; Yardley et al., 2023; Yeo et al., 2023.

2.1. Scientific contributions

The scientific contributions resulting from this work can be summarised as follows:

- We implemented, for the first time, an autonomous science data reduction system for a deep space spectropolarimeter, that can deliver science-ready data directly from orbit (see Albert et al., 2018; Albert et al., 2020b).
- We calibrated, for the first time, a spectropolarimeter on-board a spacecraft for dark and flat fields, without any on-ground processing involved in the process (see Albert et al., 2018; Albert et al., 2020b).
- We have designed and implemented a metadata system for the on-board data processing system of SO/PHI that helps interpret the science data and assists instrument operations in monitoring processing steps (see Albert et al., 2020a; Albert et al., 2020b).
- We demonstrated that the on-board data reduction system of SO/PHI effectively processes data with the required accuracy, despite that it is implemented under various restrictions impacting numerical precision (see Albert et al., 2019; Albert et al., 2023a).
- We applied data that arrived as a science-ready data product from orbit in a solar physics topic, investigating the intensity contrast of faculae and network features (see Albert et al., 2023b).
- We showed that combining data from two instruments observing the Sun from different points of view, helps in more accurately determining the magnetic field of features close to the solar limb, thereby describing their behaviour in relation to their magnetic field better (see Albert et al., 2023b).
- We also demonstrated, that with the second point of view of the Sun, we can also identify faculae and network features better, allowing us to include more of them in the analysis, particularly extending the range towards those associated with lower magnetic fields (see Albert et al., 2023b).

3. Background

The Sun is a variable star. On its surface, sunspots emerge and dissolve, and it exhibits eruptive coronal mass ejections. It changes its radiative output, and produces a dynamic solar wind, thereby creating an ever-changing heliosphere – almost uniquely due to its magnetic field.

The magnetic nature of the Sun, however, is far from unique; in fact, magnetism appears to be a fundamental aspect of our Universe. Magnetic fields are observed everywhere from Earth and our Solar System, to other stars, interstellar space and far-away galaxies, and they often influence the processes around them. Magnetic fields influence the evolution of gas clouds, and through magnetic pressure they contribute to balancing gas disks against gravitation. Magnetic fields also remove angular momentum through magnetic breaking which is an essential component of star formation during protostellar cloud collapse, but they can also slow down stellar rotation. Magnetic fields control the density and distribution of cosmic rays, and can protect planets from this hazardous-to-life radiation. Magnetic fields seem to be woven into the fabric of our Universe; therefore, we must study and understand them if we hope to understand our world.

3.1. Solar magnetism and its photospheric manifestations

3.1.1. A brief overview

The global solar magnetic field is believed to originate in a **large-scale dynamo mechanism**, which is generally thought to be located in deeper layers of the Sun. From here, as we understand it today, magnetic field strands break out, emerge to the surface and continue further out into the corona and heliosphere. The magnetic field manifests itself in a wide range of spatial and temporal scales through this journey as the balance of forces governing its behaviour change. Understanding the behaviour of these manifestations can answer key questions about the origin of the solar magnetic field, the nature of the physical processes that are involved in its evolution, and ultimately about the past, present and future of our Sun.

The large-scale dynamo mechanism is often considered to be located between the radiative and convective zone, and to be created by a two-step

process. Helioseismic investigations show that there is a large variation in the rotation in the solar interior, with a rotational shear layer (called the tachocline) located at approximately the bottom of the convection zone. This is a dynamic region, that couples the solar interior, which rotates approximately as a rigid body, with the convection zone that has a strong differential rotation depending on latitude (Christensen-Dalsgaard, 2002; Howe et al., 2000). Today it is often thought, that this rotationally induced velocity shear is the first necessary step to generate the dynamo, which changes the poloidal magnetic field into a toroidal one by what is known as the Ω-effect. To produce a dynamo, however, a second step is needed, to disturb the symmetry of the toroidal field and turn this newly generated toroidal field back into poloidal one. We do not yet know the exact mechanism responsible for this. Several proposals (and their combinations) have been put forward, including that the small scale turbulent motions twist the toroidal field into the poloidal one (the so-called α-effect, Parker, 1955), that the transformation is achieved by emerging magnetic flux (Babcock-Leighton effect, Babcock, 1961; Leighton, 1969), or that it occurs through instabilities in the toroidal magnetic field (Dikpati and Gilman, 2001; Ferriz-Mas and Schüssler, 1994; Ossendrijver, 2000). The different models are successful in reproducing various aspects and manifestations of the solar dynamo (discussed in the next paragraphs); however, they do not yet offer a comprehensive picture.

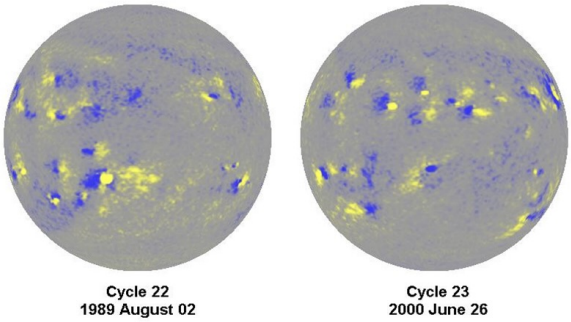

Figure 3.1. The global photospheric line-of-sight magnetic field at the height of solar activity, in two subsequent solar cycles. Yellow colour indicates positive polarity, while the blue colour shows negative polarity. Image credit: D. Hathaway, NASA/MSFC.

As the toroidal magnetic field amplifies, it becomes unstable to magnetic buoyancy. Consequently, some magnetic flux rises from the lower layers of the Sun towards the photosphere (the favoured physical image for this is in the form of flux ropes), where it surfaces (see also Centeno et al., 2017). From there, it continues further out into the corona and heliosphere. At the point where it surfaces in the photosphere, we observe bipolar magnetic regions (see fig. 3.1). These areas of **flux emergence** vary from large active regions, forming sunspot groups (with magnetic flux, $\Phi_B \sim 10^{23}$ Mx, lasting for months), to the smallest ephemeral regions, detectable only through magnetograms (with $\Phi_B < 10^{19}$ Mx, living for less than a day). They emerge at mid to low heliographic latitudes (Lat. $< 45°$), with an 11-years periodic change in their emergence latitude from high to low (see, e.g. Solanki et al., 2006). As a consequence of this, plotting the latitude of sunspot emergence over time, results in a plot called the butterfly diagram (see fig. 3.2). Active regions are generally oriented in a rough East-West direction (with some tilt in their latitude), creating a leading and a following part with respect to the solar rotation. The tilt angle has a strong relationship to the heliographic latitude where it emerges, approximately corresponding to half of it. This proportionality is called *Joy's law*. The leading spots have the same magnetic polarity in each hemisphere; however, they are opposite from one hemisphere to the other. They also stay the same for 11 years, after which they reverse (see figures 3.1 and 3.2). These regularities in the two hemispheres are referred to as *Hale's Polarity law* (Hale, 1908).

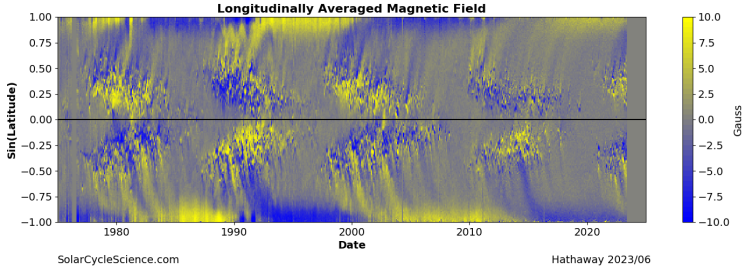

Figure 3.2. Butterfly diagram (also called time-latitude diagrams or synoptic magnetogram), showing four 11-year cycles. The positive and negative magnetic fields are shown with yellow and blue, respectively. It illustrates Hale's polarity laws, Joy's law, and polar field reversals. Image credit: D. Hathaway, NASA/MSFC.

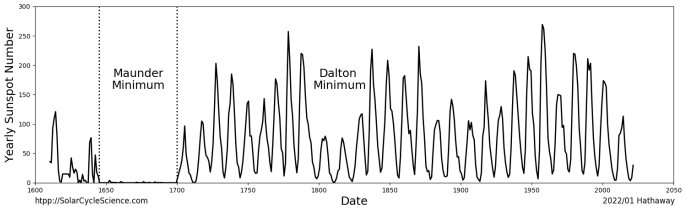

Figure 3.3. Sunspot numbers from the early 1600-s to 2022. Periods of remarkably low or nearly no magnetic activity are marked as Maunder and Dalton minima. Image credit: D. Hathaway, NASA/MSFC.

The variation of solar activity over a longer time-scale is shown in Fig. 3.3. While it clearly displays the 11-year activity cycle, we can also observe that the strength of the cycle varies over longer time scales as well. Within the 11 years of the activity cycle, during periods of low solar activity, the solar magnetic field arranges itself into a dipole configuration. At these times, we find stronger field concentrations in the polar regions, and the lower latitudes exhibit predominantly small-scale magnetic fields. These small-scale magnetic fields are distributed in a way that results in lower flux density. In contrast, at the height of the solar activity, the magnetic field is weaker at the poles and has larger scale, strong features at lower latitudes. At the end of each active period, the polarity at the poles of the Sun changes with respect to the previous low-activity period, creating a 22-year magnetic cycle. This change is thought to be driven by the dynamo, however a number of its details are still unclear (see, e.g., Cameron and Schüssler, 2007; Cameron and Schüssler, 2015; Gizon et al., 2020; Solanki et al., 2006). Regardless of the phase within the solar cycle, terms like *quiet Sun* and *active regions* are commonly used to describe regions with the absence or presence of strong magnetic fields, such as sunspots or their remnants after decay (see also section 3.1.3).

Modelling indicates, that the evolution of magnetic flux after its emergence may largely be a surface phenomenon (see Solanki et al., 2006). This implies that to understand the forces governing the evolution of the magnetic field, we must understand the fundamental interaction of the magnetic field with the plasma flows of the surface. In other words, we need a brief introduction to magnetohydrodynamics (MHD).

3.1.2. Shortly about magnetohydrodynamics

The solar plasma is a conducting, globally neutral fluid, composed of charged particles. If we now impose a magnetic field (**B**), then by moving the conductor relative to **B** (the equivalent of plasma flows within the magnetic field), we create a change of flux density, which according to *Faraday's law*, gives rise to an electric field. This, for a volume of conducting plasma, can be expressed as:

$$\nabla \times \mathbf{E} = -\frac{\partial \mathbf{B}}{\partial t}, \tag{3.1}$$

where **B** is the magnetic field vector, **E** is the electric field vector, and $\nabla\times$ is the curl operator. This electric field, in turn, induces a current density, **J**, according to *Ohm's law*:

$$\mathbf{J} = \sigma(\mathbf{E} + \mathbf{v} \times \mathbf{B}), \tag{3.2}$$

where σ is the conductivity of the fluid, and **v** is the velocity field of the plasma flow. The direction of this induced current density is perpendicular to the magnetic field.

This newly induced current density **J** must induce its own magnetic field as well, according to *Ampère's law*:

$$\nabla \times \mathbf{B} = \mu_0 \mathbf{J} + \mu_0 \epsilon_0 \frac{\partial \mathbf{E}}{\partial t}, \tag{3.3}$$

where μ_0 is the magnetic constant (i.e. the magnetic permeability of vacuum), and ϵ_0 is the electric constant (i.e. the vacuum permittivity). The term $\mu_0\epsilon_0\frac{\partial \mathbf{E}}{\partial t}$ is necessary for wave propagation in free space, however in MHD calculations it is approximated to 0. This newly induced field adds to the imposed magnetic field, opposing it (in adherence with the laws of energy conservation). Expressing **E** (equation 3.2) and **J** (equation 3.3), and substituting it in equation 3.1, leads to:

$$\frac{\partial \mathbf{B}}{\partial t} = \nabla \times (\mathbf{v} \times \mathbf{B}) - \nabla \times (\eta \nabla \times \mathbf{B}), \tag{3.4}$$

where $\eta = (\mu_0\sigma)^{-1}$ is the magnetic diffusivity of the fluid. If we assume, that η is constant in the plasma, and consider the fact that $\nabla \cdot B = 0$, i.e. the divergence of a magnetic field is always 0, meaning that there are no sinks or sources (or in other words magnetic monopoles do not exist) we arrive to the most commonly used form of the **magnetic induction equation**:

$$\frac{\partial \mathbf{B}}{\partial t} = \nabla \times (\mathbf{v} \times \mathbf{B}) + \eta \nabla^2 \mathbf{B}, \tag{3.5}$$

where ∇^2 is the Laplacian operator. This equation describes the change in an imposed magnetic field that happens due to motion of the plasma, and it is the sum of an induction term due to plasma flows (first term on right-hand side), and a diffusion term (second term on the right-hand side). Possible mechanisms for diffusion could be particle collisions or the motion of the plasma across the field lines.

The combined imposed and induced magnetic field interacts with the induced current density, and gives rise to the *Lorentz force*:

$$\mathbf{F} = \mathbf{J} \times \mathbf{B}. \tag{3.6}$$

This force acts on the plasma generally in the opposite direction of $\mathbf{v}$, to inhibit the relative movement of the fluid and the magnetic field. Thus, it is necessary to apply a force in order to move the plasma in the presence of the magnetic field.

Considering the magnitudes of the imposed and induced magnetic fields, with a simple approximation, we can state that the strength of the imposed magnetic field is proportional to the induced current density. This, in turn, is proportional to the imposed magnetic field, the velocity (and let us define here a characteristic velocity of the flow, u), and the conductivity of the fluid, σ. We can also state that the magnitude of the induced magnetic field is also proportional to the length scale of the flow, expressed through a characteristic length scale, l. The reason for this is, that the induced current density would induce magnetic fields of different magnitudes over different lengths. With these considerations we arrive to the approximation $B_{\text{induced}}/l \sim \sigma u B_{\text{imposed}}$. If we now express the ratio of the newly induced and the imposed magnetic field, we can conclude that it is proportional to $u\sigma l$. This product is called the *magnetic Reynolds number* and is typically denoted as R_m.

In the case that R_m is infinite, the induced magnetic field is infinitely larger than the imposed one, meaning that the magnetic field will appear to move together with the plasma. This is the so-called **frozen-in condition**, or *Alfvén's theorem*, implying that the movement of the magnetic field and the plasma will happen together. Whether the plasma will follow the magnetic field lines, or the magnetic field lines will follow the plasma, is determined by the relation of the magnetic and the plasma pressure: the one that has higher pressure will influence the motion. The ratio of these two quantities is the so-called plasma-β:

$$\beta = p_{\text{plasma}}/p_{\text{magnetic}}, \tag{3.7}$$

where p symbolises pressure.

In solar plasma, although we naturally do not reach infinitely large magnetic Reynolds numbers, in most cases, $R_m \gg 1$. As a consequence, in most cases the diffusion term in eq. (3.5) is also negligible (i.e., as the plasma cannot cross the field lines, the most efficient way of diffusion is excluded). This, in the solar photosphere, manifests in the field lines following the plasma flows as a consequence of the dense atmosphere where $\beta > 1$. In contrast, in the corona, it is the plasma flows that align with the magnetic field lines as a consequence of the fairly low density plasma and in comparison strong magnetic fields, resulting in $\beta < 1$.

3.1.3. Magnetic flux evolution, and the variety of magnetic structures

Let us now return to the journey of magnetic flux that emerged to the surface and formed bipolar active regions. These strong magnetic structures **decay** over time. The mechanisms that are responsible for the decay are magnetic diffusion and fragmentation (see Harvey and Harvey, 1973). Fragmentation is a consequence of the various flows moving the flux tubes and breaking them up into parts (see, e.g. Strecker et al., 2021). The mechanism of diffusion is thought to possibly be due to turbulent, as well as convective motions, spreading the flux gradually (Galloway and Weiss, 1981; Meyer et al., 1974; Peng et al., 2024; Petrovay and Moreno-Insertis, 1997). The full process is still not well understood, see Martínez Pillet, 2002 for an overview. Generally, as the active regions decay, the flux is spread out, decreasing the flux density.

Let us now consider low, and evenly distributed vertical magnetic flux on the solar surface, and consider what would happen to it in the presence of the convective surface flows. The accelerating or breaking effect of the Lorentz force upon the motion in the vertical direction can be neglected (i.e. the diffusion term of equation 3.5 is negligible); however, horizontal flows transport the magnetic flux. As a consequence, in a convection cell (or on a larger scale, in a supergranule), the horizontal components of the convective motion carry the magnetic flux with them. As these flows are directed towards the edges of the granules (and supergranules), they create concentrations of magnetic field in the intergranular lanes - in areas that harbour gas downflows as a consequence of convection. If the fields that concentrate in these regions have opposing polarities, they cancel each other out (i.e. magnetic reconnection occurs); otherwise, if they are of the same polarity, they intensify.

Once a mechanism for increasing the magnetic flux density exists, we must consider a limit where the Lorentz force becomes strong enough to counteract the convective motion, leading to equipartition between kinetic and magnetic energy densities. The magnetic field necessary for this state (i.e., the photospheric equipartition field) is a few hundred Gauss ($\sim$ 500 G). This is the point where the magnetic field starts to suppress convection in the region.

The gas within this region, in the growing absence of convection, becomes a thermal insulator and hence behaves adiabatically. The surrounding atmosphere, however, is a superadiabatic environment. This means that the temperature gradient outside this region is higher than inside it.

We now assume that the gas is already flowing downwards due to convective motion at the edge of granules and supergranules – a necessary assumption for the ensuing effects. As the gas descends inside this region, it becomes cooler than its surroundings at the same height. This gas then will also be denser than its surroundings; therefore, in order to maintain hydrostatic equilibrium it must be removed from this area. As it cannot move across the field lines, gravity creates a downdraft, accelerating the already existing downflow. As there is no new material delivered by convective motion, the region becomes partially evacuated.

As a result of this partial evacuation, the magnetic concentration compresses, causing the magnetic field to increase in order to restore the horizontal pressure balance between its interior and the external atmosphere. As a result, magnetic strengths in the kilogauss range are reached (see also Parker, 1978 for theoretical description, Nagata et al., 2008; Utz et al., 2014 for observation and Danilovic, Schüssler, and Solanki, 2010a for simulations of this process). Such concentrations are generally referred to as **kilogauss flux tubes** (or simply flux tubes). Due to their partially evacuated nature, flux tubes are buoyant in the surrounding plasma, and they generally have a surface-vertical orientation (see Buehler et al., 2015; Jafarzadeh et al., 2014). The same process, but assuming plasma upflows instead of downflows is thought to achieve the exact opposite effect, that is, disperse the magnetic field (see, e.g. Bellot Rubio et al., 2001; Spruit, 1979).

Such small flux tubes of kilogauss magnetic field concentrations are abundant on the solar surface. They can be called **faculae**, which are especially abundant in active regions, where they form so-called *plages*. Plage areas are rich in various manifestations of small scale magnetic fields, and exhibit structures creating abnormal granulation, micropores, ribbons, flowers, and strings (see Narayan and Scharmer, 2010). Kilogauss strength magnetic concentrations also appear in the quiet Sun, where supergranular

flows create the so-called **magnetic network**, roughly outlining the supergranular cells (see Buehler et al., 2019 for a comparison of magnetic field concentrations associated with plage and magnetic network, respectively). These small features behave dynamically, constantly deformed by the granulation and supergranulation, fragmented by shear, and driven against other nearby concentrations where they predominantly merge or cancel, depending on their respective polarities, or more rarely dissolve and fade away (see Bellot Rubio et al., 2001; Keys et al., 2014; Schrijver et al., 1997). Moreover, they have a large contribution to the photospheric radiative output (see Krivova et al., 2006).

Small magnetic concentrations are also found, however, in supergranular interiors, which we call **internetwork** (see Bellot Rubio and Orozco Suárez, 2019; Sánchez Almeida et al., 2010). The abundance of these structures, as well as the fact that they evolve on time scales shorter than the typical lifetime of active regions, hints at the likelihood that these structures are not the result of decaying active regions (Cattaneo, 1999; Sánchez Almeida et al., 2003). Moreover, their dependence on the solar cycle has been highly debated, see, e.g. Buehler et al., 2013; Faurobert and Ricort, 2015, 2021; Korpi-Lagg et al., 2022; Meunier, 2018. Whether these structures are at all related to the global large scale dynamo, or if they are produced by a separate **small scale dynamo**, and to what extent such a small scale dynamo would interact with the large scale one, is highly debated in the literature (see, Brandenburg and Subramanian, 2005; Cattaneo, 1999; Danilovic, Schüssler, and Solanki, 2010b; Rempel, 2014; Vögler and Schüssler, 2007; Warnecke et al., 2023).

Outside these strong magnetic concentrations, the magnetic field is much weaker and more horizontal with respect to the solar surface, covering the majority of it (see de Wijn et al., 2009 for a review).

Some of these various magnetic structures leave an imprint on the photosphere, making them not only visible due to a change in the magnetic field, but also due to changes in the solar intensity. In order to understand how these various magnetic features look like, we must first discuss what solar intensity is, and what influences it.

3.1.4. The brightness of the Sun

Describing how the Sun and its features look is equivalent, with the help of modern day detectors, to discussing how many photons we intercept. Since each photon carries a certain amount of energy (dependent on its wavelength), we can equate the intercepted number of photons to the intercepted energy. Let us now explore what we need in order to use the radiation coming from the Sun as an observational method, that helps us understand various physical processes.

We define **intensity** (I_λ, also known as brightness or specific intensity), as the amount of energy transported through an area dA at the location $\mathbf{r}$ (could also be defined by x, y, z coordinates), in a given direction $\mathbf{l}$ (which could also be defined by azimuth and elevation θ, and Ω), in the solid angle $d\Omega$, in a time interval dt, and within a certain wavelength band-pass $d\lambda$:

$$I_\lambda(\mathbf{r}, \mathbf{l}, t) = \frac{dE_\lambda}{\mu dA dt d\lambda d\Omega}. \tag{3.8}$$

In the above equation, $\mu \equiv cos(\theta)$ scales the intensity with the projection of the propagation direction compared to the surface normal, θ being the angle between the normal to dA, and the direction $\mathbf{l}$.

This means, that if we can measure the energy that we receive, and we know all the other variables from the set-up of the measurement, we can calculate the specific intensity. Intensity is a useful quantity, because on the one hand, it describes the radiation field fully, and on the other hand, as long as there are no intensity sources or sinks along its path, it does not change with distance. Generally speaking, in the context of observations, we discuss the observed intensity. However, often, we discuss rather relative intensity of various features, – a dimensionless quantity that describes ratio of the intensity of a certain feature to the mean intensity of the quiet Sun (generally) at the centre of the solar disc at a defined wavelength.

Let us now consider what kind of variations we may observe in the intensity, and how we can interpret them. As the radiation that emerges from the Sun passes through the solar atmosphere, it is absorbed and re-emitted several times before reaching the solar surface. As radiation passes through a gas, it interacts with its atoms, and there are two possible outcomes of these interactions: intensity can be attenuated through absorption or intensified through emission. Both these processes involve the interaction of atoms with energy.

Absorption is the result of such interactions when a photon is either absorbed, and the energy is disposed of in a way that does not emit a photon, or that the wavelength or direction of the emitted photon is altered, such

that it does not contribute any longer to the observed intensity. When the direction of a photon is altered, it is called scattering. Similarly, **emission** is the result from interactions where new photons are emitted, or the wavelength or direction of a photon has changed in a way that it now contributes to the observed intensity.

We now consider radiation travelling through a volume of gas, which, in the case of the Sun, could be the solar atmosphere. The change to the intensity of the radiation occurring henceforth, can be characterised by the emission and absorption introduced by atomic interactions with the gas. Accordingly, we can introduce corresponding **emission** and **absorption coefficients**. The emission coefficient (ϵ_λ) is defined as the intensity added along the beam by local emission over a path length ds:

$$\epsilon_\lambda = \frac{dI_\lambda^{\text{emitted}}}{ds}. \tag{3.9}$$

Meanwhile, the absorption coefficient (κ_λ, often also called opacity) as the portion of the intensity that is removed from the beam of light, per unit of path length:

$$\kappa_\lambda = -\frac{1}{I_\lambda}\frac{dI_\lambda^{\text{absorbed}}}{ds}. \tag{3.10}$$

With these definitions, we can express the **transfer of radiation** through the gas volume over a path s as the change in its intensity over this path:

$$\frac{I_\lambda(s)}{ds} = \epsilon_\lambda(s) - \kappa_\lambda I_\lambda. \tag{3.11}$$

From these coefficients, let us now define a few parameters useful for observing radiation. We begin with a quantity called the **monochromatic optical depth**, which describes how far the observer's view penetrates into the gas. This quantity combines the absorption coefficients and the path length of the beam through the gas (which would be very difficult to determine on its own) into one value, as:

$$d\tau_\lambda \equiv -\kappa_\lambda(s)ds. \tag{3.12}$$

Another valuable quantity is the **source function**, which characterises with a single parameter, the intensity change induced by the gas, combining the emission and absorption coefficients:

$$S_\lambda \equiv \frac{\epsilon_\lambda}{\kappa_\lambda}. \tag{3.13}$$

In other words, the source function describes the intensity added to the ray per unit optical path, connecting the local physical quantities of the gas with the intensity perceived by the observer.

Using the monochromatic source function, S_λ, and the monochromatic optical depth, τ_λ, we can express the equation of radiative transfer in its most commonly used form:

$$\frac{I_\lambda(s)}{d\tau_\lambda} = I_\lambda(s) - S_\lambda. \tag{3.14}$$

The formal solution to this equation, assuming no interaction between the radiation and the coefficients in the equation, and subject to the boundary conditions of intensity I_λ^0 and I_λ^+, is expressed as:

$$I_\lambda^+ = I_\lambda^0 e^{-\tau_\lambda} + \int_0^{\tau_\lambda} S_\lambda(t) e^{-t} dt, \tag{3.15}$$

where the integration variable t represents the extent to which our view traverses from 0, that is the top of the atmosphere, to τ_λ, our optical depth. It is important to note that this solution is applicable only when the emission and absorption coefficients are known.

To find practical solutions to the radiative transfer equation, various assumptions are made. One of the common approximations is axial symmetry, assuming that the observed gas consists of parallel layers, known as the **plane parallel approximation**. This assumes that the gas varies only along the z axis, and not along the x and y axes, effectively reducing the three spatial dimensions to a single one. With this assumption, we can express the radiative transfer equation with the help of $\mu \equiv cos(\theta)$, where θ is the deviation of our observation angle from the perpendicular, as:

$$\mu \frac{dI_\lambda}{d\tau_\lambda} = I_\lambda - S_\lambda, \tag{3.16}$$

to which the formal solution is:

$$I_\lambda^+(\mu) = I_\lambda^0 e^{-\tau'_\lambda/\mu} + \frac{\int_0^{\tau'_\lambda/\mu} S_\lambda(t) e^{-t} dt}{\mu}, \tag{3.17}$$

where τ'_λ is the optical depth at $\mu = 1$.

Another, realistic approximation for the solar photosphere is that the incident light, I_λ^0, is negligible, meaning, that **our object is semi-infinite**. In other words, we assume that the Sun is opaque enough so that no radiation from its other side will influence our observations.

Another common approximation for the solar photosphere is the so-called **Eddington-Barbier approximation**, which assumes that S_λ varies linearly with τ_λ. In this case, we arrive at:

$$I_\lambda^+ \simeq S_\lambda(\tau_\lambda = \mu). \tag{3.18}$$

This implies that the radiation emerging at the surface is determined by the conditions at $\tau_\lambda = \mu$. In other words, the photons escaping the surface collectively represent the value of the source function S_λ at $\tau_\lambda = \mu$.

Let us now define a **spectral line**, as a variation in intensity with respect to the continuum intensity, over a narrow wavelength range. It is called an emission line when its intensity surpasses that of the continuum, and an absorption line when it is lower, both as consequences of atomic processes.

We can now examine the source function of the spectral line, S_λ^l, and of the continuum, S_λ^c. Let us assume local thermodynamic equilibrium (LTE), which means that matter locally is in thermodynamic equilibrium and its properties are governed by it; however, radiation may deviate from that.[1] In LTE, the effects of the line formation on the source function can be neglected (see e.g, Jefferies, 1968), resulting in both S_λ^l and S_λ^c being equal to the Planck function, B_λ. However, S_λ varies along the depth of the medium. Additionally, the atomic processes which create the line create a shallower depth of formation of the line intensity compared to that of the continuum. In other words, at the line wavelength, the view of the observer is obscured, and the observed region lies further outward. Considering now LTE, where $S_\lambda^l(z) = S_\lambda^c(z)$, one observes a spectral line only if the source function varies with depth.

The characteristics of spectral lines, including their profile and the specific wavelength at which they appear, can undergo changes due to various physical processes. These changes serve as indicators that allow for monitoring and understanding different aspects of these processes. For instance, the Doppler shift reflects the atmospheric motions along the line of sight of the observer by shifting the spectral lines to higher or lower frequencies. Magnetic fields exert an influence on the polarisation of light, thereby altering the shape of the line profile when observing its polarised components. For a more in-depth discussion of the effects of magnetic fields on spectral lines, see section 3.2.1.

[1] LTE is often assumed in the modelling of photospheric absorption lines; however, in many lines non-LTE effects are introduced by various phenomena. Studies examining these effects include Athay and Lites, 1972; Bruls et al., 1992; Holzreuter and Solanki, 2015; Lites, 1972; Rutten and Kostik, 1982; Rutten, 1988; Shchukina and Trujillo Bueno, 2001; Smitha et al., 2023.

3.1.5. What magnetic features look like

After presenting what influences the observed intensity, we are now equipped to discuss the appearance of magnetic structures. We restrict the discussions to their appearance at the continuum wavelength intensity.

In section 3.1.4, we have established that the source function of the continuum (in local thermal equilibrium, LTE) is the Planck function (B_λ). Therefore, when considering the continuum intensity of various solar structures, the underlying question to be answered is always what is the temperature at the observed optical depth, and often related, at what height does the optical depth $\tau = 1$ lie.

Let us now discuss the various patterns that emerge (see section 3.1.3), and start with the feature that covers most of the solar surface: **granulation**. The granules are convection cells, with hot plasma emerging in their centres, and cooler plasma descending at their boundaries. Therefore, we observe them as bright features with darker edges (see Bray et al., 1984, 2009; Nordlund et al., 2009 for more details).

The kilogauss strength flux tubes, that form faculae and the magnetic network, are generally described as the bright features of the solar photosphere (see the bright areas surrounding the active region in Fig. 3.5 and the bright points between the granules in Fig. 3.6). Their brightness varies strongly with their size, and the angle of observation. Firstly, let us consider that we look straight into a flux tube. Because convection is suppressed by the strong magnetic field, and hence convective energy transport is inhibited, flux tubes would basically have lower temperature than their convective surroundings. This is indeed the case for larger flux tubes at a zero-degree angle, just as in the case of sunspots or pores (discussed later). Due to the lower temperature, these larger flux tubes appear darker than the mean intensity of the surrounding granulation – despite the fact that we consider faculae and network generally the photospheric bright features (see also Riethmüller and Solanki, 2017). However, unlike the larger flux tubes, thinner flux tubes are optically thin to radiation streaming in from the sides, which also heats the gas remaining inside them. At the same time, as a consequence of the lower plasma density, inside the flux tube the optical depth $\tau = 1$ lies deeper in the atmosphere (see, e.g. Danilovic, Schüssler, and Solanki, 2010a discussing also the relation of flux tube size and the height of $\tau = 1$). As a consequence of the higher temperature in the deeper layers, small flux tubes reach higher temperatures through radiative heating from the sides compared to the mean surface temperature, making them appear brighter than their surroundings. See also Wiehr et al., 2004 for a discussion on the sizes of flux tubes. The diameter of the flux tube is directly

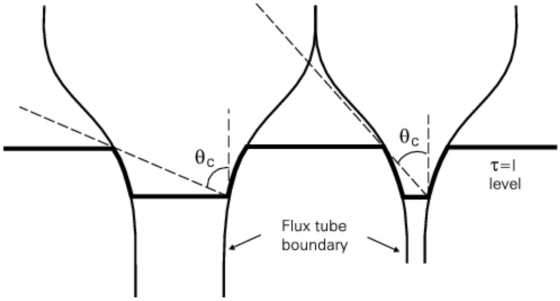

Figure 3.4. The wineglass model of flux tubes, which explains their brightness variation in relation to the angle of observation. The thick line marks the $\tau = 1$ optical depth, that lies lower inside the flux tube due to the lower gas pressure. The walls of the flux tube are hot due to the surrounding convection. θ_c marks the point, where the line of sight meets the lowest (i.e. hottest) part of the wall. Figure adapted from Solanki et al., 2006.

related to the magnetic pressure inside it, that is, the amount of magnetic flux that is concentrated in the area that it occupies. Studies, investigating the relationship of magnetic flux density and facular or network brightness include Kahil et al., 2019; Kobel et al., 2011. Studies observing the brightness variation of a flux tube during its lifetime are Nagata et al., 2008 and Utz et al., 2014.

Let us now consider various angles of observations. When we look at flux tubes from an angle, our line of sight will meet the hot walls of the flux tubes. Increasing our observation angle increases the observed intensity, until we reach θ_c, which is where we see directly the wall that is at the deepest point in the photosphere; therefore, it is the hottest. As illustrated in fig. 3.4, the value of θ_c is influenced by the diameter of the flux tube. At angles larger than θ_c, we again observe a decrease in intensity, until (possibly) the surrounding granules obscure our line of sight. The exact reasons for the change in the brightness at high observation angles is still not well understood, mainly due to observational constraints. An opportunity for improving observational data is presented in Albert et al., 2023b, see appendix F. The relationship between the intensity of faculae and network to both the observed magnetic flux density and the observation angle has been studied, for instance, also in Ortiz et al., 2002; Yeo et al., 2013.

Let us now discuss the appearance of flux emergence regions. The smallest of them, the ephemeral regions, induce no observable change in the continuum intensity, while the larger sunspots are the most prominent photospheric features. **Sunspots** on the large scale have a cool umbra (over 1000 K cooler than the quiet Sun on average), and a somewhat warmer penumbra (still about 300 K cooler than the quiet Sun; see Borrero and Ichimoto, 2011 for a detailed overview of sunspot structure). Figure 3.5 shows an active region, recorded by the high resolution telescope of the SO/PHI instrument.

Dark features that only have umbra, and show no penumbra, are called **pores** (also sometimes naked sunspots, if the pore evolved through a sunspot loosing its penumbra). Pores are often observed in active regions (just as in fig. 3.5), and can be associated with flux emergence (see, e.g. García-Rivas et al., 2024), or with sunspot decay (see Strecker and Bello González, 2022). The magnetic conditions of pore formation is studied in García-Rivas et al., 2021. The "counterpart" to pores also exists in the Sun: penumbrae can form also without umbra, which are usually referred to as **orphan penumbrae**. Studies that observed these structures include Buehler et al., 2016; Jurčák et al., 2014; Zuccarello et al., 2014, while Hirzberger et al., 2005; Jurčák et al., 2017 show the interaction of pores and orphan penumbrae.

On the small scale, inside the dark umbra, we often observe light bridges (see the bright lines dividing a sunspots in fig. 3.6). These bright features are connected to the penumbra, protruding into the sunspot, sometimes dividing it all the way through. Their fine structure can look like filaments, or can look more like granules. Often, but not necessarily, light bridges are the sign of sunspot decay. Other small scale features in the umbra are small bright points, so-called umbral dots, which appear as a consequence of magneto-convection (see fig. 3.6, and Schüssler and Vögler, 2006). These features are bright compared to the umbra. While their brightness is not straightforward to determine due to their small size, to date it is thought that while they appear bright, most of them are still darker than the undisturbed quiet Sun (see Solanki et al., 2006).

In the penumbra, we find a filamentary structure, which is most often radially aligned. We find two distinct brightness distributions among filaments: brighter ones, named intraspines, and darker ones, named spines (the darker and brighter relationship holds only locally).

The angle of observation also influences how a sunspot appears. When a sunspot is observed close to the limb, the umbra, and often part of the disc centre-side of the penumbra is not visible. This is known as the *Wilson effect*. It is best explained to be due to a 400 to 800 km difference in optical depth

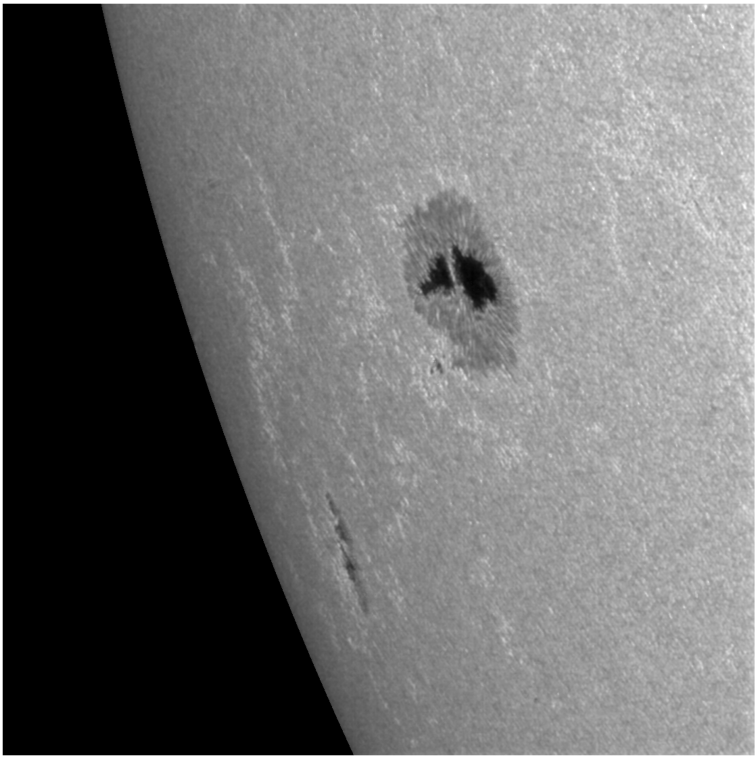

Figure 3.5. An active region, consisting of two sunspots and a few pores, close to the solar limb. The surrounding bright structures belong to a plage region, surrounding the sunspots. In the closer sunspot we can observe a light bridge, that divides it. Data from the SO/PHI instrument, by the high resolution telescope.

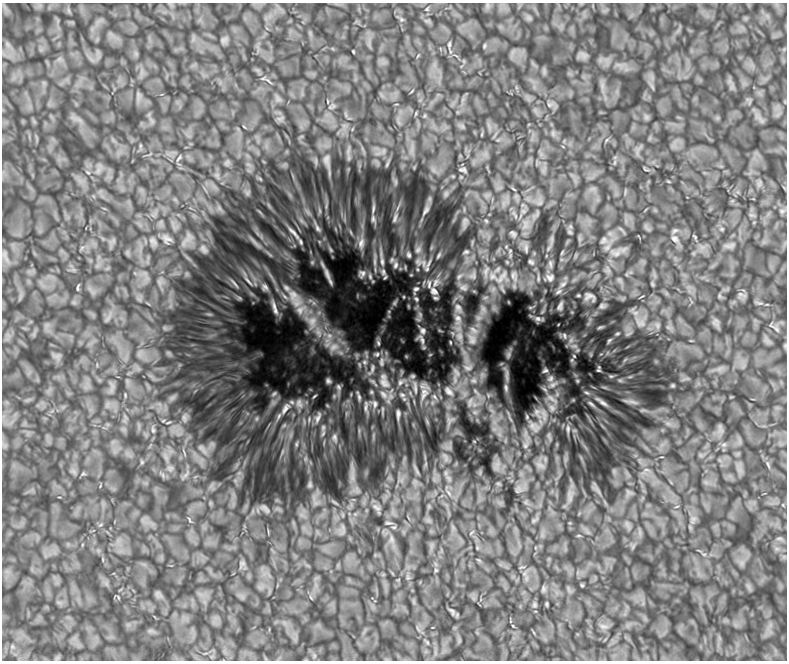

Figure 3.6. High resolution image of a sunspot. On the large scale, we can clearly identify the umbra (dark region) and the penumbra of the sunspot (the filamentary transition region between the granulation and the umbra). On the small scale, we can see several examples for light bridges of various widths, some that divide the sunspot, and one that just extends into it. The small bright point details inside the umbra are umbral dots; while the small bright points between the granules are faculae. Data from the GRIS spectropolarimeter at the GREGOR telescope (Collados et al., 2012), courtesy of J. S. Castellanos Durán.

of the umbra, compared to the quiet Sun, with a rather abrupt change at the umbral boundary. This difference is called the Wilson depression (see Wilson and Maskelyne, 1774).

Studying the intensity of photospheric features helps us not only in understanding their nature, but as the abundance of these features is strongly related to solar activity, their study also aids us in understanding solar variability. An important aspect of solar variability research, naturally, is the influence of the variations on Earth (see e.g., Foukal et al., 2006; Foukal and Milano, 2001; Haigh, 2007; Lean et al., 2002; Solanki and Krivova, 2004). In this context, we define the **total solar irradiance** (TSI) as the wavelength-integrated radiation flux illuminating Earth at its average distance from the Sun, characterising the Earth-facing hemisphere of the Sun. The TSI is observed directly since 1978 by space-borne radiometers, and these observations are complemented by models in order to further our understanding of the nature of its variations. Generally, surface magnetism is considered to be the main driver of TSI variations, see e.g, Domingo et al., 2009; Fröhlich, 2006; Solanki et al., 2005; Yeo and Krivova, 2019; Yeo et al., 2014, 2023.

3.2. Observing photospheric magnetism

3.2.1. Effects of magnetic field on radiation

Until now, we have considered the intensity of the light at various wavelengths, how its interaction with atmospheric particles can change the intensity, and how various magnetic structures appear at continuum intensity. However, physical phenomena, such as the Zeeman and Hanle effects, in certain spectral lines formed in the presence of magnetic fields, influence the polarisation of the light. Observing these changes in polarisation allows us to infer the magnetic conditions at the formation height of the observed spectral line. Let us begin by establishing the basic concepts and notations of polarisation, before we continue discussing magnetic effects on the radiation.

Basics of polarimetry

When discussing the polarisation of light, we are referring to the orientation of the planes in which the electromagnetic wave oscillates with respect to the direction of propagation. In this context, when we use the term *polarisation*, we are referring to the orientation of the electric field oscillations, implying the presence of magnetic field oscillations in the orthogonal plane as well.

The orientation of the oscillation plane in **unpolarised light** may be in any of the directions, without preference to any of them. A beam of light may contain waves with all possible directions. The light is said to be **polarised**, when the direction of oscillation is well defined. Linear polarisation occurs when the wave oscillates in a single plane. To an observer looking in the direction of propagation, the wave oscillates linearly. Circularly polarised light consists of two waves that are 90° out of phase with each other and perpendicular, both having the same amplitude. When observed in the direction of propagation, the oscillation plane of the wave appears to move on a circle. Elliptical polarisation is similar to the circular one, but the amplitude of the two waves may not be identical, and their phase may be different from 90°. As a result, they appear to be moving on an ellipse rather than a circle.

The polarisation of an electromagnetic wave can be described using various formalisms. The one most commonly used in solar photospheric observations is the **Stokes formalism**. The Stokes vector describes the wave train in terms of idealised filters, without providing information about the phase. It comprises four parameters: I, Q, U and V, where I represents total

intensity, Q is the intensity difference between the horizontal and vertical polarisation, U denotes the intensity difference between the linear polarisation at $+45^\circ$ and -45°, and V is the intensity difference between the right and left-handed circular polarisation.

Let us first consider the theoretical case of a single, monochromatic wave train of electromagnetic radiation propagating in the z direction. If the electric vector from the x, y plane is expressed as:

$$E_x = \xi_x cos\phi,\ E_y = \xi_y cos(\phi + \varepsilon), \tag{3.19}$$

where ξ_x and ξ_y is the amplitude of the wave, the phase is $\phi = \omega t - kz$ (where ω is the angular frequency and k is the wave number), and ε is the phase difference between E_x and E_y, then the Stokes vector ($\mathbf{I}$) is defined as:

$$\mathbf{I} = \begin{pmatrix} I \\ Q \\ U \\ V \end{pmatrix} = \begin{pmatrix} \xi_x^2 + \xi_y^2 \\ \xi_x^2 - \xi_y^2 \\ 2\xi_x\xi_y \mathrm{cos}\varepsilon \\ 2\xi_x\xi_y \mathrm{sin}\varepsilon \end{pmatrix}. \tag{3.20}$$

When expanding this definition to the real case, where a light beam is a superposition of light trains, with various wavelengths within a small spectral width, various amplitudes and phases, the Stokes parameters become temporal averages over an observation period:

$$\mathbf{I} = \begin{pmatrix} < \xi_x^2 + \xi_y^2 > \\ < \xi_x^2 - \xi_y^2 > \\ 2 < \xi_x\xi_y \mathrm{cos}\varepsilon > \\ 2 < \xi_x\xi_y \mathrm{sin}\varepsilon > \end{pmatrix}. \tag{3.21}$$

To describe changes in the polarisation of the light that passes through a medium, that is, how the Stokes vector changes, we use the characteristic **Mueller matrix** of the medium:

$$\begin{pmatrix} I_{\mathrm{out}} \\ Q_{\mathrm{out}} \\ U_{\mathrm{out}} \\ V_{\mathrm{out}} \end{pmatrix} = \begin{pmatrix} M_{11}M_{12}M_{13}M_{14} \\ M_{21}M_{22}M_{23}M_{24} \\ M_{31}M_{32}M_{33}M_{34} \\ M_{41}M_{42}M_{43}M_{44} \end{pmatrix} \cdot \begin{pmatrix} I_{in} \\ Q_{in} \\ U_{in} \\ V_{in} \end{pmatrix}, \tag{3.22}$$

where "$\cdot$" denotes matrix multiplication, M denotes the Mueller matrix, and the subscripts "in" and "out" mark the interface of the system, i.e. the incoming and transformed light. With this formalism, we may treat several effects as one system, described by a single Mueller matrix:

$$\boldsymbol{M}_{total} = \boldsymbol{M}_1 \cdot \boldsymbol{M}_2 \cdot \ ... \ \cdot \boldsymbol{M}_n, \tag{3.23}$$

where $\boldsymbol{M}_{total}$ is the Mueller matrix of the system, and $\boldsymbol{M}_1$ to $\boldsymbol{M}_n$ are the Mueller matrices of the different parts of the system.

The Zeeman effect and the radiative transfer of polarised light

The polarisation of the light can be changed through light-matter interactions and by magnetic field. Light-matter interactions are reflection, transmission, scattering, dichroism (i.e. the physical effect of asymmetric absorption of two orthogonal polarisation states of an incoming beam), or birefringence (i.e. polarisation-dependence of the refractive index of a medium). Effects that change the polarisation of the light in the presence of a magnetic field include the Hanle effect (depolarisation effect through scattering), Zeeman effect (the magnetic field-induced splitting of atomic energy levels), Faraday rotation (a rotation of the polarisation under magnetic field, caused by circular birefringence) and Faraday depolarisation (depolarisation caused by the Faraday rotation). In the following, we restrict the discussion to the Zeeman effect, and consider the other effects out of scope for this work (see for more details del Toro Iniesta, 2003; Stenflo, 1994; Trujillo Bueno et al., 2017).

The **Zeeman effect** is the physical phenomenon, where the magnetic field breaks the symmetries of the oscillation frequencies of electrons in an atom in the different spatial components. To describe the phenomena, let us introduce a few quantum physical notions.

To describe the orbitals of electrons in an atom, we define four *quantum numbers*: principal (n), angular (l), magnetic (m), and spin (s). The principal quantum number describes the size of the orbital, the angular quantum number describes its shape, the magnetic quantum number describes its orientation in space, while the spin quantum number describes the spin angular momentum of the electron. As electrons orbit and spin around the atomic nucleus, we can define three couplings inside the atoms: coupling of orbital angular momenta due to Coulombic repulsion of electrons, coupling of their spin angular momenta due to spin statistics, and the coupling of the spin and orbital momenta, referred to as LS-coupling. We consider now an electron with an orbital angular momentum $\mathbf{L}$, spin angular momentum $\mathbf{S}$, and total angular momentum under LS-coupling $\mathbf{J} = \mathbf{L} + \mathbf{S}$. The **magnetic dipole moment** of the electron ($\boldsymbol{\mu}$) is the magnetic moment resulting from the angular momentum $\mathbf{J}$, and depends on the orbital quantum number l:

$$\boldsymbol{\mu} = \mu_B \sqrt{l(l+1)}, \tag{3.24}$$

where μ_B is the Bohr magneton. For a given value of l, the magnetic quantum number m takes values from $-l$ to l, including zero, resulting in $2l + 1$ orbital orientations in a subshell.

When the atom is exposed to a weak magnetic field (weak in comparison to the LS-coupling), the magnetic field discernibly disturbs the magnetic

moment of some of its electrons.[2] It exerts a torque on the magnetic dipole moment of electrons in open shells, directing them towards alignment with the magnetic field. The work applied in rotating the electrons in that orbital alters its energy level, resulting in a change in the energy levels proportional to m. Consequently, the $2l+1$ orbital orientations result in the splitting of the energy levels into $2l+1$ sub-levels. The energy shift between the sub-levels (and also the resulting Zeeman wavelength splitting, λ_B) increases proportionally with the field strength B, influenced by two factors: the magnetic quantum number m and the *Landé g-factor*, g_{LS}. The change in the energy levels can be expressed as:

$$\Delta E = -g_{LS}\mu_B m B. \tag{3.25}$$

The Landé g-factor depends on the quantum numbers, and can be expressed as:

$$g_{LS} = \frac{3}{2} + \frac{s(s+1) - l(l+1)}{2j(j+1)}, \tag{3.26}$$

where $j \equiv l + s$ is the total angular momentum quantum number. When $j = 0$, the Landé factor loses its meaning, because the levels do not split. The ΔE keeps its linear increase with the increase of B until the magnetic field strength becomes comparable to the internal field of the atom. This is the strong field limit of the Zeeman effect. Magnetic fields stronger than the internal field of the atom disrupt the coupling between the spin and orbital motions, leading to the *Paschen-Back effect.*

When the transition occurs between an energy level with quantum number $j = 0$ (unsplit) and $j = 1$ (with three sub-levels), it is referred to as the **normal Zeeman effect**. Any other case, involving the splitting of both levels in the transition, is termed the **anomalous Zeeman effect**, see Fig. 3.7.

The Zeeman components, that arise from the splitting of the energy levels, contribute to the absorption and dispersion effects of light. They create the *Zeeman pattern*, that is the alteration of absorption lines in the presence of magnetic field (see more details in del Toro Iniesta, 2003). Therefore, we need to account for these effects in the radiative transfer equation, **arriving to the radiative transfer of polarised light**. We describe it in the Stokes formalism, by using the so-called *propagation matrix*, $\boldsymbol{K}$ (for its derivation see del Toro Iniesta, 2003). $\boldsymbol{K}$ is somewhat similar to a Mueller matrix (see Eq. 3.22), and it describes the impact of the Zeeman effect on the radiative transfer.

[2] While the magnetic field affects the magnetic moment of the entire atom, its effect on the nucleus is negligible.

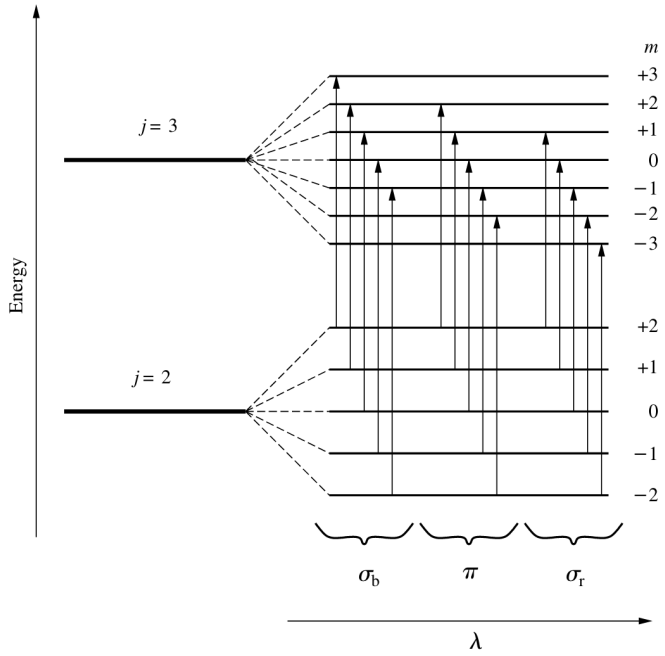

Figure 3.7. Transitions between the lower level $j = 2$ and upper level $j = 3$ in the presence of an external magnetic field, due the Zeeman effect. Levels with quantum numbers 2 and 3, in the presence of magnetic field are split into 5 and 7 sub-levels, respectively. The left and right sides of the figure show the absence and presence of magnetic field, respectively. The vertical arrows show the possible transitions between energy levels (marked σ_b for $\Delta m = +1$, π for $\Delta m = 0$, σ_r for $\Delta m = -1$). These various transitions are inversely correlated with different wavelengths at which they occur, indicated by the lower axis. Figure adapted from del Toro Iniesta, 2003.

With $\boldsymbol{K}$, similar to equation 3.14, the radiative transfer equation for polarised light becomes:

$$\frac{d\mathbf{I}_\lambda}{d\tau_{\lambda_0}} = \boldsymbol{K}(\mathbf{I}_\lambda - \mathbf{S}_\lambda), \tag{3.27}$$

where $\mathbf{I}_\lambda$ is the Stokes vector at the wavelength λ, τ_{λ_0} is the continuum optical depth, $\mathbf{S}_\lambda = (B_\lambda, 0, 0, 0)^T$ is the source function vector, with B_λ being the Planck function. This holds under several approximations, including that the continuum radiation is unpolarised (see del Toro Iniesta, 2003 for the full extent of approximations).

3.2.2. Spectropolarimeters

Observing the Zeeman pattern is possible with **spectropolarimeters**, which observe the intensity of light as a function of wavelength and polarisation. These observations can be single points (unresolved stars or integrated light of the Sun as a star), or spatially resolved in 1 to 2 dimensions. These observations are often complemented with a temporal dimension to create a three to five dimensional data cube, allowing also the study of the evolution of the observed features.

Due to the high dimensionality of the data, it is very challenging to simultaneously image it on a 2-dimensional space (a detector). To address this challenge, numerous instrument designs have emerged, each involving a trade-off between the extent or resolution of different dimensions (see also Iglesias and Feller, 2019 for an overview). Despite the variety of implementations, all spectropolarimeters rely on a common set of basic building blocks: components for analysing the polarimetric and spectral properties of the light. These components can be treated as distinct entities within the instrument.

To **measure the polarisation** of the incoming light, we must transform the polarisation signals into light intensities before they reach the detector. This is necessary because, detectors rely on the photoelectric effect, and therefore can only measure light intensities, not directly polarisation. It should be noted that there are developments in the direction of creating micropolarisers, that can be integrated into the detector, thereby creating a component that directly measures the polarisation (see for a review Iglesias and Feller, 2019, as well as Zhou et al., 2021), however the underlying principle remains the same: the conversion of polarisation signals to intensities prior to imaging. For this conversion, two components are required in the optical train: a modulator and an analyser. The modulator changes the polarisation of the incoming signal, producing modulation states, in which it

combines the elements of the Stokes vector with different (known) ratios. Following the modulator, the analyser filters or splits the linearly polarised parts of the light. This entire system is acting on the incoming Stokes vector and transforms it with its characteristic Mueller matrix. For an overview of various elements used for this purpose, see del Toro Iniesta, 2003; Gandorfer, 2002; Stenflo, 1994.

In addition to the polarisation intentionally induced by the optical elements in the spectropolarimeter, we must also consider unintentional polarisation caused by other optical components, such as entrance windows, lenses, and mirrors, or even the atmosphere in the case of ground-based observations. In the Stokes formalism, we treat the whole system (including the atmosphere, telescope and polarising elements) as one, defined by the product of the Mueller matrices of each of these elements.

The fact that detectors record only the intensity levels means that we can record only the first row of the Mueller matrix. Therefore, to determine all four unknown incoming Stokes parameters, at least 4 measurements are necessary, with different Mueller matrices. Recording these four measurements is possible through temporal or spatial modulation, or a combination of the two methods. Temporal modulation is achieved by combining the modulator and analyser into a single device, which can be switched between various polarisation states, and allows differently polarised components of the light to be imaged at different times. Spatial modulation splits the incoming wave into its differently polarised components, simultaneously imaging them on multiple sensors or different regions of the same sensor. This technique is known as multiple-beam spectroscopy, made possible with the use of polarising beam splitters. Multiple beam spectroscopy is typically combined with temporal modulation, allowing the recording of two states at a time (called dual-beam).

The relationship between the incoming Stokes vector and the recorded intensities is described by the modulation matrix of the system. In the case of four different measurements, this can be expressed as:

$$\mathbf{I}_m = \begin{pmatrix} I_m^{(1)} \\ I_m^{(2)} \\ I_m^{(3)} \\ I_m^{(4)} \end{pmatrix} = \begin{pmatrix} M_1^{(1)} & M_2^{(1)} & M_3^{(1)} & M_4^{(1)} \\ M_1^{(2)} & M_2^{(2)} & M_3^{(2)} & M_4^{(2)} \\ M_1^{(3)} & M_2^{(3)} & M_3^{(3)} & M_4^{(3)} \\ M_1^{(4)} & M_2^{(4)} & M_3^{(4)} & M_4^{(4)} \end{pmatrix} \cdot \begin{pmatrix} I_{in} \\ Q_{in} \\ U_{in} \\ V_{in} \end{pmatrix} = \boldsymbol{M'} \cdot \mathbf{I}_{in}, \quad (3.28)$$

where the subscript m indicates measurement, and in marks incoming light. $M_1^{(i)}$ to $M_4^{(i)}$ is the first row of the Mueller matrix describing the polarimetric system for each of the four different measurements that results

in the recorded intensities $\mathbf{I}_m = I_m^{(i)}$, with index $i = \{1 \cdots 4\}$. $\boldsymbol{M'}$ is the modulation matrix, and $\mathbf{I}_{in}$ is the incoming Stokes vector.

The polarimeter portion of the instrument may be combined with any **spectrometer**. We can, for example, record the spectrum in the function of one spatial direction along a slit (called a slit spectrometer). Additionally, we can also scan the second spatial dimension with the slit, achieving two-dimensional images. This method prioritise spectral resolution over spatial resolution. Another approach is to scan the spectral line using a tunable narrowband filter, enabling the simultaneous recording of the two spatial dimensions. This is usually referred to as an imaging spectrometer. Spectrometry is well discussed in a great number of textbooks, see e.g. Léna et al., 2012.

We obtain the magnetic field vector from these measurements (in the case of the Zeeman effect) through an inverse method. This method involves synthesising spectropolarimetric line profiles by solving the polarised RTE, with an initial guess of the magnetic field. Subsequently, an iterative minimisation method is used to match the measured profiles based on a merit function (typically χ^2), until a satisfactory fit is achieved. For a detailed description of this process, see del Toro Iniesta, 2003. An overview of different techniques is given in de la Cruz Rodríguez and van Noort, 2017.

3.2.3. Solar spectropolarimeters on ground, in space and in-between

The first proposal on the magnetic nature of sunspots came from George E. Hale, in his paper Hale, 1908, based on observations conducted at the Snow telescope on Mount Wilson. He extended a slit spectrograph into a spectropolarimeter, in which he could adjust the length of the slit by covering potions of it, to selectively transmit light from selected features. Initially, only light from the umbra was chosen, and then, for reference, the nearby quiet Sun areas were imaged. The exposure times of the photographs of the sunspots ranged from a few minutes to over an hour (during which the alignment was maintained by a clock). Figure 3.8 shows a section of the photographs taken using this instrument. These images show the Zeeman splitting that he observed in the 5918.77 Å spectral line in the sunspot (and its lack in the quiet Sun), suggesting that sunspots have a magnetic nature.

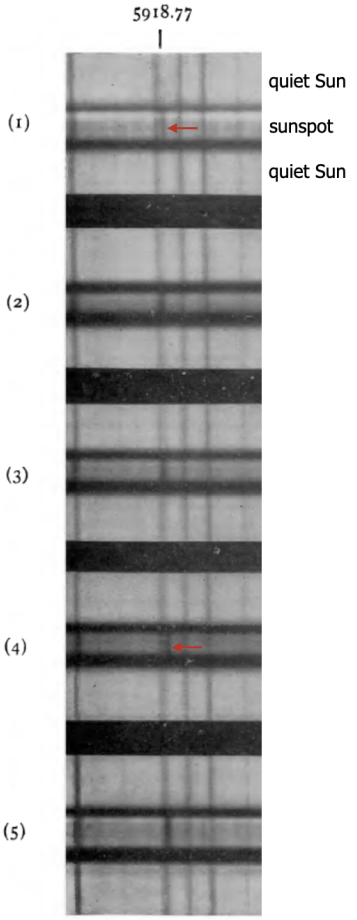

Figure 3.8 Five photographs (numbered 1-5) of sunspot spectrum, taken by George E. Hale at the Snow telescope on Mount Wilson. In each image, the central portion displays the sunspot spectrum, while the edges depict the quiet Sun, captured in close proximity to the sunspot. (1) and (4) show spectra at circular polarisation in one direction, (2) and (3) show spectra with circular polarisation in the other direction. (5) is the total intensity, imaged by removing the polarimeter from the light path. These observations, for the first time, measure the circular polarisation in a sunspot (see the Zeeman splitting indicated by the red arrows), proving the magnetic nature of the umbra. Adapted from Hale, 1908.

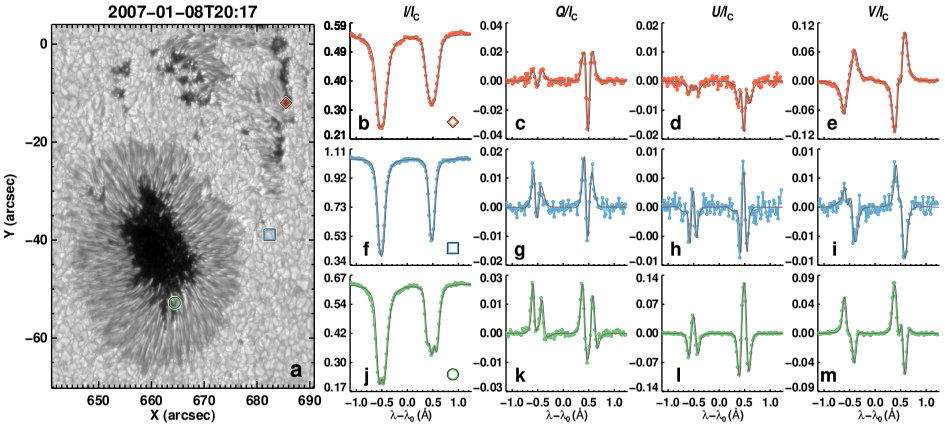

Figure 3.9. Observation of an active region by the Spectro-Polarimeter on-board Hinode (see Ichimoto et al., 2008; Kosugi et al., 2007; Lites et al., 2013; Tsuneta et al., 2008). The high spatial resolution reveals the complex structures, and allows their study. Besides the spatial resolution, the instrument also provides the full Stokes vector with a very good wavelength sampling. Panel "a" shows the continuum Stokes I image. The Stokes profiles of the pixels marked in this image (red, blue and green) are shown in Panels "b" to "m". The Stokes profiles are normalised to the mean of the quiet Sun area in the data at the continuum intensity (denoted as I_c). The grey line shows the model atmosphere which was fitted to the measurements. Data from the MODEST catalogue, see Castellanos Durán et al., 2024, courtesy of J. S. Castellanos Durán.

The **improvements in spectropolarimeters** have been primarily driven by the demand for higher spatial and spectral resolutions, as well as the need for higher polarimetric accuracy in the data. For a visual comparison of this evolution, see fig. 3.9 in contrast to fig. 3.8. In fig. 3.9, data from Spectro-Polarimeter on-board the Hinode spacecraft (see Ichimoto et al., 2008; Kosugi et al., 2007; Lites et al., 2013; Tsuneta et al., 2008) illustrates how high spatial resolution reveals intricate structural details within the observed active region. It also provides the full Stokes profiles with a well-sampled wavelength dimension, allowing for the fitting of complex atmospheric models to the measurements (the model atmosphere shown in fig. 3.9 is from the MODEST catalogue, see Castellanos Durán et al., 2024).

Generally, in spectropolarimetry, we strive towards increasing resolution in the spatial, spectral, and time dimensions of the data, to allow for more precise measurements. We can imagine, however, that an infinitely small sample in any of these dimesions would have no photons. This means, that the amount of photons is inversely proportional to the resolution, and therefore, our observations will always remain photon starved. To make due with the light that we receive, the trends in instrument development is towards better efficiency, more precise optical elements, more advanced sensors, as well as techniques to recover weak signals from measurement noise. Telescope size can also be increased to the same effect, as long as we do not intend to profit from the now newly possible higher resolution. In combination with these efforts, different approaches emerged for recording the four-dimensional spectropolarimetric data on two-dimensional image detectors, giving rise to a variety of approaches. Tables 3.1 and 3.2 give an overview of ground-based solar spectropolarimeters operating in the visible and infrared portion of the spectrum, which offer full Stokes polarimetry. These instruments are operated at various observatories, see Fig. 3.10 for their locations. Table 3.5 shows spectropolarimeters that operate in space, or have been launched on stratospheric balloons and sounding rockets. Tables 3.3, 3.4, and 3.6 offer a glance into the variety of implementations of these instruments, presenting some of their details. For more detailed overviews of spectropolarimetry, and some major scientific advances that it contributed to, as well as for prospects on future projects see Iglesias and Feller, 2019; Kleint and Gandorfer, 2017; Lagg et al., 2017.

The most convenient place to build and operate a solar telescope is **on the ground**. We can build large buildings to house them, and we encounter the least amount of constraints in their size, weight, flexibility and lifetime. However, by doing so, we have a significant challenge: *atmospheric seeing*. By atmospheric seeing we mean rapid local changes to the refractive in-

dex of the air due to atmospheric turbulence. This degrades image quality by smearing out the scene, and it induces polarimetric cross-talk (i.e., the uncontrolled mixing of the Stokes signals). Mitigating the effects of atmospheric seeing is possible on telescope level, on instrument level, or in post-processing. Strategies for telescopes include careful site selection, domeless or open designs (e.g. the Dutch Open Solar Telescope), evacuated light paths (e.g. the Domeless Solar Tower Telescope), adaptive optics (e.g. the Swedish Solar Telescope). The ideal instrument-level solution is freezing the motion of the atmosphere by increasing the time resolution of the data (see the Fast Solar Polarimeter, Iglesias et al., 2016), or short of that, reducing the seeing-induced polarimetric cross talk by the simultaneous recording of the Stokes vector (see the ZIMPOL instruments, Povel, 2001). Post-facto enhancement of data is possible with image reconstruction techniques (e.g. speckle reconstruction, see Weigelt, 1977, Multi Frame Blind Deconvolution and its variations, see van Kampen and Paxman, 1998, and its full generalisation, the Multi Object Multi Frame Blind Deconvolution, MOMFBD, see van Noort et al., 2005).

Overcoming seeing altogether is only possible by elevating the observatories above the atmosphere. The minimum elevation needed is into the stratosphere, which can be achieved by **balloons and sounding rocket** missions. Balloon experiments can provide several days of uninterrupted solar observations when launched from polar regions during summer. A highly successful balloon experiment has been Sunrise, launched from Kiruna, Sweden, in 2009, 2013, and 2024 (see Barthol et al., 2011; Berkefeld et al., 2011; Gandorfer et al., 2011; Solanki et al., 2010, 2017). Both the 2009 and 2013 Sunrise missions carried a spectropolarimeter (see Martínez Pillet et al., 2011), which delivered many important results (see, e.g., Bello González et al., 2010; Borrero et al., 2010; Danilovic, Beeck, et al., 2010; Lagg et al., 2010; Martínez González et al., 2011; Steiner et al., 2010, to mention but a few). The fully reconfigured instrument suit, that had flown successfully in 2024, carried three spectropolarimeters operating at various wavelengths (see Álvarez Herrero et al., 2022; Feller et al., 2020; Katsukawa et al., 2020). To mention but just one successful rocket experiment equipped with spectropolarimeters, the Chromospheric Lyman-alpha Spectropolarimeter (CLASP, see Narukage et al., 2011, 2016) imaged Lyman-alpha lines in the UV portion of the spectrum, inferring solar magnetic field properties from the Hanle effect (see Ishikawa et al., 2023). A summary of these instruments is given in tables 3.5 and 3.6.

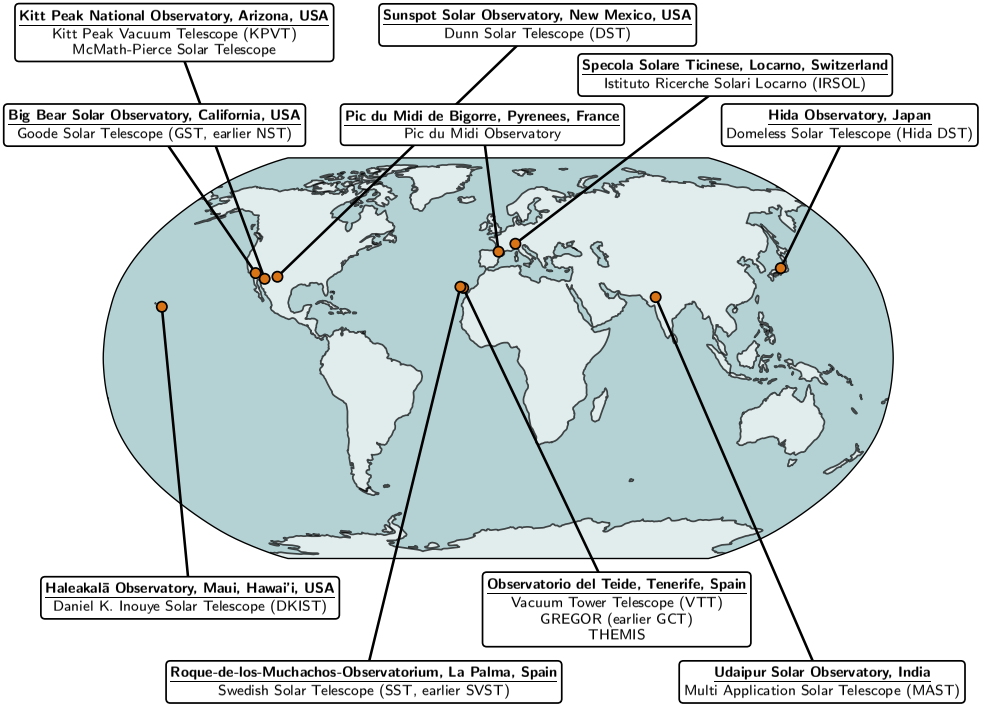

Figure 3.10. Ground based observatories around the world, that are equipped with full stokes solar spectropolarimeters. The instruments and some of their technical details are presented in Tables 3.1, 3.2, 3.3, and 3.4.
Image courtesy: P. H. Kärräng.

Table 3.1. Summary of ground-based solar spectropolarimeter implementations for full Stokes polarimetry in the visible and infrared wavelengths.

Instrument	Abbreviation	References	First light	Location(s)
Göttingen Fabry-Pérot spectrometer	Göttingen FPI	Bendlin and Volkmer, 1995	1990	VTT
Zurich Imaging Stokes polarimeter I,II	ZIMPOL-I,II	Povel, 2001	1994 (I), 1998 (II)	IRSOL, McMath-Pierce, DST, SST, VTT
Advanced Stokes Polarimeter	ASP	Tomczyk et al., 1992	1992	DST
Spectropolarimeter	IRSOL	Bianda et al., 1998	1995	IRSOL
La Palma Stokes Polarimeter	LPSP	Martínez Pillet et al., 1999	1998	SVST
Tenerifa Infrared Polarimeter I,II	TIP I,II	Martínez Pillet et al., 1999 (I), Collados et al., 2007 (II)	1998 (I), 2006 (II,VTT), 2008 (II,GREGOR)	VTT, GREGOR
Multiline spectroscopy mode of THEMIS	THEMIS/MTR	López Ariste et al., 2000	1999	THEMIS
Multichannel subtractive double pass mode of THEMIS	THEMIS/MSDP	Mein, 2002	2000	THEMIS
Diffraction Limited Spectro-Polarimeter	DLSP	Sankarasubramanian et al., 2004	2002	DST
Polarimetric Littrow Spectrograph	POLIS	Schmidt et al., 2003	2002	VTT
Interferometric BIdimensional Spectrometer	IBIS	Cavallini, 2006	2003	DST
Vector Spectromagnetograph for SOLIS	SOLIS/VSM	Keller et al., 2003	2003*	UA Agricultural Campus, Tucson, KPVT, GST
Lunette Jean Rösch	LJR	Arnaud et al., 2006	2004	Pic-du-Midi Observatory
Spectro-POlarimeter for INfrared and Optical Regions	SPINOR	Socas-Navarro et al., 2006	2004	DST
Visible Imaging Polarimeter	VIP**	Beck et al., 2010	2005	KPVT

Notes. [*] first light after significant upgrades; [**] VIP is an upgrade to the Telecentric Etalon SOlar Spectrometer (TESOS), Kentischer et al., 1998;

Table 3.2. Part 2 to Table 3.1.

Instrument	Abbreviation	References	First light	Location(s)
Spectropolarimetric capabilities of the Hida Domeless Solar Telescope	Hida	Hanaoka, 2009	2007	Hida DST
CRisp Imaging SpectroPolarimeter	CRISP	Scharmer et al., 2008	2008	SST
Facility InfraRed Spectropolarimeter	FIRS	Jaeggli et al., 2010	2009	DST
GREGOR Fabry-Pérot Interferometer	GFPI	Puschmann et al., 2012	2011	GREGOR
The GREGOR Infrared Spectrograph + TIP I,II	GRIS + TIP I,II	Collados et al., 2012	2012	GREGOR
Second Generation Near-Infrared Imaging Spectro-polarimeter	NIRIS	Cao et al., 2012	2015	GST
Fast Solar Spectropolarimeter	FSPI, FSPII	Iglesias et al., 2016	2015 (I), 2016 (II)	DST, SST
MAST Polarimeter	MAST Polarim.	Mathew, 2009	2015	MAST
Microlensed Hyperspectral Imager	MiHI	van Noort et al., 2022	2017*	SST
Multi-slit Image slicer based collimator-camera prototype + GRIS + TIP II	MuSICa p. + GRIS + TIP II	Calcines et al., 2014	2018	GREGOR
Visible Spectropolarimeter	ViSP	de Wijn et al., 2022	2021	DKIST
Diffraction Limited Near Infrared Spectropolarimeter	DL-NIRSP	Jaeggli et al., 2022	2021	DKIST
Cryogenic Near Infrared Spectropolarimeter	Cryo-NIRSP	Fehlmann et al., 2016	2022	DKIST
Helium SpectroPolarimeter	HeSP	priv. comm. M. van Noort, 2024	2022	SST
Polarimetric extension to the Fast Imaging Solar Spectrograph	FISS-SP	priv. comm. M. van Noort, 2024	2022	GST
Visible Tunable Filter	VTF	Schmidt et al., 2014		DKIST

Notes. [*] 2017 is the first year in which MiHI operated as a spectropolarimeter.

Table 3.3. Technical details of ground-based spectropolarimeter implementations for full Stokes polarimetry in the visible and infrared wavelengths. Theit locations are shown in Fig. 3.10. For an overview of these optical elements see e.g. Clarke, 2010, and for more details on spectrometry see Léna et al., 2012. See also Iglesias and Feller, 2019 for a more detailed discussion on spectropolarimeters.

Instrument	**Polarimetry**		**Spectrometry**	**Wavelength** [nm]
	Elements	**Modulation**		
Göttingen FPI	FLCs[1], Savart plate	single-beam	FPI[2]	
ZIMPOL-I,II	various, incl. piezo-elastic modulators, FLCs, Pockels cells	sinlge-beam	slit / FPI	$316-700$
ASP	rotating retarder, polarising beamsplitter	dual-beam	slit	$510-630$
IRSOL	rotatble $\lambda/2$ plate, Savart plate	single-beam	slit	>350
LSPS	FLCs, polarising beam splitter	dual-beam	slit	$450-750$
TIP I,II	FLCs, polarising beam splitter	dual-beam	any	$1000-2300$ (I), $400-2300$ (II)
THEMIS/MTR	rotating quarter-wave plates, polarising beam-splitter	dual-beam	slit	$500-900$
THEMIS/MSDP	rotating quarter-wave plates, polarising beam-splitter	dual-beam	MSDP[3]	$500-900$
DLSP	FLC, half and quarter wave retarders, linear polariser	single-beam	slit	630.25
POLIS	rotating retarder, zero order wave-plate, polarising beam splitter	dual-beam	slit	397, 630.15, 630.25
IBIS	NLCs[4], polarising beam splitter	dual-beam	FPIs	$580-860$
SOLIS/VSM	FLCs, Savart plate, polarising beam splitter	dual-beam	slit	630, 854, 1083[*]
LJR	LCVRs[5], linear polariser	single-beam	slit, MSDP[**]	$390-700$
SPINOR	rotating waveplate, polarising beam splitter	dual-beam	slit	$430-1565$
VIP	LCVRs, Wollaston prism	dual-beam	FPI	$450-750$

Notes. [*] Full Stokes polarimetry is only possible at 630 nm; [**] Only the slit spectrometer provides full Stokes polarimetry. [1] Ferro-electric Liquid Crystal Variable Retarder; [2] Fabry–Pérot interferometer; [3] Multichannel subtractive double pass; [4] Nematic Liquid Crystal Variable Retarder; [5]Liquid Crystal Variable Retarder

Table 3.4. Part 2 to Table 3.3.

Instrument	Polarimetry		Spectrometry	Wavelength [nm]
	Elements	Modulation		
Hida	FLCs, plate polariser	single-beam	slit	589.6, 630.3, 656.3
CRISP	LCVR, beam splitter	dual-beam	FPIs	510 – 860
FIRS	LCVRs, Wollaston prism	single-beam	multi slit	1083, 1565
GFPI	FLCs, polarising beam-splitters	dual-beam	FPI	530 – 860
GRIS+TIP I,II	FLC, polarising beam splitter	dual-beam	slit	1000 – 1800
NIRIS	rotating zero order waveplate, double Wollaston prisms	dual-beam	FPI	1000 – 1700
FSPI, FSPII	FLCs, $\lambda/4$ plate, $\lambda/2$ retarder, linear polariser (I), polarising beam-splitter (II)	single-beam (I), dual-beam (II)	any	450 – 750
MAST Polarim.	LCVRs, linear polariser		FPI	600 – 900
MiHI	FLCs, polarising beam splitter	dual-beam *	integral field, microlens array	450 – 750
MuSICa p.+ GRIS + TIP II	FLCs, polarising beam splitter	dual-beam	integral field, image slicer	1000 – 2300
ViSP	rotating retarders, polarising beamsplitter	dual-beam	slit (3 arms)	380 – 900
DL-NIRSP	rotating retarder, Wollaston prism	dual-beam	integral field, optical fibers	500 – 1800
Cryo-NIRSP	rotating retarder, polarising beam splitter	dual-beam	slit	1000 – 5000
HeSP	FLCs, polarising beam splitter	dual-beam	integral field, microlens array	10830
FISS-SP	FLCs, polarising beam splitter	dual beam		500 – 850
VTF	FLCs, polarising beam splitter	dual-beam	FPI	520 – 870

Notes. [*] prior to 2018, the polarimeter of MiHi was configured as single-beam.

Table 3.5. Selected solar spectropolarimeter implementations for full Stokes polarimetry for stratospheric balloons, sounding rockets and space missions.

Instrument	Abbreviation	References	Launch	Mission
Stratospheric balloon				
Imaging Magnetograph eXperiment	IMAX	Martínez Pillet et al., 2011	2009 (I), 2013 (II)	Sunrise I,II
Sunrise Chromospheric Insfrared Spectropolarimeter	SCIP	Katsukawa et al., 2020		Sunrise III
Sunrise Ultra-violet Spectropolarimeter and Imager	SUSI	Feller et al., 2020		Sunrise III
Tunable Magnetograph	TuMag	Álvarez Herrero et al., 2022		Sunrise III
Sounding rocket				
Chromospheric LAyer SpectroPolarimeter 1,2	CLASP 1,2	Narukage et al., 2011 (1), Narukage et al., 2016 (2)	2015 (1), 2019 (2)	CLASP
Spacecraft				
Michelson Doppler Imager	SOHO/MDI	Scherrer et al., 1995	1995	SOHO
Spectro-Polarimeter	Hinode/SP	Ichimoto et al., 2008	2006	Hinode
Narrowband Filter Imager	Hinode/NFI	Ichimoto et al., 2007	2006	Hinode
Helioseismic and Magnetic Imager	SDO/HMI	Schou et al., 2012	2010	SDO
Polarimetric and Helioseismic Imager	SO/PHI	Solanki et al., 2020	2020	Solar Orbiter

Table 3.6. Technical details of spectropolarimeter implementations for sounding rockets, stratospheric balloons and space missions, performing full Stokes polarimetry.

Instrument	Polarimetry		Spectrometry	Wavelength [nm]
	Elements	Modulation		
		Stratospheric balloon		
IMAX	LCVRs, polarising beam-splitter	dual-beam	FPI	524.9 – 632.8
SCIP	rotating waveplates, polarising beamsplitter	dual-beam	slit	770, 850
SUSI	rotating waveplate, polarising beamsplitter		slit	309 – 417
TuMag	LCVRs, polarising beam-splitter	dual-beam	FPI	525.02, 525.06, 517.3
		Sounding rocket		
CLASP 1,2	rotating waveplate, linear polariser	single-beam	slit	121.6(1), 280(2)
		Spacecraft		
SOHO/MDI	wave plates, polarising beam-splitters	single-beam	tunable Michelson interferometers, fixed Lyot filter	676.8
Hinode/SP	rotating waveplate, Savart-plate	dual-beam	slit	630.08 – 630.32
Hinode/NFI	rotating waveplate, polariser	single-beam	Lyot-type filter	517.2, 525.0, 557.6, 589.6, 630.0, 656.3
SDO/HMI	rotating waveplates, polarising beam-splitter	single-beam	tunable Michelson interferometers, tunable and fixed Lyot filters	617.3
SO/PHI	NLCs, linear polariser	single-beam	FPI	617.3

Another way of elevating the observatory above the atmosphere is by placing it in space. **Space observatories** are significantly more expensive than their ground-based or balloon-borne counterparts, however they are unrivalled in that they are able provide nearly or continuous 24-hour observations for decades, depending on their orbit design (such as the SDO/HMI, see Schou et al., 2012, or the planned Vigil/PMI, see Staub et al., 2020). They can also ensure access to unique vantage points (such as SO/PHI, see Solanki et al., 2020), as well as enable the observation of wavelengths that are inaccessible from the ground (see Stenflo, 2013 for a discussion). However, it must be noted, that at the present time, space missions offer far less flexibility compared to ground-based observations. Instrument concepts cannot be easily tested, replaced with improved versions, or repaired in space. In addition, there are stringent constraints on parameters like mass, volume, power consumption, telemetry data rates, and operational flexibility. Instrument designs tend to be simplified to ensure smooth operation, and often require special components that are capable of withstanding the launch and space environment. Furthermore, the diameter of the telescopes on space observatories are typically much smaller than their ground-based counterparts due to the high costs and technological limitations. As such, they can be seen as complementary to their ground-based counterparts.

To date, four space observatories have been launched with spectropolarimeters for studying the Sun. The Solar and Heliospheric Observatory (SOHO, launch date: 1995, see Domingo et al., 1995) orbits the L1 Sun-Earth Lagrangian point, enabling continuous observations. Among its instruments is the Michelson Doppler Imager (MDI, Scherrer et al., 1995), primarily designed as an imaging spectrometer for studying the manifestations of solar oscillations in the photosphere, however it has the possibility to insert polarisers in the light-path, enabling the measurement of the line-of-sight magnetic field. The Hinode mission (Kosugi et al., 2007) orbits Earth in a sun-synchronous orbit. It carries two spectropolarimeters for full Stokes polarimetry: the Spectro-Polarimeter (SP, see Ichimoto et al., 2008; Lites et al., 2013; Tsuneta et al., 2008), and the Narrowband Filter Instrument (NFI, see Ichimoto et al., 2007). The Solar Dynamics Observatory (SDO, see Pesnell et al., 2012) orbits Earth in geosynchronous orbit, carrying the Helioseismic and Magnetic Imager (HMI, see Schou et al., 2012), performing polarimetric measurements with unprecedented coverage since its launch. The latest space-observatory with a spectropolarimeter is the Solar Orbiter (see Müller et al., 2020). The mission has a heliocentric orbit, which during its lifetime gradually leaves the ecliptic plane. It carries the Polarimetric and Helioseismic Imager (SO/PHI, see Solanki et al., 2020, and also section 3.2.4), the first

spectropolarimeter on a deep space probe. SO/PHI is the first spectropolarimeter to offer a point of view that is out of the Sun-Earth line, and from 2025 also out of the ecliptic plane. See also tables 3.5 and 3.6 for a summary of these instruments.

The various space observatories have different operational concepts. For example, SDO/HMI provides unprecedented observational coverage. This not only facilitates long-term studies (see, e.g., Barekat et al., 2016; Irbah et al., 2019; Komm et al., 2020; Korpi-Lagg et al., 2022), but also serves as a reliable source to complement observations from ground-based or other space-based instruments (see, e.g., Albert et al., 2023b; Guglielmino et al., 2016; Huang et al., 2014; Schou et al., 2023; Scullion et al., 2014, among others). In contrast, SO/PHI provides data more sparsely, however, these data sets are unique due to Solar Orbiter's unprecedented orbit, enabling new studies (see, e.g. Albert et al., 2023b; Loeschl et al., 2024; Schou et al., 2023; Valori et al., 2023; Yang et al., 2023).

3.2.4. The Solar Orbiter / Polarimetric Helioseismic Imager

Solar Orbiter is a deep space mission for helioscience, launched in 2020, with unique orbit design. It carries a complementary suite of in-situ and remote sensing instruments to work together in studying the Sun (see Auchère et al., 2020; Müller et al., 2020; Zouganelis et al., 2020, and references therein, while fig. 3.11 shows an illustration of the spacecraft and its payload). The spacecraft orbits the Sun in highly elliptical orbits, approaching it as close as 0.28 Astronomical Units (AU). It leaves the ecliptic plane, to reach 25° heliocentric latitude during the nominal lifetime, and a final 34° angle in its extended mission phase. Figure 3.12 illustrates the evolution of the orbits during the lifetime of the mission.

As coordinated science is one of the main objectives of the Solar Orbiter mission, strong efforts are made to produce data sets overarching the different methods used in solar physics. This influenced decisions from the selection of the instrument suite, to the operating concept of the spacecraft and instruments. The unprecedented combination of measurements, and their unique vantage point enables new ways to study the Sun. Data from Solar Orbiter, beside combining the instruments it carries, is also used jointly with data from other space observatories and ground based telescopes (see Auchère et al., 2020; Velli et al., 2020 for discussions, and e.g., Albert et al., 2023b; Janvier et al., 2023; Kahil et al., 2022b; Yardley et al., 2023 for already published studies).

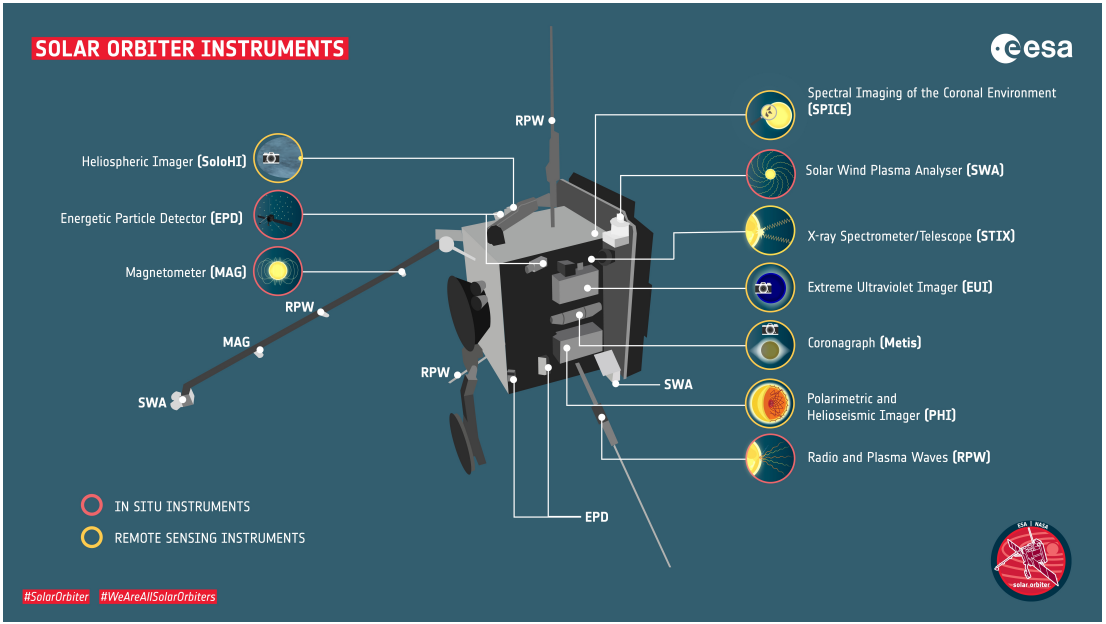

Figure 3.11. Solar Orbiter carries a unique combination of in-situ and remote sensing instruments to observe the Sun with different, complementary methods. Image credit: ESA. Acknowledgement: Work performed by ATG medialab under contract for ESA.

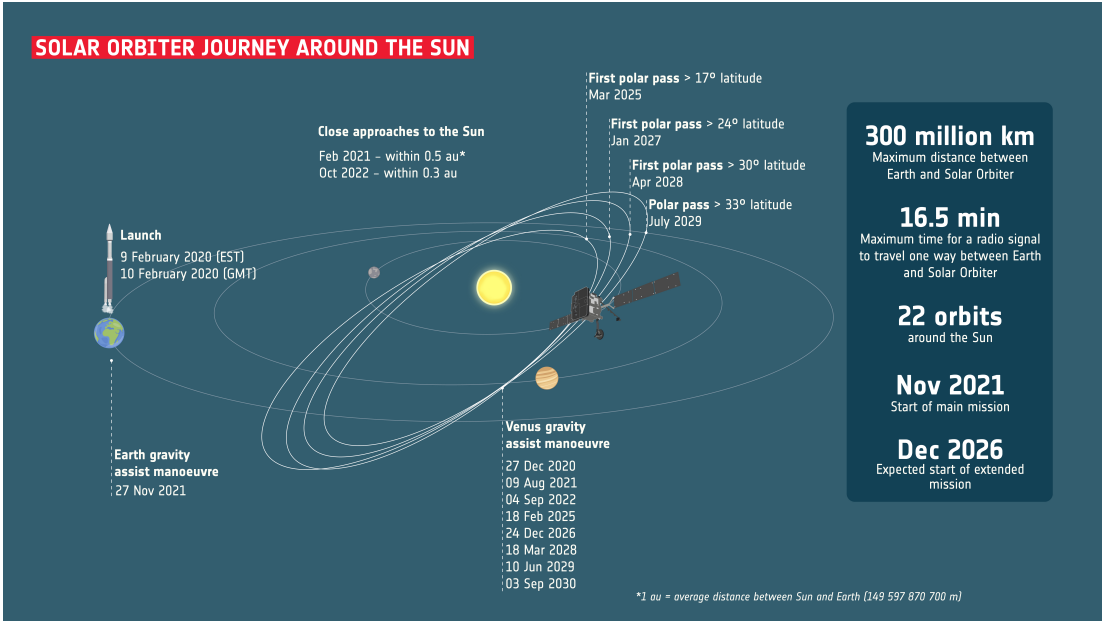

Figure 3.12. The orbits of Solar Orbiter are heliocentric, and highly elliptical. Arriving to the science orbits is achieved by a number of gravity assist manoeuvres with Earth and Venus. The orbital parameters are changed throughout its lifetime to move out of the ecliptic plane. Image credit: ESA - S.Poletti.

The **Polarimetric and Helioseismic Imager (PHI)** is the imaging spectropolarimeter on Solar Orbiter. It takes images of the Sun in the light of the FeI 617.3 nm absorption line, at six different wavelengths and four differently modulated polarisation states (one of the wavelengths sampled is at the continuum close by the line). We have a solar spectropolarimeter on a deep space mission for the first time, which besides the exciting science prospects, brings also a number of new challenges.

As it is sometimes the case for space-borne remote sensing payloads, the term *instrument* refers to both what is technically the telescope and the instrument itself, fully integrated into one system. SO/PHI can toggle bewteen two telescopes: the Full Disk Telescope (FDT) and the High Resolution Telescope (HRT, see Gandorfer et al., 2018), with aperture diameters of 17.5 mm and 140 mm, respectively. Both the telescopes ensure diffraction limited imaging at an angular resolution of a few arcseconds for FDT, and 1 arcsec for HRT. The image is critically sampled by a sensor, resulting in plate scales of 3.52 arcsec and 0.5 arcsec for the FDT and HRT, respectively. The HRT light path includes an additional image stabilisation system to compensate for spacecraft jitter, consisting of a camera, a tip-tilt mirror, and dedicated processing firmware inside the digital processing unit, collectively forming the correlation tracker. The instrument switches between the two telescopes with a feed-select mechanism. Light enters the instrument through the heat rejection entrance windows (HREWs), located in the heat shield of the spacecraft, allowing less than 4% of the total energy to pass the window through spectral filtering. See fig. 3.13 for the optical scheme of the SO/PHI instrument.

The **polarimetric modulation** of the light is done separately for the two telescopes, by two identical but separate polarisation modulation packages (PMPs). The modulator consists of two anti-parallel nematic liquid crystal variabler retarders (abbreviated NLC hereafter), oriented with their fast axes 45° with respect to each other. The NLCs contain anisotropic molecules, which can be oriented by an electric field. The analyser is a linear polariser, aligned with the fast axis of the first NLC.

The **spectral tuning** of the instrument is based on a Fabry-Pérot interferometer, and an order sorting prefilter. The light, at its entrance into the instrument, is filtered by the HREW, and only a 30 nm band is admitted, centred around the science wavelength. The order sorting prefilter is a 3-cavity interference filter, with a transmission profile with 0.28 nm full width at half maximum, designed to allow for the spacecraft orbital motion. The narrow band filtering is an opto-electrical, $LiNbO_3$ Fabry-Pérot etalon. The etalon crystal changes its refractive index when voltage is applied to it with

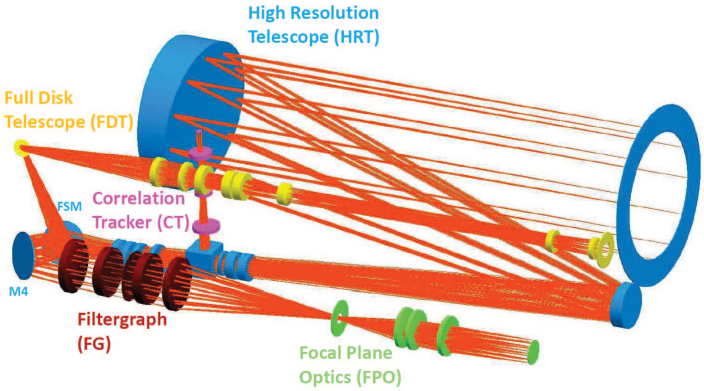

Figure 3.13. The optical design of SO/PHI. It is composed of two telescopes, a high resolution and a full disk telescope, switched with the feed select mechanism (marked as FSM on figure). Both light paths have a polarisation modulation package, containing both the modulator and analyser. They feed a common filtergraph, and record the image on the same focal plane assembly. Based on Figures 6 and 10 in Solanki et al., 2020.

0.3513 nm/V, called the tuning constant. See fig. 3.14 for the profiles of the filters.

The focal plane assembly of SO/PHI uses an active pixel sensor to record images. The sensor utilises CMOS technology and reads out pixels in rolling shutter mode. After the read-out, the data is transmitted to the Data Processing Unit.

The Data Processing Unit (DPU, Bubenhagen et al., 2013; Fiethe et al., 2007, 2012), illustrated in fig. 3.15, consists of the following processing components:

1. a Leon-3FT System Controller Microprocessor, responsible of decoding telecommands, system command, and telemetry packaging,
2. two Xilinx Virtex-4 Reconfigurable Field Programmable Gate Arrays (RFPGA-s), which are reconfigured for various functions in flight during data processing (see also Lange, 2020; Lange et al., 2017),
3. a Microsemi RTAX System Supervisor Field Programmable Gate Array (FPGA), which is radiation hardened and has a triple modular redundant design, supervising the dynamic reconfiguration of the system.

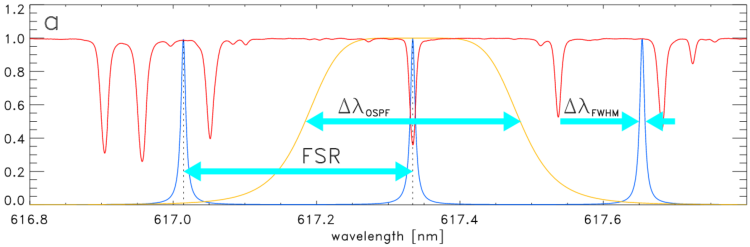

Figure 3.14. The SO/PHI spectrometric filter profile. The red line shows the solar spectrum in the vicinity of SO/PHI's working wavelength (see Neckel and Labs, 1984). The yellow line shows the profile of the order sorting prefilter ($\Delta\lambda_{OSPF}$ denoting its full width at half maximum), while the blue lines show the tunable filter profiles ($\Delta\lambda_{FWHM}$ denoting its full width at half maximum). The FSR denotes the free spectral range between the peaks of the tunable filter. Figure adapted from Solanki et al., 2020.

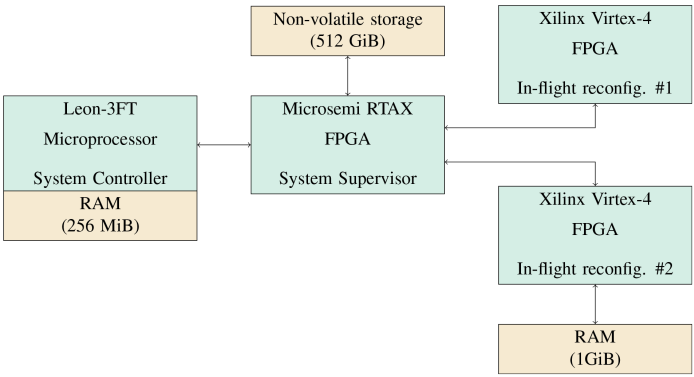

Figure 3.15. Main components of the SO/PHI Data Processing Unit (DPU). The green elements show the processing units, while the orange ones show the memory elements. Figure adapted from Albert et al., 2020b.

The DPU is complemented with a large non-volatile storage (512 GiB) for storing data at the instrument level. The microprocessor is equipped with 256 MiB processing memory, while one of the RFPGA-s is assisted with a 1 GiB processing memory in the image processing.

SO/PHI operations

Solar Orbiter implements an off-line commanding strategy, which means that all instrument commands must be defined before operations begin, in an iterative process. The commands are refined at various time scales, starting 6 months in advance, and finally specifying the commands 2 weeks prior to observations. This iterative process allows for coordination between the various instruments. Occasionally, short-term pointing decisions are made with as little as 3 days in advance, however these are only affecting the spacecraft attitude. This opportunity is given to be able to react to the unpredictable and dynamic solar scene. The operational constraints of the spacecraft require knowledge of the power requirements, telemetry needs, and Electromagnetic Compatibility (EMC) budget at the time of planning. This eliminates the possibility of autonomous on-board decision-making regarding instrument operations.

Many of the SO/PHI observations are placed at strategic points in each orbit. At these times of interest, the instrument can be operated within a handful of standard operation modes, observing time series at various cadences and for various time lengths. These are complemented with regular, single data sets of the full solar disc at a daily cadence. Observations and calibrations and data processing are all planned in coordination. It is made sure, that close condition calibration data is available for all the observations, and the science data sets are matched up with appropriate calibration data by the ground operations team. Operations are supported by a limited amount of low-latency data (with a maximum latency of 24h), aiming to provide an insight into the solar scene and assist with short-term decision-making regarding pointing.

Besides the regular observations, engineering tasks are also carried out regularly in the orbits. These times provide an opportunity to update and test the firmware and software of the instrument, as well as opportunity to perform other necessary engineering tests. Furthermore, there are also windows for servicing activities, such as detector annealing, that is, the heating up of the sensor to restore its state prior to the accumulated effects of radiation.

3.3. Science data reduction pipelines

3.3.1. Pipeline design

Data reduction is the process through which we transform raw observations into data that is ready for scientific use. It involves the removal of the effect of the mediums through which light passes (e.g., effects of the telescope and the instrument), as well as the elimination of data from sources outside of the scope of the observations (e.g. traces of highly energetic particles on the detector). This process consists of two main steps: first, determining the *calibration data*, which defines how we can correct instrumental effects, and second, applying this data to *calibrate the science data sets*. Additionally, data reduction can modify the data to better suit certain scientific purposes, such as, pixel binning or averaging of data sets.

Understanding the required steps for data reduction, along with their specific details, demands an understanding of both the instrument itself and the scientific objectives of the data.

The data reduction approach is shaped by key questions:

1. Who are the users of the data?
    a) *Instrument team.* During the prototype phase, data can undergo varied processing tailored to current instrument development needs. Standardised data pipelines may not be used.
    b) *Observers.* Observers may be utilising data to aid subsequent observations or analyse the data sets themselves. While a good level of instrument knowledge is present, a readily available, customisable pipeline is valuable for observers, as it reduces effort and improves the documentation of the data analysis.
    c) *Scientific community.* Broad user bases require standardised and well-documented data reduction for consistent data quality. Advanced users may access intermediate data levels and source code for added flexibility.
2. How much data is reduced?
    a) *Low data rate.* Manual reduction suits short time series or infrequent observations. Data sets can be processed individually, or in small batches, with the flexibility to specify various input files, including the calibration data.
    b) *High data rate.* Automation is crucial for data volumes that surpass what can be treated individually. Such processing involves minimal or no operator interaction, and it often includes the automated selection of the correct calibration data, or the automatic initiation of the processing.

3. How diverse is the data?
    a) *Unique.* During instrument development, observations are often performed with specific goals, and then each observation may be treated individually.
    b) *Various.* Adaptable data reduction pipelines are necessary when our data is from various targets, locations, or with varying data quality. In such cases different methods may be necessary for different data sets.
    c) *Comparable.* Highly efficient data reduction is possible when data sets exhibit little variation. Such systems, however, must include robust Failure Detection, Isolation, and Recovery capabilities to manage unexpected failures without significant disruptions to the data reduction.
4. How is communication with the instrument established?
    a) *Direct.* Ground-based observatories in accessible locations often allow on-site operations and data processing. Alternatively, data can also be transferred to off-site clusters.
    b) *Indirect.* Data from distributed telescope arrays or remote locations, raises questions about where different parts of data reduction should occur. Transferring large data amounts is generally feasible with the ever-developing ground infrastructure.
    c) *Limited.* Balloon-borne, sounding rocket missions, and space observatories face severe data transfer constraints. In the first two cases, large storage can allow for full data access after the recovery of the mission. In the case of deep space missions, the data budget is often a very important limiting factor.
5. How much time is available for data reduction?
    a) *Post-observations.* Data reduction timelines are flexible for many branches of astronomy, prioritising high-quality results over quick processing. As long as data remains relevant, the processing may take months without significant consequences.
    b) *(Near) real time.* Data can be time-critical when it is used immediately in decisions regarding observations or provided as a service, such as space weather monitoring. Such cases demand dedicated, quick-look data reduction pipelines, even if some accuracy and fault tolerance are sacrificed for speed. Processing may also be time-sensitive due to storage limitations, for example that the processing of the current data set must be completed before the next one is acquired. In such cases, pipelines are optimised for speed, potentially trading off complexity and data quality to meet time requirements.

3.3.2. State of the art in data reduction pipelines

We present a selection of the currently implemented data reduction pipelines in table 3.7. These pipelines are designed to process scientific data, offering a diverse range of implementations that exemplify the key questions guiding their design, as discussed in section 3.3.1. It is important to note that the categorisation presented here is qualitative, primarily serving as an indicator of what can be expected from the bibliographic references. The list is organised by the communication method with the instrument.

Science data reduction pipelines are typically executed on large computational resources, such as computing clusters. Prior to the Solar Orbiter mission, only three space science instruments were identified in the literature that performed scientific data reduction in orbit, utilising limited computational resources. These instruments are the Ion Release Module (IRM) on the Active Magnetospheric Particle Tracer Experiment (AMPTE), the Rème Plasma Analyzer on the Giotto Halley's Comet mission (see Curtis et al., 1989 for both of these instruments) and the Michelson Doppler Imager (MDI) on the Solar and Heliospheric Observatory (SOHO) (Scherrer et al., 1995). In all three cases, this approach was implemented to minimise the necessary data download and maximise the science return.

The AMPTE/IRM and the Giotto Halley's Comet mission/Rème Plasma Analyzer computed moments and calculated electron and ion pitch angle distribution of the analysed plasma on-board. The data reduction was carried out in real-time for both these instruments, with the time available for calculations determined by the measurement cadence. To meet the requirement with the available hardware, all operations were meticulously accounted for and partially coded in Assembly language. These were early attempts, during which the computing technology used dates back to the period between 1979 and 1982. While they were partially successful, they faced notable challenges, particularly concerning instrument calibration, and did not set a precedent for similar approaches in the following years.

Table 3.7. An impression of various selected astronomical data reduction pipelines.

Pipeline	Application	User range	Data rate	Data diversity	Commun.	Timing
CRISPRED [a]	Solar spectropol.	Observers and Sc. comm.	Low	Varied	Direct	Post obs.
sTools [b]	Solar spectrometry	Scientific community	Low	Varied	Direct	Post obs.
GPIES [c]	Exoplanet survey	Scientific community	High	Comparable	Direct	Near RT, Post obs.
IRIS [d]	Astronomical spectrom.	Observers and Sc. comm.	Low	Varied	Direct	Near RT, Post obs.
ORAC-DR [e]	Astronomical spectrom.	Observers and Sc. comm.	High	Varied	Direct	Post obs.
SIFONI [f]	Spectrometry	Observers	Low	Varied	Direct	Near RT, Post obs.
ESO Reflex [g]	Astronomy	Observers	High	Comparable	Direct	Post obs.
Cryo-NIRSP [h]	Solar spectropol.	Observers	High	Varied	Direct	Near RT
BANZAI [i]	Time-domain astronomy	Observers and Sc. comm.	High	Comparable	Indirect	Post obs.
ASTRI [j]	Cherenkov Telescopes	Scientific community	High	Comparable	Indirect	Post obs.
RTPhos [k]	Astron. Photometry	Observers	Low	Varied	Indirect	Near RT
Liverpool Tel. [l]	Astronomy	Observers	Low	Varied	Indirect	Near RT, Post obs.
IRM & Rème [m*]	Plasma physics	Observers	High	Comparable	Limited	Real time
MDI [n*]	Solar spectropol.	Scientific community	High	Comparable	Limited	Near RT, Post obs.
SDO/HMI [o]	Solar spectropol.	Scientific community	High	Comparable	Limited	Near RT, Post obs.
SO/PHI [p*]	Solar spectropol.	Scientific community	Low	Varied	Limited	Post obs.

Notes. [a] de la Cruz Rodríguez et al., 2015; [b] Kuckein et al., 2016; [c] Wang et al., 2018; [d] G. Walth et al., 2016; G. L. Walth et al., 2018; Chapin et al., 2020; [e] Cavanagh et al., 2003; [f] Hummel et al., 2006; [g] Freudling et al., 2013; [h] Williams et al., 2020; [i] McCully et al., 2018; [j] Lombardi et al., 2018; [k] Bogosavljevic and Ioannou, 2016; [l] Smith et al., 2016; [m] Curtis et al., 1989; [n] Scherrer et al., 1995; [o] Couvidat et al., 2016; [p] Solanki et al., 2020, see also section 3.3.3; [*] implements data reduction on limited computational resources to cope with data rate limitations.

In solar spectropolarimetry, the pioneer in on-board data processing was SOHO/MDI. Due to telemetry limitations, it performs some initial data reduction steps before the telemetry downlink. Using arithmetic operations and look-up tables, it calculates part of its data products on-board. This process is supplemented by additional processing on the ground. Calibration data processing is also performed on the ground, and the results are uploaded to the instrument for use in data reduction, resulting in a data reduction pipeline that is distributed between ground and on-board systems. Despite the fact that it has been regarded as a successful approach, when planning the successor instrument, the Helioseismic and Magnetic Imager (HMI) for the Solar Dynamics Observatory (SDO), the advantages of the geostationary orbit, with the ability to download all data for ground processing, were considered significant (see Schou et al., 2012).

3.3.3. Data processing on-board SO/PHI

The on-board data processing capabilities of SO/PHI are significantly more advanced than those implemented by similar instruments in the past. It performs on-board instrument calibration, it applies calibration data on the science data, it prepares the science data for the inversion of the Radiative Transfer Equation (RTE), followed by the inversion process itself.

Motivation

One SO/PHI observation comprises 24 images (4 polarisation states at 6 wavelengths). Each image contains 2048×2048 pixels and each pixel has 32 bits accuracy (in a 24.8 fixed point notation); therefore, one data set amounts to 402 MiB. Some usual observing programs require an observation every minute for up to six hours.

Moreover, for spectropolarimetric measurements, it is crucial to accurately determine the instrumental properties to avoid biases in the results. Some of these properties depend heavily on the instrumental environment, such as temperature. Given the highly elliptical orbits of Solar Orbiter (SO), the environment experienced by SO/PHI changes significantly within each orbit. Consequently, the classical approach of measuring several of these properties on the ground before launch would not provide sufficient accuracy. Instead, they must be determined from data collected in orbit, as close to operating conditions as possible. These properties, determined in flight, include the *dark field* of the sensor, the *flat field* of the instrument for both the HRT and FDT telescopes, and the *polarimetric cross-talk coefficients* from Stokes I to Q, U, and V, and Stokes V to Q and U.

Solar Orbiter's orbits, which are in resonance with Venus, result in constantly changing distances to Earth, leading to fluctuations in the available communication bandwidth. The guaranteed telemetry for SO/PHI is about 6 GiB in each orbit. Although, in practice the telemetry is two to four times the guaranteed amount, this would still only allow us to download less than 100 raw data sets in each orbit, a significant discrepancy from the desired amount. This challenge is further compounded by the necessity for calibration data, which is also collected in orbit.

To address this challenge, we extended the on-board processing scheme. The SO/PHI is characterised in flight through dedicated observations conducted for this purpose. From these observations, we derive the calibration data on-board, which is used to correct the raw science observables directly in orbit. This on-board correction aims to eliminate the need for downloading calibration data, and prepares the data set for the inversion of the polarised RTE. The science data reduction pipeline produces the sought physical parameters: the three components of the magnetic field vector (magnitude, azimuth, and elevation), and the line of sight velocity, complemented by the continuum total intensity image.

Overview of the processing

The SO/PHI must execute all on-board data reduction with a high degree of autonomy. Solar Orbiter's orbit design is such, that at times, the spacecraft is behind the Sun from Earth's point of view, providing an additional vantage point for solar observations. However, this position interrupts communications for a few days time and increases data latency to up to six months. These are periods when the instrument collects both science and calibration data, necessitating the capability to execute all functions without operator intervention. The data processing does not occur in real-time but during intervals when the instrument is not actively observing. Therefore, in theory, data processing could be limited to times when user interaction is possible; however, it would both use valuable telemetry volume, and severely complicate operations. Therefore, all data processing is implemented to execute autonomously.

The on-board processing scheme generates various data products at its different stages. The DPU initiates all data processing at the read-out stage by accumulating multiple *frames* into a single *image*. These images are acquired according to the commanded data acquisition scheme, scanning the six wavelengths and four polarisation states, and are organised into a *data set*, referred to as *raw data set*. These can be science data, or collected for instrument calibration and characterisation with separate observation

programs. The observed data sets are subsequently transferred to the non-volatile memory, where they can be stored for later processing.

Any further processing can be executed at a later point in time, starting by reading these data sets from the non-volatile memory. We have three types of processing pipelines: (1) calculation of operational parameters, (2) instrument characterisation, and (3) science data processing. For the correct functioning of SO/PHI, the operational parameters need to be determined. These are the optimal *focus position*, *exposure time*, and the correct *filtergraph voltages* for the adequate sampling of the absorption line. Based on data observed for this purpose, we calculate these parameters, and apply the necessary changes to the instrument, which must precede any other observation. The calibration data processing routines determine the dark and flat fields. Once they are determined, they are stored for later usage, serving as input for the science data processing. The results of the science data processing pipeline are also stored in the non-volatile memory, awaiting a command that initiates their compression and packaging into *telemetry packets*, and then their transfer to the spacecraft platform, from where they will be transmitted to ground.

For the detailed description of SO/PHI's on-board data processing system, see Albert et al., 2018; Albert et al., 2020b; Albert et al., 2020a, presented in appendices A to C. For details on the verification of the system, see Albert et al., 2019; Albert et al., 2023a, shown in appendices D, and E. For the application of the results from the on-board pipeline, see Albert et al., 2023b in appendix F.

4. Conclusions and outlook

The Polarimetric and Helioseismic Imager on-board the Solar Orbiter spacecraft is the first spectropolarimeter to fly on a deep space mission, and as a pioneer, it has faced various challenges. One of these challenges is the large discrepancy between the produced data volume, and the available telemetry. To address this problem, we implemented full on-board data reduction, including the inversion of the radiative transfer equation, done for the very first time for a solar spectropolarimeter. This work presents the design, implementation and verification of the high level software system that performs the scientific data reduction.

The data reduction system of SO/PHI has successfully delivered physical parameters from orbit that could be used in studies of solar phenomena. While the system works successfully, another significant upgrade is currently underway to maximise the data quality it delivers. A considerable effort has been invested in understanding the behaviour of the data received from SO/PHI, and in finding methods to further improve its quality. Many of these procedures are well consolidated on ground, and can be incorporated into the on-board processing. This means, adding further data processing steps both to the instrument characterisation and the science data reduction pipelines. Another essential aspect to be investigated during this period is the optimisation of the pipeline run-time to ensure that the planned increase of complexity does not delay data processing beyond the available time.

SO/PHI's data on-board processing system represents a new step in the context of on-board processing of scientific data. While its implementation presented a significant effort, its success demonstrates the viability of this option for future instruments. As an example, the Photospheric Magnetic Field Imager (PMI) on-board the Vigil mission (see Staub et al., 2020), currently in implementation, is facing similar challenges as SO/PHI did due to the limited telemetry volumes. The PMI implements a similar approach, basing its processing scheme on that implemented for SO/PHI, with the increased requirement for near real-time results. In a different application, the eXTP mission, that is an X-ray astronomical observatory in development, also opted for on-board processing to maximise data rate for two of their instruments (see Xiong et al., 2022). The aforementioned instruments are by far not unique in facing severe telemetry limitations, and the processing of the science observations on-board can be a powerful tool to enable missions and instruments that would not be feasible otherwise.

Bibliography

Albert, K., Hirzberger, J., Busse, D., Blanco Rodríguez, J., Castellanos Durán, J. S., Cobos Carrascosa, J. P., Fiethe, B., Gandorfer, A., Guan, Y., Kolleck, M., Lagg, A., Lange, T., Michalik, H., Solanki, S. K., del Toro Iniesta, J. C., & Woch, J. (2019). Performance Analysis of the SO/PHI Software Framework for On-board Data Reduction. *Proc. ASP Conference Astronomical Data Analysis Software and Systems XXVIII*.

Albert, K., Hirzberger, J., Busse, D., Castellanos Durán, J. S., Gutierrez-Marques, P., & Kolleck, M. (2020a). Metadata and their importance in SO/PHI's on-board data processing. *Proc. ASP Conference Astronomical Data Analysis Software and Systems XXIX*.

Albert, K., Hirzberger, J., Busse, D., Lange, T., Kolleck, M., Fiethe, B., Orozco Suárez, D., Woch, J., Schou, J., Blanco Rodríguez, J., Gandorfer, A., Guan, Y., Cobos Carrascosa, J. P., Hernández Expósito, D., del Toro Iniesta, J. C., Solanki, S. K., & Michalik, H. (2018). Autonomous on-board data processing and instrument calibration software for the SO/PHI. *Proc. SPIE, Software and Cyberinfrastructure for Astronomy V*, *707*, 10707 - 10707 –9. https://doi.org/10.1117/12.2311718

Albert, K., Krivova, N. A., Hirzberger, J., Solanki, S. K., Moreno Vacas, A., Orozco Suárez, D., Albelo Jorge, N., Appourchaux, T., Alvarez-Herrero, A., Blanco Rodríguez, J., Gandorfer, A., Gutierrez-Marques, P., Kahil, F., Kolleck, M., Volkmer, R., del Toro Iniesta, J. C., Woch, J., Fiethe, B., Pérez-Grande, I., … Valori, G. (2023b). Intensity contrast of solar network and faculae close to the solar limb, observed from two vantage points. *Astron. Astrophys.*, *678*, Article A163, A163. https://doi.org/10.1051/0004-6361/202346037

Albert, K., Hirzberger, J., Castellanos Durán, J. S., Orozco Suárez, D., Woch, J., Michalik, H., & Solanki, S. K. (2023a). Accuracy Analysis of the On-board Data Reduction Pipeline for the Polarimetric and Helioseismic Imager on the Solar Orbiter Mission. *Solar Phys.*, *298*(4), Article 58, 58. https://doi.org/10.1007/s11207-023-02149-y

Albert, K., Hirzberger, J., Kolleck, M., Jorge, N. A., Busse, D., Rodríguez, J. B., Carrascosa, J. P. C., Fiethe, B., Gandorfer, A., Germerott, D., Guan, Y., Guerrero, L., Gutierrez-Marques, P., Expósito, D. H., Lange, T., Michalik, H., Suárez, D. O., Schou, J., Solanki, S. K., … Woch, J. (2020b). Autonomous on-board data processing and instrument calibration software for the Polarimetric and Helioseismic Imager on-board the

Solar Orbiter mission. *J. of Astron. Telescopes, Instrum., and Syst.*, *6*, Article 048004, 048004. https://doi.org/10.1117/1.JATIS.6.4.048004

Álvarez Herrero, A., Fernández-Medina, A., Cebollero, M., Garranzo-García, D., Núñez, A., Gonzalo, A., Sánchez, A., Villanueva, J., García Parejo, P., Campos-Jara, A., Silva-López, M., San Julián, R., & Laguna, H. (2022, August). TuMag for SUNRISE III mission: development of the optical unit of an imaging spectropolarimeter. In C. J. Evans, J. J. Bryant, & K. Motohara (Eds.), *Proc. SPIE, Ground-based and Airborne Instrumentation for Astronomy IX* (121842G, Vol. 12184). https://doi.org/10.1117/12.2629391

Arnaud, J., Roudier, T., Malherbe, M., & Moity, J. (2006, December). Solar Spectro-Polarimetry at Pic-du-Midi/LJR. In R. Casini & B. W. Lites (Eds.), *Proc. ASP Conference Solar Polarization 4* (p. 167, Vol. 358).

Athay, R. G., & Lites, B. W. (1972). F i Ionization and Excitation Equilibrium in the Solar Atmosphere. *Astrophys. J.*, *176*, 809. https://doi.org/10.1086/151679

Auchère, F., Andretta, V., Antonucci, E., Bach, N., Battaglia, M., Bemporad, A., Berghmans, D., Buchlin, E., Caminade, S., Carlsson, M., Carlyle, J., Cerullo, J. J., Chamberlin, P. C., Colaninno, R. C., Davila, J. M., De Groof, A., Etesi, L., Fahmy, S., Fineschi, S., … Zouganelis, I. (2020). Coordination within the remote sensing payload on the Solar Orbiter mission. *Astron. Astrophys.*, *642*, Article A6, A6. https://doi.org/10.1051/0004-6361/201937032

Babcock, H. W. (1961). The Topology of the Sun's Magnetic Field and the 22-YEAR Cycle. *Astrophys. J.*, *133*, 572. https://doi.org/10.1086/147060

Bailén, F. J., Orozco Suárez, D., Blanco Rodríguez, J., del Toro Iniesta, J. C., Strecker, H., Moreno Vacas, A., Santamarina Guerrero, P., Hirzberger, J., Albert, K., Albelo Jorge, N., Appourchaux, T., Alvarez-Herrero, A., Gandorfer, A., Germerott, D., Guerrero, L., Gutierrez-Marques, P., Kahil, F., Kolleck, M., Solanki, S. K., … Valori, G. (2024). Determination of the SO/PHI-HRT wavefront degradation using multiple defocused images. *Astron. Astrophys.*, *681*, Article A58, A58. https://doi.org/10.1051/0004-6361/202346019

Barekat, A., Schou, J., & Gizon, L. (2016). Solar-cycle variation of the rotational shear near the solar surface. *Astron. Astrophys.*, *595*, Article A8, A8. https://doi.org/10.1051/0004-6361/201628673

Barthol, P., Gandorfer, A., Solanki, S. K., Schüssler, M., Chares, B., Curdt, W., Deutsch, W., Feller, A., Germerott, D., Grauf, B., Heerlein, K., Hirzberger, J., Kolleck, M., Meller, R., Müller, R., Riethmüller, T. L., Tomasch, G., Knölker, M., Lites, B. W., … Schmidt, E. (2011). The

Sunrise Mission. *Solar Phys.*, *268*(1), 1–34. https://doi.org/10.1007/s11207-010-9662-9

Beck, C., Bellot Rubio, L. R., Kentischer, T. J., Tritschler, A., & Del Toro Iniesta, J. C. (2010). Two-dimensional solar spectropolarimetry with the KIS/IAA Visible Imaging Polarimeter. *Astron. Astrophys.*, *520*, Article A115, A115. https://doi.org/10.1051/0004-6361/200913441

Bello González, N., Franz, M., Martínez Pillet, V., Bonet, J. A., Solanki, S. K., del Toro Iniesta, J. C., Schmidt, W., Gandorfer, A., Domingo, V., Barthol, P., Berkefeld, T., & Knölker, M. (2010). Detection of Large Acoustic Energy Flux in the Solar Atmosphere. *Astrophys. J. Lett.*, *723*(2), L134–L138. https://doi.org/10.1088/2041-8205/723/2/L134

Bellot Rubio, L., Rodríguez Hidalgo, I., Collados, M., Khomenko, E., & Ruiz Cobo, B. (2001). Observation of Convective Collapse and Upward-moving Shocks in the Quiet Sun. *Astrophys. J.*, *560*(2), 1010–1019. https://doi.org/10.1086/323063

Bellot Rubio, L., & Orozco Suárez, D. (2019). Quiet Sun magnetic fields: an observational view. *Living Rev. in Sol. Phys.*, *16*(1), Article 1, 1. https://doi.org/10.1007/s41116-018-0017-1

Bendlin, C., & Volkmer, R. (1995). The two-dimensional spectrometer in the German Vacuum Tower Telescope/Tenerife. From observations to results. *Astron. Astrophys. Suppl.*, *112*, 371.

Berkefeld, T., Schmidt, W., Soltau, D., Bell, A., Doerr, H. P., Feger, B., Friedlein, R., Gerber, K., Heidecke, F., Kentischer, T., v. d. Lühe, O., Sigwarth, M., Wälde, E., Barthol, P., Deutsch, W., Gandorfer, A., Germerott, D., Grauf, B., Meller, R., … Title, A. M. (2011). The Wave-Front Correction System for the Sunrise Balloon-Borne Solar Observatory. *Solar Phys.*, *268*(1), 103–123. https://doi.org/10.1007/s11207-010-9676-3

Bianda, M., Solanki, S. K., & Stenflo, J. O. (1998). Hanle depolarisation in the solar chromosphere. *Astron. Astrophys.*, *331*, 760–770.

Bogosavljevic, M., & Ioannou, Z. (2016). Implementing a real-time data stream for time-series stellar photometry. *Proc. SPIE, Software and Cyberinfrastructure for Astronomy IV*, *9913*, 9913 - 9913 –9. https://doi.org/10.1117/12.2232248

Borrero, J. M., Martínez-Pillet, V., Schlichenmaier, R., Solanki, S. K., Bonet, J. A., del Toro Iniesta, J. C., Schmidt, W., Barthol, P., Gandorfer, A., Domingo, V., & Knölker, M. (2010). Supersonic Magnetic Upflows in Granular Cells Observed with SUNRISE/IMAX. *Astrophys. J. Lett.*, *723*(2), L144–L148. https://doi.org/10.1088/2041-8205/723/2/L144

Borrero, J. M., & Ichimoto, K. (2011). Magnetic Structure of Sunspots. *Living Rev. in Sol. Phys.*, *8*(1), Article 4, 4. https://doi.org/10.12942/lrsp-2011-4

Brandenburg, A., & Subramanian, K. (2005). Astrophysical magnetic fields and nonlinear dynamo theory. *Physics Reports*, *417*(1-4), 1–209. https://doi.org/10.1016/j.physrep.2005.06.005

Bray, R. J., Loughhead, R. E., & Durrant, C. J. (1984). *The solar granulation.*

Bray, R. J., Loughhead, R. E., & Durrant, C. J. (2009). *The Solar Granulation.*

Bruls, J. H. M. J., Rutten, R. J., & Shchukina, N. G. (1992). The formation of helioseismology lines. I. NLTE effects in alkali spectra. *Astron. Astrophys.*, *265*(1), 237–256.

Bubenhagen, F., Fiethe, B., Lange, T., Michalik, H., & Michel, H. (2013). Reconfigurable platforms for data processing on scientific space instruments. *Proc. of 2013 NASA/ESA Conference on Adaptive Hardware and Systems (AHS-2013)*, 63–70.

Buehler, D., Lagg, A., & Solanki, S. K. (2013). Quiet Sun magnetic fields observed by Hinode: Support for a local dynamo. *Astron. Astrophys.*, *555*, Article A33, A33. https://doi.org/10.1051/0004-6361/201321152

Buehler, D., Lagg, A., Solanki, S. K., & van Noort, M. (2015). Properties of solar plage from a spatially coupled inversion of Hinode SP data. *Astron. Astrophys.*, *576*, Article A27, A27. https://doi.org/10.1051/0004-6361/201424970

Buehler, D., Lagg, A., van Noort, M., & Solanki, S. K. (2016). Formation of a solar Hα filament from orphan penumbrae. *Astron. Astrophys.*, *589*, Article A31, A31. https://doi.org/10.1051/0004-6361/201527571

Buehler, D., Lagg, A., van Noort, M., & Solanki, S. K. (2019). A comparison between solar plage and network properties. *Astron. Astrophys.*, *630*, Article A86, A86. https://doi.org/10.1051/0004-6361/201833585

Calchetti, D., Stangalini, M., Jafarzadeh, S., Valori, G., Albert, K., Albelo Jorge, N., Alvarez-Herrero, A., Appourchaux, T., Balaguer Jiménez, M., Bellot Rubio, L. R., Blanco Rodríguez, J., Feller, A., Gandorfer, A., Germerott, D., Gizon, L., Guerrero, L., Gutierrez-Marques, P., Hirzberger, J., Kahil, F., … Woch, J. (2023). Spectropolarimetric investigation of magnetohydrodynamic wave modes in the photosphere: First results from PHI on board Solar Orbiter. *Astron. Astrophys.*, *674*, Article A109, A109. https://doi.org/10.1051/0004-6361/202245826

Calcines, A., López, R. L., Collados, M., & Vega Reyes, N. (2014, July). MuSICa image slicer prototype at 1.5-m GREGOR solar telescope. In S. K. Ramsay, I. S. McLean, & H. Takami (Eds.), *Proc. SPIE, Ground-based and Airborne Instrumentation for Astronomy V* (p. 91473I, Vol. 9147). https://doi.org/10.1117/12.2053577

Cameron, R., & Schüssler, M. (2007). Solar Cycle Prediction Using Precursors and Flux Transport Models. *Astrophys. J.*, *659*(1), 801–811. https://doi.org/10.1086/512049

Cameron, R., & Schüssler, M. (2015). The crucial role of surface magnetic fields for the solar dynamo. *Science*, *347*(6228), 1333–1335. https://doi.org/10.1126/science.1261470

Cao, W., Goode, P. R., Ahn, K., Gorceix, N., Schmidt, W., & Lin, H. (2012, December). NIRIS: The Second Generation Near-Infrared Imaging Spectro-polarimeter for the 1.6 Meter New Solar Telescope. In T. R. Rimmele, A. Tritschler, F. Wöger, M. Collados Vera, H. Socas-Navarro, R. Schlichenmaier, M. Carlsson, T. Berger, A. Cadavid, P. R. Gilbert, P. R. Goode, & M. Knölker (Eds.), *Proc. of Second ATST-EAST meeting: Magnetic fields from the photosphere to the corona.* (p. 291, Vol. 463).

Castellanos Durán, J. S., Milanovic, N., Korpi-Lagg, A., Löptien, B., van Noort, M., & Solanki, S. K. (2024). The MODEST catalog of depth-dependent spatially coupled inversions of sunspots observed by Hinode/SOT-SP. *arXiv e-prints*, Article arXiv:2403.06960, arXiv:2403.06960. https://doi.org/10.48550/arXiv.2403.06960

Cattaneo, F. (1999, January). Dynamo Theory and the Origin of Small Scale Magnetic Fields. In A. Hanslmeier & M. Messerotti (Eds.), *Motions in the solar atmosphere* (pp. 119–137, Vol. 239). https://doi.org/10.1007/978-94-015-9331-1_5

Cavallini, F. (2006). IBIS: A New Post-Focus Instrument for Solar Imaging Spectroscopy. *Solar Phys.*, *236*(2), 415–439. https://doi.org/10.1007/s11207-006-0103-8

Cavanagh, B., Hirst, P., Jenness, T., Economou, F., Currie, M. J., Todd, S., & Ryder, S. D. (2003). ORAC-DR: One Pipeline for Multiple Telescopes. In H. E. Payne, R. I. Jedrzejewski, & R. N. Hook (Eds.), *Proc. ASP Confrerence Astronomical Data Analysis Software and Systems XII* (p. 237, Vol. 295).

Centeno, R., Blanco Rodríguez, J., Del Toro Iniesta, J. C., Solanki, S. K., Barthol, P., Gandorfer, A., Gizon, L., Hirzberger, J., Riethmüller, T. L., van Noort, M., Orozco Suárez, D., Berkefeld, T., Schmidt, W., Martínez Pillet, V., & Knölker, M. (2017). A Tale of Two Emergences: Sunrise II Observations of Emergence Sites in a Solar Active Region. *Astrophys. J. Suppl.*, *229*(1), Article 3, 3. https://doi.org/10.3847/1538-4365/229/1/3

Chapin, E. L., Dunn, J., Nakamoto, T., Sohn, J. S., Surya, A., Johnson, C., Wright, S., Zonca, A., Andersen, D., Chisholm, E., Gillies, K., Hayano, Y., Herriot, G., Kerley, D., Larkin, J., & Suzuki, R. (2020, December). The Infrared Imaging Spectrograph (IRIS) for TMT: final software

design update. In J. C. Guzman & J. Ibsen (Eds.), *Proc. SPIE, Software and Cyberinfrastructure for Astronomy VI* (114520R, Vol. 11452). https://doi.org/10.1117/12.2561952

Christensen-Dalsgaard, J. (2002). Helioseismology. *Reviews of Modern Physics*, *74*(4), 1073–1129. https://doi.org/10.1103/RevModPhys.74.1073

Clarke, D. (2010). The Basics of Polarimetric Elements. In *Stellar polarimetry* (pp. 101–126). Wiley-Blackwell. https://doi.org/10.1002/9783527628322.ch6

Collados, M., Lagg, A., Díaz Garcí A, J. J., Hernández Suárez, E., López López, R., Páez Mañá, E., & Solanki, S. K. (2007, May). Tenerife Infrared Polarimeter II. In P. Heinzel, I. Dorotovič, & R. J. Rutten (Eds.), *The physics of chromospheric plasmas* (p. 611, Vol. 368).

Collados, M., López, R., Páez, E., Hernández, E., Reyes, M., Calcines, A., Ballesteros, E., Díaz, J. J., Denker, C., Lagg, A., Schlichenmaier, R., Schmidt, W., Solanki, S. K., Strassmeier, K. G., von der Lühe, O., & Volkmer, R. (2012). GRIS: The GREGOR Infrared Spectrograph. *Astronomische Nachrichten*, *333*(9), 872. https://doi.org/10.1002/asna.201211738

Couvidat, S., Schou, J., Hoeksema, J. T., Bogart, R. S., Bush, R. I., Duvall, T. L., Liu, Y., Norton, A. A., & Scherrer, P. H. (2016). Observables Processing for the Helioseismic and Magnetic Imager Instrument on the Solar Dynamics Observatory. *Solar Phys.*, *291*(7), 1887–1938.

Curtis, D. W., Carlson, C. W., Lin, R. P., Paschmann, G., & Reme, H. (1989). Onboard data analysis techniques for space plasma particle instruments. *Review of Sci. Instr.*, *60*, 372–380. https://doi.org/10.1063/1.1140441

Danilovic, S., Beeck, B., Pietarila, A., Schüssler, M., Solanki, S. K., Martínez Pillet, V., Bonet, J. A., del Toro Iniesta, J. C., Domingo, V., Barthol, P., Berkefeld, T., Gandorfer, A., Knölker, M., Schmidt, W., & Title, A. M. (2010). Transverse Component of the Magnetic Field in the Solar Photosphere Observed by SUNRISE. *Astrophys. J. Lett.*, *723*(2), L149–L153. https://doi.org/10.1088/2041-8205/723/2/L149

Danilovic, S., Schüssler, M., & Solanki, S. K. (2010a). Magnetic field intensification: comparison of 3D MHD simulations with Hinode/SP results. *Astron. Astrophys.*, *509*, Article A76, A76. https://doi.org/10.1051/0004-6361/200912283

Danilovic, S., Schüssler, M., & Solanki, S. K. (2010b). Probing quiet Sun magnetism using MURaM simulations and Hinode/SP results: support for a local dynamo. *Astron. Astrophys.*, *513*, Article A1, A1. https://doi.org/10.1051/0004-6361/200913379

de la Cruz Rodríguez, J., Löfdahl, M. G., Sütterlin, P., Hillberg, T., & Rouppe van der Voort, L. (2015). CRISPRED: A data pipeline for the CRISP imaging spectropolarimeter. *Astron. Astrophys.*, *573*, Article A40, A40. https://doi.org/10.1051/0004-6361/201424319

de la Cruz Rodríguez, J., & van Noort, M. (2017). Radiative Diagnostics in the Solar Photosphere and Chromosphere. *Space Sci. Rev.*, *210*(1), 109–143. https://doi.org/10.1007/s11214-016-0294-8

de Wijn, A. G., Casini, R., Carlile, A., Lecinski, A. R., Sewell, S., Zmarzly, P., Eigenbrot, A. D., Beck, C., Wöger, F., & Knölker, M. (2022). The Visible Spectro-Polarimeter of the Daniel K. Inouye Solar Telescope. *Solar Phys.*, *297*(2), Article 22, 22. https://doi.org/10.1007/s11207-022-01954-1

de Wijn, A. G., Stenflo, J. O., Solanki, S. K., & Tsuneta, S. (2009). Small-Scale Solar Magnetic Fields. *Space Sci. Rev.*, *144*(1-4), 275–315. https://doi.org/10.1007/s11214-008-9473-6

del Toro Iniesta, J. C. (2003). *Introduction to spectropolarimetry*. Cambridge university press.

Dikpati, M., & Gilman, P. A. (2001). Flux-Transport Dynamos with α-Effect from Global Instability of Tachocline Differential Rotation: A Solution for Magnetic Parity Selection in the Sun. *Astrophys. J.*, *559*(1), 428–442. https://doi.org/10.1086/322410

Domingo, V., Ermolli, I., Fox, P., Fröhlich, C., Haberreiter, M., Krivova, N., Kopp, G., Schmutz, W., Solanki, S. K., Spruit, H. C., Unruh, Y., & Vögler, A. (2009). Solar Surface Magnetism and Irradiance on Time Scales from Days to the 11-Year Cycle. *Space Sci. Rev.*, *145*(3-4), 337–380. https://doi.org/10.1007/s11214-009-9562-1

Domingo, V., Fleck, B., & Poland, A. I. (1995). SOHO: The Solar and Heliospheric Observatory. *Space Sci. Rev.*, *72*(1), 81–84. https://doi.org/10.1007/BF00768758

Faurobert, M., & Ricort, G. (2015). Solar-cycle variations of the internetwork magnetic field. *Astron. Astrophys.*, *582*, Article A95, A95. https://doi.org/10.1051/0004-6361/201526298

Faurobert, M., & Ricort, G. (2021). Magnetic flux structuring of the quiet Sun internetwork. Center-to-limb analysis of solar-cycle variations. *Astron. Astrophys.*, *651*, Article A21, A21. https://doi.org/10.1051/0004-6361/202140705

Fehlmann, A., Giebink, C., Kuhn, J. R., Messersmith, E. J., Mickey, D. L., Scholl, I. F., James, D., Hnat, K., Schickling, G., & Schickling, R. (2016, August). Cryogenic near infrared spectropolarimeter for the Daniel K. Inouye Solar Telescope. In C. J. Evans, L. Simard, & H. Takami (Eds.),

Proc. SPIE, Ground-based and Airborne Instrumentation for Astronomy VI (p. 99084D, Vol. 9908). https://doi.org/10.1117/12.2232218

Feller, A., Gandorfer, A., Iglesias, F. A., Lagg, A., Riethmüller, T. L., Solanki, S. K., Katsukawa, Y., & Kubo, M. (2020). The SUNRISE UV Spectropolarimeter and imager for SUNRISE III. *Proc. SPIE, Society of Photo-Optical Instrumentation Engineers (SPIE) Conference Series*, *11447*, Article 11447AK, 11447AK. https://doi.org/10.1117/12.2562666

Ferriz-Mas, A., & Schüssler, M. (1994). Waves and Instabilities of a Toroidal Magnetic Flux Tube in a Rotating Star. *Astrophys. J.*, *433*, 852. https://doi.org/10.1086/174694

Fiethe, B., Bubenhagen, F., Lange, T., Michalik, H., Michel, H., Woch, J., & Hirzberger, J. (2012). Adaptive hardware by dynamic reconfiguration for the Solar Orbiter PHI instrument. *Proc. of 2012 NASA/ESA Conference on Adaptive Hardware and Systems (AHS)*, 31–37.

Fiethe, B., Michalik, H., Dierker, C., Osterloh, B., & Zhou, G. (2007). Reconfigurable system-on-chip data processing units for space imaging instruments. *Proc. of the conference on Design, automation and test in Europe*, 977–982.

Foukal, P., Fröhlich, C., Spruit, H., & Wigley, T. M. L. (2006). Variations in solar luminosity and their effect on the Earth's climate. *Nature*, *443*(7108), 161–166. https://doi.org/10.1038/nature05072

Foukal, P., & Milano, L. (2001). A measurement of the quiet network contribution to solar irradiance variation. *Geophys. Res. Lett.*, *28*(5), 883–886. https://doi.org/10.1029/2000GL012072

Freudling, W., Romaniello, M., Bramich, D. M., Ballester, P., Forchi, V., García-Dabló, C. E., Moehler, S., & Neeser, M. J. (2013). Automated data reduction workflows for astronomy. The ESO Reflex environment. *Astron. Astrophys.*, *559*, Article A96, A96. https://doi.org/10.1051/0004-6361/201322494

Fröhlich, C. (2006). Solar Irradiance Variability Since 1978. Revision of the PMOD Composite during Solar Cycle 21. *Space Sci. Rev.*, *125*(1-4), 53–65. https://doi.org/10.1007/s11214-006-9046-5

Galloway, D. J., & Weiss, N. O. (1981). Convection and magnetic fields in stars. *Astrophys. J.*, *243*, 945–953. https://doi.org/10.1086/158659

Gandorfer, A., Grauf, B., Barthol, P., Riethmüller, T. L., Solanki, S. K., Chares, B., Deutsch, W., Ebert, S., Feller, A., Germerott, D., Heerlein, K., Heinrichs, J., Hirche, D., Hirzberger, J., Kolleck, M., Meller, R., Müller, R., Schäfer, R., Tomasch, G., … Schmidt, E. (2011). The Filter Imager SuFI and the Image Stabilization and Light Distribution System ISLiD of

the Sunrise Balloon-Borne Observatory: Instrument Description. *Solar Phys.*, *268*(1), 35–55. https://doi.org/10.1007/s11207-010-9636-y

Gandorfer, A., Grauf, B., Staub, J., Bischoff, J., Woch, J., Hirzberger, J., Solanki, S. K., Álvarez-Herrero, A., García Parejo, P., Schmidt, W., Volkmer, R., Appourchaux, T., & del Toro Iniesta, J. C. (2018, July). The High Resolution Telescope (HRT) of the Polarimetric and Helioseismic Imager (PHI) onboard Solar Orbiter. In M. Lystrup, H. A. MacEwen, G. G. Fazio, N. Batalha, N. Siegler, & E. C. Tong (Eds.), *Proc. SPIE, Space Telescopes and Instrumentation 2018: Optical, Infrared, and Millimeter Wave* (106984N, Vol. 10698). https://doi.org/10.1117/12.2311816

Gandorfer, A. (2002, October). Instrumentation for optical magnetometry. In H. Sawaya-Lacoste (Ed.), *SOLMAG 2002. Proceedings of the Magnetic Coupling of the Solar Atmosphere Euroconference* (pp. 19–25, Vol. 505).

García-Rivas, M., Jurčák, J., & Bello González, N. (2021). Magnetic properties on the boundary of an evolving pore. *Astron. Astrophys.*, *649*, Article A129, A129. https://doi.org/10.1051/0004-6361/202039661

García-Rivas, M., Jurčák, J., Bello González, N., Borrero, J. M., Schlichenmaier, R., & Lindner, P. (2024). Onset of penumbra formation. *arXiv e-prints*, Article arXiv:2403.18455, arXiv:2403.18455. https://doi.org/10.48550/arXiv.2403.18455

Gizon, L., Cameron, R. H., Pourabdian, M., Liang, Z.-C., Fournier, D., Birch, A. C., & Hanson, C. S. (2020). Meridional flow in the Sun's convection zone is a single cell in each hemisphere. *Science*, *368*(6498), 1469–1472. https://doi.org/10.1126/science.aaz7119

Guglielmino, S. L., Zuccarello, F., Romano, P., Cristaldi, A., Ermolli, I., Criscuoli, S., Falco, M., & Zuccarello, F. P. (2016). A Multi-instrument Analysis of a C4.1 Flare Occurring in a δ Sunspot. *Astrophys. J.*, *819*, Article 157, 157. https://doi.org/10.3847/0004-637X/819/2/157

Haigh, J. D. (2007). The Sun and the Earth's Climate. *Living Rev. in Sol. Phys.*, *4*(1), Article 2, 2. https://doi.org/10.12942/lrsp-2007-2

Hale, G. E. (1908). On the Probable Existence of a Magnetic Field in Sun-Spots. *Astrophys. J.*, *28*, 315. https://doi.org/10.1086/141602

Hanaoka, Y. (2009). Spectropolarimetry with the Hida Domeless Solar Telescope. *Pub. Astron. Soc. Japan*, *61*, 357. https://doi.org/10.1093/pasj/61.2.357

Harvey, K., & Harvey, J. (1973). Observations of Moving Magnetic Features near Sunspots. *Solar Phys.*, *28*(1), 61–71. https://doi.org/10.1007/BF00152912

Hirzberger, J., Stangl, S., Gersin, K., Jurčák, J., Puschmann, K. G., & Sobotka, M. (2005). The structure of a penumbral connection between solar

pores. *Astron. Astrophys.*, *442*(3), 1079–1086. https://doi.org/10.1051/0004-6361:20053257

Holzreuter, R., & Solanki, S. K. (2015). Three-dimensional non-LTE radiative transfer effects in Fe i lines. III. Line formation in magnetohydrodynamic atmospheres. *Astron. Astrophys.*, *582*, Article A101, A101. https://doi.org/10.1051/0004-6361/201526373

Howe, R., Christensen-Dalsgaard, J., Hill, F., Komm, R. W., Larsen, R. M., Schou, J., Thompson, M. J., & Toomre, J. (2000). Dynamic Variations at the Base of the Solar Convection Zone. *Science*, *287*(5462), 2456–2460. https://doi.org/10.1126/science.287.5462.2456

Huang, Z., Madjarska, M. S., Xia, L., Doyle, J. G., Galsgaard, K., & Fu, H. (2014). Explosive Events on a Subarcsecond Scale in IRIS Observations: A Case Study. *The Solar Phys. Journal*, *797*(2), 88. http://stacks.iop.org/0004-637X/797/i=2/a=88

Hummel, W., Modigliani, A., Szeifert, T., & Dumas, C. (2006). Data flow operations and quality control of SINFONI [Integral Field Spectroscopy: Techniques and Data Production]. *New Astronomy Reviews*, *50*(4), 412–415. https://doi.org/https://doi.org/10.1016/j.newar.2006.02.037

Ichimoto, K., Lites, B., Elmore, D., Suematsu, Y., Tsuneta, S., Katsukawa, Y., Shimizu, T., Shine, R., Tarbell, T., Title, A., Kiyohara, J., Shinoda, K., Card, G., Lecinski, A., Streander, K., Nakagiri, M., Miyashita, M., Noguchi, M., Hoffmann, C., & Cruz, T. (2008). Polarization Calibration of the Solar Optical Telescope onboard Hinode. *Solar Phys.*, *249*, 233–261. https://doi.org/10.1007/s11207-008-9169-9

Ichimoto, K., Suematsu, Y., Shimizu, T., Katsukawa, Y., Noguchi, M., Nakagiri, M., Miyashita, M., Tsuneta, S., Tarbell, T. D., Shine, R. A., Hoffmann, C. M., Cruz, T., Lites, B. W., & Elmore, D. F. (2007, October). Calibration of the SOT Polarization. In K. Shibata, S. Nagata, & T. Sakurai (Eds.), *Proc. ASP Confreence New Solar Physics with Solar-B Mission* (p. 39, Vol. 369).

Iglesias, F. A., Feller, A., Nagaraju, K., & Solanki, S. K. (2016). High-resolution, high-sensitivity, ground-based solar spectropolarimetry with a new fast imaging polarimeter. I. Prototype characterization. *Astron. Astrophys.*, *590*, Article A89, A89. https://doi.org/10.1051/0004-6361/201628376

Iglesias, F., & Feller, A. (2019). Instrumentation for solar spectropolarimetry: state of the art and prospects. *Optical Engineering*, *58*, Article 082417, 082417. https://doi.org/10.1117/1.OE.58.8.082417

Irbah, A., Mecheri, R., Damé, L., & Djafer, D. (2019). Variations of Solar Oblateness with the 22 yr Magnetic Cycle Explain Apparently In-

consistent Measurements. *Astrophys. J. Lett.*, *875*(2), Article L26, L26. https://doi.org/10.3847/2041-8213/ab16e2

Ishikawa, R., Trujillo Bueno, J., Alsina Ballester, E., Belluzzi, L., del Pino Alemán, T., McKenzie, D. E., Auchère, F., Kobayashi, K., Okamoto, T. J., Rachmeler, L. A., & Song, D. (2023). Evidence for the Operation of the Hanle and Magneto-optical Effects in the Scattering Polarization Signals Observed by CLASP2 across the Mg II h and k Lines. *Astrophys. J.*, *945*(2), Article 125, 125. https://doi.org/10.3847/1538-4357/acb64e

Jaeggli, S. A., Lin, H., Mickey, D. L., Kuhn, J. R., Hegwer, S. L., Rimmele, T. R., & Penn, M. J. (2010). FIRS: a new instrument for photospheric and chromospheric studies at the DST. *Memorie della Societa Astronomica Italiana*, *81*, 763.

Jaeggli, S. A., Lin, H., Onaka, P., Yamada, H., Anan, T., Bonnet, M., Ching, G., Huang, X.-P., Kramar, M., McGregor, H., Nitta, G., Rae, C., Robertson, L., Schad, T. A., Toyama, P., Young, J., Berst, C., Harrington, D. M., Liang, M., … Sueoka, S. R. (2022). The Diffraction-Limited Near-Infrared Spectropolarimeter (DL-NIRSP) of the Daniel K. Inouye Solar Telescope (DKIST). *Solar Phys.*, *297*(10), Article 137, 137. https://doi.org/10.1007/s11207-022-02062-w

Jafarzadeh, S., Solanki, S. K., Lagg, A., Bellot Rubio, L. R., van Noort, M., Feller, A., & Danilovic, S. (2014). Inclinations of small quiet-Sun magnetic features based on a new geometric approach. *Astron. Astrophys.*, *569*, Article A105, A105. https://doi.org/10.1051/0004-6361/201423414

Janvier, M., Mzerguat, S., Young, P. R., Buchlin, É., Manou, A., Pelouze, G., Long, D. M., Green, L., Warmuth, A., Schuller, F., Démoulin, P., Calchetti, D., Kahil, F., Bellot Rubio, L., Parenti, S., Baccar, S., Barczynski, K., Harra, L. K., Hayes, L. A., … Volkmer, R. (2023). A multiple spacecraft detection of the 2 April 2022 M-class flare and filament eruption during the first close Solar Orbiter perihelion. *Astron. Astrophys.*, *677*, Article A130, A130. https://doi.org/10.1051/0004-6361/202346321

Jefferies, J. T. (1968). *Spectral line formation.*

Jurčák, J., Bello González, N., Schlichenmaier, R., & Rezaei, R. (2017). A distinct magnetic property of the inner penumbral boundary. II. Formation of a penumbra at the expense of a pore. *Astron. Astrophys.*, *597*, Article A60, A60. https://doi.org/10.1051/0004-6361/201628547

Jurčák, J., Bellot Rubio, L. R., & Sobotka, M. (2014). Orphan penumbrae: Submerging horizontal fields. *Astron. Astrophys.*, *564*, Article A91, A91. https://doi.org/10.1051/0004-6361/201322340

Kahil, F., Gandorfer, A., Hirzberger, J., Calchetti, D., Sinjan, J., Valori, G., Solanki, S. K., van Noort, M., Albert, K., Albelo Jorge, N., Alvarez-Herrero, A., Appourchaux, T., Bellot Rubio, L. R., Blanco Rodríguez, J., Feller, A., Fiethe, B., Germerott, D., Gizon, L., Guerrero, L., … Woch, J. (2023). Wavefront error of PHI/HRT on Solar Orbiter at various heliocentric distances. *Astron. Astrophys.*, *675*, Article A61, A61. https://doi.org/10.1051/0004-6361/202346033

Kahil, F., Gandorfer, A., Hirzberger, J., Orozco Suárez, D., Albert, K., Albelo Jorge, N., Appourchaux, T., Álvarez-Herrero, A., Blanco Rodríguez, J., Germerott, D., Guerrero, L., Gutierrez Marquez, P., Sinjan, J., Calchetti, D., Kolleck, M., Solanki, S. K., del Toro Iniesta, J. C., Volkmer, R., Woch, J., … Valori, G. (2022a, August). Image quality of data products of the high resolution telescope of the polarimetric and helioseismic imager. In L. E. Coyle, S. Matsuura, & M. D. Perrin (Eds.), *Proc. SPIE, Space Telescopes and Instrumentation 2022: Optical, Infrared, and Millimeter Wave* (121803F, Vol. 12180). https : //doi.org/10.1117/12.2628942

Kahil, F., Hirzberger, J., Solanki, S. K., Chitta, L. P., Peter, H., Auchère, F., Sinjan, J., Orozco Suárez, D., Albert, K., Albelo Jorge, N., Appourchaux, T., Alvarez-Herrero, A., Blanco Rodríguez, J., Gandorfer, A., Germerott, D., Guerrero, L., Gutiérrez Márquez, P., Kolleck, M., del Toro Iniesta, J. C., … Gissot, S. (2022b). The magnetic drivers of campfires seen by the Polarimetric and Helioseismic Imager (PHI) on Solar Orbiter. *Astron. Astrophys.*, *660*, Article A143, A143. https://doi.org/10.1051/0004-6361/202142873

Kahil, F., Riethmüller, T. L., & Solanki, S. K. (2019). Intensity contrast of solar plage as a function of magnetic flux at high spatial resolution. *Astron. Astrophys.*, *621*, Article A78, A78. https://doi.org/10.1051/0004-6361/201833722

Katsukawa, Y., del Toro Iniesta, J. C., Solanki, S. K., Kubo, M., Hara, H., Shimizu, T., Oba, T., Kawabata, Y., Tsuzuki, T., Uraguchi, F., Nodomi, Y., Shinoda, K., Tamura, T., Suematsu, Y., Ishikawa, R., Kano, R., Matsumoto, T., Ichimoto, K., Nagata, S., … Lagg, A. (2020, December). Sunrise Chromospheric Infrared SpectroPolarimeter (SCIP) for sunrise III: system design and capability. In C. J. Evans, J. J. Bryant, & K. Motohara (Eds.), *Proc. SPIE, Ground-based and Airborne Instrumentation for Astronomy VIII* (114470Y, Vol. 11447). https://doi.org/10.1117/12.2561223

Keller, C. U., Harvey, J. W., & Giampapa, M. S. (2003, February). SOLIS: an innovative suite of synoptic instruments. In S. L. Keil & S. V. Avakyan

(Eds.), *Proc. SPIE, Innovative Telescopes and Instrumentation for Solar Astrophysics* (pp. 194–204, Vol. 4853). https://doi.org/10.1117/12.460373

Kentischer, T. J., Schmidt, W., Sigwarth, M., & von Uexkuell, M. (1998). TESOS, a double Fabry-Perot instrument for solar spectroscopy. *Astron. Astrophys., 340*, 569–578.

Keys, P. H., Mathioudakis, M., Jess, D. B., Mackay, D. H., & Keenan, F. P. (2014). Dynamic properties of bright points in an active region. *Astron. Astrophys., 566*, Article A99, A99. https://doi.org/10.1051/0004-6361/201322987

Kleint, L., & Gandorfer, A. (2017). Prospects of Solar Magnetometry—From Ground and in Space. *Space Sci. Rev., 210*(1-4), 397–426. https://doi.org/10.1007/s11214-015-0208-1

Kobel, P., Solanki, S. K., & Borrero, J. M. (2011). The continuum intensity as a function of magnetic field. I. Active region and quiet Sun magnetic elements. *Astron. Astrophys., 531*, Article A112, A112. https://doi.org/10.1051/0004-6361/201016255

Komm, R., Howe, R., & Hill, F. (2020). Solar-Cycle Variation of the Subsurface Flows of Active- and Quiet-Region Subsets. *Solar Phys., 295*(3), Article 47, 47. https://doi.org/10.1007/s11207-020-01611-5

Korpi-Lagg, M. J., Korpi-Lagg, A., Olspert, N., & Truong, H. .-. (2022). Solar-cycle variation of quiet-Sun magnetism and surface gravity oscillation mode. *Astron. Astrophys., 665*, Article A141, A141. https://doi.org/10.1051/0004-6361/202243979

Kosugi, T., Matsuzaki, K., Sakao, T., Shimizu, T., Sone, Y., Tachikawa, S., Hashimoto, T., Minesugi, K., Ohnishi, A., Yamada, T., Tsuneta, S., Hara, H., Ichimoto, K., Suematsu, Y., Shimojo, M., Watanabe, T., Shimada, S., Davis, J. M., Hill, L. D., … Golub, L. (2007). The Hinode (Solar-B) Mission: An Overview. *Solar Phys., 243*, 3–17. https://doi.org/10.1007/s11207-007-9014-6

Krivova, N. A., Solanki, S. K., & Floyd, L. (2006). Reconstruction of solar UV irradiance in cycle 23. *Astron. Astrophys., 452*(2), 631–639. https://doi.org/10.1051/0004-6361:20064809

Kuckein, C., Denker, C., Verma, M., Balthasar, H., Manrique, S. G., Louis, R., & Diercke, A. (2016). sTools–a data reduction pipeline for the GREGOR Fabry-Pérot Interferometer and the High-resolution Fast Imager at the GREGOR solar telescope. *Proc. of the International Astronomical Union, 12*(S327), 20–24.

Lagg, A., Solanki, S. K., Riethmüller, T. L., Martínez Pillet, V., Schüssler, M., Hirzberger, J., Feller, A., Borrero, J. M., Schmidt, W., del Toro Iniesta, J. C., Bonet, J. A., Barthol, P., Berkefeld, T., Domingo, V., Gandorfer, A.,

Knölker, M., & Title, A. M. (2010). Fully Resolved Quiet-Sun Magnetic flux Tube Observed with the SUNRISE/IMAX Instrument. *Astrophys. J. Lett.*, *723*(2), L164–L168. https://doi.org/10.1088/2041-8205/723/2/L164

Lagg, A., Woch, J., Krupp, N., & Solanki, S. K. (2004). Retrieval of the full magnetic vector with the He I multiplet at 1083 nm. Maps of an emerging flux region. *Astron. Astrophys.*, *414*, 1109–1120. https://doi.org/10.1051/0004-6361:20031643

Lagg, A., Lites, B., Harvey, J., Gosain, S., & Centeno, R. (2017). Measurements of Photospheric and Chromospheric Magnetic Fields. *Space Sci. Rev.*, *210*(1), 37–76. https://doi.org/10.1007/s11214-015-0219-y

Lange, T. (2020, September). *A flexible, heterogeneous image processing framework for spaceborne reconfigurable data processing modules* [Doctoral dissertation]. https://doi.org/10.24355/dbbs.084-202009241113-0

Lange, T., Fiethe, B., Michel, H., Michalik, H., Albert, K., & Hirzberger, J. (2017). On-board processing using reconfigurable hardware on the solar orbiter PHI instrument. *Proc. of 2017 NASA/ESA Conference on Adaptive Hardware and Systems (AHS)*, 186–191.

Lean, J. L., Wang, Y. .-., & Sheeley, N. R. (2002). The effect of increasing solar activity on the Sun's total and open magnetic flux during multiple cycles: Implications for solar forcing of climate. *Geophys. Res. Lett.*, *29*(24), Article 2224, 2224. https://doi.org/10.1029/2002GL015880

Leighton, R. B. (1969). A Magneto-Kinematic Model of the Solar Cycle. *Astrophys. J.*, *156*, 1. https://doi.org/10.1086/149943

Léna, P., Rouan, D., Lebrun, F., Mignard, F., & Pelat, D. (2012). *Observational astrophysics*. Springer Science & Business Media.

Lites, B. W., Akin, D. L., Card, G., Cruz, T., Duncan, D. W., Edwards, C. G., Elmore, D. F., Hoffmann, C., Katsukawa, Y., Katz, N., Kubo, M., Ichimoto, K., Shimizu, T., Shine, R. A., Streander, K. V., Suematsu, A., Tarbell, T. D., Title, A. M., & Tsuneta, S. (2013). The Hinode Spectro-Polarimeter. *Solar Phys.*, *283*(2), 579–599. https://doi.org/10.1007/s11207-012-0206-3

Lites, B. W. (1972, January). *Observation and Analysis of the Solar Neutral Iron Spectrum*. [Doctoral dissertation, University of Colorado, Boulder].

Loeschl, P., Valori, G., Hirzberger, J., Schou, J., Solanki, S. K., Orozco Suárez, D., Albert, K., Albelo Jorge, N., Appourchaux, T., Alvarez-Herrero, A., Blanco Rodríguez, J., Gandorfer, A., Germerott, D., Guerrero, L., Gutierrez-Marques, P., Kahil, F., Kolleck, M., del Toro Iniesta, J. C., Volkmer, R., … Torralbo, I. (2024). A first rapid synoptic magnetic field map using SDO/HMI and SO/PHI data. *Astron. Astrophys.*, *681*, Article A59, A59. https://doi.org/10.1051/0004-6361/202346046

Lombardi, S., Antonelli, L. A., Bigongiari, C., Cardillo, M., Lucarelli, F., Perri, M., Stamerra, A., & Visconti, F. (2018, July). ASTRI data reduction software in the framework of the Cherenkov Telescope Array. In J. C. Guzman & J. Ibsen (Eds.), *Proc. SPIE, Software and Cyberinfrastructure for Astronomy V* (107070R, Vol. 10707). https://doi.org/10.1117/12.2311293

López Ariste, A., Rayrole, J., & Semel, M. (2000). First results from THEMIS spectropolarimetric mode. *Astron. Astrophys. Suppl., 142*, 137–148. https://doi.org/10.1051/aas:2000144

Martínez González, M. J., Asensio Ramos, A., Manso Sainz, R., Khomenko, E., Martínez Pillet, V., Solanki, S. K., López Ariste, A., Schmidt, W., Barthol, P., & Gandorfer, A. (2011). Unnoticed Magnetic Field Oscillations in the Very Quiet Sun Revealed by SUNRISE/IMaX. *Astrophys. J. Lett., 730*(2), Article L37, L37. https://doi.org/10.1088/2041-8205/730/2/L37

Martínez Pillet, V. (2002). Decay of sunspots. *Astronomische Nachrichten, 323*, 342–348. https://doi.org/10.1002/1521-3994(200208)323:3/4<342::AID-ASNA342>3.0.CO;2-5

Martínez Pillet, V., Collados, M., Sánchez Almeida, J., González, V., Cruz-Lopez, A., Manescau, A., Joven, E., Paez, E., Diaz, J., Feeney, O., Sánchez, V., Scharmer, G., & Soltau, D. (1999, January). LPSP & TIP: Full Stokes Polarimeters for the Canary Islands Observatories. In T. R. Rimmele, K. S. Balasubramaniam, & R. R. Radick (Eds.), *Proc. of ASP Conference High Resolution Solar Physics: Theory, Observations, and Techniques* (p. 264, Vol. 183).

Martínez Pillet, V., del Toro Iniesta, J. C., Álvarez-Herrero, A., Domingo, V., Bonet, J. A., González Fernández, L., López Jiménez, A., Pastor, C., Gasent Blesa, J. L., Mellado, P., Piqueras, J., Aparicio, B., Balaguer, M., Ballesteros, E., Belenguer, T., Bellot Rubio, L. R., Berkefeld, T., Collados, M., Deutsch, W., … Vargas Domínguez, S. (2011). The Imaging Magnetograph eXperiment (IMaX) for the Sunrise Balloon-Borne Solar Observatory. *Solar Phys., 268*(1), 57–102. https://doi.org/10.1007/s11207-010-9644-y

Mathew, S. K. (2009, June). A New 0.5m Telescope (MAST) for Solar Imaging and Polarimetry. In S. V. Berdyugina, K. N. Nagendra, & R. Ramelli (Eds.), *Proc. ASP Conference Solar Polarization 5: In Honor of Jan Stenflo* (p. 461, Vol. 405).

McCully, C., Volgenau, N. H., Harbeck, D.-R., Lister, T. A., Saunders, E. S., Turner, M. L., Siiverd, R. J., & Bowman, M. (2018, July). Real-time processing of the imaging data from the network of Las Cumbres Observatory Telescopes using BANZAI. In J. C. Guzman & J. Ibsen

(Eds.), *Proc. SPIE, Software and Cyberinfrastructure for Astronomy V* (107070K, Vol. 10707). https://doi.org/10.1117/12.2314340

Mein, P. (2002). The MSDP of THEMIS: Capabilities, first results and prospects. *Astron. Astrophys., 381*, 271–278. https://doi.org/10.1051/0004-6361:20011418

Meunier, N. (2018). Solar chromospheric emission and magnetic structures from plages to intranetwork: Contribution of the very quiet Sun. *Astron. Astrophys., 615*, Article A87, A87. https://doi.org/10.1051/0004-6361/201730817

Meyer, F., Schmidt, H. U., Weiss, N. O., & Wilson, P. R. (1974). The growth and decay of sunspots. *Mon. Not. Roy. Astron. Soc., 169*, 35–57. https://doi.org/10.1093/mnras/169.1.35

Müller, D., St. Cyr, O. C., Zouganelis, I., Gilbert, H. R., Marsden, R., Nieves-Chinchilla, T., Antonucci, E., Auchère, F., Berghmans, D., Horbury, T. S., Howard, R. A., Krucker, S., Maksimovic, M., Owen, C. J., Rochus, P., Rodriguez-Pacheco, J., Romoli, M., Solanki, S. K., Bruno, R., … Williams, D. (2020). The Solar Orbiter mission. Science overview. *Astron. Astrophys., 642*, Article A1, A1. https://doi.org/10.1051/0004-6361/202038467

Nagata, S., Tsuneta, S., Suematsu, Y., Ichimoto, K., Katsukawa, Y., Shimizu, T., Yokoyama, T., Tarbell, T. D., Lites, B. W., Shine, R. A., Berger, T. E., Title, A. M., Bellot Rubio, L. R., & Orozco Suárez, D. (2008). Formation of Solar Magnetic Flux Tubes with Kilogauss Field Strength Induced by Convective Instability. *Astrophys. J. Lett., 677*(2), L145. https://doi.org/10.1086/588026

Narayan, G., & Scharmer, G. B. (2010). Small-scale convection signatures associated with a strong plage solar magnetic field. *Astron. Astrophys., 524*, Article A3, A3. https://doi.org/10.1051/0004-6361/201014956

Narukage, N., McKenzie, D. E., Ishikawa, R., Trujillo-Bueno, J., De Pontieu, B., Kubo, M., Ishikawa, S.-n., Kano, R., Suematsu, Y., Yoshida, M., Rachmeler, L. A., Kobayashi, K., Cirtain, J. W., Winebarger, A. R., Asensio Ramos, A., del Pino Aleman, T., Štępán, J., Belluzzi, L., Larruquert, J. I., … Carlsson, M. J. L. (2016, July). Chromospheric LAyer SpectroPolarimeter (CLASP2). In J.-W. A. den Herder, T. Takahashi, & M. Bautz (Eds.), *Proc. SPIE, Space Telescopes and Instrumentation 2016: Ultraviolet to Gamma Ray* (p. 990508, Vol. 9905). https://doi.org/10.1117/12.2232245

Narukage, N., Tsuneta, S., Bando, T., Kano, R., Kubo, M., Ishikawa, R., Hara, H., Suematsu, Y., Katsukawa, Y., Watanabe, H., Ichimoto, K., Sakao, T., Shimizu, T., Kobayashi, K., Robinson, B., Kim, T., Winebarger, A., West, E., Cirtain, J., … Carlsson, M. (2011). Overview of Chromo-

spheric Lyman-Alpha SpectroPolarimeter (CLASP). *Proc. SPIE, 8148*, 8148 - 8148 –17. https://doi.org/10.1117/12.894290

Neckel, H., & Labs, D. (1984). The solar radiation between 3300 and 12500 Å. *Solar Phys.*, *90*(2), 205–258. https://doi.org/10.1007/BF00173953

Nölke, J. D., Solanki, S. K., Hirzberger, J., Peter, H., Chitta, L. P., Kahil, F., Valori, G., Wiegelmann, T., Orozco Suárez, D., Albert, K., Albelo Jorge, N., Appourchaux, T., Alvarez-Herrero, A., Blanco Rodríguez, J., Gandorfer, A., Germerott, D., Guerrero, L., Gutierrez-Marques, P., Kolleck, M., … Smith, P. (2023). Coronal voids and their magnetic nature. *Astron. Astrophys.*, *678*, Article A196, A196. https://doi.org/10.1051/0004-6361/202346040

Nordlund, Å., Stein, R. F., & Asplund, M. (2009). Solar Surface Convection. *Living Rev. in Sol. Phys.*, *6*(1), Article 2, 2. https://doi.org/10.12942/lrsp-2009-2

Ortiz, A., Solanki, S. K., Domingo, V., Fligge, M., & Sanahuja, B. (2002). On the intensity contrast of solar photospheric faculae and network elements. *Astron. Astrophys.*, *388*, 1036–1047. https://doi.org/10.1051/0004-6361:20020500

Ossendrijver, M. A. J. H. (2000). Grand minima in a buoyancy-driven solar dynamo. *Astron. Astrophys.*, *359*, 364–372.

Parker, E. N. (1978). Hydraulic concentration of magnetic fields in the solar photosphere. VI. Adiabatic cooling and concentration in downdrafts. *Astrophys. J.*, *221*, 368–377. https://doi.org/10.1086/156035

Parker, E. N. (1955). Hydromagnetic Dynamo Models. *Astrophys. J.*, *122*, 293. https://doi.org/10.1086/146087

Peng, Y., Xue, Z., Qu, Z., Wang, J., Xu, Z., Yang, L., & Zhou, Y. (2024). The Decay of Two Adjacent Sunspots Associated with Moving Magnetic Features. *Astrophys. J.*, *960*(2), Article 95, 95. https://doi.org/10.3847/1538-4357/ad063e

Pesnell, W. D., Thompson, B. J., & Chamberlin, P. C. (2012). The Solar Dynamics Observatory (SDO). *Solar Phys.*, *275*(1), 3–15. https://doi.org/10.1007/s11207-011-9841-3

Petrovay, K., & Moreno-Insertis, F. (1997). Turbulent Erosion of Magnetic Flux Tubes. *Astrophys. J.*, *485*(1), 398–408. https://doi.org/10.1086/304404

Povel, H. P. (2001). Ground-based Instrumentation for Solar Magnetic Field Studies, with Special Emphasis on the Zurich Imaging Polarimeters ZIMPOL-I and II. In G. Mathys, S. K. Solanki, & D. T. Wickramasinghe (Eds.), *Proc. of ASP Conference Magnetic Fields Across the Hertzsprung-Russell Diagram, vol. 256* (p. 543, Vol. 248).

Puschmann, K. G., Denker, C., Kneer, F., Al Erdogan, N., Balthasar, H., Bauer, S. M., Beck, C., Bello González, N., Collados, M., Hahn, T., Hirzberger, J., Hofmann, A., Louis, R. E., Nicklas, H., Okunev, O., Martínez Pillet, V., Popow, E., Seelemann, T., Volkmer, R., … Woche, M. (2012). The GREGOR Fabry-Pérot Interferometer. *Astronomische Nachrichten*, *333*(9), 880. https://doi.org/10.1002/asna.201211734

Reardon, K. P., Rimmele, T., Tritschler, A., Cauzzi, G., Wöger, F., Uitenbroek, H., Tsuneta, S., & Berger, T. (2009, December). Service-Mode Observations for Ground-Based Solar Physics. In B. Lites, M. Cheung, T. Magara, J. Mariska, & K. Reeves (Eds.), *Proc. of The Second Hinode Science Meeting: Beyond Discovery-Toward Understanding* (p. 332, Vol. 415). https://doi.org/10.48550/arXiv.0909.1522

Rempel, M. (2014). Numerical Simulations of Quiet Sun Magnetism: On the Contribution from a Small-scale Dynamo. *Astrophys. J.*, *789*(2), Article 132, 132. https://doi.org/10.1088/0004-637X/789/2/132

Riethmüller, T. L., & Solanki, S. K. (2017). The dark side of solar photospheric G-band bright points. *Astron. Astrophys.*, *598*, Article A123, A123. https://doi.org/10.1051/0004-6361/201629773

Rutten, R. J., & Kostik, R. I. (1982). Empirical NLTE analyses of solar spectral lines. III - Iron lines versus LTE models of the photosphere. *Astron. Astrophys.*, *115*(1), 104–114.

Rutten, R. J. (1988, January). The NLTE formation of iron lines in the solar photosphere. In R. Viotti, A. Vittone, & M. Friedjung (Eds.), *IAU Colloq. 94: Physics of Formation of FE II Lines Outside LTE* (pp. 185–210, Vol. 138). https://doi.org/10.1007/978-94-009-4023-9_23

Sánchez Almeida, J., Bonet, J. A., Viticchié, B., & Del Moro, D. (2010). Magnetic Bright Points in the Quiet Sun. *Astrophys. J. Lett.*, *715*(1), L26–L29. https://doi.org/10.1088/2041-8205/715/1/L26

Sánchez Almeida, J., Emonet, T., & Cattaneo, F. (2003, January). The Polarized Spectrum Emerging from Fast Dynamo Simulations. In J. Trujillo-Bueno & J. Sanchez Almeida (Eds.), *Proc. ASP Conference, Solar Polarization* (p. 293, Vol. 307).

Sankarasubramanian, K., Gullixson, C., Hegwer, S., Rimmele, T. R., Gregory, S., Spence, T., Fletcher, S., Richards, K., Rousset, E., Lites, B., Elmore, D., Streander, K., & Sigwarth, M. (2004, February). The Diffraction Limited Spectro-Polarimeter: a new instrument for high-resolution solar polarimetry. In S. Fineschi & M. A. Gummin (Eds.), *Proc. SPIE, Telescopes and Instrumentation for Solar Astrophysics* (pp. 207–218, Vol. 5171). https://doi.org/10.1117/12.508790

Scharmer, G. B., Narayan, G., Hillberg, T., de la Cruz Rodriguez, J., Löfdahl, M. G., Kiselman, D., Sütterlin, P., van Noort, M., & Lagg, A. (2008). CRISP Spectropolarimetric Imaging of Penumbral Fine Structure. *Astrophys. J. Lett.*, *689*(1), L69. https://doi.org/10.1086/595744

Scherrer, P. H., Bogart, R. S., Bush, R. I., Hoeksema, J. T., Kosovichev, A. G., Schou, J., Rosenberg, W., Springer, L., Tarbell, T. D., Title, A., Wolfson, C. J., Zayer, I., & MDI Engineering Team. (1995). The Solar Oscillations Investigation - Michelson Doppler Imager. *Solar Phys.*, *162*, 129–188. https://doi.org/10.1007/BF00733429

Schmidt, W., Beck, C., Kentischer, T., Elmore, D., & Lites, B. (2003). POLIS: A spectropolarimeter for the VTT and for GREGOR. *Astronomische Nachrichten*, *324*(4), 300–301. https://doi.org/10.1002/asna.200310101

Schmidt, W., Bell, A., Halbgewachs, C., Heidecke, F., Kentischer, T. J., von der Lühe, O., Scheiffelen, T., & Sigwarth, M. (2014, July). A two-dimensional spectropolarimeter as a first-light instrument for the Daniel K. Inouye Solar Telescope. In S. K. Ramsay, I. S. McLean, & H. Takami (Eds.), *Proc. SPIE, Ground-based and Airborne Instrumentation for Astronomy V* (91470E, Vol. 9147). https://doi.org/10.1117/12.2056322

Schou, J., Hirzberger, J., Orozco Suárez, D., Albert, K., Albelo Jorge, N., Appourchaux, T., Alvarez-Herrero, A., Blanco Rodríguez, J., Gandorfer, A., Germerott, D., Guerrero, L., Gutierrez-Marques, P., Kahil, F., Kolleck, M., Solanki, S. K., del Toro Iniesta, J. C., Volkmer, R., Woch, J., Fiethe, B., … Valori, G. (2023). The ratio of horizontal to vertical displacement in solar oscillations estimated from combined SO/PHI and SDO/HMI observations. *Astron. Astrophys.*, *673*, Article A84, A84. https://doi.org/10.1051/0004-6361/202345946

Schou, J., Scherrer, P. H., Bush, R. I., Wachter, R., Couvidat, S., Rabello-Soares, M. C., Bogart, R. S., Hoeksema, J. T., Liu, Y., Duvall, T. L., Akin, D. J., Allard, B. A., Miles, J. W., Rairden, R., Shine, R. A., Tarbell, T. D., Title, A. M., Wolfson, C. J., Elmore, D. F., … Tomczyk, S. (2012). Design and Ground Calibration of the Helioseismic and Magnetic Imager (HMI) Instrument on the Solar Dynamics Observatory (SDO). *Solar Phys.*, *275*, 229–259. https://doi.org/10.1007/s11207-011-9842-2

Schrijver, C. J., Title, A. M., van Ballegooijen, A. A., Hagenaar, H. J., & Shine, R. A. (1997). Sustaining the Quiet Photospheric Network: The Balance of Flux Emergence, Fragmentation, Merging, and Cancellation. *Astrophys. J.*, *487*(1), 424–436. https://doi.org/10.1086/304581

Schüssler, M., & Vögler, A. (2006). Magnetoconvection in a Sunspot Umbra. *Astrophys. J. Lett.*, *641*(1), L73–L76. https://doi.org/10.1086/503772

Scullion, E., Van der Voort, L. R., Wedemeyer, S., & Antolin, P. (2014). Unresolved fine-scale structure in solar coronal loop-tops. *Astrophys. J.*, *797*(1), 36.

Shchukina, N., & Trujillo Bueno, J. (2001). The Iron Line Formation Problem in Three-dimensional Hydrodynamic Models of Solar-like Photospheres. *Astrophys. J.*, *550*(2), 970–990. https://doi.org/10.1086/319789

Sinjan, J., Calchetti, D., Hirzberger, J., Kahil, F., Valori, G., Solanki, S. K., Albert, K., Albelo Jorge, N., Alvarez-Herrero, A., Appourchaux, T., Bellot Rubio, L. R., Blanco Rodríguez, J., Feller, A., Gandorfer, A., Germerott, D., Gizon, L., Gómez Cama, J. M., Guerrero, L., Gutierrez-Marques, P., … Woch, J. (2023). Magnetic fields inferred by Solar Orbiter: A comparison between SO/PHI-HRT and SDO/HMI. *Astron. Astrophys.*, *673*, Article A31, A31. https://doi.org/10.1051/0004-6361/202245830

Smith, R. J., Piascik, A. S., Steele, I. A., & Barnsley, R. M. (2016, July). Automated spectral reduction pipelines. In G. Chiozzi & J. C. Guzman (Eds.), *Proc. SPIE, Software and Cyberinfrastructure for Astronomy IV* (p. 991317, Vol. 9913). https://doi.org/10.1117/12.2232771

Smitha, H. N., van Noort, M., Solanki, S. K., & Castellanos Durán, J. S. (2023). Non-LTE formation of the Fe I 6173 Å line in the solar atmosphere. *Astron. Astrophys.*, *669*, Article A144, A144. https://doi.org/10.1051/0004-6361/202245130

Socas-Navarro, H., Elmore, D., Pietarila, A., Darnell, A., Lites, B. W., Tomczyk, S., & Hegwer, S. (2006). Spinor: Visible and Infrared Spectro-Polarimetry at the National Solar Observatory. *Solar Phys.*, *235*(1-2), 55–73. https://doi.org/10.1007/s11207-006-0020-x

Solanki, S. K., Barthol, P., Danilovic, S., Feller, A., Gandorfer, A., Hirzberger, J., Riethmüller, T. L., Schüssler, M., Bonet, J. A., Martínez Pillet, V., del Toro Iniesta, J. C., Domingo, V., Palacios, J., Knölker, M., Bello González, N., Berkefeld, T., Franz, M., Schmidt, W., & Title, A. M. (2010). SUNRISE: Instrument, Mission, Data, and First Results. *Astrophys. J. Lett.*, *723*(2), L127–L133. https://doi.org/10.1088/2041-8205/723/2/L127

Solanki, S. K., del Toro Iniesta, J. C., Woch, J., Gandorfer, A., Hirzberger, J., Alvarez-Herrero, A., Appourchaux, T., Martínez Pillet, V., Pérez-Grande, I., Sanchis Kilders, E., Schmidt, W., Gómez Cama, J. M., Michalik, H., Deutsch, W., Fernandez-Rico, G., Grauf, B., Gizon, L., Heerlein, K., Kolleck, M., … Zouganelis, I. (2020). The Polarimetric and Helioseismic Imager on Solar Orbiter. *Astron. Astrophys.*, *642*, Article A11, A11. https://doi.org/10.1051/0004-6361/201935325

Solanki, S. K., Krivova, N. A., & Wenzler, T. (2005). Irradiance models. *Advances in Space Research*, *35*(3), 376–383. https://doi.org/10.1016/j.asr.2004.12.077

Solanki, S. K., Riethmüller, T. L., Barthol, P., Danilovic, S., Deutsch, W., Doerr, H. .-., Feller, A., Gandorfer, A., Germerott, D., Gizon, L., Grauf, B., Heerlein, K., Hirzberger, J., Kolleck, M., Lagg, A., Meller, R., Tomasch, G., van Noort, M., Blanco Rodríguez, J., … Lecinski, A. (2017). The Second Flight of the Sunrise Balloon-borne Solar Observatory: Overview of Instrument Updates, the Flight, the Data, and First Results. *Astrophys. J. Suppl.*, *229*(1), Article 2, 2. https://doi.org/10.3847/1538-4365/229/1/2

Solanki, S. K., Inhester, B., & Schüssler, M. (2006). The solar magnetic field. *Reports on Progress in Physics*, *69*(3), 563–668. https://doi.org/10.1088/0034-4885/69/3/R02

Solanki, S. K., & Krivova, N. A. (2004). Solar Irradiance Variations: From Current Measurements to Long-Term Estimates. *Solar Phys.*, *224*(1-2), 197–208. https://doi.org/10.1007/s11207-005-6499-8

Spruit, H. C. (1979). Convective collapse of flux tubes. *Solar Phys.*, *61*(2), 363–378. https://doi.org/10.1007/BF00150420

Staub, J., Fernandez-Rico, G., Gandorfer, A., Gizon, L., Hirzberger, J., Kraft, S., Lagg, A., Schou, J., Solanki, S. K., del Toro Iniesta, J. C., Wiegelmann, T., & Woch, J. (2020). PMI: The Photospheric Magnetic Field Imager. *Jour. of Sp. Weather and Sp. Climate*, *10*, Article 54, 54. https://doi.org/10.1051/swsc/2020059

Steiner, O., Franz, M., Bello González, N., Nutto, C., Rezaei, R., Martínez Pillet, V., Bonet Navarro, J. A., del Toro Iniesta, J. C., Domingo, V., Solanki, S. K., Knölker, M., Schmidt, W., Barthol, P., & Gandorfer, A. (2010). Detection of Vortex Tubes in Solar Granulation from Observations with SUNRISE. *Astrophys. J. Lett.*, *723*(2), L180–L184. https://doi.org/10.1088/2041-8205/723/2/L180

Stenflo, J. (1994). *Solar Magnetic Fields: Polarized Radiation Diagnostics* (Vol. 189). https://doi.org/10.1007/978-94-015-8246-9

Stenflo, J. (2013). Stokes polarimetry of the Zeeman and Hanle effects. In M. C. E. Huber, A. Pauluhn, J. L. Culhane, J. G. Timothy, K. Wilhelm, & A. Zehnder (Eds.), *Observing photons in space: A guide to experimental space astronomy* (pp. 583–598). Springer New York. https://doi.org/10.1007/978-1-4614-7804-1_33

Strecker, H., & Bello González, N. (2022). Evolution of the flow field in decaying active regions. II. Converging flows at the periphery of naked

spots. *Astron. Astrophys.*, *664*, Article A195, A195. https://doi.org/10.1051/0004-6361/202142564

Strecker, H., Schmidt, W., Schlichenmaier, R., & Rempel, M. (2021). On the (in)stability of sunspots. *Astron. Astrophys.*, *649*, Article A123, A123. https://doi.org/10.1051/0004-6361/202040199

Tomczyk, S., Elmore, D. F., Lites, B. W., Dunn, R. B., Skumanich, A., Schuenke, J. A., Streander, K. V., Leach, T. W., Chambellan, C. W., & Lacey, L. B. (1992). The Advanced Stokes Polarimeter: A New Instrument for Solar Magnetic Field Research. *Bulletin of the American Astronomical Society*, *180*, Article 51.08, 51.08.

Trujillo Bueno, J., Landi Degl'Innocenti, E., & Belluzzi, L. (2017). The Physics and Diagnostic Potential of Ultraviolet Spectropolarimetry. *Space Sci. Rev.*, *210*(1), 183–226. https://doi.org/10.1007/s11214-016-0306-8

Tsuneta, S., Ichimoto, K., Katsukawa, Y., Nagata, S., Otsubo, M., Shimizu, T., Suematsu, Y., Nakagiri, M., Noguchi, M., Tarbell, T., Title, A., Shine, R., Rosenberg, W., Hoffmann, C., Jurcevich, B., Kushner, G., Levay, M., Lites, B., Elmore, D., … Owens, J. K. (2008). The Solar Optical Telescope for the Hinode Mission: An Overview. *Solar Phys.*, *249*, 167–196. https://doi.org/10.1007/s11207-008-9174-z

Utz, D., del Toro Iniesta, J. C., Bellot Rubio, L. R., Jurčák, J., Martínez Pillet, V., Solanki, S. K., & Schmidt, W. (2014). The Formation and Disintegration of Magnetic Bright Points Observed by Sunrise/IMaX. *Astrophys. J.*, *796*(2), Article 79, 79. https://doi.org/10.1088/0004-637X/796/2/79

Valori, G., Calchetti, D., Moreno Vacas, A., Pariat, É., Solanki, S. K., Löschl, P., Hirzberger, J., Parenti, S., Albert, K., Albelo Jorge, N., Álvarez-Herrero, A., Appourchaux, T., Bellot Rubio, L. R., Blanco Rodríguez, J., Campos-Jara, A., Feller, A., Gandorfer, A., García Parejo, P., Germerott, D., … Woch, J. (2023). Stereoscopic disambiguation of vector magnetograms: First applications to SO/PHI-HRT data. *Astron. Astrophys.*, *677*, Article A25, A25. https://doi.org/10.1051/0004-6361/202345859

van Kampen, W. C., & Paxman, R. G. (1998, November). Multiframe blind deconvolution of infinite-extent objects. In L. R. Bissonnette (Ed.), *Proc. SPIE, Propagation and Imaging through the Atmosphere II* (pp. 296–307, Vol. 3433). https://doi.org/10.1117/12.330227

van Noort, M., Bischoff, J., Kramer, A., Solanki, S. K., & Kiselman, D. (2022). A prototype of a microlensed hyperspectral imager for solar observations. *Astron. Astrophys.*, *668*, Article A149, A149. https://doi.org/10.1051/0004-6361/202243464

van Noort, M., Rouppe Van Der Voort, L., & Löfdahl, M. G. (2005). Solar Image Restoration By Use Of Multi-frame Blind De-convolution With

Multiple Objects And Phase Diversity. *Solar Phys.*, *228*(1-2), 191–215. https://doi.org/10.1007/s11207-005-5782-z

Velli, M., Harra, L. K., Vourlidas, A., Schwadron, N., Panasenco, O., Liewer, P. C., Müller, D., Zouganelis, I., St Cyr, O. C., Gilbert, H., Nieves-Chinchilla, T., Auchère, F., Berghmans, D., Fludra, A., Horbury, T. S., Howard, R. A., Krucker, S., Maksimovic, M., Owen, C. J., … Williams, D. (2020). Understanding the origins of the heliosphere: integrating observations and measurements from Parker Solar Probe, Solar Orbiter, and other space- and ground-based observatories. *Astron. Astrophys.*, *642*, Article A4, A4. https://doi.org/10.1051/0004-6361/202038245

Vögler, A., & Schüssler, M. (2007). A solar surface dynamo. *Astron. Astrophys.*, *465*(3), L43–L46. https://doi.org/10.1051/0004-6361:20077253

Walth, G., Wright, S. A., Weiss, J., Larkin, J. E., Moore, A. M., Chapin, E. L., Do, T., Dunn, J., Ellerbroek, B., Gillies, K., Hayano, Y., Johnson, C., Marshall, D., Riddle, R. L., Simard, L., Sohn, J. M., Suzuki, R., & Wincentsen, J. (2016, August). The Infrared Imaging Spectrograph (IRIS) for TMT: data reduction system. In G. Chiozzi & J. C. Guzman (Eds.), *Proc. SPIE, Software and Cyberinfrastructure for Astronomy IV* (99134A, Vol. 9913). https://doi.org/10.1117/12.2233076

Walth, G. L., Wright, S. A., Rundquist, N.-E., Andersen, D., Chapin, E., Chisholm, E., Do, T., Dunn, J., Ellerbroek, B., Gillies, K., Hayano, Y., Johnson, C., Larkin, J., Nakamoto, T., Riddle, R., Simard, L., Smith, R., Suzuki, R., Sohn, J. M., … Zhang, K. (2018, July). The Infrared Imaging Spectrograph (IRIS) for TMT: advancing the data reduction system. In J. C. Guzman & J. Ibsen (Eds.), *Proc. SPIE, Software and Cyberinfrastructure for Astronomy V* (p. 1070731, Vol. 10707). https://doi.org/10.1117/12.2314228

Wang, J. J., Perrin, M. D., Savransky, D., Arriaga, P., Chilcote, J. K., De Rosa, R. J., Millar-Blanchaer, M. A., Marois, C., Rameau, J., Wolff, S. G., Shapiro, J., Ruffio, J.-B., Maire, J., Marchis, F., Graham, J. R., Macintosh, B., Ammons, S. M., Bailey, V. P., Barman, T. S., … Wiktorowicz, S. J. (2018). Automated data processing architecture for the Gemini Planet Imager Exoplanet Survey. *J. of Astron. Telescopes, Instrum., and Syst.*, *4*, Article 018002, 018002. https://doi.org/10.1117/1.JATIS.4.1.018002

Warnecke, J., Korpi-Lagg, M. J., Gent, F. A., & Rheinhardt, M. (2023). Numerical evidence for a small-scale dynamo approaching solar magnetic Prandtl numbers [Publisher: Nature Publishing Group]. *Nature Astronomy*, 1–7. https://doi.org/10.1038/s41550-023-01975-1

Weigelt, G. P. (1977). Modified astronomical speckle interferometry "speckle masking". *Optics Communications*, *21*(1), 55–59. https://doi.org/10.1016/0030-4018(77)90077-3

Wiehr, E., Bovelet, B., & Hirzberger, J. (2004). Brightness and size of small-scale solar magnetic flux concentrations. *Astron. Astrophys.*, *422*, L63–L66. https://doi.org/10.1051/0004-6361:200400019

Williams, R., Hubbard, J. R., Scholl, I. F., Fehlmann, A., Greer, A., & Goodrich, B. D. (2020, December). Building the on-summit data processing pipeline for the cryogenic near infrared spectropolarimeter instrument on the Daniel K. Inouye Solar Telescope. In J. C. Guzman & J. Ibsen (Eds.), *Proc. SPIE, Software and Cyberinfrastructure for Astronomy VI* (p. 1145217, Vol. 11452). https://doi.org/10.1117/12.2560230

Wilson, A., & Maskelyne, N. (1774). Observations on the Solar Spots. *Philosophical Transactions of the Royal Society of London Series I*, *64*, 1–30.

Xiong, H., Argan, A., Baudin, D., Bayer, J., Bouyjou, F., De Angelis, N., Del Monte, E., Evangelista, Y., Favre, Y., Feroci, M., Galvez, J.-L., Gevin, O., Hedderman, P., Hernanz, M., Kole, M. R., Meuris, A., Pliego-Caballero, S., Santangelo, A., Tenzer, C., … Zampa, G. (2022, August). The digital data processing concepts of the large area detector and the wide field monitor onboard eXTP. In J.-W. A. den Herder, S. Nikzad, & K. Nakazawa (Eds.), *Proc. SPIE, Space Telescopes and Instrumentation 2022: Ultraviolet to Gamma Ray* (121816F, Vol. 12181). https://doi.org/10.1117/12.2630462

Yang, D., Gizon, L., Barucq, H., Hirzberger, J., Orozco Suárez, D., Albert, K., Albelo Jorge, N., Appourchaux, T., Alvarez-Herrero, A., Blanco Rodríguez, J., Gandorfer, A., Germerott, D., Guerrero, L., Gutierrez-Marques, P., Kahil, F., Kolleck, M., Solanki, S. K., del Toro Iniesta, J. C., Volkmer, R., … Valori, G. (2023). Direct assessment of SDO/HMI helioseismology of active regions on the Sun's far side using SO/PHI magnetograms. *Astron. Astrophys.*, *674*, Article A183, A183. https://doi.org/10.1051/0004-6361/202346030

Yardley, S. L., Owen, C. J., Long, D. M., Baker, D., Brooks, D. H., Polito, V., Green, L. M., Matthews, S., Owens, M., Lockwood, M., Stansby, D., James, A. W., Valori, G., Giunta, A., Janvier, M., Ngampoopun, N., Mihailescu, T., To, A. S. H., van Driel-Gesztelyi, L., … Federov, A. (2023). Slow Solar Wind Connection Science during Solar Orbiter's First Close Perihelion Passage. *Astrophys. J. Suppl.*, *267*(1), Article 11, 11. https://doi.org/10.3847/1538-4365/acd24b

Yeo, K. L., & Krivova, N. A. (2019). Intensity contrast of solar network and faculae. II. Implications for solar irradiance modelling. *Astron. As-*

trophys., *624*, Article A135, A135. https://doi.org/10.1051/0004-6361/201935123

Yeo, K. L., Krivova, N. A., & Solanki, S. K. (2014). Solar Cycle Variation in Solar Irradiance. *Space Sci. Rev.*, *186*(1-4), 137–167. https://doi.org/10.1007/s11214-014-0061-7

Yeo, K. L., Krivova, N. A., Solanki, S. K., Hirzberger, J., Orozco Suárez, D., Albert, K., Albelo Jorge, N., Appourchaux, T., Alvarez-Herrero, A., Blanco Rodríguez, J., Gandorfer, A., Gutierrez-Marques, P., Kahil, F., Kolleck, M., del Toro Iniesta, J. C., Volkmer, R., Woch, J., Fiethe, B., Pérez-Grande, I., … Valori, G. (2023). Reconstruction of total solar irradiance variability as simultaneously apparent from Solar Orbiter and Solar Dynamics Observatory. *Astron. Astrophys.*, *679*, Article A25, A25. https://doi.org/10.1051/0004-6361/202345872

Yeo, K. L., Solanki, S. K., & Krivova, N. A. (2013). Intensity contrast of solar network and faculae. *Astron. Astrophys.*, *550*, Article A95, A95. https://doi.org/10.1051/0004-6361/201220682

Zhou, C., Xie, Y., Ren, J., Wei, Z., Du, L., Zhang, Q., Xie, Z., Liu, B., Lei, T., & Yuan, X. (2021). Spin separation based on-chip optical polarimeter via inverse design. *Nanophotonics*, *11*(4), Article 455, 455. https://doi.org/10.1515/nanoph-2021-0455

Zouganelis, I., De Groof, A., Walsh, A. P., Williams, D. R., Müller, D., St Cyr, O. C., Auchère, F., Berghmans, D., Fludra, A., Horbury, T. S., Howard, R. A., Krucker, S., Maksimovic, M., Owen, C. J., Rodríguez-Pacheco, J., Romoli, M., Solanki, S. K., Watson, C., Sanchez, L., … Zhukov, A. N. (2020). The Solar Orbiter Science Activity Plan. Translating solar and heliospheric physics questions into action. *Astron. Astrophys.*, *642*, Article A3, A3. https://doi.org/10.1051/0004-6361/202038445

Zuccarello, F., Guglielmino, S. L., & Romano, P. (2014). Evolution and Dynamics of Orphan Penumbrae in the Solar Photosphere: Analysis from Multi-instrument Observations. *Astrophys. J.*, *787*(1), Article 57, 57. https://doi.org/10.1088/0004-637X/787/1/57

A. Report on the design and implementation efforts of the data processing pipeline

In our contribution to the Society of Photo-Optical Instrumentation Engineers (SPIE) conference for Astronomical Telescopes + Instrumentation in 2018, titled "Autonomous on-board data processing and instrument calibration software for the SO/PHI" (see Albert et al., 2018), we presented the design of the software, emphasizing its key features and considerations. We showcased the current state of the pipeline and demonstrated its capabilities by processing data acquired by the SDO/HMI instrument, adjusted to represent SO/PHI observations.

Contributions to the publication: K. Albert took a primary role in the design of the data reduction software, collaborating closely with the teams that worked on the lower level software and firmware on the one end, and the instrument science team, on the other end. She prepared and analysed the data, and prepared the manuscript.

PROCEEDINGS OF SPIE

SPIEDigitalLibrary.org/conference-proceedings-of-spie

Autonomous on-board data processing and instrument calibration software for the SO/PHI

Albert, K., Hirzberger, J., Busse, D., Lange, T., Kolleck, M., et al.

K. Albert, J. Hirzberger, D. Busse, T. Lange, M. Kolleck, B. Fiethe, D. Orozco Suárez, J. Woch, J. Schou, J. Blanco Rodriguez, A. Gandorfer, Y. Guan, J. P. Cobos Carrascosa, D. Hernández Expósito, J. C. del Toro Iniesta, S. K. Solanki, H. Michalik, "Autonomous on-board data processing and instrument calibration software for the SO/PHI," Proc. SPIE 10707, Software and Cyberinfrastructure for Astronomy V, 107070O (6 July 2018); doi: 10.1117/12.2311718

SPIE.

Event: SPIE Astronomical Telescopes + Instrumentation, 2018, Austin, Texas, United States

Autonomous on-board data processing and instrument calibration software for the SO/PHI

K. Albert[a], J. Hirzberger[a], D. Busse[a], T. Lange[b], M. Kolleck[a], B. Fiethe[b], D. Orozco Suárez[c], J. Woch[a], J. Schou[a], J. Blanco Rodríguez[d], A. Gandorfer[a], Y. Guan[b], J.P. Cobos Carrascosa[c], D. Hernández Expósito[d], J.C. del Toro Iniesta[c], S. K. Solanki[a], and H. Michalik[b]

[a]Max Planck Institute for Solar System Research, Justus-von-Liebig-Weg 3, Göttingen, Germany
[b]Institute of Computer and Network Engineering at the TU Braunschweig, Hans-Sommer-Straße 66, Braunschweig, Germany
[c]Instituto de Astrofísica de Andalucía (IAA - CSIC), Apartado 3004, Granada, Spain
[d]Universidad de Valencia, Catedrático José Beltrán 2, Paterna (Valencia), Spain

ABSTRACT

The extension of on-board data processing capabilities is an attractive option to reduce telemetry for scientific instruments on deep space missions. The challenges that this presents, however, require a comprehensive software system, which operates on the limited resources a data processing unit in space allows.
We implemented such a system for the Polarimetric and Helioseismic Imager (PHI) on-board the Solar Orbiter (SO) spacecraft. It ensures autonomous operation to handle long command-response times, easy changing of the processes after new lessons have been learned and meticulous book-keeping of all operations to ensure scientific accuracy. This contribution presents the requirements and main aspects of the software implementation, followed by an example of a task implemented in the software frame, and results from running it on SO/PHI.
The presented example shows that the different parts of the software framework work well together, and that the system processes data as we expect. The flexibility of the framework makes it possible to use it as a baseline for future applications with similar needs and limitations as SO/PHI.

1. INTRODUCTION

Many state of the art scientific space instruments produce more data than what is possible to download to ground. This discrepancy is especially significant when, due to the orbit design, the mission can only ensure a low amount of telemetry. One way to reduce the necessary telemetry is to extend the on-board processing capabilities of the instrument.
This strategy is adapted for the Polarimetric and Helioseismic Imager (PHI).[1] PHI is the first imaging solar spectropolarimeter on-board a deep space mission: the Solar Orbiter (SO). It will image the solar photosphere in the light of the Fe I 617.3 nm absorption line, at six wavelengths and in four polarisation states of light. This spectral line is sensitive to the magnetic field (through the Zeeman effect) and to the line of sight (LOS) velocities in the photosphere (due to the Doppler effect). Through the measurements described we can determine characteristics of the magnetic field and the LOS velocity at the average of the formation height for the absorption line. To retrieve these quantities the polarised radiative transfer equation (RTE) must be inverted.[2]
SO/PHI implements on-board autonomous instrument calibration and on-board autonomous science data analysis including RTE inversion. This means that the calibration data can be directly applied on-board to the science observables without adding to the telemetry volume. Therefore the necessary telemetry is reduced to the continuum intensity, the magnetic field vector and the LOS velocity instead of the raw science observables.

Further author information: (Send correspondence to K.A.)
K.A.: albert@mps.mpg.de, +49 551 384 979-186
J.H.: hirzberger@mps.mpg.de
D.B.: busse@mps.mpg.de

Software and Cyberinfrastructure for Astronomy V, edited by Juan C. Guzman, Jorge Ibsen, Proc. of SPIE
Vol. 10707, 107070O · © 2018 SPIE · CCC code: 0277-786X/18/$18 · doi: 10.1117/12.2311718

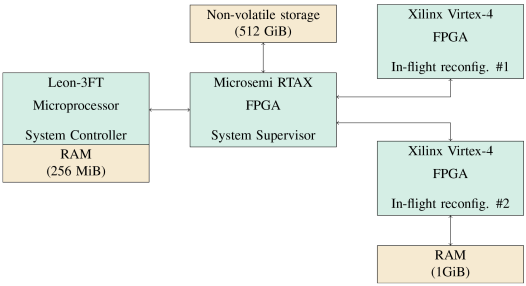

Figure 1: The data processing of SO/PHI is distributed between a Leon-3FT microprocessor and Xilinx Virtex-4 RFPGAs. These units are aided by memories of different capacities. Data is stored in the non-volatile memory.

These functions are implemented for the first time on this type of instrument with the limited computational resources a space instrument offers. Comparable systems have been implemented on the AMPTE IRM 3D Plasma Instrument, the Giotto RPA Experiment[3] and the SOHO/MDI.[4] However, all these cases are considerably more limited in capability than the system implemented for SO/PHI.
The hardware available for data processing[5,6] integrates a system controller microprocessor, a system supervisor Field Programmable Gate Array (FPGA), and two dynamically reconfigurable FPGAs (RFPGAs). See fig. 1. The processing is aided with a 1 GiB processing memory connected to one of the RFPGAs, and a much smaller, 256 MiB memory connected to the microprocessor, of which only a part is available for image processing. A non-volatile storage of 512 GiB is available for storing data in the instrument. The in flight reconfigurability of the two Xilinx FPGAs enables us to take a time-sharing approach, saving volume, mass and energy.
SO/PHI captures science images during dedicated observation windows along the orbits, each lasting for 10 days. An in-orbit calibration campaign is associated with each observation window with the aim of characterising the instrument in the observational conditions. The data processing is done after the observation window, using the data collected in the calibration campaign. The planning of the operations and the data processing is done together and on long term, well ahead of the time of their execution. This includes the specification of all input and output addresses, as well as the selection of the correct calibration data for the reduction of the dataset.
In the following we describe the software frame for the on-board data calibration and on-board data pre-processing steps performed before the inversion of the RTE.

2. REQUIREMENTS OF THE DATA PROCESSING SYSTEM

The data processing system of SO/PHI performs three different tasks. It:

- determines the optimal operational parameters for the instrument (e.g. focus position) from dedicated datasets, refining the result in a second observation,
- calculates the calibration data from datasets obtained during dedicated observations,
- processes the raw science observables by removing the instrumental effects, inverting the RTE and compressing the data.

The processing tasks involve computationally demanding image processing steps. To shorten run time, these functions are implemented in one of the two RFPGAs. However, a back-up solution, implemented in the microprocessor is also required to facilitate early testing during development, as well as to contribute to fault tolerance. This results in the need of ensuring that the same task can run on two platforms with different amount of processing memory.
To reduce the implementation complexity of the RFPGA functions, a fixed point notation has been adapted for the processing system. To maintain the requirements for scientific accuracy the images are rescaled before the processing steps are applied to them.

Due to the novelty of the mission a number of questions related to the data processing steps may only be answered after first light. This requires the possibility for easy changes in the task implementations.
Due to the autonomous execution and no access to the intermediate results, the only record of the operations is kept in a processing log file, as part of the metadata of each dataset. The metadata recording therefore must be integral and secure, as well as provide data that facilitates error search and improvement of the algorithms.

3. IMPLEMENTATION OF THE DATA PROCESSING SYSTEM

We take a unified approach to the tasks, implementing them in the form of pipelines. A pipeline is defined to be a series of operations executed on the same target (a dataset or a subset of a dataset). All pipelines start with loading the target from the non-volatile memory into the processing memory, and end by either storing the result dataset in the non-volatile memory, or by returning a calculated parameter.
To implement the computationally demanding functions on the RFPGAs we define several FPGA configurations, each of them containing dedicated hardware logic that implements parts of the on-board processing (e.g. RTE inversion, or a group of different image processing functions), and load them into the RFPGAs as needed.[7]
To fulfil the requirement on easily changing the pipelines a block approach is taken. The blocks access the image processing functions running on the RFPGAs, or the microprocessor in back-up implementation, and combine them into useful steps. To facilitate changing their order, they have a unified interface. Within the pipeline all blocks have the same target, loaded as the first step of the pipeline into the processing memory. The blocks ensure that the target at their interface is scaled to be represented on the maximum number of available bits. All blocks may load additional data necessary for the processing steps, which are discarded at their termination. Each block must also determine the dataset history, to facilitate their free ordering. The parameters necessary for this are not passed as variables in-between the blocks, instead they are transferred through the metadata. All blocks are executed sequentially, and a pipeline is manipulating the target only through blocks.
Due to the requirement on executing the pipeline both with and without the RFPGAs, the pipeline must run with different amounts of processing memory. In the back-up solution, the memory cannot hold a full dataset. Therefore, the pipeline is parametrised and can be configured to run on a subset of the full dataset. In many steps the pipeline needs one image of the dataset. However, there are exceptions in which corresponding pixels from multiple images are necessary. Consequently, we split the pipeline into an image linear and image parallel part, each running on a part of the full dataset: a number of images or a number of rows from all images.
Error handling is done with two error levels: errors and warnings, based on their severity. Errors interrupt the processing, while warnings are checked on ground to evaluate the correctness of the results. Both are marked in the return value of all operations, blocks and pipelines. In order to log multiple warnings and errors detected, the return values are defined as bit masks.
The metadata of a dataset contains all relevant information and is recorded at different times: at image acquisition, and at data processing. The information is organised by entries, containing parameters that form a logical unit (e.g. the return value and parameters of the image processing functions), and the metadata file is treated as a log.

4. EXAMPLE PIPELINE AND ITS RUN

To demonstrate how the system works, we take an example of a science data pre-processing pipeline, consisting of 3 steps: dark field subtraction, flat field division, and polarimetric demodulation. This is the minimum that is needed for pre-processing, and would be followed by RTE inversion for full on-board analysis.
Each step becomes a block, and the whole pipeline is split into the image linear and image parallel part. Each of these starts with the loading of the target dataset, and ends with the storage of the result (see fig. 2). Each block scales the datasets to adapt to the defined scaling interface between them, and to calculate the results at the required accuracy. The blocks also check the history of the target dataset and adapt the calibration data applied to them. Additional verifications generate warnings to determine possible problem-sources on ground. Each pipeline is inside a loop and is executed the number of times necessary to process the whole dataset, when this is split into sub-parts.
The input data for the demonstration is generated from images taken by the SDO/HMI instrument,[9] transformed into Stokes images with the SO/PHI instrument simulator, SOPHISM.[8] See fig. 3a to 3d.

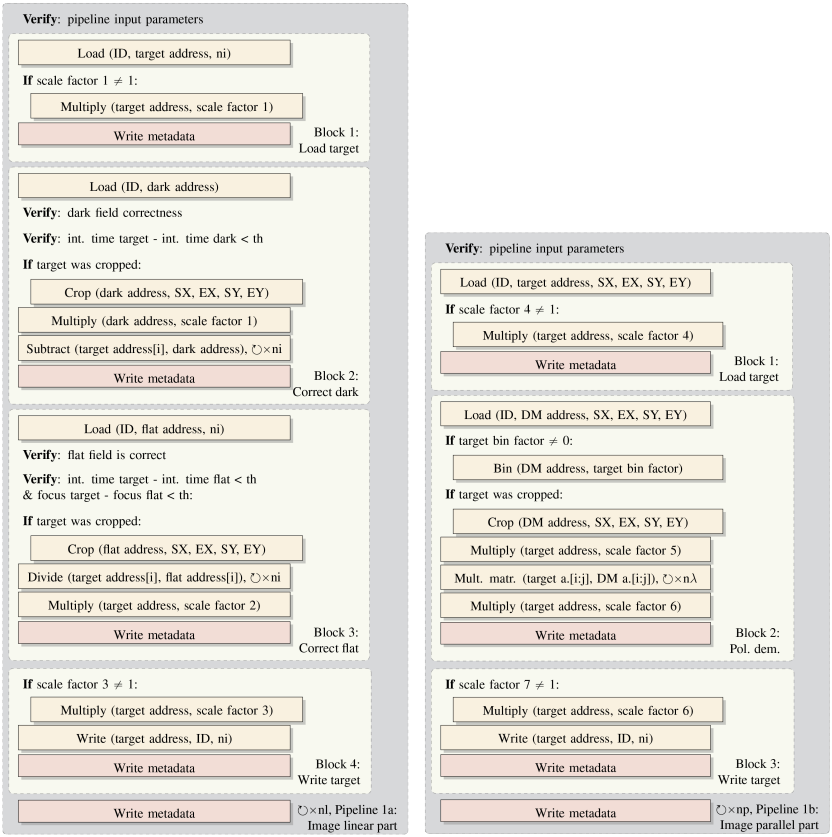

(a) Image linear part. (b) Image parallel part.

Figure 2: Example science data processing pipeline. In (a): the parameter ni denotes the number of images processed at a given time, while nl is the number of times the image linear portion of the pipeline has to run to process the whole dataset. In (b): nλ denotes the number of wavelengths processed at a given time, while np denotes the iterations of the image parallel part of the pipeline necessary for the full processing of the dataset.

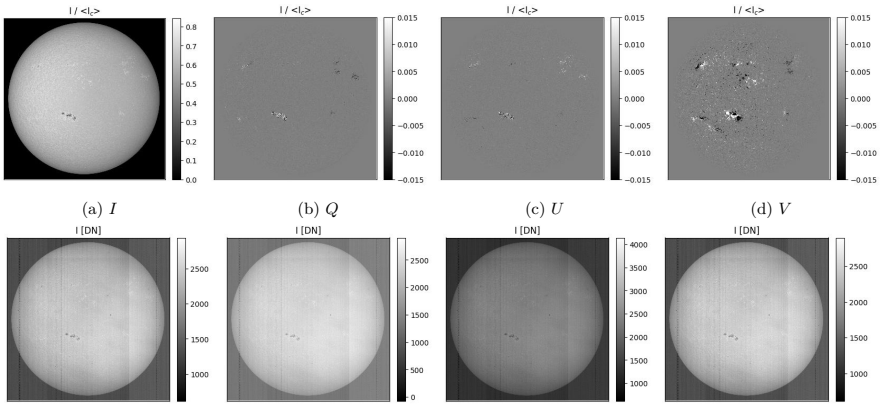

(a) I (b) Q (c) U (d) V

(e) I_1 (f) I_2 (g) I_3 (h) I_4

Figure 3: Test dataset at line centre. (a) - (d): Stokes images from SOPHISM.[8] (e) - (h): Input to the pipeline, Stokes images modified according to eq. (1). The input images show the dark field (the stripes), and the flat field (smudges and dust grains). These effects are compensated by applying the calibration data shown in fig. 4, then demodulated to arrive at the Stokes images once again.

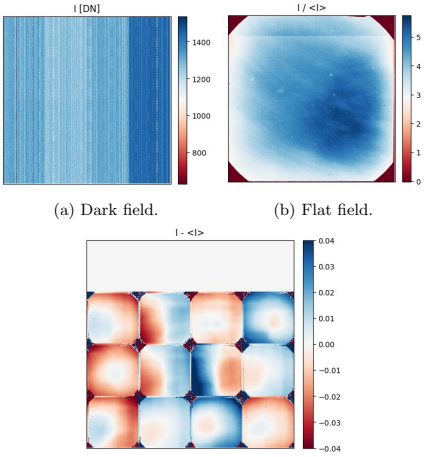

(a) Dark field. (b) Flat field.

(c) DM Uniformity across FOV.

Figure 4: The calibration data used in the test run is recorded in the laboratory. (a): The dark field shows the characteristic sensor pattern: four distinct vertical stripes and row-to-row horizontal variations. (b): The flat field used in the tests is the same for all wavelengths and modulation states. (c): The variation of the 4×4 demodulation matrix elements across the FOV, treated as a dataset of 16 images.

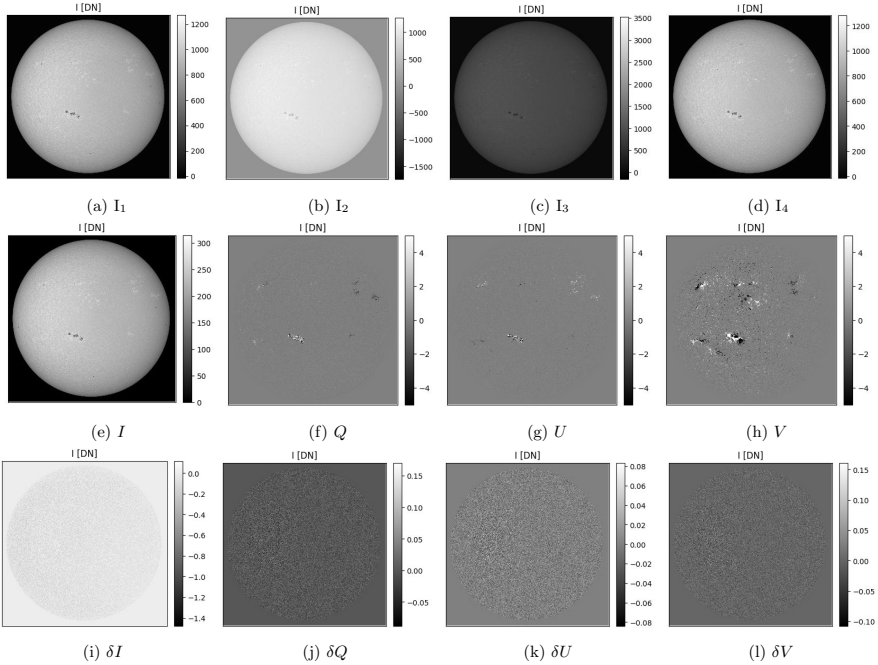

(a) I_1 (b) I_2 (c) I_3 (d) I_4

(e) I (f) Q (g) U (h) V

(i) δI (j) δQ (k) δU (l) δV

Figure 5: Result dataset at line centre. (a) - (d): Input images corrected for the effects of dark and flat field. (e) - (h): Result of the demodulation of the images in fig. 5a to 5d. (i) - (l): The difference after demodulation when executing the pipeline in floating point representation on a desktop, and executing it in fixed point representation on SO/PHI. The differences occur inside the solar disk in form of quantisation noise. (The units are in fixed point DN-s.)

Table 1: The metadata from the image linear pipeline portion shows all executed blocks, ending with the entry by the pipeline. Parameter 1 shows the ID of the Target Dataset (TD), Dark Field (DF), Flat Field (FF) and Result Dataset (RD). The dataset is processed in the RFPGA, treating all 24 images (see image start (S) and end (E)), and the full field of view (see row and column start (S) and end (E)) at once. The flat correction block generates a warning about produced NaN-s, which is also shown in the pipeline return.

Return value	Function ID	param. 1	param. 2	image S	image E	row S	row E	col. S	col. E
Correct	Load	TD ID	0	0	23	0	2047	0	2047
Correct	Correct Dark	DF ID	0	0	23	0	2047	0	2047
W: NaNs	Correct Flat	FF ID	0	0	23	0	2047	0	2047
Correct	Store	RD ID	0	0	23	0	2047	0	2047
W: NaNs	Linear ppln.	RD ID	0	0	23	0	2047	0	2047

These images are further manipulated to represent the raw observables, according to the following equation:

$$\boldsymbol{I}_{\lambda}^{\mathrm{input}}(x,y) = c_1 c_2[\boldsymbol{M}(x,y) \cdot \boldsymbol{I}_{\lambda}^{\mathrm{Stokes}}(x,y)]I^{\mathrm{Flat}}(x,y) + I^{\mathrm{Dark}}(x,y), \tag{1}$$

where "·" stands for matrix multiplication, λ denotes the wavelength, x and y denote the image row and column size, $\boldsymbol{I}_{\lambda}^{\mathrm{input}}$ is the created test dataset, a 1×4 matrix of images at 6 different wavelengths, $\boldsymbol{I}_{\lambda}^{\mathrm{Stokes}}$ is the 1×4 matrix of Stokes images created with SOPHISM at 6 wavelengths, which can be expressed for any of the wavelengths as:

$$\boldsymbol{I}^{\mathrm{Stokes}} = [I, Q, U, V]^T,$$

$\boldsymbol{M}$ is the instrument Modulation Matrix, a 4×4 matrix of images, describing how the instrument transforms the sought Stokes images into practically measurable light levels for each pixel of its field of view (FOV), applied for all wavelengths, c_1 is the constant that scales the normalised images to represent the number of incident photons in 20 ms exposure time, c_2 is the constant that converts the pixels from number of photons accumulated on the detector to Digital Numbers (DN-s), I_{Flat} is one image, the normalised flat field of the telescope, applied to all wavelengths and polarisation states, and I_{Dark} is the dark field image of the sensor at 20 ms integration time in DN-s, the same for all wavelengths and polarisation states.

The pipeline removes the dark field and the flat field from the input images, then demodulates them to arrive to the Stokes images. The calibration data applied by the pipeline is recorded in the laboratory, using the SO/PHI Flight Model (see fig. 4). The dark field is the offset of the image detector, while the flat field shows the gain variations across the FOV caused by the optics. The Demodulation Matrix is the inverse of the Modulation Matrix used in eq. (1). The test is run on a model of SO/PHI, which is representative in its data processing unit.

We compare the output of the pipeline run on SO/PHI to results produced on the desktop with floating point calculations on the same input data. We expect these to give similar results with differences within an error margin, coming from the pixel quantisation in fixed point notation. The differences are as we expect them, appearing as quantisation noise over the solar disk. The standard deviation of the differences is 0.05% for the Stokes I/I_r image, and 6%, 5.3% and 1.8% for Q/Q_r, U/U_r and V/V_r, respectively, where I_r, Q_r, U_r and V_r denote the resulting Stokes images from the reference pipeline. The polarimetric errors coming from the fixed point representation are 0.017%, 0.015% and 0.016% for Q/I_c, U/I_c and V/I_c, respectively, where I_c is the Stokes I at continuum wavelength. These values are within the SO/PHI scientific requirements, and may be further optimised by adjusting the scaling parameters.

The metadata entries, recorded to summarise the blocks and pipelines executed on the dataset, contain their ID, given parameters and return values. See table 1. To keep a complete record, in addition to these, entries from other sources are also logged (e.g. entries from the image processing operations, or describing the dataset).

5. CONCLUSIONS

SO/PHI is the first solar imaging spectropolarimeter to perform autonomous on-board instrument calibration and autonomous data reduction. The data processing involved with these tasks is implemented in a software framework distributed between a microprocessor and two RFPGAs. The microprocessor controls the RFPGAs, which implement functions with long computational times to accelerate them (e.g. image processing functions). The framework is designed to ensure the implementation of a large variety of algorithms, and their easy modification when necessary, while operating with limited memory resources. To ensure that the autonomous process can be fully recovered on ground, a metadata log is kept about all operations performed, their parameters and return values. A warning system is implemented for supporting the scientists on ground to find possible errors in the processing. The presented results demonstrate the integrity of the system and its ability to process the data.
The data processing software frame has the following key features:

- block approach,
- pipeline implementation of tasks,
- parametrised pipelines for processing data in sub-sets,
- wide error detection and handling,
- a system for maintaining required accuracy during fixed point operations,
- extensive metadata logging.

The software system was developed for the specific needs of the SO/PHI instrument on-board the Solar Orbiter, to cope with the telemetry limitations. However, due to the adaptability of the system, it is planned to serve as basis for on-board data processing systems for future instruments in similarly challenging orbits. A more detailed description of the SO/PHI data processing system will be given in a paper currently in preparation.

Acknowledgements

This work was carried out in the framework of the International Max Planck Research School (IMPRS) for Solar System Science at the Max Planck Institute for Solar System Research (MPS). Solar Orbiter is a mission lead by the European Space Agency (ESA) with significant contribution from National Aeronautics and Space Administration (NASA). The SO/PHI instrument is supported by the German Aerospace Center (DLR) through Grant 50 OT 1201. The Spanish contribution has been partly funded by the Spanish Research Agency under project ESP2016-77548-C5, partially including European FEDER funds. The solar data used in the test are the courtesy of NASA/SDO HMI science team.

REFERENCES

[1] Gandorfer, A., Solanki, S. K., Woch, J., Martínez Pillet, V., Álvarez Herrero, A., and Appourchaux, T., "The Solar Orbiter Mission and its Polarimetric and Helioseismic Imager (SO/PHI)," *Journal of Physics Conference Series* **271**, 012086 (Jan. 2011).

[2] del Toro Iniesta, J. C. and Ruiz Cobo, B., "Inversion of the radiative transfer equation for polarized light," *Living Reviews in Solar Physics* **13**, 4 (Nov. 2016).

[3] Curtis, D. W., Carlson, C. W., Lin, R. P., Paschmann, G., and Reme, H., "On-board data analysis techniques for space plasma particle instruments," *Review of Scientific Instruments* **60**, 372–380 (Mar. 1989).

[4] Scherrer, P. H., Bogart, R. S., Bush, R. I., Hoeksema, J. T., Kosovichev, A. G., Schou, J., Rosenberg, W., Springer, L., Tarbell, T. D., Title, A., Wolfson, C. J., Zayer, I., and MDI Engineering Team, "The Solar Oscillations Investigation - Michelson Doppler Imager," *Solar Physics* **162**, 129–188 (Dec. 1995).

[5] Fiethe, B., Michalik, H., Dierker, C., Osterloh, B., and Zhou, G., "Reconfigurable system-on-chip data processing units for space imaging instruments," *Proceedings of the conference on Design, automation and test in Europe* , 977–982, EDA Consortium (2007).

[6] Fiethe, B., Bubenhagen, F., Lange, T., Michalik, H., Michel, H., Woch, J., and Hirzberger, J., "Adaptive hardware by dynamic reconfiguration for the Solar Orbiter PHI instrument," *2012 NASA/ESA Conference on Adaptive Hardware and Systems (AHS)* , 31–37, IEEE (2012).

[7] Lange, T., Fiethe, B., Michel, H., Michalik, H., Albert, K., and Hirzberger, J., "On-board processing using reconfigurable hardware on the solar orbiter PHI instrument," *2017 NASA/ESA Conference on Adaptive Hardware and Systems (AHS)* , 186–191, IEEE (2017).

[8] Blanco Rodríguez, J., del Toro Iniesta, J. C., Orozco Suárez, D., Martínez Pillet, V., Bonet, J. A., Feller, A., Hirzberger, J., Lagg, A., Piqueras, J., and Gasent Blesa, J. L., "SOPHISM: An End-To-End software instrument simulator," *The Astrophysical Journal Supplement Series* (Submitted).

[9] Schou, J., Scherrer, P. H., Bush, R. I., Wachter, R., Couvidat, S., Rabello-Soares, M. C., Bogart, R. S., Hoeksema, J. T., Liu, Y., Duvall, T. L., Akin, D. J., Allard, B. A., Miles, J. W., Rairden, R., Shine, R. A., Tarbell, T. D., Title, A. M., Wolfson, C. J., Elmore, D. F., Norton, A. A., and Tomczyk, S., "Design and Ground Calibration of the Helioseismic and Magnetic Imager (HMI) Instrument on the Solar Dynamics Observatory (SDO)," *Solar Physics* **275**, 229–259 (Jan. 2012).

B. Details of the data processing pipeline

In the peer-reviewed publication titled "Autonomous on-board data processing and instrument calibration software for the Polarimetric and Helioseismic Imager on-board the Solar Orbiter mission" (see Albert et al., 2020b), we provided an in-depth description of the software system responsible for processing SO/PHI data. This publication builds upon our earlier work in Albert et al., 2018, presenting a consolidated design and a data processing pipeline encompassing all essential functionalities. We aimed to provide a reference for the scientific community, describing the process from the raw to the science-ready data. Moreover, we also aimed to introduce the system's design to the engineering community, offering insights into on-board processing options and potential solutions. The publication details the requirements of the on-board data processing system, the strategies used to meet these requirements, and the trade-offs made in the process. Additionally, we demonstrated the system's efficiency by analysing the time taken to process data, and additional insights are offered by a look at the corresponding CPU load during the process.

Contributions to the publication: K. Albert took the main role in designing the data reduction software, which can work with the lower software and firmware levels, and fulfils the scientific requirements. She designed the main features of the data reduction system, such as, the block approach, the interfaces between the blocks, the structure of the metadata, the error-handling concept, and the data precision management with the fixed point number representation. She also worked together with the firmware team to define the necessary functionalities, their requirements, and worked on the high level validation of the firmware. She also worked on the implementation and testing of the data reduction software, as an integral part of a three-member team. She prepared the test data, implemented the timing measurements in the data reduction pipeline, ran the data processing, and analysed the results. She also prepared the manuscript.

Autonomous on-board data processing and instrument calibration software for the Polarimetric and Helioseismic Imager on-board the Solar Orbiter mission

Kinga Albert[a,*] **Johann Hirzberger**[a] **Martin Kolleck**[a] **Nestor Albelo Jorge**[a] **Dennis Busse**[a] **Julian Blanco Rodríguez**[b] **Juan Pedro Cobos Carrascosa**[c] **Björn Fiethe**[d] **Achim Gandorfer**[a] **Dietmar Germerott**[a] **Yejun Guan**[d] **Lucas Guerrero**[a] **Pablo Gutierrez-Marques**[a] **David Hernández Expósito**[c] **Tobias Lange**[d] **Harald Michalik**[d] **David Orozco Suárez**[c] **Jesper Schou**[a] **Sami K. Solanki**[a,e] **José Carlos del Toro Iniesta**[c] **and Joachim Woch**[a]

[a]Max-Planck-Institut für Sonnensystemforschung, Göttingen, Germany
[b]Universidad de Valencia, Paterna, Valencia, Spain
[c]Instituto de Astrofísica de Andalucía—Consejo Superior de Investigaciones Científicas, Apartado, Granada, Spain
[d]Institute of Computer and Network Engineering at the Technical University Braunschweig, Braunschweig, Germany
[e]Kyung Hee University, School of Space Research, Yongin, Gyeonggi-Do, South Korea

Abstract. A frequent problem arising for deep space missions is the discrepancy between the amount of data desired to be transmitted to the ground and the available telemetry bandwidth. A part of these data consists of scientific observations, being complemented by calibration data to help remove instrumental effects. We present our solution for this discrepancy, implemented for the Polarimetric and Helioseismic Imager on-board the Solar Orbiter mission, the first solar spectropolarimeter in deep space. We implemented an on-board data reduction system that processes calibration data, applies them to the raw science observables, and derives science-ready physical parameters. This process reduces the raw data for a single measurement from 24 images to five, thus reducing the amount of downlinked data, and in addition, renders the transmission of the calibration data unnecessary. Both these on-board actions are completed autonomously.
 [DOI: 10.1117/1.JATIS.6.4.048004]

Keywords: spectropolarimetry; solar physics; space observatory; on-board data processing; data pipelines.

Paper 20063 received Jun. 5, 2020; accepted for publication Nov. 19, 2020; published online Dec. 18, 2020.

1 Introduction

Today's space missions are progressing in ambition and complexity, and the state-of-the-art instrumentation that they carry can produce vast amounts of data. This is especially true for remote sensing instruments, often producing multi-dimensional, high-resolution data products. In addition to that, the required precision and orbits with highly variable environments often require calibration data to be acquired on board as well. However, all raw observables and calibration data often cannot be transmitted to the ground due to low amounts of telemetry, especially in the case of deep space missions. These can, however, be processed on-board to result in calibrated, science-ready data that are more compact, hence increasing the science return of the mission. This processing often requires a high degree of autonomy, due to the limited telemetry and telecommand, which sometimes is also paired with long turnaround times.

*Address all correspondence to Kinga Albert, albert@mps.mpg.de

Solar Orbiter[1] (SO) is a mission for helioscience. It will follow unique, highly elliptical orbits around the Sun, with the closest approach at 0.28 astronomical units, and it will move out of the ecliptic plane during its lifetime to reach an inclination of 33° (including the extended mission phase). This provides a view of the polar regions of the Sun. To achieve the science goals, the spacecraft will carry a suite of four *in-situ* and six remote sensing instruments.

The Polarimetric and Helioseismic Imager[2] (SO/PHI) is part of the remote sensing package. It is a spectropolarimeter imaging the solar photosphere in the light of the Fe I 617.3-nm Zeeman sensitive absorption line. It takes images of the Sun in four polarization states of the light at six different wavelengths. Due to the Zeeman and Doppler effects, these observables carry information about the magnetic field vector and the flow velocities at the formation region of the spectral line in the solar atmosphere. Through the inversion of the radiative transfer equation (RTE), the magnetic field vector and the line of sight (LOS) velocity can be determined.[3]

SO/PHI is the first imaging spectropolarimeter to fly on a deep space mission, facing unprecedented challenges. It has an extremely low amount of guaranteed telemetry, it will see highly variable environment (especially large changes of temperature and radiation), and experience long command-response turnaround times. To cope with these restrictions, unprecedented for this type of instrument, SO/PHI implements autonomous on-board data reduction and autonomous on-board instrument calibration. The on-board data reduction consists of data pre-processing, i.e., the removal of instrumental effects and the inversion of the RTE[4–6]). The on-board instrument calibration includes both the characterization of the instrument (i.e., calculation of the flat and dark field) and the determination of the optimal operational parameters (e.g., integration time).

In the domain of on-board data processing, we most often find cases for data characterization: data are sorted into different categories, or they identify features, such as ice or clouds.[7–9] In these cases, the necessary accuracy is determined by the algorithms used, without the goal of producing data for further scientific analysis, posing a different set of challenges. There are few precedents for scientific on-board data analysis. The Active Magnetospheric Particle Tracer Explorers Ion Release Module 3D Plasma Instrument and the Giotto RPA Experiment, three decades ago, computed moments of the distribution function and calculated pitch angle distribution on-board to minimize telemetry.[10] The reduction was done in real time for both these instruments, with severe resource limitations compared to today's state of the art, therefore the efforts were mainly concentrated on meeting the timing requirements. The solar wind analyzer on-board the SO calculates the moments of particle velocity distribution functions on-board through look-up-tables and implements an intelligent telemetry management system to meet the limitations set by the mission.[11] Another instrument, more comparable to SO/PHI, also implementing on-board data processing, is the Michelson Doppler Imager on-board the Solar and Heliospheric Observatory.[12] Due to telemetry limitations, it performs some of the initial steps of the data reduction prior to data downlink. It uses arithmetic operations and look-up-tables to calculate part of the observables, complemented by additional processing and calibration on ground. Instrumental effects are entirely determined on ground and uploaded to the instrument to be used in the data processing.

Typical calibration of an imaging spectropolarimeter[13–15] is based on extensive ground measurements. However, the precise calibration parameters (e.g., gain tables, dark current levels, and instrumental polarization parameters) are expected to change during the lifetime of most instruments, therefore calibration data are collected regularly. The calibration images are then analyzed and processed by the scientists operating the instrument on ground. The highly elliptical orbits of the SO mission introduce changes in several of the instrumental properties due to their temperature dependence (especially strong for the dark and the flat fields) and brings challenges due to changing Doppler shift and image scales. These dynamic changes render ground measurements insufficient and requires SO/PHI to collect calibration data from orbit as close to observational conditions as possible. To avoid the download of these data, SO/PHI processes them on-board, autonomously.

SO/PHI's data processing software is a first in multiple aspects. It implements complete autonomous on-board processing for spectropolarimetric solar data from the instrument characterization to the calculation of the final science data products using the inversion of the RTE. These steps distribute their calculations between hardware and software and are integrated seamlessly into a software framework, which runs on the SO/PHI data processing unit (DPU) with

limited computational resources. As the system's objective is to reduce data volume and increase science return, intermediate data products in nominal operations will not be available. Therefore, the robustness of the software is essential.

2 The SO/PHI Instrument

To provide an overview of the SO/PHI instrument, we describe its working principle, the available hardware for data processing and its operation concept.

2.1 *Instrument Principle*

SO/PHI images the Sun with two different optical paths.[16] One of the paths images the full solar disk at any point along the orbit, called the full disk telescope [with a 2° field of view (FOV)], while the other collects data with high spatial resolution, named the high-resolution telescope (HRT, with a 0.28° FOV).[17] The optical path of the HRT is additionally equipped with an image stabilization system, consisting of a correlation tracker camera and a tip-tilt mirror. Each optical path has its polarization modulation package, containing nematic liquid crystal variable retarders and a linear polarizer, to transform the polarization signals into intensity levels.[18] Both paths scan the photospheric line through a common narrow-band tunable filter system.[2,19] Finally, they lead to the common focal plane assembly (FPA), where the images are recorded on 2048 × 2048 pixels by a custom-built active pixel sensor (also referred to as CMOS sensor). Both apertures penetrate the heat shield of the spacecraft and are protected by a heat rejection entrance window, which filters out all spectral components of the solar light outside of a 30-nm passband around the observed absorption line.

A science data set recorded by SO/PHI can be described by the following equation:

$$I_m^{obs.}(\lambda,x,y)=\left[\left[c\sum_{p=1}^{4}M_{mp}(\lambda,x,y)S_p(\lambda,x,y)\right]*A_m(\lambda,x,y)\right]I_m^{\text{flat}}(\lambda,x,y)+I^{\text{dark}}(x,y), \quad (1)$$

where "*" stands for convolution. The indices m and p run over the four polarimetric modulation states, λ denotes the wavelength, and x and y are the spatial image coordinates in pixels. $\boldsymbol{I}^{obs.}$ is the recorded data set, a four element vector of images at six different wavelengths, while $\boldsymbol{S}$ is a four element vector (Stokes vector) which describes the polarimetric state of the incoming sunlight[20] and which can be expressed as

$$\boldsymbol{S}(\lambda,x,y)=\begin{bmatrix}I(\lambda,x,y)\\ Q(\lambda,x,y)\\ U(\lambda,x,y)\\ V(\lambda,x,y)\end{bmatrix}.$$

$\boldsymbol{M}$ is the polarimetric modulation matrix, a 4 × 4 matrix of images, describing how the instrument transforms the polarization degrees of incoming sunlight into practically measurable light levels (intensities) for each pixel of its FOV, $\boldsymbol{A}$ are optical aberrations SO/PHI introduces, $\boldsymbol{I}^{\text{flat}}$ are the flat fields (gain tables) of the telescope, depending both on wavelength and polarization states, c is a constant gain factor that converts the pixels from number of photons accumulated on the detector to digital numbers (DN-s), and I^{dark} is the dark field of the sensor in DN-s, the same for all wavelengths and polarization states. For further details on solar spectropolarimetry see Ref. 3.

2.2 *Data Processing Hardware*

All data processing in SO/PHI is implemented in the DPU,[21–23] see Fig. 1. The DPU integrates a Leon-3FT microprocessor inside a GR712RC as central processing unit (CPU) which is a radiation-hardened processor by Gaisler, a Microsemi RTAX field-programmable gate array (FPGA) and two static random-access memory-based Xilinx Virtex-4 FPGAs, communicating through a

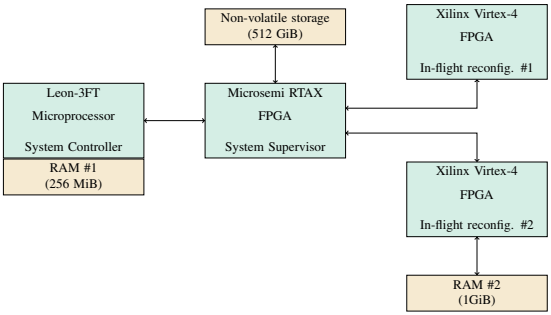

Fig. 1 The data processing of SO/PHI is performed on the DPU hardware. It runs distributed between a Leon-3FT microprocessor and two Xilinx Virtex-4 FPGAs. These processing units are aided by memories of different capacities. For long term data storage, a large capacity non-volatile memory is available.

SoCWire[24,25] network. The microprocessor is designated as the system controller, running the Real-Time Executive for Multiprocessor Systems[26] operating system, in version 4.10, implementing communications with the spacecraft, controlling image processing and memory transfers. The Microsemi FPGA is radiation hardened, and it implements the essential functions for the instrument (e.g., communication interfaces). It also acts as the system supervisor for the configuration of the reconfigurable Xilinx Virtex-4 FPGAs (RFPGAs) that are reconfigured dynamically during processing. The RFPGAs are used for data processing, compression, data accumulation and image stabilization in a time-sharing approach, saving volume, mass, and energy.

The memory budget of the DPU consists of memories aiding processing and non-volatile memory facilitating storage. A 256-MiB memory is attached to the system controller, of which 128 MiB are available to use for image processing. A 1-GiB fast synchronous dynamic random-access memory (SDRAM) supports the RFPGA designated for data pre-processing. A 512-GiB non-volatile NAND-Flash image data storage is available for storing the raw images awaiting processing, and the final products waiting for the last steps performed by the instrument: compression, packaging of telemetry packets, and transmission to the spacecraft platform.

2.3 *Instrument Operations*

SO implements an off-line commanding strategy. This strategy places the outline of commands and the establishment of final command parameters ahead of operations. They are defined in an iterative process, in a time frame of seven months to one week prior to their execution. Nominally, SO/PHI acquires data during three observation windows along one orbit, each of these windows lasting for 10 days. These windows are placed at special points of interests: closest approach and maximum and minimum solar latitude. There is a calibration campaign associated with each observation window, and a dedicated data processing campaign, taking place after the observations, and may last for the rest of the orbit. The operational constraints of the spacecraft require SO/PHI to anticipate its power, produced telemetry, electromagnetic compatibility, and time budget for all its operations. Consequently, all operations are planned and commanded from ground without autonomous decisions regarding the processing steps.

3 Requirements of the Data Processing System

The data processing system of SO/PHI is required to perform three different functionalities: process the raw science observables, calculate the calibration data from dedicated observations, and determine the optimal operational parameters for observations.

A typical science data processing pipeline for a spectropolarimeter is composed of pre-processing, the inversion of the RTE, and compression (see Fig. 2). The main aim of the pre-processing is to remove instrumental effects that appear in the recorded images [see Eq. (1)]. To achieve this in the simplest case, the following equations are applied:

$$I_m^{corr.}(\lambda, x, y) = [I_m^{obs.}(\lambda, x, y) - I^{\mathrm{dark}}(x, y)]/I^{\mathrm{flat}}(x, y), \tag{2}$$

$$S_p(\lambda, x, y) = \sum_{m=1}^{4} D_{pm}(x, y) I_m^{corr.}(\lambda, x, y), \tag{3}$$

where $\boldsymbol{D}$ is the demodulation matrix, expressed as

$$\boldsymbol{D}(\lambda, x, y) = \boldsymbol{M}(\lambda, x, y)^{-1}. \tag{4}$$

During pre-processing, we consider the term $\boldsymbol{A}$ (optical aberrations) negligible, and the dependence of $\boldsymbol{D}$ on λ, and the dependence of $\boldsymbol{I}^{\mathrm{flat}}$ on λ and p [see Eq. (1)]. The pipeline, however, must be able to correct the images without the simplifications as well, if found necessary in the future. This implies adding a number of optional steps. In addition, we know, based on experience that $\boldsymbol{D}$ usually deviates slightly from the real polarimetric behavior of the instrument. Therefore, further corrections are applied to remove the so-called cross-talks[3] (linear dependencies between the Stokes images). Furthermore, we may bin or crop the data sets to discard unused FOV (e.g., a full disk image not filling the entire detector) and to balance the downlink capabilities with the requirements of different science cases.

The implemented RTE inversion method is based on the Milne–Eddington approximation.[27] It is an iterative process, operating on all the 24 images at once, pixel by pixel. We shorten its run-time by estimating the starting conditions for the inversion through numerical calculations,

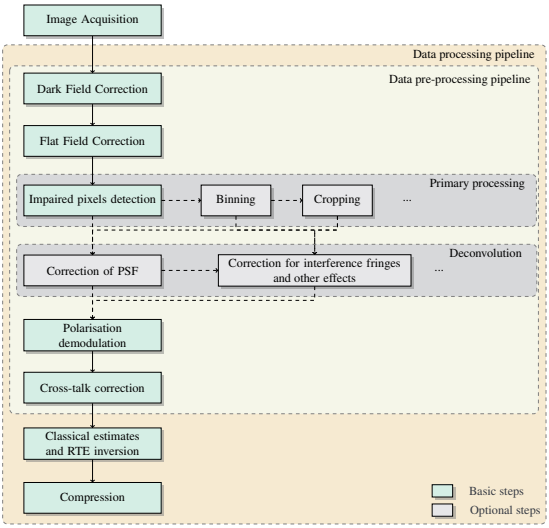

Fig. 2 The on-board science data processing on SO/PHI follows the typical ground processing used for spectropolarimeters. It consists of mandatory (basic, shaded green in the figure) and optional steps (shaded light gray). Some of the optional steps will be used in specific science cases, for others we decide during instrument commissioning whether they are necessary.

called classical estimates.[20,28,29] The final step is the compression of the resulting images with the Consultative Committee for Space Data Systems (CCSDS), CCSDS 122.0-B-1 algorithm, which only takes place before download.[30] This compression is only applied on the images, compression of metadata is possible with Zlib's[31] deflate algorithm on the already prepared telemetry packets. The saving of intermediate data products must be possible at certain steps of the processing. This is foreseen to be used extensively in the instrument commissioning phase to aid error search, and it adds opportunities for the extension and modification of processing for certain science cases (e.g., time averaging of pre-processed data sets, before the inversion of the RTE).

On-board instrument characterization involves dedicated observations, from which we derive the instrument characteristics. Some of these characteristics (e.g., the dark field) are computed regularly and determined on-board, while others are expected to be calculated more sporadically on ground and uploaded to the instrument (e.g., the optical point spread function). The on-board characterization process does not allow the interaction of scientists with the collected data, therefore it has to be autonomous.

The calculation of operational parameters requires immediate processing of the data after the observations in near real time. This is to calculate the starting point for a second iteration refining the results. They all require calculation of image qualifying parameters (e.g., contrast) for a series of images, and the methods have widely varying complexity.

The users of the system can be assigned to two categories: the scientists that describe the functionalities to be performed (e.g., defining what must be done to the science data before inversion) and the scientists operating the instrument (e.g., defining which pipeline to be executed on which data set and its parameters). A well-structured, simple definition of the processing functions is required to avoid user mistakes and to optimize on-board software updates. The main goals are describing the functions in an easily modifiable way, reducing code duplication, and creating standard error checks.

The computational demand of the performed functionalities is high due to the many image processing functions they contain. We shorten run-time by running the image processing functions in the RFPGAs. However, a back-up solution for the pre-processing portion of the pipeline, implemented in software is also required, excluding the RTE inversion and the CCSDS 122.0-B-1 compression (obtaining the physical parameters in the back-up solution would be possible with the classical estimates). The back-up solution with its significantly reduced implementation time aids the software development and testing and increases to the fault tolerance of the instrument by being able to take over these functionalities if necessary.

The number representation of the data has been chosen to be a fixed-point format during the processing, wherever possible. While the fixed-point format saves RFPGA resources, it comes with a significant overhead: all data must be scaled during the processing operations to avoid precision loss in decimals.

A metadata log associated with each data set must be created, recording the steps performed on the data set in full integrity. This is necessary both for scientific purposes and to offer a possibility for error search and improvement of the algorithms.

4 Implementation of the Data Processing System

To present the implemented system, we show its high-level structure and how a pipeline is constructed in the defined frame (Secs. 4.1 and 4.2). Later we describe the data scaling necessary to achieve the required scientific accuracy with the fixed-point representation in Sec. 4.3. Next, we show the implemented error handling (Sec. 4.4) and finally we describe the metadata logging system (Sec. 4.5).

4.1 *Software Architecture*

The data processing software is organized on three layers, see Fig. 3. The lowermost layer (primitives) implements the image processing functions, e.g., addition of images or Fourier transform of an image. These are implemented both as RFPGA functionalities[32] and as software functions running on the system controller microprocessor. Due to the large number of functions one

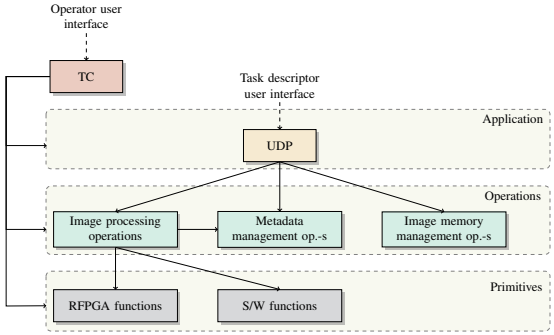

Fig. 3 The data processing software is organized on three layers. This organization facilitates information hiding, and the removal of responsibilities from the application developer (task descriptor).

RFPGA configuration is not sufficient, therefore the RFPGA is reconfigured on demand, during the processing. The necessity for reconfiguration is determined by the on-board software when there is a call to a function that is not available in the currently loaded configuration.

The second abstraction layer (operations) hides hardware details from the application and implements other lower-level functionalities. It integrates the primitives into image processing operations, hiding the hardware details. The image processing operations record metadata directly from this layer to improve metadata collection completeness by removing the full responsibility from the application developer. This layer also provides the functions for data transfer between different memories, and the functions for recording and storing metadata.

The application layer is where the processing functionalities are described, through user defined programs (UDPs). The UDPs are a special category of applications that are not compiled into the on-board software but handled by a UDP manager. Therefore, uploading a new UDP does not require a full on-board software exchange (on-board software is possible through UDP exchanges, full on-board software exchange, or FPGA configuration exchanges). The application layer further logs metadata, containing information that is only known on higher layers (e.g., the division of images performed is part of the flat fielding of the data set with a given ID).

We use three different languages in the architecture. On the primitives layer, the RFPGA firmware is described in Very High-Speed Integrated Circuit Hardware Description Language. The corresponding software functions in the same layer, and the operations layer is written in C. The application layer is written in On-board Command Language (OCL),[33] a high-level programming language based on C implemented for space instrumentation.

4.2 *Pipeline Construction*

To unify the approach to data processing, all of its three functionalities (science observables processing, calibration data calculation, and determination of operational parameters) are implemented in form of pipelines. We extend the definition of a pipeline to a series of changes done to a target (a data set, a number of data sets, or a subset of a data set), resulting either in parameters, or a new data set and their associated metadata. Observed data sets are available in the non-volatile data storage. The data sets are identified by a data set ID and each has a metadata file associated with them. They may contain multiple images, e.g., different wavelengths and polarization states in the case of a science observation, or different focal positions in case of a focusing observation. The pipelines are implemented in the application layer, and therefore are written in the form of UDPs. A block approach is adapted in its definition to achieve the required flexibility.

A pipeline block is defined as a unit that executes a number of functions on its input data, forming a logical unit and writes dedicated metadata. The abstraction level of a block is decided

from case to case. In respect to Fig. 2, some blocks are defined as much smaller functionalities that are performed more often, e.g., store data to non-volatile memory and can be added anywhere in the pipeline. In other cases, some of the separate blocks are combined, e.g., all Fourier space operations are performed in one block to avoid multiple Fourier transforms of the data set. To support their combination in multiple ways, a unified block interface is defined. Within a pipeline, blocks have a common target: a data set or part of a data set that is loaded into the processing memory. A block may load additional data for the processing step as needed (e.g., demodulation matrix), which is not written back to the non-volatile memory or passed to further blocks. Therefore all changes done to it are lost after the block. Due to the possibility of different combination of the blocks, the history of the data set inside each block must be determined, for which the interface is through the metadata file (e.g., if we cropped our data set in the first step, we also need to crop our dark field to the same area of the detector).

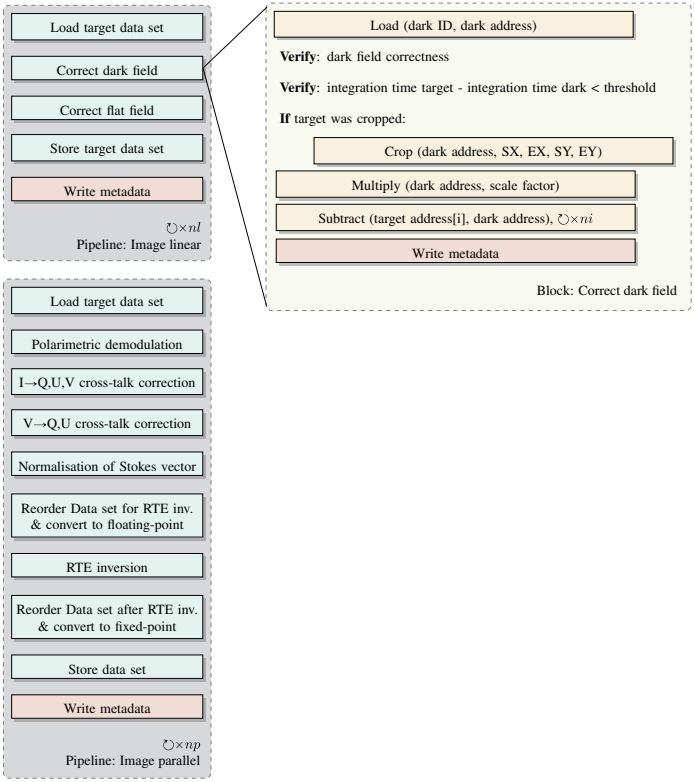

Fig. 4 Example science data processing pipeline. The pipeline is split into two parts to enable its execution with memory budget restriction. The image linear part processes a number of images at a time, the image parallel part processes a number of rows of all 24 images at the same time. The parameters *nl* and *np* are the number of times the image linear and image parallel portion of the pipeline has to run to process the whole data set, respectively. In the implementation detail of the dark field, *ni* denotes the number of images processed.

All pipelines are built by combining pipeline blocks into a processing sequence. They execute the blocks sequentially, i.e. continuing to a new block is possible only once the previous block is finished. Each pipeline also writes metadata specific to it and finally stores the metadata file into the non-volatile memory. The way pipelines are built is also specific to their memory needs and available memory on the two different platforms we run them on (RFPGA or only system controller). In some cases, this means running the sequence of blocks several times, with different subsets of the data set, and in some other cases to split a pipeline into parts, executed one after another.

To show how a pipeline is formed in the system described, we take an example for a science data processing pipeline (see Fig. 4). To cope with processing memory limitations, the pipeline is split into two parts: an image linear part, which processes a number of images of the data set at once, and into an image parallel part, which processes a number of rows of all images of the data set. This is necessary because we have operations that require the full image (e.g., a Fourier transform), and operations that require pixels from several images at once (e.g., polarimetric demodulation, RTE inversion). The two pipelines are executed nl and np times, respectively, both being equal to 1 in the nominal case, when we use the RFPGAs. We also show the implementation details of the dark field correction block, as an example.

4.3 *Data Scaling*

As a method for saving resources, a 24.8 fixed-point notation has been adapted for number representation during data processing, wherever possible (i.e., using a fixed number of 24 bits for the integer part, and 8 bits for the decimal part). Due to this, in all operations performed on the data, the accuracy must be optimized, considering the number of bits on which both the input and the result are represented. This varies from case to case; therefore, a uniform interface is defined for all pipeline blocks (target is scaled up to the most possible bits). All scaling necessary for maintaining accuracy in the process is performed inside the blocks, returning to the same scaling in the end. The obtained accuracy with this scheme is investigated in Ref. 34.

The single frames are obtained from the FPA in 12-bits digital depth, filling the detector well to a predefined level. The correct filling of the detector well is ensured by the exposure time calibration. A number of frames are accumulated into an image (the number of accumulations is determined by the required signal-to-noise ratio), then the image is shifted to the left by 8 bits, which are the decimal part of the numbers, all 0 at this time. Therefore, a raw data set is represented effectively on 12.8-bits digital depth, multiplied by the number of accumulations. This value is written into the metadata, and based on this, at the beginning of the pipeline we calculate the shift necessary to have all its images effectively represented on 23.8 bits (reserving a bit for sign). This scaling is already applied during the loading of the data set into the processing memory, ensuring the correct block interface.

There are three instances during the data processing, where the 24.8 fixed-point notation is abandoned: Fourier domain operations, the RTE inversion, and the compression. The Fourier domain operations are performed in floating-point, as the required accuracy could not be achieved by fixed-point implementation. The same is true for the RTE inversion. Both modules use IEEE 754 single-precision floating-point format. The reason for using 32 bits during the processing is to maximize the computational accuracy in the performed operations (e.g., divisions), however a 16-bit representation of the final results fulfils our requirements. Therefore, the images of the final result are represented on 16 bits, which is also the input to the compression module.

In the case of calibration data, the optimal scaling is ensured by the pipeline creating it. It is always represented on the fewest bits possible, while maintaining its required accuracy. The scaling is written into the metadata and read from there in the processing blocks that apply them to the science data set.

4.4 *Error Handling*

Error handling is done on all software layers. The guiding principle is to find errors on the lowest possible levels, to isolate them, and to aid error search in case of failures. Table 1 summarizes the detected error types.

Table 1 Error detection and handling on the different software organization layers. Each organization layer (see Fig. 3) implements error detection, with the objective of finding the errors as low in the hierarchy as possible. Based on the severity of the error, they are classified into Errors and Warnings, and different actions are taken at their detection.

Software layer	Scope	Handling	Action
Primitives	Detection of overflow and marking them as NaN-s	Warning	Continue
	Correct handling of NaN-s in operations	None	Continue
Operations	Correct memory addressing	Error	Abort
Application	Correct input parameters	Error	Abort
	Data matching (e.g., focus)	Warning	Continue
	Calibration data quality	Warning	Continue
	Operation errors (e.g., calibration method disturbed by solar scene)	Warning	Continue

On the layer of the Primitives, it is ensured that the image processing functions do not return overflows as valid numbers. This is done by replacing these pixels with a value defined as not a number (NaN), assigned to the lowest negative number on 32 bits (0×80000000, in two-s complement). On the same layer, it is also made sure that these values are not treated as numbers (e.g., division of a NaN with any number results in NaN). NaN-s may be replaced later through the interpolation of surrounding pixels; therefore, we keep track of all generated NaN-s in a bit mask image, along with other information regarding the data set (e.g., magnetic signal strength, pixels outside solar disk). This mask in the end is encoded into the final results of the pipeline through pixel values that could otherwise not appear (e.g., negative or NaN values) to obtain the information on ground without adding to the data volume.

In the operation layer, it is made sure that the inputs to the primitive functions are valid. For example, we check that we do not address any invalid memory positions by calculating the end address of a data set based on the start address and the size of the data.

The application layer is responsible for ensuring that the data sent to the lower layers is meaningful, e.g., that the target image has the same integration time as the dark field or that the flat field had no errors during its generation. It is also on the application layer that the parameters received in the pipeline are verified, e.g., that the target data set of the science data processing pipeline is raw data and contains the expected number of images. Additionally, also on this level, errors related to the solar scene are detected (e.g., when a flat field with the required precision cannot be obtained due to a sunspot in the FOV during the calibration window).

Each function has a return parameter, indicating warnings and errors detected by it. Warnings are small failures that do not affect the execution of the pipeline and are only recorded in the metadata of the data set for evaluation on ground. Errors are problems that make it impossible or meaningless for the pipeline to continue (e.g., no data set with the specified ID was found). In case of error, the execution is interrupted, the metadata is saved, and the instrument continues with the execution of the next command that was received from ground.

4.5 *Metadata Management*

The metadata of a data set comes from different sources.

- The planning process at which time we assign identifiers to the data sets acquired during the calibration campaign.
- The calibration campaign at which time we calculate values that are part of the calibration data.

- The instrument, recording all the current settings at the time of the data set acquisition.
- The data processing, recording all steps performed, their parameters, and return values.

The information from the planning process and calibration campaign is collected in a so-called Processing Environment, describing all information necessary for processing a science data set. This is written into the metadata of the data set at the time of its acquisition, also complemented by the instrument parameters. It is this metadata that is read and appended during the processing of the data set. Furthermore, we may override the Processing Environment written into the data set with the current one set on-board, if the processing plan changes later on.

The metadata generated during processing is created on multiple organization levels to ensure completeness. It is always recorded into metadata entries, each entry being part of one of the following categories.

- Operation entry, recorded by the operation layer functions.
- UDP entry, recorded on application layer, either by a pipeline block or a pipeline.
- Data summary entry, containing target parameters that are dynamic during the execution of the pipeline, recorded at the end of each UDP.

Each metadata entry starts with an ID, marking its category. In the case of the first two categories, the data that follows indicate the operation or UDP executed, its target, the input parameters, and return value. The data summary entry records the start and end indices of processed images within the target data set, and information about which part of the sensor the data belongs to, how it was binned and scaled, and data type and format. At the recording of each metadata entry a time-stamp is added automatically.

More information and an example on the usage of the metadata are detailed in Ref. 35.

5 Execution of a Science Data Processing Pipeline

To illustrate the operation of the data processing system, we run the pipeline presented in Fig. 4. The tests are performed on the flight spare model of SO/PHI. The target data set and all necessary calibration data are loaded into the non-volatile memory, as if they had been acquired previously by the instrument.

The interaction with the on-board software is through the Ground Support Equipment Operating System (GSEOS) software package.[36] GSEOS is used for all interactions with the instrument, modeling telecommands, and monitoring and displaying the values of the housekeeping telemetry packets.

5.1 *Input Data*

Data from the Helioseismic and Magnetic Imager on-board the Solar Dynamics Observatory (SDO/HMI)[12] is used to generate the input data set to the pipeline. SDO/HMI investigates the same absorption line, and the data are further processed with the SO/PHI Software siMulator (SOPHISM),[37] to produce a Stokes vector as similar as possible to one that SO/PHI would obtain, in 2048×2048 pixel resolution, see Fig. 5. There is one important difference, however, that the wavelength sampling of HMI is different, which is not taken into consideration during the pipeline execution. Therefore, the results are expected to contain some errors due to this approximation. Furthermore, the data set used is of a lower level, and neither the filter profiles nor the spacecraft velocity is removed, therefore, we expect an error in the v_{LOS}. These images are further manipulated to represent the raw observables, approximating Eq. (1), according to the following equation:

$$I_m^{\mathrm{input}}(\lambda, x, y) = \left[c \cdot c' \sum_{p=1}^{4} M_{mp}(x, y) S_p(\lambda, x, y) \right] I^{\mathrm{flat}}(x, y) + I^{\mathrm{dark}}(x, y), \tag{5}$$

where $\boldsymbol{S}$ is created with SOPHISM, and c' is the constant that scales the normalized images to represent the number of incident photons in 20-ms exposure time.

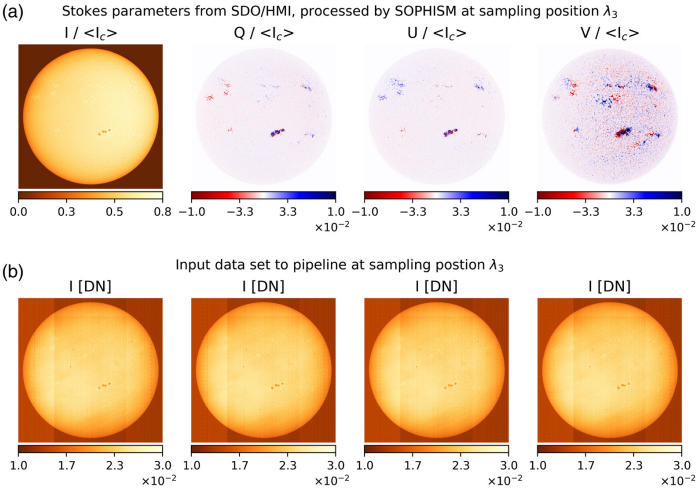

Fig. 5 Test data set at the third wavelength sample. (a) The input to the pipeline are the Stokes images from SO/PHI Software siMulator (SOPHISM).[37] (b) The input images are obtained applying Eq. (5) and show similar light levels in all polarization states as a result of the modulation. The data also show the effect of the dark field (stripes) and the flat field (smudges and dust grains).

The calibration data applied is recorded in the laboratory, using the flight model of SO/PHI, and is shown in Fig. 6. The dark field, acquired in a dark chamber, shows the characteristic sensor pattern: the four distinct horizontal stripes, created using four different channels for image read-out. The flat field has been recorded with the use of a lamp to ensure the most uniform illumination possible. It shows a gradient pattern and a number of dust grains inside the instrument. It has been normalized to its mean intensity, then scaled to be represented on 10 bits total, translating to 2 bits integer and 8 bits decimal part in the fixed-point notation. The demodulation matrix has been determined during the ground calibration campaign with the use of a polarization calibration unit (described in Ref. 38). Its field dependence varies with a standard deviation between $5 \cdot 10^{-9}$ (for $\mathbf{D}_{1,3}$) and 1.12 (for $\mathbf{D}_{4,1}$).

5.2 *Output Data*

We execute the full pipeline on the data set in the nominal configuration, processing all images at the same time. As we do not induce any cross-talk effects into the test data, we set the corresponding parameters to 0, and in consequence, the two cross-talk correction blocks from Fig. 4 do not execute. In this test, we configure the RTE inversion to determine all possible output images it can provide. In regular operations, we set the output of the inversion to be only the four images of interest ($\boldsymbol{B} = (|\boldsymbol{B}|, \gamma, \phi)$, and v_{LOS}), however, the inversion module is able to return nine parameters in total. For comparison, we also execute the image linear part of the pipeline in back-up configuration, processing four images at a time. This run creates six different output data sets, each containing a subset of the full result.

The result of the pre-processing [see Fig. 7, calculated according to Eqs. (2) and (3)] is $\boldsymbol{S}$, which will be the input to the RTE inversion. After the dark- and flat-field correction, the solar scene is undisturbed by instrumental artefacts. In areas of low illumination levels (e.g., dust grains on the sensor, or areas masked by a field stop), NaN-s are produced during the flat-field

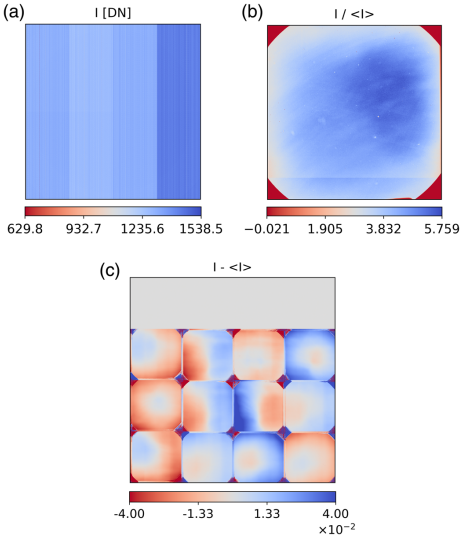

Fig. 6 The calibration data used in the test run were recorded in the laboratory. (a) The dark field shows the characteristic sensor pattern: four distinct vertical stripes due to the four different readout channels. (b) The flat field used in the tests shows a gradient across the FOV, and a few dust-grains. (c) The 4×4 demodulation matrix, $\boldsymbol{D}$, depends on the FOV. To show this dependence in the plot, we subtract from each of the elements their spatial mean.

correction through division by zero. In an ideal flat field, all pixels located behind the field stop would be 0, resulting in an area of uniform NaN-s in the corners after the division. However, due to the imperfection of the dark-field correction, some pixels reach sufficiently large values to not produce a NaN. The Stokes vector, obtained after the polarimetric demodulation, differs slightly from $\boldsymbol{S}$ in Eq. (5) due to the limited numerical accuracy. These images already show the presence of the magnetic field, which will be quantified by the inversion of the RTE.

The final results of the pipeline are the continuum intensity and the results of the RTE inversion: the magnetic field vector $\boldsymbol{B} = (|\boldsymbol{B}|, \gamma, \phi)$, described through its magnitude, azimuth and inclination, and v_{LOS} (see Fig. 8). All values outside of the solar disk are meaningless for the RTE inversion, therefore, it cannot converge, resulting in noise as output. The $|\boldsymbol{B}|$ is stronger in the umbra of the active region and weaker in the penumbra as expected. In γ, we can see the opposing polarities that compose the active region, while ϕ shows the fan-like pattern, originating in the center of the round magnetic features, consistent with the orientation of the magnetic field in such features. The v_{LOS} over the full disk shows the spectral shift due to the rotation of the Sun and the spacecraft velocity, on top of the intrinsic shifts due to plasma motion. The slight bias to one side is due to the lack of filter profile corrections in the used SDO/HMI data set. The v_{LOS} in the active region shows strong flows of opposing directions in the penumbra, known as Evershed flows,[39] driven by the magnetic activity. We analyze the accuracy of the pipeline in Ref. 34.

On ground, the image data and associated metadata are converted into files according to the Flexible Image Transport System.[40] While the metadata on-board is written into a continuous unit, the converter separates the header entries into separate American Standard Code for Information Interchange tables based on their origin. The metadata associated with the processing, recorded from UDP level, reflects the steps taken by the pipeline, its parametrization, and shows the success of the blocks (see Tables 2 and 3). Based on this table, we also have an

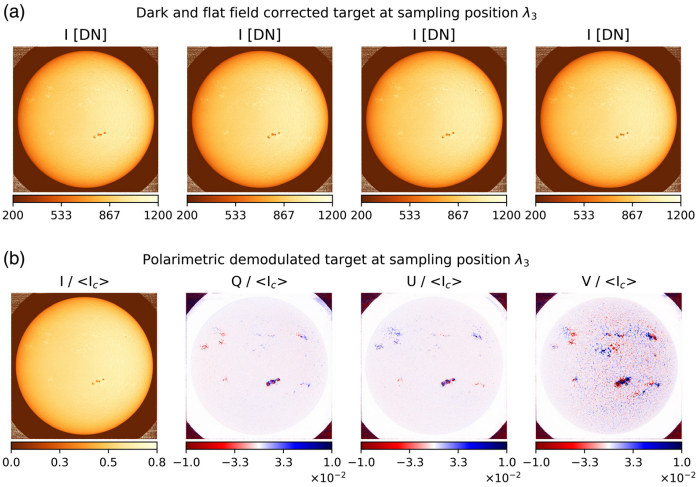

Fig. 7 Step-wise results of the pre-processing on the input data set from Fig. 5. (a) The third wavelength sample in the four different polarization states (4 out of 24 images) after dark- and flat-field correction of $\boldsymbol{I}_{\lambda}^{\text{recorded}}(x, y)$, see Eq. (2). The white pixels in the image corners are NaN-s produced during the processing through division by sufficiently small numbers to produce an overflow. (b) Result of the pre-processing, the third wavelength sample of the normalized Stokes vector (4 out of 24 images), see Eq. (3).

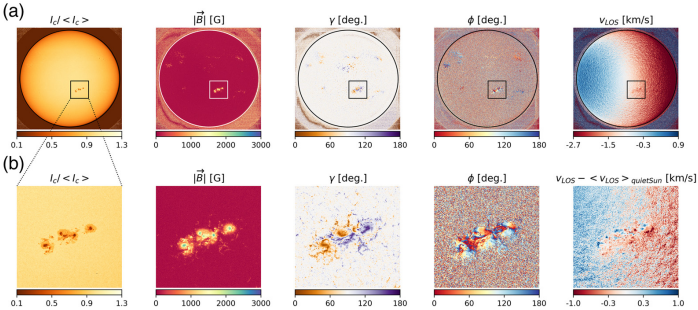

Fig. 8 (a) The five resulting images from the full pipeline, continuum intensity (I_c), the components of the magnetic field vector $\boldsymbol{B} = (|\boldsymbol{B}|, \gamma, \phi)$, and the LOS velocity, v_{LOS}. v_{LOS} is plotted on a scale centered around the spacecraft velocity, −0.9 km/s ($\langle v_{\text{LOS}} \rangle$ at disk center). The circular contour marks the solar limb, and the square shows the region magnified in the next row. (b) Detail of the full FOV, showing the active region. The v_{LOS} was corrected for the mean quiet Sun intensity in this region.

overview of any warnings or failures during the execution. The metadata recorded during the dark fielding block from operation level reflects the implementation shown in Fig. 4, giving an insight into the lower-level information that we can access (see Table 4). See Ref. 35 for more detail on the usage of metadata.

Table 2 Excerpt of metadata recorded from UDP level, during nominal execution of the pipeline, showing all steps taken, and their parameters. In cases where we have more parameters than what can be recorded in one entry, several entries are added by the same UDP. The timestamp shows the on-board time during the execution. The return value shows success in most cases (0), with some steps creating NaN pixels in the result (10). The start and end indices show that the full data set is processed at once, and how the number of images changes during the processing through extension with the mask, the inversion, and the encoding of the mask into the I_c image.

	Timestamp											
Explan.[a]	December 20, 2019	Re.[b]	UDP[c]	Data ID	ln 1[d]	ln 2	S #[e]	E #[f]	S row[g]	E row	S col.[h]	E col.
Load[i]	13:45:21	0	1351	90030	512	0	0	23	0	2047	0	2047
Dark c.[j]	13:45:28	0	1363	90070	8388608	0	0	24	0	2047	0	2047
Flat c.[k]	13:46:07	10	1365	90080	4	0	0	24	0	2047	0	2047
Lin. p.[l]	13:46:38	0	7002	90030	90070	90080	0	24	0	2047	0	2047
Lin. p.	13:46:38	0	7002	90030	0	24	0	24	0	2047	0	2047
Lin. p.	13:46:38	0	7002	90030	24	65535	0	24	0	2047	0	2047
Load	13:52:44	0	1351	92030	1	0	0	24	0	2047	0	2047
Demod.[m]	13:55:06	10	1366	90060	512	0	0	24	0	2047	0	2047
Norm.[n]	13:55:42	10	1371	0	49868192	2048	0	24	0	2047	0	2047
NaN en.[o]	13:55:55	0	1356	0	0	0	0	24	0	2047	0	2047
Reord.[p]	13:56:18	0	1372	0	0	0	0	24	0	2047	0	2047
Inv.[q]	15:05:06	0	1374	0	511	1	0	10	0	2047	0	2047
Reord.	15:05:28	0	1375	0	0	0	0	9	0	2047	0	2047
Par. p.[r]	15:05:36	0	7003	92030	90060	25	0	9	0	2047	0	2047
Par. p.	15:05:36	0	7003	92030	2048	5	0	9	0	2047	0	2047
Par. p.	15:05:36	0	7003	92030	−3803904	1779456	0	9	0	2047	0	2047
Par. p.	15:05:36	0	7003	92030	73216	4096	0	9	0	2047	0	2047
Par. p.	15:05:36	0	7003	92030	−256	−445	0	9	0	2047	0	2047
Par. p.	15:05:36	0	7003	92030	128	49868192	0	9	0	2047	0	2047
Par. p.	15:05:36	0	7003	92030	2048	511	0	9	0	2047	0	2047
Par. p.	15:05:36	0	7003	92030	1	115	0	9	0	2047	0	2047

Note: UDP identifiers: 1351, Load data set; 1363, Subtract dark field; 1365, Divide by flat field; 1366, Polarimetric demodulation; 1371, Stokes vector normalization; 1356, NaN encoding; 1372, Reorder images for RTE inversion; 1374, RTE inversion; 1375, Reorder images after RTE inversion; 7002, Image linear pipeline; 7003, Image parallel pipeline. *Data set ID-s*: ID 90030, the science data; $I_\lambda^{\text{input}}(x, y)$; ID 90070, $I^{\text{Dark}}(x, y)$; ID 90080, $I^{\text{Flat}}(x, y)$; ID 90060, demodulation matrix; $\boldsymbol{D}(x, y)$.

[a]Additional explanation (not part of metadata).
[b]Return value.
[c]UDP identifiers.
[d]First input parameter (var. content).
[e]Start index.
[f]End index.
[g]Start row.
[h]Start column.
[i]Load data set.
[j]Dark field correction.
[k]Flat field correction.
[l]Linear pipeline.
[m]Polarimetric demodulation.
[n]Stokes vector normalization.
[o]NaN encoding.
[p]Image reordering (before and after RTE inversion).
[q]RTE inversion.
[r]Parallel pipeline.

Table 3 Excerpt of metadata recorded from UDP level, during the execution of the linear part of the pipeline in back-up configuration. In this configuration we process four images at a time and obtain six output data sets. Here we show the metadata of the first one of the six. The entries indicate that the first four images have been loaded (indices 0 to 3) with full FOV (0 to 2047), extended during the processing with the mask image, index 4.

	Timestamp											
Explan.[a]	December 21, 2019	Re.[b]	UDP[c]	Data ID	In 1[d]	In 2	S #[e]	E #[f]	S row[g]	E row	S col.[h]	E col.
Load[i]	11:15:52.0000	0	1351	90010	512	0	0	3	0	2047	0	2047
Dark c.[j]	11:18:10.0000	0	1363	90070	8388608	0	0	4	0	2047	0	2047
Flat c.[k]	11:21:39.0000	0	1365	90080	4	0	0	4	0	2047	0	2047
Lin. p.[l]	11:23:14.0000	0	7002	90010	90070	90080	0	4	0	2047	0	2047
Lin. p.	11:23:14.0000	0	7002	90010	0	24	0	4	0	2047	0	2047
Lin. p.	11:23:14.0000	0	7002	90010	4	65535	0	4	0	2047	0	2047

Note: UDP identifiers: 1351, Load data set; 1363, Subtract dark field; 1365, Divide by flat field; 7002, Image linear pipeline; Data set ID-s: ID 90030, the science data; $I_{\lambda}^{\text{input}}(x,y)$, ID 90070, $I^{\text{Dark}}(x,y)$, and ID 90080, $I^{\text{Flat}}(x,y)$.
[a]Additional explanation (not part of metadata).
[b]Return value.
[c]UDP identifiers.
[d]First input parameter (var. content).
[e]Start index.
[f]End index.
[g]Start row.
[h]Start column.
[i]Load data set.
[j]Dark field correction.
[k]Flat field correction.
[l]Linear pipeline.

5.3 *System Metrics*

The CPU load during the processing reflects the pipeline implementation and the underlying on-board software (see Figs. 9 and 10). These profiles are dominated by the memory transfers and the image processing operations, together with the necessary RFPGA related actions. Whenever reading the non-volatile memory, the DPU used 100% due to a background task that polls the queue of the non-volatile storage to transmit the next data chunks. As soon as everything is in the queue, the load drops to a lower level, until the transfer is finished. In case of writing to the non-volatile memory, the system controller is in full control of the data transfer, eliminating the need for synchronization. Therefore, it can write at 100% capacity, which is also the reason that it takes shorter time than reading. This is the reason for the nominal configuration to show 100% load at memory transfers between the non-volatile storage and RAM #2. Transferring from non-volatile memory to RAM #1 shows a different load profile due to the different implementation of the data transfer. In this case, the non-volatile memory controller waits for a confirmation from the system controller before transmitting a new chunk, resulting in a slower transfer (the case of the back-up configuration). During RFPGA configurations, the CPU load is high (~95%), creating peaks at each reconfiguration. The system controller runs the image processing pipeline in parallel with a scrubbing task, that uses all idle time to rewrite the RFPGA configurations part by part to defend against radiation effects. This keeps the CPU load high even during times when a low load would be expected otherwise (e.g., during the RTE inversion, performed by the RFPGA, the combination of the scrubbing and the memory transfers keeps the load high). In the case of the back-up configuration, image processing functions run on the DPU, and use its full capacity.

The run-time of the pipeline is significantly shorter in the nominal configuration than in back-up mode. We measure it by extracting the number of processor ticks occurred during the

Table 4 Excerpt of metadata recorded on operation level by the dark field subtraction block, during nominal execution of the pipeline, see Fig. 4. The return values all show success (0). The processing memory addresses show that the dark field is loaded to the address 419430400, scaled to match the target in the same location, then it is subtracted from each image of the target data set (loaded to address 0). There are 24 entries for subtraction in total (four shown here), each recording the increment of addresses from image to image in the target data set. The scalar input values show the dark-field ID and the scale factor.

	Timestamp									
Explan.[a]	December 20, 2019	Operation	Re.[b]	Addr. 1[c]	Addr. 2	Addr. 3	Im. row	Im. col.[d]	Sc. 1[e]	Sc. 2
Load[f]	13:45:24	PROC_LOAD	0	0	0	419430400	0	0	0	90070
Scale[g]	13:45:24	PROC_F_MUL_S	0	419430400	0	419430400	2048	2048	131072	0
Sub. 1[h]	13:45:24	PROC_F_SUB_I	0	0	419430400	0	2048	2048	0	0
Sub. 2	13:45:24	PROC_F_SUB_I	0	16777216	419430400	16777216	2048	2048	0	0
⋮										
Sub. 23	13:45:28	PROC_F_SUB_I	0	369098752	419430400	369098752	2048	2048	0	0
Sub. 24	13:45:28	PROC_F_SUB_I	0	385875968	419430400	385875968	2048	2048	0	0

Note: Operations: PROC_LOAD, loading from volatile memory to processing memory; PROC_F_MUL_S, multiplication by scalar; PROC_F_SUB_I, subtraction of images.
[a]Additional explanation (not part of metadata).
[b]Return value.
[c]Memory address 1.
[d]Image columns
[e]Scalar input 1.
[f]Load dark field.
[g]Scale dark field to match target data set.
[h]Subtract dark field from image 1 of data set.

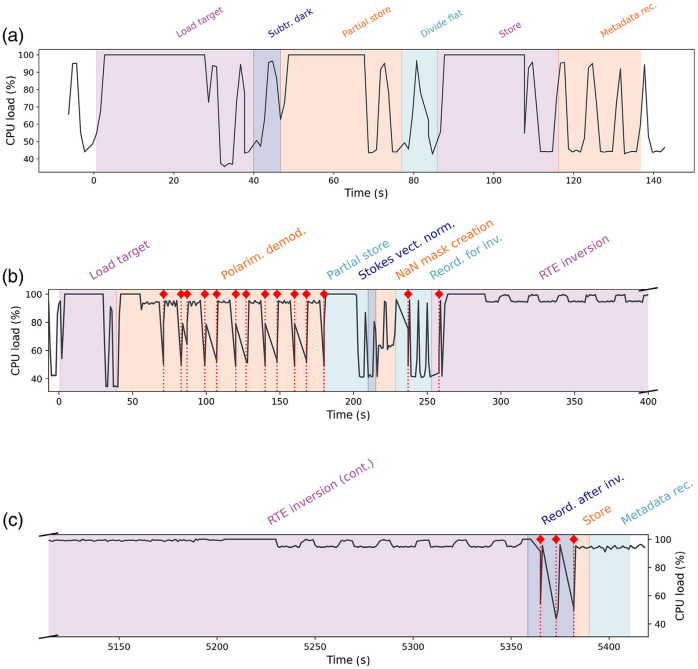

Fig. 9 CPU load during the execution of the (a) image linear and (b, c) image parallel pipelines in nominal configuration. The colours show the execution of different pipeline blocks (see Fig. 4). The red dotted lines with diamonds indicate the times of RFPGA reconfigurations. During the polarimetric demodulation, there are 12 reconfigurations, which will be entirely removed in the future. The full pipeline takes little over 1.5 h to complete.

execution, where one tick corresponds to 2.5 ms. To execute the image linear pipeline in nominal mode takes just over 2 min, while the image parallel pipeline takes a little over 90 min. The majority of the processing time is made up by RTE inversion block, the duration of which varies based on the science mode it operates in. The configuration used during this test writes all nine possible outputs, while if we choose only the four results of interest (as aimed to be configured in nominal mission phase), it runs ∼30 min faster. Moreover, the desired implementation of the inversion is to read the data from the RAM #2 and write the results to the non-volatile memory, from where they will be read back to the RAM #2 to continue their processing. However, the current implementation writes the data in chunks from the RAM #2 to RAM #1, the RTE inversion module reads the input from here and writes the results to the same memory, which are then read back to the RAM #2. This implementation introduces additional data transfer operations of the input data, transfers between different memories which have longer transfer time and prohibits parallel read and write operations which would be possible if the input and output were transferred between different memories. In this setup, the time of the inversion itself (together with reading and writing RAM #1) is 71.41 min, the time of the input data transfer from RAM #2 to RAM #1 is 10.88 min, while the time of the output data transfer from RAM #1 to RAM #2 is 2.7 min.

The RFPGA configurations are optimized to reduce the execution time by minimizing the number of reconfigurations during science data processing (each reconfiguration takes between

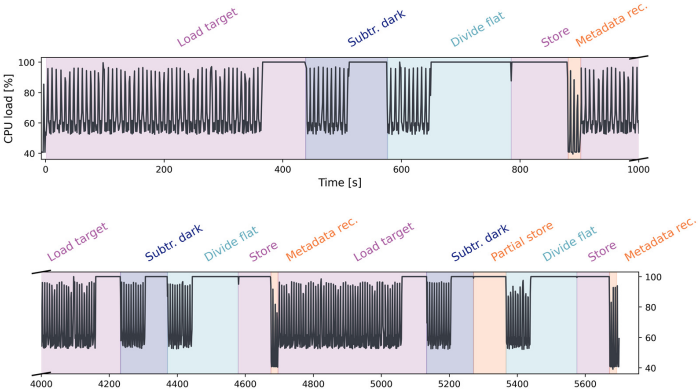

Fig. 10 CPU load during the image linear pipeline execution in back-up configuration. The colours indicate the execution of different pipeline blocks (see Fig. 4). In back-up mode, we only process four images of the full data set at a time, due to the size limitation of RAM #1. Therefore, the pipeline executes a loop, repeating the block sequence "Load target, Subtr. dark, Divide flat, and Store, Metadata rec." six times in total (only three shown). The image linear part runs in a little over 1.5 h in back-up mode, a significant time increase compared to nominal mode.

2 and 4 s). There is none necessary during the linear pipeline, while in the parallel pipeline, there are five reconfigurations outside of the polarimetric demodulation block, which has twelve. This latter block requires such a high number, because the matrix multiplication is in a separate configuration. However, this operation will be re-implemented in the future as a UDP, calling other low-level operations, eliminating all reconfigurations in the polarimetric demodulation block. Time wise, this will save the reconfiguration times (12 times 3 s on average), this final implementation has been measured to execute in 92 s for a full data set.[41]

Running the full pipeline in the nominal mode with all nine possible outputs, on the full FOV, requires a little over 1.5 h. This time is reduced to close to 1 h when we store only the four outputs of interest: the three components of the magnetic field vector and the flow velocities. This is the time required for processing each of the acquired data sets, which may amount to several hundred in each orbit. This time may further be reduced by cropping and binning, depending on science case.

In contrast, the linear pipeline runs in over 90 min in back-up configuration. This increase originates both from the longer execution time of the primitive functions and the longer memory transfer times (between the non-volatile memory and RAM #1). This large increase indicates that the execution of the full pre-processing in back-up configuration would have a significant influence on the science operations.

6 Summary and Conclusions

We have detailed the implementation of the on-board data processing system of SO/PHI: the requirements and the different parts that implement them. To show the synergy of its components, we defined and ran a science data processing pipeline. The partial and final results are as expected from the input data set, reducing the 24 raw images into five images of scientific interest. The recorded metadata show all steps performed on-board, which is used both on-board as integral part of the system, and on ground: for verification, possible error search and during scientific analysis.

We also showed system metrics for a more detailed view of the system, and we assess the time frame in which different parts of the pipeline run. The processing of a full data set takes a

little over 1.5 h, the majority of the time being used for the inversion of the RTE. Several points of improvement have also been pointed out, planned for the next version of the on-board software.

The main challenge that SO/PHI's on-board data reduction system faces is to implement complex scientific data analysis in the lack of human interaction. The most important tools in overcoming this challenge are the metadata- and the error handling systems. Moreover, it was necessary to adapt algorithms that are routinely ran on computer clusters on ground, to a space-qualified computing system. This is achieved by the custom hardware design, the use of distributed processing between a CPU and RFPGA-s, the custom firmware that the RFPGA-s use, and the software architecture. Due to the limitations, we use fixed-point number representation wherever possible, which has proven to require significant effort to maintain the required accuracy during scientific processing.

While the lower layers of the software are hardware specific, the two highest layers can be embedded into different systems. We are currently working on integrating it with our instrument simulator, SOPHISM[37] to enable the running of our pipelines on a desktop. Furthermore, the flexibility of the pipeline definition promises the possibility of using the system for future missions.

This data processing system takes the full science data reduction of a solar spectropolarimeter for the first time on-board the spacecraft. It enables new avenues for future missions with challenging orbits that can provide new points of views, at the cost of reduced telemetry volumes.

Acknowledgments

This work was carried out in the framework of the International Max Planck Research School for Solar System Science at the Max Planck Institute for Solar System Research. Solar Orbiter is a mission led by the European Space Agency with contribution from the National Aeronautics and Space Administration (NASA). The Polarimetric and Helioseismic Imager instrument is supported by the German Aerospace Center (DLR) under grant Nos. 50 OT 1201 and 50 OT 1901. The Spanish contribution has been partly funded by the Spanish Research Agency under projects under grant Nos. ESP2016-77548-C5 and RTI2018-096886-B-C5, partially including European FEDER funds. IAA-CSIC members acknowledge and funds from the Spanish Ministry of Science and Innovation "Centro de Excelencia Severo Ochoa" Program under grant No. SEV-2017-0709. The solar data used in the tests are the courtesy of NASA/SDO HMI science team. Parts of the work shown in this paper have been introduced at the SPIE Astronomical Telescopes + Instrumentation conference.[42]

References

1. D. Müller et al., "The Solar Orbiter mission. Science overview," *Astron. Astrophys.* **642**, A1 (2020).
2. S. K. Solanki et al., "The polarimetric and Helioseismic imager on Solar Orbiter," *Astron. Astrophys.* **642**, A11 (2020).
3. J. C. del Toro Iniesta, *Introduction to Spectropolarimetry*, Cambridge University Press, Cambridge (2003).
4. J. P. C. Carrascosa et al., "The RTE inversion on FPGA aboard the Solar Orbiter PHI instrument," *Proc. SPIE* **9913**, 991342 (2016).
5. J. P. C. Carrascosa et al., "Scientific computing and fault mitigation on FPGA aboard the Solar Orbiter PHI instrument," in *NASA/ESA Conf. Adapt. Hardware and Syst.*, IEEE, pp. 1–8 (2015).
6. J. P. C. Carrascosa et al., "SIMD architecture on FPGA for scientific computing aboard a space instrument," *J. Syst. Archit.* **62**, 1–11 (2016).
7. R. Castano et al., "Oasis: onboard autonomous science investigation system for opportunistic rover science," *J. Field Rob.* **24**(5), 379–397 (2007).
8. M. Neugebauer et al., "Genesis on-board determination of the solar wind flow regime," *Space Sci. Rev.* **105**, 661–679 (2003).

9. G. Rabideau et al., "Mission operations of earth observing-1 with onboard autonomy," in *2nd IEEE Int. Conf. Space Mission Challenges Inf. Technol.*, Vol. 7, p. 373 (2006).
10. D. W. Curtis et al., "On-board data analysis techniques for space plasma particle instruments," *Rev. Sci. Instrum.* **60**, 372–380 (1989).
11. L. Amoruso et al., "Solar wind analyzer-the Solar Orbiter milestone towards on-board intelligent decision making systems," in *Proc. Int. Astronaut. Cong.*, p. A7, The International Astronautical Federation (IAF) (2018).
12. P. H. Scherrer et al., "The Helioseismic and Magnetic Imager (HMI) investigation for the Solar Dynamics Observatory (SDO)," *Sol. Phys.* **275**, 207–227 (2012).
13. S. Couvidat et al., "Observables processing for the Helioseismic and Magnetic Imager instrument on the Solar Dynamics Observatory," *Sol. Phys.* **291**(7), 1887–1938 (2016).
14. P. H. Scherrer et al., "The solar oscillations investigation—Michelson Doppler Imager," *Sol. Phys.* **162**, 129–188 (1995).
15. J. de la Cruz Rodríguez et al., "CRISPRED: a data pipeline for the CRISP imaging spectropolarimeter," *Astron. Astrophys.* **573**, A40 (2015).
16. A. Gandorfer et al., "The Solar Orbiter mission and its polarimetric and helioseismic imager (SO/PHI)," *J. Phys. Conf. Ser.* **271**, 012086 (2011).
17. A. Gandorfer et al., "The high resolution telescope (HRT) of the Polarimetric and Helioseismic Imager (PHI) onboard Solar Orbiter," *Proc. SPIE* **10698**, 106984N (2018).
18. A. Alvarez-Herrero et al., "The polarization modulators based on liquid crystal variable retarders for the PHI and METIS instruments for the Solar Orbiter mission," *Proc. SPIE* **10563**, 105632Z (2017).
19. C. Dominguez-Tagle et al., "Filtergraph calibration for the polarimetric and helioseismic imager," *Trans. Jpn. Soc. Aeronaut. Space Sci.* **12**, Tk_25–Tk_27 (2014).
20. E. L. Degl'Innocenti and M. Landolfi, *Polarization in Spectral Lines*, Vol. 307, Kluwer Academic (2004).
21. F. Bubenhagen et al., "Reconfigurable platforms for data processing on scientific space instruments," in *NASA/ESA Conf. Adapt. Hardware and Syst.*, pp. 63–70 (2013).
22. B. Fiethe et al., "Reconfigurable system-on-chip data processing units for space imaging instruments," in *Proc. Conf. Des., Autom. and Test Europe*, EDA Consortium, pp. 977–982 (2007).
23. B. Fiethe et al., "Adaptive hardware by dynamic reconfiguration for the Solar Orbiter PHI instrument," in *NASA/ESA Conf. Adapt. Hardware and Syst.*, IEEE, pp. 31–37 (2012).
24. B. Osterloh et al., "Socwire: a network-on-chip approach for reconfigurable system-on-chip designs in space applications," in *NASA/ESA Conf. Adapt. Hardware and Syst.*, IEEE, pp. 51–56 (2008).
25. B. Osterloh et al., "Architecture verification of the SoCWire NoC approach for safe dynamic partial reconfiguration in space applications," in *NASA/ESA Conf. Adapt. Hardware and Syst.*, IEEE, pp. 1–8 (2010).
26. "RTEMS real time operating system (RTOS)."
27. D. O. Suárez and J. C. del Toro Iniesta, "The usefulness of analytic response functions," *Astron. Astrophys.* **462**(3), 1137–1145 (2007).
28. M. Semel, "Contribution à létude des champs magnétiques dans les régions actives solaires," *Ann. Astrophys.* **30**, 513–513 (1967).
29. D. E. Rees and M. D. Semel, "Line formation in an unresolved magnetic element: a test of the centre of gravity method," *Astron. Astrophys.* **74**, 1–5 (1979).
30. D. H. Expósito et al., "Image compression on reconfigurable FPGA for the SO/PHI space instrument," *Proc. SPIE* **10707**, 107072F (2018).
31. "ZLIB."
32. T. Lange et al., "On-board processing using reconfigurable hardware on the Solar Orbiter PHI instrument," in *NASA/ESA Conf. Adapt. Hardware and Syst.*, IEEE, pp. 186–191 (2017).
33. T. Wittrock, "Flexible Operational Sequencing of Complex Spaceborne Instruments – TheSoftware System OCL," *54th Int. Astronaut. Congr. Int. Astronaut. Fed., Int. Acad. Astronaut., Int. Inst. Space Law*, Bremen, Germany (2012).

34. K. Albert et al., "Performance analysis of the SO/PHI software framework for on-board data reduction," in *Astron. Data Anal. Software and Syste. XXVIII, ASP Conf. Ser.*, Astronomical Society of the Pacific (2019).
35. K. Albert et al., "Metadata and their importance in SO/PHI's on-board data processing," in *Astron. Data Anal. Software and Syste. XXVIII, ASP Conf. Ser.*, Astronomical Society of the Pacific (Submitted).
36. "IDA GSESOS V software package," http://www.gseos.de/index.htm (accessed 1 September 2018).
37. J. B. Rodríguez et al., "SOPHISM: an end-to-end software instrument simulator," *Astrophys. J. Suppl. Ser.* **237**, 35 (2018).
38. J. Schou et al., *Polarization Calibration of the Helioseismic and Magnetic Imager (HMI) Onboard the Solar Dynamics Observatory (SDO)*, pp. 327–355, Springer US, New York (2012).
39. J. Evershed, "Radial movement in sun-spots," *Mon. Not. R. Astron. Soc.* **69**, 454 (1909).
40. D. C. Wells, E. W. Greisen, and R. H. Harten, "FITS—a flexible image transport system," *Astron. Astrophys. Suppl.* **44**, 363 (1981).
41. T. Lange et al., "Evaluation of a hardware accelerated on-board processing pipeline for Solar Orbiter's PHI instrument," in *ASD-Eurospace Conf. Data Syst. Aerosp.*, DASIA, Oxford (2018).
42. K. Albert et al., "Autonomous on-board data processing and instrument calibration software for the SO/PHI," *Proc. SPIE* **10707**, 107070O (2018).

Kinga Albert is a PhD candidate at the Max Planck Institute for Solar System Research, working is on the on-board data reduction of the PHI on the Solar Orbiter mission. She received her MSc degree in spacecraft design from the Luleå University of Technology in Sweden in 2014 and has been a young graduate trainee at the European Space Agency from 2014–2015. Her research interests include solar spectropolarimetry, science data processing pipelines, and autonomous operations.

Johann Hirzberger is a senior scientist at the Max Planck Institute for Solar System Research and working on instrumentation projects. He leads the operations and calibration of the PHI on the ESA/NASA Solar Orbiter space mission. After receiving his PhD from the University of Graz/Austria, he has worked on ground based solar observations at the Institute for Astronomy in Göttingen/Germany and at the Institute of Physics in Graz/Austria. His main research topics are high resolution solar astrophysics, solar spectro-polarimetry and image processing.

Martin Kolleck is a software engineer who has been working on instrument control software for 15 years at the Max Planck Institute for Solar System Research. His work encompasses the design and implementaion of on-board software, and ground support software and instrument operations for the Sunrise I and II missions and the PHI instrument for the ESA-NASA Solar Orbiter mission.

Juan Pedro Cobos Carrascosa received his MSc and PhD degrees in computer architecture from the University of Granada in 2007 and 2016, respectively. He is computer engineer at the Instituto de Astrofísica de Andalucía (IAA-CSIC) from 2008. He participated in the PHI instrument for ESA's Solar Orbiter mission, specifically in the RTE inversion on FPGA. His research interests include high-performance scientific computing on FPGA and embedded computer architectures for space instrumentation.

David Orozco Suárez is currently a Ramón y Cajal research fellow at IAA-CSIC working primarily on the PHI for the ESA-NASA Solar Orbiter mission and on the stratospheric balloon-borne mission Sunrise. He has worked at the National Astronomical Observatory of Japan after receiving his PhD from the University of Granada (Spain), with a grant from the Japanese Society for the Promotion of Science and at the Instituto de Astrofísica de Canarias (IAC) with an ERC's Marie Curie fellowship. His field of interest is polarimetry, solar magnetic fields, and the development of space-based vector polarimeters in the solar physics field.

David Hernández Expósito is an electronic engineer at IAC, currently working in the development of the on-board data processing system for the instruments SCIP and TuMaG of the Sunrise mission. He has worked at IAA-CSIC with major responsibilities in the development of the FPGA image compression core for the PHI instrument aboard the ESA-NASA Solar Orbiter mission. His work focuses on FPGA development for astrophysics instrumentation, specifically image processing and compression.

Biographies of the other authors are not available.

C. Discussion on the importance of metadata for the pipeline

Our contribution to the Astronomical Data Analysis Software & Systems (ADASS) conference series in 2019, titled "Metadata and Their Importance in SO/PHI's On–Board Data Processing" (see Albert et al., 2020a), delved deeper into the metadata recording system, an integral component of the software framework. Metadata, serving as a bridge between various processing steps and encompassing information from commanding to download, plays a pivotal role in the data processing system. This publication explored the multifaceted use of metadata on-board and its significance for both the operations team on the ground and scientists utilising the science-ready data products. We presented an illustrative example of metadata usage in detecting and understanding an on-board processing error. **Contributions to the publication:** K. Albert took the primary role in designing the metadata recording system, and defined the way that it integrates into the data processing system. She prepared the test data, ran the test, and prepared the manuscript.

Astronomical Data Analysis Software and Systems XXIX
ASP Conference Series, Vol. 527
R. Pizzo, E.R. Deul, J-D. Mol, J. de Plaa and H. Verkouter, eds.

Metadata and Their Importance in SO/PHI's On–Board Data Processing

K. Albert, J. Hirzberger, D. Busse, J. S. Castellanos Durán,
P. Gutiérrez–Marqués, and M. Kolleck

Max Planck Institute for Solar System Research, Göttingen, Germany
albert@mps.mpg.de

Abstract. To cope with the telemetry limitations, the Polarimetric and Helioseismic Imager on Solar Orbiter does full on–board data processing. Metadata are central to the autonomous processing flow, crucial for providing science ready data sets to the community, as well as important in the blind debugging process that will occur in the commissioning phase. We designed a custom metadata logging system for SO/PHI. This paper shows how the logged information is used in the blind debugging scenario.

1. Introduction

State of the art scientific instrumentation, especially those deployed in deep space, often produce more data than can be downloaded. This is the case for the Polarimetric and Helioseismic Imager (PHI, Solanki et al. 2018) on–board the Solar Orbiter (SO, Müller et al. 2013) spacecraft. SO/PHI is an imaging spectropolarimeter, recording four–million–pixel images at six wavelengths in four polarisation states to retrieve five physical quantities: magnetic field strength, inclination, azimuth, line–of–sight velocity and temperature map. The limitations on telemetry from Solar Orbiter would allow downloading ≈30 raw science data sets in each orbit. An orbit (≈160 days) typically accommodates 30 days of observations at strategic points, therefore this would mean little data return. In addition, due to accuracy requirements of SO/PHI, instrument characterisation must be done in orbit, right before the observations, a significant addition to the necessary telemetry.

To maximise science return and cope with telemetry constraints we implemented full on–board data processing in SO/PHI (see Albert et al. 2018a; Lange et al. 2017). The instrument calculates operational parameters for data acquisition, determines calibration data, which is then applied to the science data sets, before reducing them to the final physical quantities of interest by inverting the radiative transfer equation (RTE, see Fig. 1). These steps are done for the first time in orbit, with severely limited hardware when compared to ground processing (see Albert et al. 2018b), without free entry points for verification and without full access to partial results.

Metadata play a central role in the design of the on–board data processing system. Each data set has its own associated metadata file, created at image acquisition, containing all hardware parameters and processing plans. All processing steps add their own entries to this information, generating a full log of the processing. This file is then used both on–board and on ground.

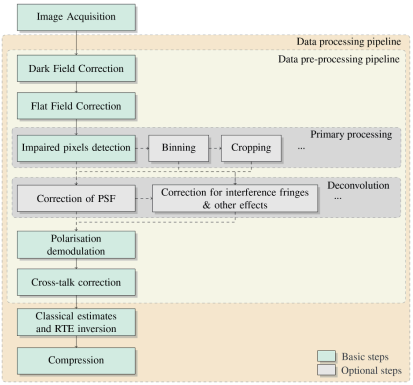

Figure 1. Typical processing pipeline for spectropolarimetric science data with compulsory and optional steps.

2. The metadata system

Metadata are crucial to the success of SO/PHI. Due to the on–board processing, the most important source of information on the data reduction details is what we record in the process. As the data are for the wide scientific community, the metadata must describe the data sets in their entirety, including all information necessary for their scientific use.

2.1. Recording

There are four different sources of metadata: the planning process, the calibration campaign, the instrument, and the data processing system. In the planning process we define processing parameters, such as the data set identifiers for calibration data. We write these into the so called processing environment, which is a file located on–board. The processing environment is further extended during the calibration campaign with other calculated values. It is then written into the metadata of the data set at acquisition, together with the instrument parameters. During the processing we enlist all operations performed with their parameters and return values, followed by higher level information regarding the reason for those steps, as well as a data set summary, showing the current parameters of the data set. Additionally, at steps where we load additional calibration data, the hardware parameters at the recording of the two data sets are also cross–checked to generate warnings for ground review. For pixel–wise information we use an additional image, treated as bit mask, to encode the pixels that reached a `NaN` value during processing at any point in time, and other areas of interest. Before data download this mask is encoded into the temperature image, where we do not loose unrecoverable information by doing so.

2.2. On–board use

The processing pipeline can be executed with the parameters recorded in the metadata of the data sets, or with the current processing environment. Each step of the processing is also based on metadata. We check the basic parameters of the data set: how many images does it contain, which area of the detector is it from, was it binned, and how is it scaled. These values determine further actions, e.g. how will we scale the data set to ensure accuracy in the upcoming operations, or the necessity of cropping or binning calibration data. The fact that this information is carried in the metadata ensures that no additional information must be passed from one step of the pipeline to the next, and the data set can be understood at any time independently from the pipeline.

2.3. On–ground use

After the data download we check whether there are any errors or warnings, and at which step did they occur, if any. At the time of commissioning we may do "blind debugging": find any error that occurred without direct access to the pipeline parameters at runtime. In such a case the metadata will provide us with information necessary to find the error source. During this period partial results will also be available to reproduce any problem encountered in flight on a ground instrument model.

Once the data set is available to the science community, some of the interests are the steps taken during the on–board processing, and the accuracy of the data set (reconstructed from the logs). In addition, pixel–wise information is also available from the masks to ensure that potentially new discoveries are not instrument artefacts.

3. Example for blind debugging

During blind debugging we use the higher level metadata. These contain an entry by each pipeline block, with name, time of execution, operation target, input parameters, data set dimensions, and return value. In addition to this we also have lower level metadata and data set summaries available.

An example for erroneous results is shown in Fig. 2, alongside the expected results for comparison. The metadata associated with the results is shown in Fig. 3. From this information it is possible to assess that there was a Feed Select Mechanism (FSM) mismatch between the processed image and the demodulation matrix, indicating that the two optical paths are not identical. It is also visible that the OperandID, referring to the ID of the demodulation matrix is not the expected one, hence there was an operator error.

4. Conclusions

Metadata are central to the success of SO/PHI. We have custom designed our metadata collection system, making it not only contain all essential information for ground use, but also be the central source of information for the processing pipelines. An example of ground use in blind debugging is presented, to illustrate how the recorded data give clues on what could have gone wrong during processing.

Acknowledgments. Workframe: International Max Planck Research School (IMPRS) for Solar System Science. Solar Orbiter: ESA, NASA. Grant: DLR 50 OT 1201.

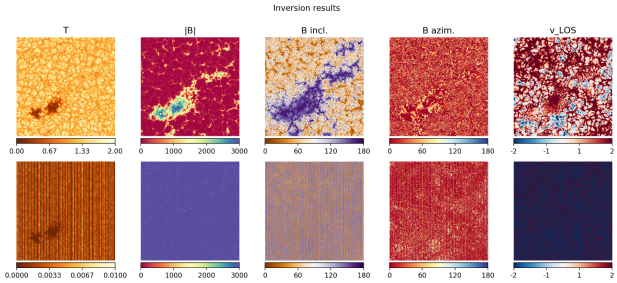

Figure 2. *Top*: Expected results. *Bottom*: Obtained, erroneous results. Data is from magnetohydrodynamics simulations (Riethmüller et al. 2017), prepared with our instrument simulator (Blanco Rodríguez et al. 2018). For testing purposes the RTE is inverted with HeLIx+. (Lagg et al. 2004).

Select / All / Invert	RecordTime A24 Time	BlockReturn A4	BlockName A5	OperandID A10	FreeParameter1 A11	FreeParameter2 A11	ImageEndIndex A3	RowEnd A5	ColumnEnd A5
	Modify	Modify	Modify	Modify	Modify	Modify	Modify	Modify	Modify
1	2019-09-25 12:50:43.0000	0	LOAD	90240	512	512	24	511	511
2	2019-09-25 12:50:44.0000	0	DARK	90270	8388608	0	24	511	511
3	2019-09-25 12:51:02.0000	0	FLAT	90280	4	0	24	511	511
4	2019-09-25 12:51:23.0000	0	PIPE1	90240	0x7F	0	24	511	511
5	2019-09-25 12:51:24.0000	0	LOAD	90240	0	0	24	511	511
6	2019-09-25 12:52:00.0000	NANS	DEMOD	90260	0	0	24	511	511
7	2019-10-01 12:10:55.0000	0	NORM	90240	49868192	0	24	511	511
8	2019-10-01 12:12:26.0000	0	NANS	90240	0	2048	24	511	511
9	2019-10-01 12:12:30.0000	0	REGR1	90240	0x1FF	1	25	511	511
10	2019-10-01 12:12:30.0000	0	REGR1	90240	5	0	25	511	511
11	2019-10-01 12:18:26.0000	0	INVER	90240	1	0	6	511	511
12	2019-10-01 12:19:09.0000	0	REGR2	90240	0x1FF	1	5	511	511
13	2019-10-01 12:19:16.0000	0	PIPE2	90240	0x7F	0	5	511	511

Select / All / Invert	RecordTime A24 Time	BlockReturn A4	BlockName A5	OperandID A10	FreeParameter1 A11	FreeParameter2 A11	ImageEndIndex A3	RowEnd A5	ColumnEnd A5
	Modify	Modify	Modify	Modify	Modify	Modify	Modify	Modify	Modify
1	2019-09-25 12:50:43.0000	0	LOAD	90240	512	512	24	511	511
2	2019-09-25 12:50:44.0000	0	DARK	90270	8388608	0	24	511	511
3	2019-09-25 12:51:02.0000	0	FLAT	90280	4	0	24	511	511
4	2019-09-25 12:51:23.0000	0	PIPE1	90240	0x7F	0	24	511	511
5	2019-09-25 12:51:24.0000	0	LOAD	90240	0	0	24	511	511
6	2019-09-25 12:52:00.0000	NFRM	DEMOD	90261	0	0	24	511	511
7	2019-10-01 12:10:55.0000	0	NORM	90240	49868192	0	24	511	511
8	2019-10-01 12:12:26.0000	0	NANS	90240	0	2048	24	511	511
9	2019-10-01 12:12:30.0000	0	REGR1	90240	0x1FF	1	25	511	511
10	2019-10-01 12:12:30.0000	0	REGR1	90240	5	0	25	511	511
11	2019-10-01 12:18:26.0000	0	INVER	90240	1	0	6	511	511
12	2019-10-01 12:19:09.0000	0	REGR2	90240	0x1FF	1	5	511	511
13	2019-10-01 12:19:16.0000	0	PIPE2	90240	0x7F	0	5	511	511

Figure 3. Excerpt of recorded metadata. *Top*: From the expected results, indicating that the result contains NaNs, as expected. *Bottom*: From erroneous results, with warning regarding the Feed Select Mechanism, and incorrect OperandID.

References

Albert, K., Hirzberger, J., Busse, D., et al. 2018a, in Proc. SPIE, vol. 707, 10707
— 2018b, in ASP Conference Series, Vol. 523
Blanco Rodríguez, J., del Toro Iniesta, J. C., & Orozco Suárez, D. e. a. 2018, ApJS, 237, 35
Lagg, A., Woch, J., Krupp, N., & Solanki, S. K. 2004, Astronomy and Astrophysics, 414, 1109
Lange, T., Fiethe, B., Michel, H., et al. 2017, in NASA/ESA Conf. on Adapt. Hardw. and Sys.
Müller, D., Marsden, R. G., Cyr, O. S., et al. 2013, Solar Physics, 285, 25
Riethmüller, T. L., Solanki, S. K., Barthol, P., et al. 2017, The Astrophysical Jour. Suppl. Series
Solanki, S., del Toro Iniesta, J., Woch, J., et al. 2018, Accepted to Astronomy and Astrophysics

D. First report on the scientific accuracy of the pipeline in development

Our contribution to the ADASS conference series in 2018, titled "Performance Analysis of the SO/PHI Software Framework for On-board Data Reduction" (see Albert et al., 2019), marked the start of our accuracy analysis for the science data reduction pipeline. While the on-board pipeline is based on typical ground-based pipeline implementations, the unique challenges of on-board operation (detailed in Albert et al., 2020b) necessitated the analysis of the achieved precision during the on-board processing. Although the pipeline was still in development at this stage, we offered a preliminary assessment of its accuracy by comparing results obtained with the on-board pipeline to those from a reference ground-based implementation. We also used an independent but comparable method for inverting the radiative transfer equation, called HeLIx+ (see Lagg et al., 2004), providing context for our results.

Contributions to the publication: K. Albert implemented the on-ground reference pipeline, that processes data with the same scaling as the on-board system (and hence enables one to one comparison). She prepared the test data, conducted the test (excluding the inversion of the radiative transfer equation), analysed the results and prepared the manuscript.

Astronomical Data Analysis Software and Systems XXVIII
ASP Conference Series, Vol. 523
P.J. Teuben, M.W. Pound, B.A. Thomas, and E.M. Warner, eds.

Performance Analysis of the SO/PHI Software Framework for On-board Data Reduction

K. Albert,[1] J. Hirzberger,[1] D. Busse,[1] J. Blanco Rodríguez,[2], J. S. Castellanos Durán[1], J. P. Cobos Carrascosa,[3] B. Fiethe,[4] A. Gandorfer,[1] Y. Guan,[4] M. Kolleck,[1] A. Lagg,[1] T. Lange,[4] H. Michalik,[4] S. K. Solanki,[1] J. C. del Toro Iniesta,[3] and J. Woch[1]

[1]*Max Planck Institute for Solar System Research, Göttingen, Germany*
albert@mps.mpg.de
[2]*Universidad de Valencia, Paterna (Valencia), Spain*
[3]*Instituto de Astrofísica de Andalucía (IAA - CSIC), Granada, Spain*
[4]*Institute of Computer and Network Engineering, TU Braunschweig, Germany*

Abstract. The Polarimetric and Helioseismic Imager (PHI) is the first deep-space solar spectropolarimeter, on-board the Solar Orbiter (SO) space mission. It faces: stringent requirements on science data accuracy, a dynamic environment, and severe limitations on telemetry volume. SO/PHI overcomes these restrictions through on-board instrument calibration and science data reduction, using dedicated firmware in FPGAs. This contribution analyses the accuracy of a data processing pipeline by comparing the results obtained with SO/PHI hardware to a reference from a ground computer. The results show that for the analyzed pipeline the error introduced by the firmware implementation is well below the requirements of SO/PHI.

1. Introduction

The Polarimetric and Helioseismic Imager (PHI) is one of ten instruments to orbit the Sun on-board Solar Orbiter (SO; see Müller et al. 2013). SO/PHI (Solanki et al. 2018), is an imaging spectropolarimeter, probing the photospheric Fe I 6173 Å absorption line.

SO/PHI records data in five dimensions: time series of data sets containing 2048×2048 pixel images of the Sun, sampling the target absorption line at six wavelengths, recording four different polarization states at each wavelength. These polarization states contain linear combinations of the Stokes parameters ($\mathbf{S} = [I, Q, U, V]^T$), a formalism to describe the polarization of light in terms of four ideal polarization filters. To arrive to the Stokes images (the input for scientific analysis), the recorded polarization states are demodulated with the demodulation matrix. These images, complemented with a wavelength dimension, encode the magnetic field vector at the mean formation height of the absorption line and the line of sight (LOS) velocity due to the Zeeman and Doppler effects. Arriving to these quantities is possible by the inversion of the Radiative Transfer Equation (RTE). See del Toro Iniesta (2003) for more details on spectropolarimetry.

SO/PHI is the first spectropolarimeter on a deep space mission, facing an unprecedented dynamic environment and telemetry limitations. These challenges are met with a full and autonomous on-board data analysis system: it determines the instrument characteristics, applies them to the science data, then derives the targeted physical pa-

rameters. This system is implemented on a data processing unit with two Field Programmable Gate Arrays (FPGAs), reconfigured in flight to perform image processing functions (Fiethe et al. 2012; Lange et al. 2017), and a microprocessor running a data processing framework that combines these functions into pipelines (Albert et al. 2018). This contribution analyses errors induced by the on-board processing.

2. The on-board data analysis software

The science data processing comprises of preprocessing and RTE inversion. The preprocessing primarily corrects the images for the dark and flat field of the instrument, and does the polarimetric demodulation. Depending on science case and the instrument parameters determined at instrument commissioning, it may have additional steps (e.g. spatial cropping or deconvolution from image artifacts). The RTE inversion transforms the 24-image spectropolarimetric dataset into 5 images of interest: azimuth, inclination and magnitude of the magnetic field, the LOS velocity and the total intensity at continuum wavelength. See Cobos Carrascosa et al. (2016) for details on SO/PHI's RTE inversion scheme. To save FPGA resources, the preprocessing functions use fixed point number representation on 24.8 bits, while the RTE inversion is on 32 bits floating point.

The most basic preprocessing pipeline for a data set from an imaging spectropolarimeter contains dark and flat field correction and polarimetric demodulation:

$$\boldsymbol{S}_\lambda(x,y) = D(x,y) \cdot [(\boldsymbol{I}^{obs}_\lambda(x,y) - I^{dark}(x,y))/I^{flat}(x,y)], \tag{1}$$

where "$\cdot$" denotes matrix multiplication, λ marks wavelength dependence, x and y are spatial dimensions. The Stokes parameters are contained in $\boldsymbol{S}$, D is the demodulation matrix, $\boldsymbol{I}^{obs}$ contains the observed data in the four modulation states. The dark field of the sensor is I^{dark}, I^{flat} is the telescope flat field, neither depending on wavelengths and modulation states (may change for the flat field after instrument commissioning).

To implement Eq. 1, we use four blocks, combined into a pipeline (see Fig. 1). The raw data is integer, represented up to 22.8 bits after accumulation (14.8 assumed in test). As the exposure time is calibrated to fill a defined percentage of the detector full well, the recorded data is ideally represented. To process the data at the highest resolution, we shift the pixel values of these images to the top of the full range ($\times 2^9$), arriving to 23.8 bits (one bit is sign). This representation is the block interface, however some blocks re-scale the images to optimize the output accuracy.

We quantify the errors introduced through on-board processing by running the pipeline on a SO/PHI ground reference model and on a ground computer (using floating point in Python). The test data is from the Solar Dynamics Observatory / Helioseismic and Magnetic Imager (see Schou et al. 2012), run through the SO/PHI instrument simulator, SOPHISM (see Blanco Rodríguez et al. 2018). This data is modulated into measured intensities, then degraded with flat and dark field obtained during ground calibration (also used by the pipeline). We compare the results of the preprocessing after flat field correction, and polarimetric demodulation (no errors are expected from subtraction). The RTE inversion is done on a ground computer, with the He-Line Information Extractor inversion code (HeLIx+; see Lagg et al. 2004). HeLIx+ assumes a Milne-Eddington approximation of the atmosphere, the same as SO/PHI's on-board inversion scheme, however the profile fitting method is different. The differences in physical parameters only indicate the expected error induced by numerical inaccura-

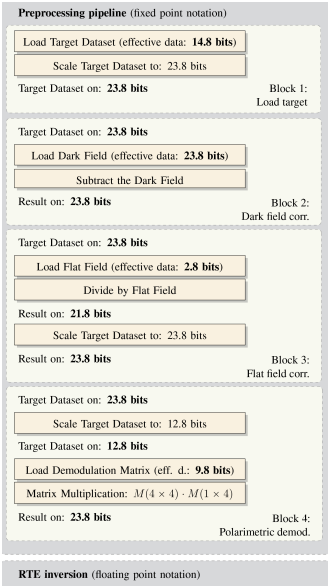

Figure 1. The studied pipeline. The preprocessing controls accuracy by scaling.

cies in preprocessing, due to the differences in the algorithms, the innate uncertainty in the results of the inversion.

3. Results

The errors from the division are below 10^{-3} (compared to the reference results), apart from a few outliers in the divisor, with Root Mean Square (RMS) around 5×10^{-5}.

SO/PHI requires the accuracy of the polarization signals (i.e. $\boldsymbol{S}$) to be better than 10^{-3}. Figure 2 shows the error histogram at one wavelength sample. All pixels comply, with their RMS in the order of 10^{-6}, leaving a large margin for other error sources. The errors decrease from the previous step due to the nature of polarimetry: it calculates the difference between signals, partially canceling previous errors. Furthermore, the error in Q is larger than in the rest of the Stokes images, due to a small term in D.

The errors after RTE inversion are only an indication of what is expected due to numerical inaccuracies. The RMS error of the magnetic field strength, azimuth, inclination (calculated in a region with strong signals) and LOS velocity (calculated in the entire solar disk) due to numerical errors are 33.64 G, 1.92°, 2.56°, and 19.00 ms^{-1}, respectively. The inversion process for this type of data set, statistically, has error RMS

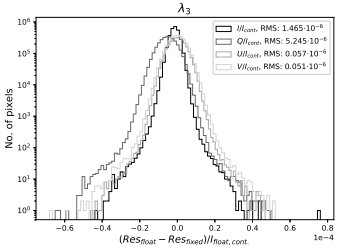

Figure 2. Histogram of polarimetric errors, showing requirement compliance.

21.9 G, 1.37°, 1.34° and 14.5 ms^{-1}, respectively. What is introduced on top of this by the numerical inaccuracies amount to 53%, 40%, 91% and 31% of the inversion error.

4. Conclusions

SO/PHI is the first instrument of its kind to perform on-board data analysis, including data preprocessing and the inversion of the RTE. These steps use computationally demanding image processing functions, implemented on FPGAs. The fixed point number representation in the on-board preprocessing was motivated by resource limitations.

The errors induced by the preprocessing conform with requirements, with a good margin for other sources. This is achieved by keeping full control over data accuracy, a significant overhead. Errors in Fourier domain processing are currently being analyzed.

Acknowledgments. Workframe: International Max Planck Research School (IMPRS) for Solar System Science. Solar Orbiter: ESA, NASA. Support grants: DLR 50 OT 1201, Spanish Research Agency ESP2016-77548-C5, European FEDER. Data: NASA/SDO HMI science team.

References

Albert, K., Hirzberger, J., Busse, D., et al. 2018, in Proc. SPIE, vol. 707, 10707
Blanco Rodríguez, J., et al. 2018, The Astrophysical Journal Supplement Series, 237, 35
Cobos Carrascosa, J. P., et al. 2016, in Proc. SPIE, vol. 9913, 9913
del Toro Iniesta, J. C. 2003, Introduction to spectropolarimetry (Cambridge university press)
Fiethe, B., Bubenhagen, F., Lange, T., Michalik, H., Michel, H., Woch, J., & Hirzberger, J. 2012, in NASA/ESA Conference on Adaptive Hardware and Systems, 31
Lagg, A., Woch, J., Krupp, N., & Solanki, S. K. 2004, Astronomy and Astrophysics, 414, 1109
Lange, T., Fiethe, B., Michel, H., Michalik, H., Albert, K., & Hirzberger, J. 2017, in NASA/ESA Conference on Adaptive Hardware and Systems, 186
Müller, D., Marsden, R. G., Cyr, O. S., et al. 2013, Solar Physics, 285, 25
Schou, J., Scherrer, P. H., Bush, R. I., et al. 2012, Solar Physics, 275, 229
Solanki, S., del Toro Iniesta, J., Woch, J., et al. 2018, Submitted to Astronomy and Astrophysics

E. Analysis of the scientific accuracy of the pipeline in development

In our peer-reviewed work titled "Accuracy analysis of the on-board data reduction pipeline for the Polarimetric and Helioseismic Imager on the Solar Orbiter mission" (see Albert et al., 2023a), we expanded upon the accuracy analysis initiated in Albert et al., 2019. This time, we assessed our (further improved) data processing pipeline using magnetohydrodynamics (MHD) simulations of a sunspot as input data, from which we synthesised a data set representative of SO/PHI observations. We performed a statistical analysis of differences across distinct features of the simulated scene, including umbra, penumbra, and quiet Sun. We examined errors introduced at each processing step, and showed that their impact is negligible on the polarimetric sensitivity and accuracy expected of the methods used (in particular that of the Milne Eddington approximation of the photosphere during the inversion of the radiative transfer equation).

Contributions to the publication: K. Albert implemented the on-ground data processing pipeline, prepared the test data (starting from synthetic observations), ran the data processing pipeline, analysed the results, and prepared the manuscript.

Solar Physics (2023) 298:58
https://doi.org/10.1007/s11207-023-02149-y

RESEARCH

Accuracy Analysis of the On-board Data Reduction Pipeline for the Polarimetric and Helioseismic Imager on the Solar Orbiter Mission

Kinga Albert[1,2] · Johann Hirzberger[1] · J. Sebastián Castellanos Durán[1,3] · David Orozco Suárez[4] · Joachim Woch[1] · Harald Michalik[5] · Sami K. Solanki[1]

Received: 8 December 2022 / Accepted: 25 March 2023 / Published online: 20 April 2023

Abstract

Context: Scientific data reduction on-board deep space missions is a powerful approach to maximise science return, in the absence of wide telemetry bandwidths. The Polarimetric and Helioseismic Imager (PHI) on-board the Solar Orbiter (SO) is the first solar spectropolarimeter that opted for this solution, and provides the scientific community with science-ready data directly from orbit. This is the first instance of full solar spectropolarimetric data reduction on a spacecraft.

Methods: In this paper, we analyse the accuracy achieved by the on-board data reduction, which is determined by the trade-offs taken to reduce computational demands and ensure autonomous operation of the instrument during the data reduction process. We look at the magnitude and nature of errors introduced in the different pipeline steps of the processing. We use an MHD sunspot simulation to isolate the data processing from other sources of inaccuracy. We process the data set with calibration data obtained from SO/PHI in orbit, and compare results calculated on a representative SO/PHI model on ground with a reference implementation of the same pipeline, without the on-board processing trade-offs.

Results: Our investigation shows that the accuracy in the determination of the Stokes vectors, achieved by the data processing, is at least two orders of magnitude better than what the instrument was designed to achieve as final accuracy. Therefore, the data accuracy and the polarimetric sensitivity are not compromised by the on-board data processing. Furthermore, we also found that the errors in the physical parameters are within the numerical accuracy of typical RTE inversions with a Milne-Eddington approximation of the atmosphere.

Conclusion: This paper demonstrates that the on-board data reduction of the data from SO/PHI does not compromise the accuracy of the processing. This places on-board data processing as a viable alternative for future scientific instruments that would need more telemetry than many missions are able to provide, in particular those in deep space.

Keywords Spectropolarimetry · On-board processing · Data pipeline · Data reduction accuracy

Extended author information available on the last page of the article

1. Introduction

The Polarimetric and Helioseismic Imager (PHI; Solanki et al., 2020) is one of the instruments on-board the Solar Orbiter mission (SO; Müller et al., 2020). Solar Orbiter is following heliocentric orbits, that incline relative to the ecliptic plane to access higher solar latitudes. SO/PHI is a spectropolarimeter scanning the photospheric Fe I 617.43 nm absorption line at two different spatial resolutions through two telescopes: the Full Disc Telescope (FDT) and the High Resolution Telescope (HRT). The HRT is stabilised with an image stabilisation system that corrects for spacecraft jitter and follows the observed features, counteracting solar rotation. SO/PHI samples the spectral line at six wavelengths, recording four polarisation states at each wavelength, from which the full Stokes vector (I, Q, U and V), describing the polarisation of the light, can be derived. To obtain a data set with a reliable signal-to-noise ratio (S/N), and offer possibilities for trade-offs between S/N and acquisition time, the instrument can parametrise its acquisition scheme. The two most commonly used acquisition schemes are: (i) scanning through the absorption line, while recording each of the four polarisation states five times, and accumulating four images in each state, which is completed in less than 100 s or (ii) scanning through the spectral line and polarimetric states a single time, accumulating 16 images in each state, completed in less than 60 s (see Solanki et al., 2020). Each data set results in twenty-four images and provides information about the magnetic-field vector and the line-of-sight velocity at an average formation height of the spectral line. We arrive at these quantities, describing the solar atmosphere, on-board the spacecraft through a full data reduction pipeline, including the inversion of the radiative transfer equation of polarised light (RTE), assuming a Milne-Eddington approximation of the solar atmosphere. We complement the output of the inversion with the total intensity image from the continuum region next to the absorption line, as well as with metadata about all the details of the data reduction, forming the science-ready data product that is made available to scientists.

In order to facilitate on-board processing, SO/PHI has a custom designed Digital Processing Unit (see Solanki et al., 2020) on which we implemented a data processing software system (see Albert et al., 2020; Lange et al., 2017). There were three major drivers in the design of the data processing system: the resource limitations of the hardware, the need for autonomy of the data processing due to the long telecommand to telemetry turnaround times, and the need for the robustness of the system (i.e., to ensure complete and correct data reduction on images from different orbital positions and different solar scenes). To meet the needs with the limited resources, we had to trade off algorithm complexity and computational accuracy.

In this paper, we analyse the effect of these trade-offs on the accuracy of the data reduction pipeline. We compare processing results of a synthetic data set on a representative hardware model of SO/PHI with a reference implementation of the data reduction without trade-offs, which represents the best possible results for the data set. We use synthetic data to exclude errors from sources outside the processing pipeline; these are crucial to analyse, however, they lie outside the scope of this paper. We show that errors accumulated during the processing are negligible and therefore we achieve the desired quality for the reduced data. We analyse the quality of the Stokes vector achieved by the on-board processing pipeline, the final accuracy of the output data, and the errors introduced during the processing.

2. The On-board Data Processing

The baseline data processing of SO/PHI consists of the standard spectropolarimetric data reduction steps (see Figure 1). The processing pipeline operates on data loaded from mass

memory where we store the acquired raw data. This is also where we store the results of the pipeline, while they wait for data compression and download.

The pipeline starts with dark-field and flat-field correction. For both of these steps, we determine the calibration data (i.e., the dark- and flat-fields) on-board by two separate processes and store them in the mass memory prior to the initiation of the data reduction. Hence, the only action performed by the pipeline is their loading and their application to the data.

The following step is the prefilter correction. The exact prefilter profiles have been determined on ground at 49 different wavelengths, given in 49 different voltages of the Filtergraph (see Solanki et al., 2020; Dominguez-Tagle et al., 2014), and uploaded to SO/PHI. The orbits of SO induce a continuous change in the radial velocity of our instrument with respect to the Sun, therefore we determine the voltages for data acquisition as part of instrument calibrations, on-board. This is done such that a reference wavelength λ_0, falls close to the minimum of the spectral line and one sample falls into the nearby continuum. At the time of the data processing, we calculate the corresponding values of the prefilter profile for the data set by linear extrapolation of the measured ones, and then apply them to the data.

The polarimetric demodulation is the step that recovers the Stokes vector from the observations. For this step, the pipeline can either use a field-dependent demodulation matrix or one that is uniform across the field of view (FOV; see Solanki et al., 2020). Preliminary analysis performed on data retrieved up to date from SO/PHI shows that the results are more accurate with a uniform demodulation matrix. Hence, the on-board pipeline currently uses the average of the FOV-dependent demodulation matrix, which was measured during the ground testing prior to launch. This is also the demodulation matrix used in this paper. Further improvement to the data demodulation is possible through polarimetric ad-hoc cross-talk correction between the different components of the Stokes vector (see Sanchez Almeida and Lites, 1992; Schlichenmaier and Collados, 2002). After the demodulation and the cross-talk correction, the pipeline normalises the resulting Stokes vector, using the disc centre continuum intensity. The latter is determined on ground and uploaded to SO/PHI.

To retrieve the physical quantities, we execute the RTE inversion on the normalised Stokes vector. The RTE inversion implemented on-board uses the Milne-Eddington model atmosphere and the Levenberg-Marquardt minimisation method (see Cobos Carrascosa et al., 2016). The RTE inversion operates on a pixel basis and needs all values of a pixel from the 24 different images. The pipeline performs this pixel sorting prior to the RTE inversion. The initial conditions for the inversion can be provided in a configuration file, or through numerical calculations, called classical estimates (Semel, 1967; Rees and Semel, 1979; Landi Degl'Innocenti and Landolfi, 2004). After the inversion, we arrive at the physical quantities: the magnetic vector, $\vec{B} = (|\vec{B}|, \gamma, \phi)$ where $|\vec{B}|$ stands for the field strength and γ and ϕ for the inclination and azimuth of the field, respectively, and line-of-sight velocity, v_{LOS}. They are then sorted back into images. Finally, the pipeline attaches the continuum intensity to them and stores them into the mass memory as the result of the data reduction.

This baseline can be further extended with other modules, such as binning and cropping, used to balance the telemetry volume with the needs of each science case. We also have the capability to further extend the pipeline in the future, e.g., with Fourier filtering to restore the data from optical effects, such as a known point spread function (PSF).

SO/PHI combines different number representations in the data processing (see Figure 1). Wherever it was possible, we opted for fixed-point representations as a method to reduce resource usage, trading off accuracy, which is one of the most important sources of accuracy loss in the pipeline. We use floating-point calculations where the accuracy of fixed-point computations did not fulfil the requirements (for instance, the inversion of the RTE). In contrast to floating-point, where number normalisation is inherent in the notation and therefore

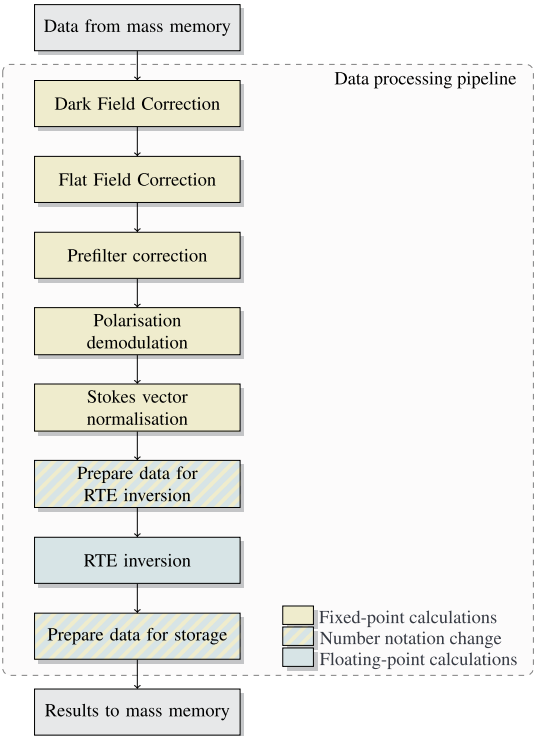

Figure 1 The current baseline data processing of SO/PHI, executed on-board the spacecraft. To enable the calculations on the limited on-board resources, we combine fixed-point and floating-point number representation in the pipeline.

the precision is better preserved, in fixed-point representation the decimal point is always in the same place, resulting in effectively different number of bits used for the representation of different magnitudes, with 0-padding. For instance, two irrational numbers differing only by a scale factor of 2, both within the range of possible numbers on the allocated bits (i.e., none of them produces overflow), would have an accuracy difference of a bit in fixed-point representation, while in floating point they would have the same accuracy. Maximising the accuracy of fixed-point representation is possible through scaling up values to effectively use as many bits as possible. SO/PHI uses in its data processing 24.8 fixed-point notation, where 24 bits are for the integer part and 8 for the decimal, and single precision, 32 bits floating point.

In order to maximise SO/PHI's processing accuracy, we must make sure that we effectively use all the available bits in the fixed-point notation by controlling the magnitude of our data in all steps of the data processing. We always scale the full data set together to maintain the information in all dimensions of the data: spatial, spectral, and polarimetric. The individual pixel values in the images have no physical meaning throughout the pipeline, it is the normalisation of the Stokes vector by the disc centre continuum quiet Sun intensity (denoted simply as I_c) that creates the suitable input to the RTE inversion module.

Our starting point for scaling the data through the pipeline is in the detector. The exposure time adjusts the brightness of the solar scene such, that it is reliably represented on 12 bits read out from the detector. Then, we accumulate a number of detector readouts to increase

the signal-to-noise ratio of the solar data, and pad the result with zeros after the decimal, to reach the 24.8 fixed-point notation. Then, we calculate the largest possible integer number that we can obtain through these operations, called from here on *maximum range*, and place it into the metadata of the data set for further reference. For instance, for 20 accumulations, the maximum range would be 20×2^{12}. At the start of the data processing, just after loading our raw data set from the mass memory, we scale up the data to use all the available bits. This is achieved by multiplying with a scale factor, calculated as the ratio of 2^{23} (the largest possible integer in two's complement on 24.8 fixed-point notation) and the current maximum range. In each operation that follows, we aim to preserve this largest possible maximum range in the result, by considering the magnitude of the operands and that of the result. For simplicity, we only keep track of the maximum range. However, in few cases the minimum range of the absolute value of the data is also relevant, for instance, when we perform divisions like that necessary to correct the flat field or the prefilter. Here, the smallest value in the divisor determines the maximum range of the result. Since these are not tracked, we make assumptions about the divisor, with the consequence that any pixels with smaller values will create an overflow and the resulting pixel will become not-a-number (NaN).

We scale all calibration data to no higher value than to represent the precision with which they are determined (e.g., in the case of the flat fields, we only use 3.8 bits). In those cases where the accuracy of the calibration data is high, we do a trade-off between the accuracy of the data and that of the calibration data. We decide all trade-offs on a case-by-case basis, based on simulations to verify which scaling gives the best precision results.

3. Test Setup

To compare the accuracy of the on-board processing pipeline to what could be achieved on-ground, and isolate it from other sources of errors (e.g., solar evolution and the accuracy of the calibration), we have chosen to process a synthetic data set. We process these data with the pipeline described in Section 2 on the Qualification Model (QM) of SO/PHI, which is fully representative in terms of the Data Processing Unit of the Flight Model. We compare the QM results to a reference pipeline run in a PC in double precision floating point, representing the best possible processing accuracy. The one exception is the RTE inversion, which is performed on the QM in both cases. In the case of the reference pipeline, we upload the RTE input data in floating point and download directly the floating point results that it produces. The data processing pipeline uses the same calibration data that we apply in the data preparation, therefore we have no inaccuracy originating from the determination method and processing of the calibration data. This means that all errors presented in this work are inaccuracies originating in the data reduction pipeline.

The test data set is a magnetohydrodynamic (MHD) simulation of a sunspot (Rempel, 2015). From this MHD cube, we synthesized the Fe I 6173 Å spectral line profiles, applying a wavelength sampling of 14 mÅ, with the SPINOR code (Frutiger et al., 2000). SPINOR relies on the STROPO routines to solve the RTE (Solanki, 1987). The simulation is 1024 × 1024 pixels, with a pixel size of 48 km. The pixel size of the HRT telescope of SO/PHI, at closest approach, corresponds to 101 km, however the dataset is not resampled in order to provide more pixels in the umbra and penumbra for statistical analysis.

We degrade the synthesized spectral line profiles in several steps, starting by convolving the wavelength dimension of the synthesised data with the transmission profile of the SO/PHI Filtergraph (see Solanki et al., 2020; Dominguez-Tagle et al., 2014):

$$S_p^{conv}(\lambda, x, y) = S_p^{synth}(\lambda, x, y) * F(\lambda), \tag{1}$$

where $*$ denotes convolution, the index p runs over the four polarimetric modulation states, λ denotes the wavelength, x and y are the spatial image coordinates in pixels. S^{synth} are the Stokes profiles synthesized from the MHD cube, F denotes the filter profile, and S^{conv} is the Stokes vector from the synthesis, convolved with the spectral profile. We then select the samples for SO/PHI from the resulting spectral profiles. The samples are defined relative to a reference wavelength (λ_0, which we chose for this test to be 6173.371 Å). λ_0 is placed in the vicinity of the absorption line minima:

$$S_p^{samp}(\lambda, x, y) = S_p^{conv}(\lambda_s, x, y), \tag{2}$$

where λ_s denotes the sample wavelengths in reference to λ_0:

$$\lambda_s = [\lambda_0 - 300\,\text{mÅ}, \lambda_0 - 140\,\text{mÅ}, \lambda_0 - 70\,\text{mÅ}, \lambda_0, \lambda_0 + 70\,\text{mÅ}, \lambda_0 + 140\,\text{mÅ}],$$

and $\vec{S}^{samp}$ is the Stokes vector sampled in wavelength.

After spectral sampling, we convolve each individual image of the data set (the 24 images, six wavelength samples and four modulation states) with the spatial PSF in the shape of a Lorentzian function, configured with the theoretical parameters of the HRT telescope, adjusted to the plate scale of the simulation:

$$S_p(\lambda, x, y) = S_p^{samp}(\lambda, x, y) * A(x, y), \tag{3}$$

where A represents the PSF of the SO/PHI HRT.

The convolution with the PSF reduces the continuum quiet Sun root-mean-square (RMS) contrast of the synthetic data from 22.83% to 7.9%. The next step is the polarimetric modulation of the synthetic data:

$$I_m^{mod}(\lambda, x, y) = k \sum_{p=1}^{4} M_{mp}(\lambda) S_p(\lambda, x, y), \tag{4}$$

where index m denotes modulation states, I_m^{mod} is the modulated data set, M_{mp} is the polarimetric modulation matrix, and S_p is the Stokes vector from Equation 3. The constant k adjusts the quiet Sun continuum mean intensity (I_c) of the data to what is representative of the SO/PHI HRT, converts the number of photons collected by the detector to digital numbers, read out from the electronics. This constant, furthermore, accounts for the frame accumulations that we perform in order to increase the signal-to-noise ratio of the data, which we adjust to 20 frames for the tests. Due to the higher RMS contrast in the test data and therefore higher dynamic range, we adjust the I_c slightly below the level observed in the SO/PHI HRT data. The ratio of I_c for the observed to the test data is 1.08. It is important to remark that this difference in I_c creates a slightly worse case from the point of view of accuracy: as the values in the test data are somewhat lower, they are represented on fewer bits when compared to SO/PHI observations. We remark, that the order in which we apply the instrumental degradation to the synthetic data has been established for the sake of convenience and to be able to correct the data in the same order with the pipeline. For instance, we have applied the polarimetric modulation here, even though the modulation package in the instrument is right after the entrance window following the beam direction. Since only the order of linear operations has been exchanged (only the dark field application is non-linear, which we apply according to the optical path), this does not affect the resulting input data.

Once we have modulated the input Stokes vector and converted the data to digital numbers, we apply the prefilter profiles, dark and flat fields to the synthetic data:

$$I_m^{obs}(\lambda, x, y) = I_m^{mod}(\lambda, x, y) I^{\mathrm{p}}(\lambda, x, y) I_m^{\mathrm{f}}(\lambda, x, y) + I^{\mathrm{d}}(x, y), \tag{5}$$

where I_m^{obs} is the data set produced to match SO/PHI observations, i.e., the input to the processing pipeline, I^{p} is the prefilter profile, which is different for each wavelength and pixel, I_m^{f} are the flat fields, depending both on wavelength and polarisation states m, and I^{d} is the dark field of the sensor, the same for all wavelengths and polarisation states.

It is worth noting that the addition of the flat field and dark field to the data further reduces its RMS contrast to 6.4%. During the first months of SO/PHI operations, we have observed the RMS contrast in SO/PHI HRT observations of the quiet Sun to be around 4.5% to 5%, which is expected to change further as SO/PHI changes its distance to the Sun. The smaller the dynamic range in the data (i.e., lower the RMS), the closer we could take all values of it to the maximum possible range, hence achieving a better overall computational accuracy. For this, we could do an adjustment to the exposure time or in the maximum range assumptions at data acquisition. This is, however, not done in the case of our test data. Therefore, the results are representative of what we would achieve on SO/PHI data. Also note, that the dark and flat fields that we apply here were calculated on ground from SO/PHI data, and calculated on-board SO/PHI, respectively. These data we downloaded during the commissioning phase of the mission. We produced these early calibration data with methods that we will improve further, however, these are representative of the flat and dark fields that we expect after fine-tuning. Furthermore, it is important, that in order to not introduce further uncertainty into the process, and be able to assess the effects of the numerical errors on the RTE inversion, we omit several effects that would appear in real data. We do not introduce noise to the data in the course of its degradation. Likewise, we use the data as instantaneous snapshots of the solar scene without considering the evolution of the solar scene, rotation of the Sun or spacecraft jitter.

We show the effects of the data degradation at the continuum wavelength in Figure 2. The most obvious effect is the reduction of the image RMS contrast. In the line profiles of the data (see Figures 3, and 4) we can see that the complex profiles from the MHD simulations smooth out significantly as a result of the convolution with the transmission profiles of the SO/PHI Filtergraph. The same operation also lowers the amplitude of the polarisation signals. The sampling of the data further removes details of the spectral shape by reducing the available information. This effect is especially strong in the sunspot profiles, due to the complex shapes. The spatial PSF convolution strongly changes the Stokes I intensity, especially in the umbral profile, as usually stray light does in real observations. We do not expect the RTE inversion to perfectly reconstruct the resulting profiles, producing especially large differences in the umbra, as it does not account for the stray light. The spatial PSF can lower the amplitude of the polarisation signals further (e.g., in quiet Sun areas), although it is not always the case (as shown here in the umbral profiles), since the final effect on each pixel depends on the surrounding signals. Note that the final degraded profiles appear different with respect to the synthesised data. This is mainly an effect of the wavelength sampling. While we sample the absorption line with symmetric offsets, the reference wavelength does not necessarily coincide with the centre of the line, causing a shift in the sampling and introducing an apparent asymmetry even in the case of symmetric profiles. This, however, does not affect the performance of the RTE inversion. The relatively few samples (only five) also contribute to the strong difference.

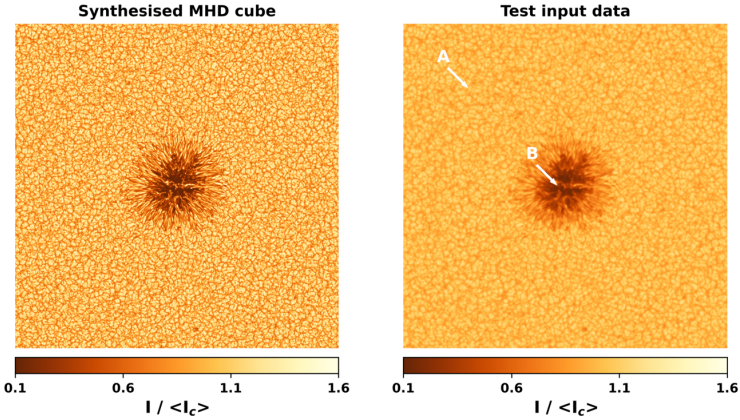

Figure 2 The data set used in the tests contains an MHD simulated sunspot (Rempel, 2015). We synthesised the spectral line and its nearby continuum from the MHD cube (left) and degraded, as described in the main text, to what we would expect from SO/PHI (right) shown here at the continuum intensity sample wavelength, $\lambda_0 - 300$ mÅ. The most obvious result of the degradation is the loss of RMS contrast. The size of the data is 1024×1024 pixels, each pixel corresponding to 48 km on the Sun. The spatial sampling is larger than what SO/PHI achieves at closest approach. However, it is preserved to provide more pixels for statistical analysis. The arrows indicate pixels for which the Stokes profiles are plotted in Figures 3 and 4.

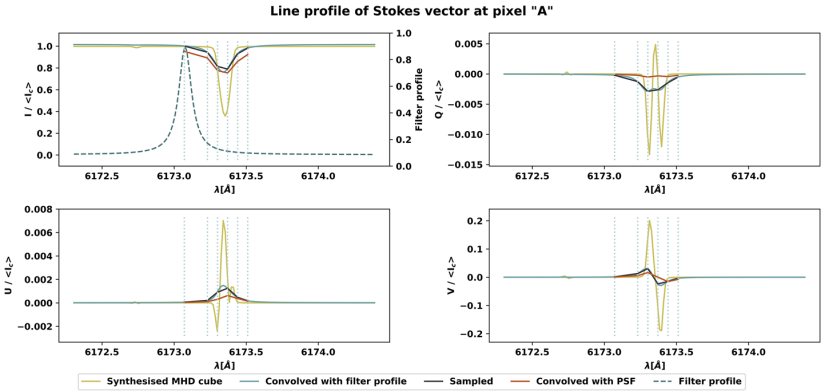

Figure 3 The spectral line profile of the input data set shows the degradation of the synthesised MHD data. We first convolve the synthesised profile with the filter profiles of SO/PHI (shown in the top left panel), then select the correct wavelength samples, followed by the convolution of the resulting images with the theoretical PSF of the instrument. This is a bright pixel from the quiet Sun. The convolution with the filter profiles significantly reduces the spectral line complexity. We indicate the location of the plotted pixel in Figure 2.

We analyse how the data pipeline changes the accuracy of the data throughout each step of the pipeline, grouping them into three categories: the input and the first steps of pre-processing, the polarimetric errors, and the physical parameters. In the first category, we start by analysing the input errors introduced by the data quantisation to fixed-point notation.

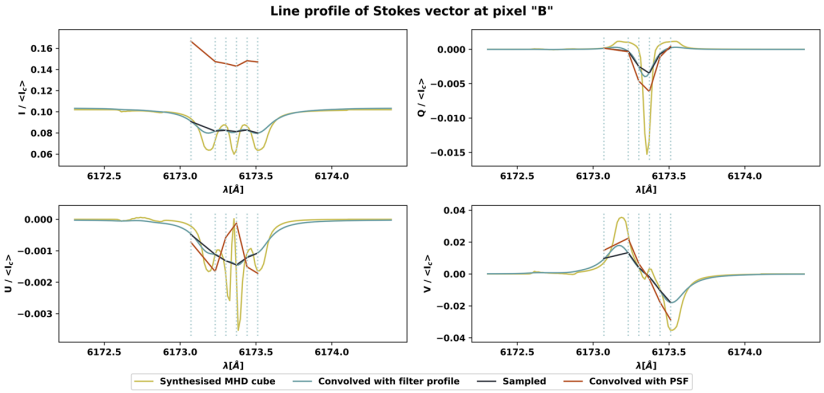

Figure 4 Same as Figure 3, for a pixel from the umbra. This dark pixel is surrounded by bright structures, therefore after applying the PSF, there is a large change in the intensity level at continuum from neighbouring pixel contributions. There is also a significant change in the U profile. This is an extreme case, with neighbouring pixels being significantly different from the one selected. Here, the PSF convolution has a much stronger effect on the final profiles, when compared to Figure 3. We indicate the location of the plotted pixel in Figure 2.

Next, we look at the early pre-processing errors, which are introduced by the first three pipeline steps: dark field, flat field and prefilter correction. The next category comprises the polarimetric sensitivity, where we evaluate the errors in the determination of the Stokes vector during the demodulation process and the cross-talk correction. Achieving a good polarimetric sensitivity of the Stokes vector is the most important requirement of SO/PHI. Finally, in the third category, we give a glimpse into the resulting physical parameters, in which we analyse the results of the inversion. These results correspond to the science ready data obtained directly on-board.

4. Analysis

For the analysis, we separate the data into three zones, based on the Stokes vector signal levels: the umbra, the penumbra and the quiet Sun. The regions are defined on the conservative side with preference on excluding pixels from them rather than including pixels that do not clearly belong. We consider > 10000, > 81000, and > 94000 pixels in the three regions, which corresponds to 1%, 7.8% and 90.5% of the full field of view, respectively. We follow this definition in the rest of the paper and mark these regions in the figures.

4.1. Input and First Steps of Pre-processing

The first source of error is the quantisation error of the input data to the pipeline. After calculating them in double precision floating-point, according to the description in Section 3, we transform the data set to the fixed-point representation as the raw data would be stored: detector read-out on 12 bits, accumulated 20 times, and padded with 0-s for the decimals. This corresponds to a maximum range of 20×2^{12}. The RMS of the error resulting from the quantisation, normalised to the image mean intensity, is between 1.55×10^{-7} and 3.5×10^{-7} across the FOV of the 24 images (the six different wavelengths and four polarisation

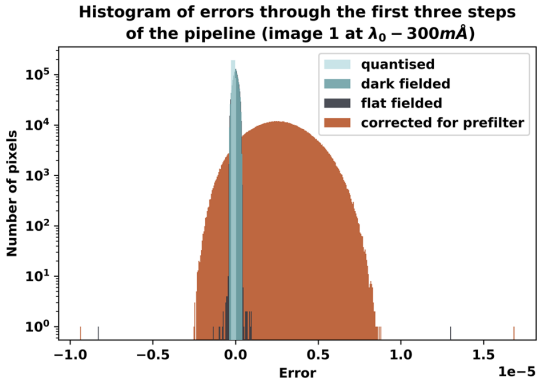

Figure 5 The histogram of errors after data quantisation and the first three steps of the pipeline shows the accuracy achieved after each step, normalised to the mean of the data. The quantisation and dark field subtraction introduces small errors. The errors introduced by the flat field division are very similar to that of the dark field correction, however, a few outliers show up from dust grains in the FOV. The prefilter correction produces a residual of the image with very low intensity due to the inaccuracy at the extrapolation of the prefilter profile to the correct voltage.

states). This is consistent with the $1 \div 2^8$ precision of the decimal in the 24.8 fixed-point representation. The profile of the histogram is flat, as expected for quantisation errors (see Figure 5), with a systematic bias towards smaller numbers in the quantised data due to using bit truncation rather than rounding.

The first steps of pre-processing are: the subtraction of the dark field from the data, the division of the data by the flat field, and the division of the data by the extrapolated prefilter profiles. After the loading of the data, the pipeline scales it up by $2^{23} \div (20 \times 2^{12}) = 102$, which is also followed by the scaling of the dark field. The errors after this step originate from data quantisation both in the input (as described before) and the dark field. The subtraction operation itself does not produce any errors inherently. After this step, we have an error RMS, ranging between 1.55×10^{-7} to 7.7×10^{-7}, normalised to the image mean in the 24 images of the data set. This step slightly changes the profile of the error histogram, removing the bias caused previously by bit truncation (see Figure 5).

The following step, the division by the flat field, divides the data with a max range 2^{23}, i.e., effectively using 24.8 bits, by data with max range 2^3, i.e., effectively using 3.8 bits. The flat field has been normalised to its mean intensity, scaled by 2^3, and we assume its minimum range to be 2^2. Any number below this may cause an overflow, however, there is still some room for smaller values, as the data does not fill up the full detector well at acquisition. After the division, we readjust the magnitude of the result to 2^{23} by multiplying it with 2^2. The errors in this step originate from the errors on the input data (as shown in previous steps), the representation error of the divisor, and the representation errors of the result. In the histogram, a few pixels with larger errors appear due to dust grains in the FOV (which translates to very small numbers in the divisor). However, these errors are only in a handful of pixels, not contributing significantly to the RMS calculated over the full FOV, which ranges between 1.56×10^{-7} and 7.7×10^{-7}, normalised to the image mean intensities.

The next step, the prefilter correction, starts with the interpolation of the prefilter. The pipeline performs this on data scaled to a maximum range of 2^{23}, then scales it down to a maximum range of 2^{10}. Furthermore, we assume a 2^9 minimum range. The interpolation of

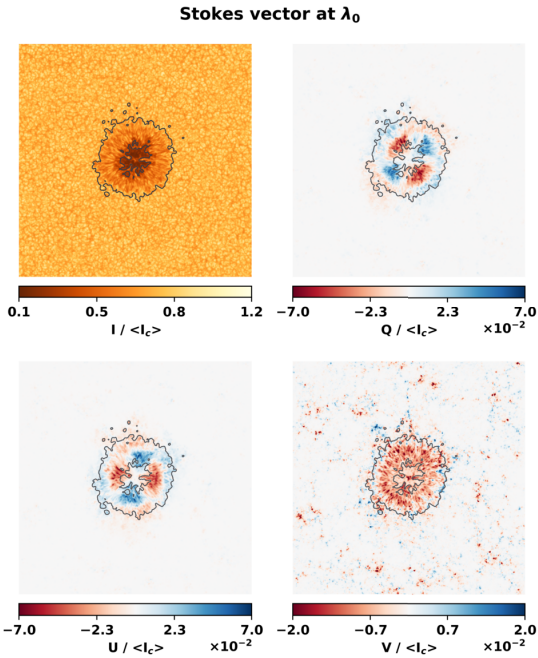

Figure 6 The normalised Stokes vector, $\vec{S}/I_c = (I, Q, U, V)/I_c$, is shown here at the reference wavelength, λ_0 (6173.371 Å), close to the minimum of the absorption line. As expected, Stokes Q/I_c and U/I_c shows the strongest signals in the penumbra. This is also true for V/I_c, which is due to the large splitting of the line in the umbra, causing a poor sampling by SO/PHI. (see Figure 3).

the data creates an error in the divisor compared to what we obtain on ground. Then, through the division, the error histogram widens: when subtracting the results, a very small amplitude residual of the data remains. The histogram profile seen in Figure 5 is the histogram of the test data. After the operation, we scale the result of the division back to 2^{23} by multiplying it with 2^9. The RMS of the error across the FOV ranges between 3.1×10^{-6} and 3.75×10^{-6}, normalised to the mean intensity of the images.

4.2. Polarimetric Errors

The Stokes vector is the output of the polarimetric demodulation of the data. The pipeline is able to do further adjustments with ad-hoc polarimetric cross-talk correction methods. However, for this study, we will limit ourselves to errors due to the demodulation process. We scale the demodulation matrix to the maximum range 2^9, for which we have to account in the input data. In order to avoid overflow, we divide the input data by $2^9 \times 4$, where the number 4 accounts for the addition of the rows in the 4×4 matrix multiplication. The result of the operation is then on a maximum range of 2^{23}. Since the values of the Stokes vector at this point do not have physical meaning, we normalised them to the mean of the quiet Sun intensity, I_c, before showing them in Figure 6. The normalisation here is performed in double precision, to show the results without the error introduced by this step, when performed on-board.

The polarimetric sensitivity requirement set for SO/PHI is 10^{-3}, which is met during the processing: the errors accumulated by the end of this step have an RMS across the FOV between 3×10^{-6} and 4.7×10^{-6} (see Figure 7). This leaves a generous margin to other sources of error and does not compromise the required polarimetric precision.

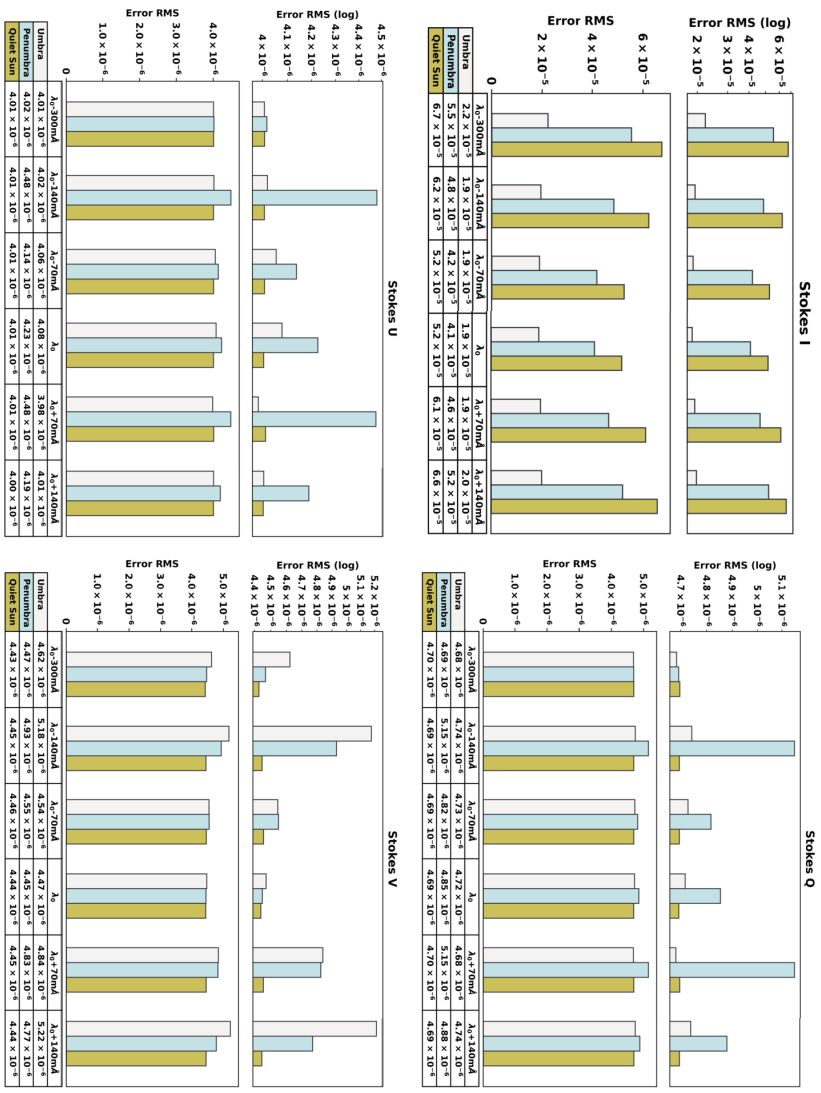

	λ_c-300mA	λ_c-140mA	λ_c-70mA	λ_0	λ_h+70mA	λ_h+140mA
Umbra	2.2×10^{-3}	1.9×10^{-3}	1.9×10^{-3}	1.9×10^{-3}	1.9×10^{-3}	2.0×10^{-3}
Penumbra	5.5×10^{-5}	4.8×10^{-5}	4.2×10^{-5}	4.1×10^{-5}	4.8×10^{-5}	5.2×10^{-5}
Quiet Sun	6.7×10^{-5}	6.2×10^{-5}	5.2×10^{-5}	5.2×10^{-5}	6.1×10^{-5}	6.6×10^{-5}

	λ_c-300mA	λ_c-140mA	λ_c-70mA	λ_0	λ_h+70mA	λ_h+140mA
Umbra	4.01×10^{-6}	4.02×10^{-6}	4.06×10^{-6}	4.08×10^{-6}	3.98×10^{-6}	4.01×10^{-6}
Penumbra	4.02×10^{-6}	4.48×10^{-6}	4.14×10^{-6}	4.23×10^{-6}	4.48×10^{-6}	4.19×10^{-6}
Quiet Sun	4.01×10^{-6}	4.01×10^{-6}	4.01×10^{-6}	4.01×10^{-6}	4.01×10^{-6}	4.00×10^{-6}

	λ_c-300mA	λ_c-140mA	λ_c-70mA	λ_0	λ_h+70mA	λ_h+140mA
Umbra	4.68×10^{-6}	4.74×10^{-6}	4.73×10^{-6}	4.72×10^{-6}	4.68×10^{-6}	4.74×10^{-6}
Penumbra	4.69×10^{-6}	5.15×10^{-6}	4.82×10^{-6}	4.85×10^{-6}	5.15×10^{-6}	4.88×10^{-6}
Quiet Sun	4.70×10^{-6}	4.69×10^{-6}	4.69×10^{-6}	4.69×10^{-6}	4.70×10^{-6}	4.69×10^{-6}

	λ_c-300mA	λ_c-140mA	λ_c-70mA	λ_0	λ_h+70mA	λ_h+140mA
Umbra	4.62×10^{-6}	5.18×10^{-6}	4.54×10^{-6}	4.47×10^{-6}	4.84×10^{-6}	5.22×10^{-6}
Penumbra	4.47×10^{-6}	4.93×10^{-6}	4.55×10^{-6}	4.45×10^{-6}	4.83×10^{-6}	4.77×10^{-6}
Quiet Sun	4.43×10^{-6}	4.45×10^{-6}	4.46×10^{-6}	4.44×10^{-6}	4.45×10^{-6}	4.44×10^{-6}

Figure 7 The RMS of the errors in the Stokes parameters varies between 4.0×10^{-6} and 6.6×10^{-5}, which leaves a good margin to meet the 10^{-3} polarimetric sensitivity requirement of SO/PHI. The errors vary by 6.5×10^{-5} across the Stokes parameters, wavelength, and solar regions, as shown in the table on the bottom. Their relation in linear scale (bottom bars) shows that Stokes Q, U, and V are very close to each other, therefore, to better see their differences, we use a logarithmic scale (top).

The errors across the different Stokes parameters, the different wavelengths, and the different regions of the data (umbra, penumbra, and quiet Sun) differ by a maximum of

1.7×10^{-6}, which is considered negligible. The variation of error is visible for I on a linear scale. However, for Q, U and V we need a logarithmic scale to illustrate the differences. The errors in the result depend on four factors: the errors that were accumulated prior to this step, the magnitude of the input data, the magnitude of the output data, and the terms of the demodulation matrix. These first and second sources oppose each-other: the so far accumulated error correlates linearly with the intensity (due to the image residual after prefilter correction), while the input data is better represented where the values are larger, therefore, it has an inverse correlation. The demodulation matrix has only positive terms in the row producing Stokes I, however, it has negative terms for Q, U, and V, producing cancellation effects.

The trend in errors in Stokes I approximately follows the intensity of the output, with only a slight deviation from this trend along the spectrum (see Figure 7). This is a case where the intensity in the final results dominates the magnitude of the errors. In Stokes Q, U and V the intensity of the result does not overpower the trend any more, and there is a cancellation effect of previous errors due to negative terms in the demodulation matrix. The result of all these values is a trend in errors that is stochastic.

4.3. Physical Parameters

We reach the final physical quantities through the RTE inverter (Cobos Carrascosa et al., 2016). The inversion module can be configured in five different modes, depending on the desired outputs, and on the initial model (apart from special debugging modes). The first three can provide all atmospheric parameters of the Milne-Eddington model (line-to-continuum absorption coefficient ratio, Doppler width, damping coefficient, source function – its slope and its value at the top of the atmosphere, magnetic field vector $\vec{B} = (|\vec{B}|, \gamma, \phi)$, and LOS velocity, v_{LOS}). These modes are: inversion starting with an initial model, called classical estimates, calculated with analytical formulae (centre of gravity technique, see Semel, 1967, and the weak-field approximation, see Landi Degl'Innocenti and Landolfi, 2004), inversion with a configurable initial model, and the classical estimates without being followed by an inversion. Aside from these modes, we have two others which only return line-of-sight (LOS) parameters: the longitudinal mode, where we only obtain LOS velocity and LOS magnetic field, and the no polarisation modulation mode, where we only obtain LOS velocity. We select the modes based on the required science return and available telemetry.

The output parameters of the inversion are also configurable. Thus, we can request only a subset of the full set of output (physical) parameters for a given mode. For the first modes that calculate all nine Milne-Eddington model parameters, in standard operations we only request the four parameters of interest: the three components of the magnetic field vector and the LOS velocity. For the other modes in standard operations, we select all available outputs.

Before we perform the RTE inversion, we must prepare the data to match the interface of the inverter. After demodulation, the data are normalised to I_c (I_c is calculated on ground). The pipeline performs this operation with I_c represented on 12.8 bits (which corresponds to it being calculated on data with maximum range 2^{12}), and scales the result to a maximum range of 2^{23}. We transform these data from fixed to floating point by assuming a 2.30 fixed-point representation. As part of the preparation of the data, the pipeline also rearranges the images to provide the inverter with a data stream that it can process (i.e., all 24 values that the same pixel in the FOV takes in the data set). A similar step takes place after the inversion to form images again.

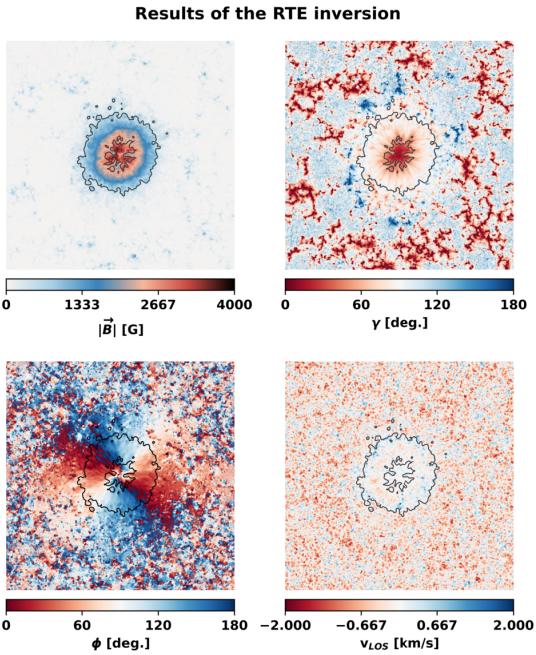

Figure 8 The results of the RTE inversion, shown here, together with the continuum intensity image, form the science ready data that is transferred to ground. The results are consistent with what is expected from such a data set: $|\vec{B}|$, γ and v_{LOS} show smooth transitions between the structures, with magnetic fields up to 4000 G. In v_{LOS} we can see the up and down flows of the solar granulation, as well as of the Evershed flow. ϕ is dominated by noise in the quiet Sun, however, it does show the fan-like structure around the penumbra, as expected.

We use the first mode of the inverter in this study, where we do the full inversion of the data, with initial conditions calculated through classical estimates. See Figure 8 for the results of the RTE inversion. These results show smooth transitions of the values over the FOV in $|\vec{B}|$, γ and v_{LOS}. In $|\vec{B}|$ we obtain magnetic fields up to 4000 G. The upper limit in the inversion module for $|\vec{B}|$ is 5000 G, which is not reached. In v_{LOS} we can see the up- and downflows of the solar granulation, as well as the Evershed flow in the penumbra (see Evershed, 1909). The upper and lower limits of the inversion module for v_{LOS} is $[-20, 20]$ km s^{-1}. In ϕ, the azimuth ambiguity disrupts the smooth transitions and is dominated by noise in the quiet Sun.

The source of the differences that we obtain between the reference pipeline and the SO/PHI processing pipeline is the small variations of the input data due to the processing. However, the stability of inversion on such a data set (considering the physics of the MHD simulation, the spectral and spatial convolutions applied, and the spectral sampling points) also determines the amount of error introduced by these small changes. In case of real SO/PHI observations, we would have an additional contribution from the inaccuracy of the calibration data. This is eliminated in this study by using the same data to degrade and calibrate the synthetic data set. In the following paragraphs, we present the results; we discuss their magnitude and significance in Section 5.

The RMS of the errors in $|\vec{B}|$ introduced by the SO/PHI pipeline vary between 16.9 G to 5.8 G from the quiet Sun to umbra, see Figure 9). Values below 1000 G show a larger disagreement as a consequence of lower signal levels, both in the case of the quiet Sun and the penumbra, showing up as a low-density scatter in Figure 10. We note that pixels with values 1000 G belong to the outer penumbra, reaching the lower limit of typical field strengths in penumbral regions. A few outliers appear also in the umbra, particularly above

	$\vec{B}$ [G]	γ [deg.]	ϕ [deg.]	v_{LOS} [km/s]
Umbra	5.8	1	2	5.50×10^{-3}
Penumbra	7.9	1	2	3.06×10^{-3}
Quiet Sun	16.9	13	38	3.49×10^{-3}

Figure 9 The RMS of the errors in the RTE inversion results primarily reflects the stability of the inversion in the different regions. It shows how the small errors in the input data, introduced through the processing, affect the final results retrieved with the same method. The error in $|\vec{B}|$ and γ is smallest in the penumbra. The determination of γ and ϕ is challenging in the quiet Sun, due to low signal levels, which is also reflected in the error RMS. v_{LOS} in the umbra has higher error due to a shallower line core and more complex profiles. (The magnitude of the errors is discussed in Section 5).

2500 G, hinting at the difficulty in inverting complex line profiles. These profiles, on one hand, are sampled by only six points, on the other hand, they are also significantly changed by the prefilter and spatial PSF convolution (see Figure 3).

The errors in the orientation of the magnetic field vector we present to integer precision. This is due to the fact, that the RTE inversion truncates these values to integer accuracy, therefore any sub-decimal precision differences between the errors in the various regions would be an artefact of this operation. The umbral and penumbral regions show the same accuracy for both the inclination, γ, and the azimuth: ϕ, 1° and 2°, respectively. (see Figure 9). In the quiet Sun, we see an error increase in both angles, a sign of lower signal strength. This results in noisy vector direction, with the correlation plot showing a large scatter across all possible values. The RMS of the errors in the quiet Sun regions is 13° and 38° for γ and ϕ, respectively. In the analysis of ϕ, we assume that any difference between the two results larger than 150° is caused by the ambiguity of the angle, and therefore we change all corresponding pixels to their supplementary angles. This results in the sharp cut at these errors, showing up as empty corners, in the last panel of Figure 10.

v_{LOS} is calculated with the best precision in the penumbra and the quiet Sun, with an error RMS between 3.0-3.5 m s^{-1} (see Figure 9). The increase of the accuracy in the penumbra is due to the stronger velocities in this region. The calculation of v_{LOS} in the umbra produces an error with 5.5 m s^{-1} RMS. These regions with higher magnetic fields produce stronger Zeeman splitting: the spectral profiles widen, become more shallow and complex. Due to our spectral sampling (as seen in Figure 4), the representation of these profiles becomes less accurate, and therefore, the sensitivity of the Stokes vector to the LOS velocity perturbations diminishes, leading to larger errors.

Using the vector magnetic field that we retrieve from the RTE inversion, we also calculate the line of sight magnetic field (B_{LOS}), for further insight. The RMS error of the B_{LOS} is 16.9 G, 7.9 G and 5.8 G for the umbra, penumbra, and quiet Sun, respectively. It shows

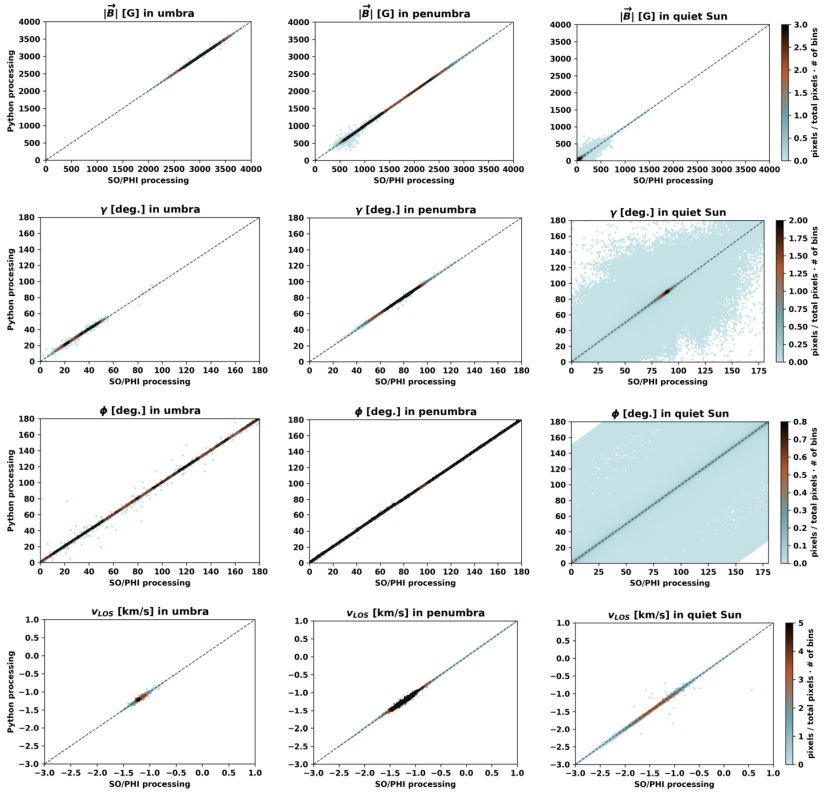

Figure 10 The correlation of the reference and SO/PHI processing results for $|\vec{B}|$, γ, ϕ and v_{LOS}. While the Stokes vector errors are uniformly distributed in these regions (see Figure 7) the scatter of the results varies significantly. This is due to the different stability of the inversion in the different regions, discussed in the main text.

the best agreement in the quiet Sun, significantly better than what $|\vec{B}|$ provided. This is due to the fact that the granules harbour weak transverse fields (see Orozco Suárez and Bellot Rubio, 2012; Danilovic, van Noort, and Rempel, 2016), which translate to small B_{LOS} values, lowering their contribution to the RMS of the error. In contrast, in the umbra and penumbra, we can observe an increase in the error. These regions harbour stronger magnetic fields, which appear at higher angles, all the way to close to vertical in the umbra. Their orientation and strength translates to strong B_{LOS} signals, creating a higher RMS error. We note, that B_{LOS} can also be computed on-board without using an inversion, with analytical formulae (see above), which is a different approach, and these values cannot be applied to it.

5. Discussion and Conclusions

Our accuracy analysis shows that the on-board processing trade-offs do not compromise the accuracy of the SO/PHI data. The comparison between the results of the fully on-board

processed data (with the necessary trade-offs) and the results obtained on-ground (without the trade-offs of the on-board processing) conveys that the errors in the determination of the final Stokes parameters are below 7×10^{-5}. This leaves a good margin for other sources of errors (e.g., calibration errors) to fulfil the 10^{-3} polarimetric sensitivity requirement of SO/PHI.

We present the errors in the physical parameters to give an idea of how the RTE inversion results may change by these processing inaccuracies. However, it is important to remark, that most input data sets intrinsically deviate from Milne-Eddington line profiles, and a tiny error in the input may cause the inversion to converge to a different local minimum, providing large differences in the physical parameters.

In Albert et al. (2019), we have done a similar analysis on a data set acquired by the Helioseismic and Magnetic Imager on-board the Solar Dynamics Observatory (SDO/HMI; Schou et al., 2012), using an earlier version of the SO/PHI data reduction pipeline. In that study, we compared the errors from the processing to a statistical analysis performed with the He-Line Information Extractor inversion code (HeLIx+; see Lagg et al., 2004). The statistical mode of HeLIx+ inverts the data with varying starting conditions, and we regard the variation of the results as a measure of the inaccuracy inherent in the inversion of the data set, amounting to 21.9 G, 1.34°, 1.37°, and 14.5 m s^{-1} for $|\vec{B}|$, γ, ϕ and v_{LOS}, respectively. The errors in the inversion results, introduced to the SDO/HMI data by the on-board processing of SO/PHI (Albert et al., 2019), are 33.64 G, 2.56°, 1.92°, and 19 m s^{-1} for the same parameters, which are slightly higher than what we find in the current study. This is due to the different input data, as well as the earlier version of the processing pipeline. It is important to note, that in the Albert et al. (2019) study we determined the errors in the magnetic field vector limiting the FOV to an area with strong polarisation signals, while for the v_{LOS} we take the full FOV into consideration.

Cobos Carrascosa et al. (2016), while verifying the implementation of the RTE inverter on-board SO/PHI, compared inversions with the C and FPGA implementation of the code for a collection of Milne-Eddington synthetic profiles (considered as ideal input, containing only symmetric profiles). These profiles were sampled with 5 mÅ steps, and selected to range between 0 and 1500 G in $|\vec{B}|$, 0 and 180° in γ and ϕ, and -2 and 2 m s^{-1} for v_{LOS}, to which they added noise with a magnitude of $10^{-3} \times I_c$. The results agree with an error RMS of 5.3 G, 4.86°, 5.77° and 5.9 m s^{-1} for $|\vec{B}|$, γ, ϕ, and v_{LOS}, respectively. However, the same comparison, performed on observations from the Swedish Solar Telescope, results in RMS errors of 69.2 G, 6.5°, 5.47°, and 79.41 m s^{-1}. This is due to several factors, including higher noise, instrumental errors, and asymmetric data profiles, which is typical of observed solar Stokes profiles (see, e.g., Solanki, 1993). The data that we analyse in this paper fall between the two tests in Cobos Carrascosa et al. (2016): we do not introduce additional noise into our data, other than what the pipeline produces (which is in the order of 7×10^{-5}), however, we do have asymmetry in some profiles. We find that the error introduced by the on-board processing pipeline is comparable to the error introduced by the inverter implementation when tested on synthetic data. The differences between the results on the different data sets indicate that the error resulting from the RTE inversion is dominated by the noise level of the data and the input data profiles, which is an inherent property of RTE inversions. This underlines the fact that the accuracy of the pipeline can be judged best by comparing the Stokes parameters instead of the results of the RTE inversion. In order to find a context for the errors of the physical parameters retrieved by the RTE inversion, we must compare them to a very similar data set.

Borrero et al. (2014) compared different Milne-Eddington inversions using data from a sunspot simulation described in Rempel (2012), which is very similar to what we used

in this work. They synthesised two absorption lines (Fe I 630.15 nm and Fe I 630.24 nm) over the whole MHD cube, and did not introduce any noise. The lines were sampled at 100 wavelength steps, 10 mÅ apart. This sampling provides more information than is available in SO/PHI observations, consequently a better reconstruction of the absorption lines is expected. Moreover, the authors cropped the field of view, such that it contains a comparable number of pixels in umbra, penumbra, and solar granulation (more precisely a ~ 200 G plage region surrounding the spot). Using this data set, they found that different Milne-Eddington inversion codes, executed on one input, produce values within an interval of 35 G, 1.2° and 10 m s^{-1} for $|\vec{B}|$, γ, and v_{LOS}, respectively. In this work, we find that the differences in the SO/PHI inversion of on-board and on ground reduced data are smaller than the differences introduced by different inversion codes executed on a single input in Borrero et al. (2014). This means, that the accuracy of the on-board processing is higher than the accuracy of a typical Milne-Eddington inversion. We furthermore note, that Borrero et al. (2014) does not discuss the errors introduced by Milne-Eddington inversions due to simplifications in the physics underlying this model. We expect these to be considerably larger than the numerical uncertainties between different Milne-Eddington codes (see Orozco Suárez et al., 2010; Castellanos Durán, 2022, and references therein).

In conclusion, the SO/PHI pipeline provides the necessary accuracy to process spectropolarimetric data with 10^{-3} polarimetric sensitivity. We show that the data processing pipeline does not compromise the accuracy of the inversion results, since it preserves the confidence interval of the Milne-Eddington RTE inversions. Comparing the results of this study with others shows that the effect of the on-board pipeline errors on the RTE inversion is below the errors produced by the RTE inversion inherently on both simulated and observed data. In this paper, we analyse the errors introduced by the on-board data processing pipeline in comparison to on-ground processing. However, these errors can be regarded as negligible or at least small compared with other sources of error.

Similar processing accuracy can be expected in other on-board data processing pipelines as well (e.g., calculating flat fields or determining polarimetric ad-hoc cross-talk correction terms), since the restrictions and solutions presented here overarch all on-board implementations. This study also shows, that while requiring a significant effort, on-board reduction of solar spectropolarimetric data is a viable option for future instruments, even with stringent limitations in computational resources. It significantly reduces telemetry requirements for SO/PHI (from 24 images, to five at most, in addition to obviating the necessity to download dark and flat fields) and will be particularly valuable for spectropolarimeters on deep-space missions.

Acknowledgments We thank Amanda Romero Avila and Philipp Löschl for their work in synthesising the MHD cube for the input data. This work was carried out in the framework of the International Max Planck Research School (IMPRS) for Solar System Science at the Technical University of Braunschweig and the University of Göttingen. Solar Orbiter is a mission led by the European Space Agency (ESA) with contribution from National Aeronautics and Space Administration (NASA). We use data provided by M. Rempel at the National Center for Atmospheric Research (NCAR). The National Center for Atmospheric Research is sponsored by the National Science Foundation.

Author contributions K.A. did the analysis, wrote the main manuscript text and prepared the figures. J.H., J.S.C.D. and D.O.S. provided advice during the analysis. All authors reviewed the manuscript.

Funding Open Access funding enabled and organized by Projekt DEAL. The SO/PHI instrument is supported by the German Aerospace Center (DLR) through grants 50 OT 1201 and 50 OT 1901. The Spanish contribution is funded by AEI/MCIN/10.13039/501100011033/ (RTI2018-096886-C5, PID2021-125325OB-C5, PCI2022-135009-2) and ERDF "A way of making Europe"; "Center of Excellence Severo Ochoa" awards to IAA-CSIC (SEV-2017-0709, CEX2021-001131-S); and a Ramón y Cajal fellowship awarded to DOS. JSCD was also funded by the Deutscher Akademischer Austauschdienst (DAAD).

Declarations

Competing interests The authors declare no competing interests.

References

Albert, K., Hirzberger, J., Busse, D., Rodríguez, J.B., Castellanos Duran, J.S., Cobos Carrascosa, J.P., et al.: 2019, Performance analysis of the SO/PHI software framework for on-board data reduction. In: *Astronomical Data Analysis Software and Systems XXVIII*, Astronomical Society of the Pacific.

Albert, K., Hirzberger, J., Kolleck, M., Jorge, N.A., Busse, D., Rodríguez, J.B., et al.: 2020, Autonomous on-board data processing and instrument calibration software for the Polarimetric and Helioseismic Imager on-board the Solar Orbiter mission. *J. Astron. Telesc. Instrum. Syst.* **6**, 048004. DOI.

Borrero, J.M., Lites, B.W., Lagg, A., Rezaei, R., Rempel, M.: 2014, Comparison of inversion codes for polarized line formation in MHD simulations–I. Milne-Eddington codes. *Astron. Astrophys.* **572**, A54. DOI.

Castellanos Durán, J.S.: 2022, Strong magnetic fields and unusual flows in sunspots. PhD thesis, University of Göttingen.

Cobos Carrascosa, J.P., Aparicio del Moral, B., Ramos Mas, J.L., Balaguer, M., López Jiménez, A.C., del Toro Iniesta, J.C.: 2016, The RTE inversion on FPGA aboard the solar orbiter PHI instrument. In: Chiozzi, G., Guzman, J.C. (eds.) *Software and Cyberinfrastructure for Astronomy IV*, p. 991342. DOI.

Danilovic, S., van Noort, M., Rempel, M.: 2016, Internetwork magnetic field as revealed by two-dimensional inversions. *Astron. Astrophys.* **593**, A93. DOI.

Dominguez-Tagle, C., Appourchaux, T., Fourmond, J.J., Philippon, A., Le Clec'h, J.-C., Bouzit, M., et al.: 2014, Filtergraph calibration for the Polarimetric and Helioseismic Imager. *Trans. Jpn. Soc. Aeronaut. Space Sci.* **12**, 25. DOI.

Evershed, J.: 1909, Radial movement in sun-spots. *Observatory* **32**, 291.

Frutiger, C., Solanki, S.K., Fligge, M., Bruls, J.H.M.J.: 2000, Properties of the solar granulation obtained from the inversion of low spatial resolution spectra. *Astron. Astrophys.* **358**, 1109.

Lagg, A., Woch, J., Krupp, N., Solanki, S.K.: 2004, Retrieval of the full magnetic vector with the He I multiplet at 1083 nm. Maps of an emerging flux region. *Astron. Astrophys.* **414**, 1109. DOI.

Landi Degl'Innocenti, E., Landolfi, M.: 2004, *Polarization in Spectral Lines* **307**, Kluwer Academic, Dordrecht. DOI.

Lange, T., Fiethe, B., Michel, H., Michalik, H., Albert, K., Hirzberger, J.: 2017, On-board processing using reconfigurable hardware on the solar orbiter PHI instrument. In: *2017 NASA/ESA Conference on Adaptive Hardware and Systems (AHS)*, 186. DOI.

Müller, D., St. Cyr, O.C., Zouganelis, I., Gilbert, H.R., Marsden, R., Nieves-Chinchilla, T., et al.: 2020, The Solar Orbiter mission. Science overview. *Astron. Astrophys.* **642**, A1. DOI.

Orozco Suárez, D., Bellot Rubio, L.R.: 2012, Analysis of quiet-sun internetwork magnetic fields based on linear polarization signals. *Astrophys. J.* **751**(1), 2. DOI. arXiv [astro-ph.SR].

Orozco Suárez, D., Bellot Rubio, L.R., Vögler, A., del Toro Iniesta, J.C.: 2010, Applicability of Milne-Eddington inversions to high spatial resolution observations of the quiet Sun. *Astron. Astrophys.* **518**, A2. DOI.

Rees, D.E., Semel, M.D.: 1979, Line formation in an unresolved magnetic element: a test of the centre of gravity method. *Astron. Astrophys.* **74**(1), 1.

Rempel, M.: 2012, Numerical sunspot models: robustness of photospheric velocity and magnetic field structure. *Astrophys. J.* **750**(1), 62. DOI.

Rempel, M.: 2015, Numerical simulations of sunspot decay: on the penumbra–Evershed flow–moat flow connection. *Astrophys. J.* **814**(2), 125. DOI.

Sanchez Almeida, J., Lites, B.W.: 1992, Observation and interpretation of the asymmetric Stokes Q, U, and V line profiles in sunspots. *Astrophys. J.* **398**, 359. DOI.

Schlichenmaier, R., Collados, M.: 2002, Spectropolarimetry in a sunspot penumbra. Spatial dependence of Stokes asymmetries in Fe I 1564.8 nm. *Astron. Astrophys.* **381**, 668. DOI.
Schou, J., Scherrer, P.H., Bush, R.I., Wachter, R., Couvidat, S., Rabello-Soares, M.C., et al.: 2012, Design and ground calibration of the Helioseismic and Magnetic Imager (HMI) instrument on the Solar Dynamics Observatory (SDO). *Solar Phys.* **275**, 229. DOI.
Semel, M.: 1967, Contribution à létude des champs magnétiques dans les régions actives solaires. *Ann. Astrophys.* **30**, 513.
Solanki, S.K.: 1987, The Photospheric Layers of Solar Magnetic Flux Tubes. PhD thesis, ETH, Zürich.
Solanki, S.K.: 1993, Smallscale solar magnetic fields–an overview. *Space Sci. Rev.* **63**(1–2), 1. DOI.
Solanki, S.K., del Toro Iniesta, J.C., Woch, J., Gandorfer, A., Hirzberger, J., Alvarez-Herrero, A., et al.: 2020, The Polarimetric and Helioseismic Imager on Solar Orbiter. *Astron. Astrophys.* **642**, A11. DOI.

Authors and Affiliations

Kinga Albert[1,2] · Johann Hirzberger[1] · J. Sebastián Castellanos Durán[1,3] · David Orozco Suárez[4] · Joachim Woch[1] · Harald Michalik[5] · Sami K. Solanki[1]

✉ K. Albert
albert@mps.mpg.de

1 Max Planck Institute for Solar System Research, Justus-von-Liebig-Weg, Göttingen, 37077, Germany

2 Technnical University of Braunschweig, Hans-Sommer-Straße, Braunschweig, 3329, Germany

3 Georg-August-Universität Göttingen, Friedrich-Hund-Platz, Göttingen, 37077, Germany

4 Instituto de Astrofísica de Andalucía (IAA–CSIC), Apartado, Granada, 3004, Spain

5 Institute of Computer and Network Engineering at the TU Braunschweig, Hans-Sommer-Straße, Braunschweig, 3329, Germany

F. Observing facular and network contrast from two different points of view

Our publication titled "Intensity contrast of solar network and faculae close to the solar limb, observed from two vantage points" (see Albert et al., 2023b) demonstrates the results of our on-board processing efforts. Using data processed entirely on-board, we combined observations from SO/PHI and SDO/HMI, obtained at an angular separation of approximately 60°, to investigate the intensity contrast of facular and network features near the solar limb. Understanding the intensity variations of these features in relation to their position on the solar disc and the associated magnetic flux measurements is crucial for flux tube physics studies, and plays an important role in solar irradiance calculations. Observing this relationship near the solar limb poses several challenges, which our approach combining observations from two vantage points addressed. We presented this method, showcasing its feasibility. The data used in the analysis was collected during Solar Orbiter's cruise phase. Despite the preliminary nature of the data processing methods at this stage of the mission, the results published in Albert et al., 2023b highlighted that the software design and its implementation fulfils the expectations, and the that the on-board data processing system produces data suitable for scientific studies.

Contributions to the publication: K. Albert combined the observations from SO/PHI and SDO/HMI, conducted the data analysis, and prepared the manuscript.

A&A 678, A163 (2023)
https://doi.org/10.1051/0004-6361/202346037

Astronomy & Astrophysics
Special issue

Solar Orbiter First Results (Nominal Mission Phase)

Intensity contrast of solar network and faculae close to the solar limb, observed from two vantage points

K. Albert[1], N. A. Krivova[1], J. Hirzberger[1], S. K. Solanki[1], A. Moreno Vacas[2], D. Orozco Suárez[2], N. Albelo Jorge[1], T. Appourchaux[3], A. Alvarez-Herrero[4], J. Blanco Rodríguez[5], A. Gandorfer[1], P. Gutierrez-Marques[1], F. Kahil[1], M. Kolleck[1], R. Volkmer[6], J. C. del Toro Iniesta[2], J. Woch[1], B. Fiethe[7], I. Pérez-Grande[9], E. Sanchis Kilders[5], M. Balaguer Jiménez[2], L. R. Bellot Rubio[2], D. Calchetti[1], M. Carmona[8], W. Deutsch[1], A. Feller[1], G. Fernandez-Rico[1,9], A. Fernández-Medina[4], P. García Parejo[4], J. L. Gasent Blesa[5], L. Gizon[1,10], B. Grauf[1], K. Heerlein[1], A. Korpi-Lagg[1], T. Lange[7], A. López Jiménez[2], T. Maue[6,11], R. Meller[1], R. Müller[1], E. Nakai[6], W. Schmidt[6], J. Schou[1], J. Sinjan[1], J. Staub[1], H. Strecker[2], I. Torralbo[9], and G. Valori[1]

(Affiliations can be found after the references)

Received 31 January 2023 / Accepted 3 September 2023

ABSTRACT

Context. The brightness of faculae and network depends on the angle at which they are observed and the magnetic flux density. Close to the limb, the assessment of this relationship has until now been hindered by the increasingly lower signal in magnetograms.

Aims. This preliminary study aims to highlight the potential of using simultaneous observations from different vantage points to better determine the properties of faculae close to the limb.

Methods. We used data from the Solar Orbiter/Polarimetric and Helioseismic Imager (SO/PHI), and the Solar Dynamics Observatory/Helioseismic and Magnetic Imager (SDO/HMI), recorded at an ∼60° angular separation of their lines of sight at the Sun. We used the continuum intensity observed close to the limb by SO/PHI and complemented it with the co-observed $B_{\rm LOS}$ from SDO/HMI, originating closer to disc centre (as seen by SDO/HMI), thus avoiding the degradation of the magnetic field signal near the limb.

Results. We derived the dependence of facular brightness in the continuum on disc position and magnetic flux density from the combined observations of SO/PHI and SDO/HMI. Compared with a single point of view, we were able to obtain contrast values reaching closer to the limb and to lower field strengths. We find the general dependence of the limb distance at which the contrast is maximum on the flux density to be at large in line with single viewpoint observations, in that the higher the flux density is, the closer the turning point lies to the limb. There is a tendency, however, for the maximum to be reached closer to the limb when determined from two vantage points. We note that due to the preliminary nature of this study, these results must be taken with caution.

Conclusions. Our analysis shows that studies involving two viewpoints can significantly improve the detection of faculae near the solar limb and the determination of their brightness contrast relative to the quiet Sun.

Key words. Sun: photosphere – Sun: magnetic fields – Sun: faculae, plages

1. Introduction

The solar photospheric magnetic field is organised into the mainly weak-field low-lying loops forming the internetwork (found predominantly in the quiet Sun), which is almost invisible in white light, and kilogauss strength magnetic flux tubes that manifest themselves as dark sunspots and pores and bright faculae and quiet Sun network (see, e.g. Solanki et al. 2006). The brightness of a given flux tube (also often referred to as a magnetic element) depends on its size and the angle to the observer.

The horizontal pressure balance with the environment leads to an evacuation of the magnetic flux-tube interior, in order to maintain hydrostatic equilibrium in the presence of magnetic pressure. Therefore, for rays roughly parallel to the axis of the flux tube, the observable layer at optical depth $\tau = 1$ lies deeper than the surrounding photosphere. Whereas inside the flux tube the magnetic field inhibits convective energy transport, the walls of the flux tubes appear bright due to heating from the surrounding convection, the so-called hot wall effect (see, e.g. Spruit 1976). The balance between the lateral radiative heating and magnetic suppression of convection within a given flux tube depends on its diameter. Flux tubes tend to be close to solar surface normal due to magnetic buoyancy (see Buehler et al. 2015; Jafarzadeh et al. 2014). Therefore, the position of a flux tube on the observed solar disc determines which part of the flux tube we see, as a consequence of the angle at which we observe it. Going from the disc centre to the limb, the hot walls of the flux tubes rotate into view, before the edge closer to the observer starts to obscure the opposite, observer-facing wall (for extensive discussions, see Solanki 1993; Carlsson et al. 2004; Keller et al. 2004).

The small-scale flux tubes forming faculae and the magnetic network are typically not resolved by full-disc magnetographs, while the kilogauss flux tubes in the internetwork have so far only been resolved in exceptional cases, for example by Lagg et al. (2010) who used The Imaging Magnetograph Experiment magnetograph on the Sunrise balloon-borne solar observatory (e.g. Solanki et al. 2010; Barthol et al. 2011; Martínez Pillet et al. 2011). Thus, the size of faculae and

network elements is difficult to assess. Instead, the magnetic flux density within the resolution element (pixel) is often used to describe the fraction of the solar surface covered by strong fields (often referred to as the magnetic filling factor). The intrinsic field strength of the flux tubes forming a network and faculae is roughly unchanged, and their average size increases with the magnetic flux density. Therefore, it is also an indirect measure of the size of the magnetic features.

Determining the relationship between facular and network brightness and the magnetic flux density as well as the distance of the faculae from the solar limb is important for our understanding and modelling of the radiant properties and thermal structure of faculae and the magnetic elements of which they are composed. This also provides a classic constraint to magnetohydrodynamic simulations (see Beeck et al. 2015) and is relevant for studying and modelling the variations of solar irradiance at timescales of days to millennia, which is driven by the intensity excess created by faculae and the intensity deficit resulting from sunspots (see Krivova et al. 2003; Solanki et al. 2013; Shapiro et al. 2017; Yeo et al. 2017, 2020). In this study, we treat the facular and network features without differentiation, and refer to them as faculae collectively (Solanki & Stenflo 1984). Criscuoli et al. (2017) and Buehler et al. (2019) show benefits of treating them separately (see also Foukal et al. 2011), and this would be interesting to address in a future study building on the current one.

Numerous studies examined the intensity contrast of faculae (i.e. their intensity relative to that of the internetwork) in relation to their magnetic flux density (see Kobel et al. 2011; Kahil et al. 2019, and references therein), as well as their distance from the disc centre (see Ortiz et al. 2002; Yeo et al. 2013). For the magnetic flux density, most studies used the line-of-sight (LOS) magnetic field ($B_{\rm LOS}$) observations, which is by far the most reliable of the magnetic components obtained from data utilising the Zeeman effect.

However, analysis of the facular contrast becomes complicated and very uncertain close to the solar limb for multiple reasons. Firstly, foreshortening effects become critical. Thus, since most of the observed magnetic field is nearly vertical, the $B_{\rm LOS}$ component becomes weak close to the limb leading to a low signal-to-noise ratio, which is further reduced due to lower light levels (limb darkening). In addition, the spatial resolution of observations is reduced, when approaching the limb, with each pixel representing an increasingly larger surface area on the Sun due to foreshortening. Within a pixel with larger coverage, the contribution of a given spatially unresolved magnetic element to the magnetogram signal and to the contrast of that pixel is smaller. Furthermore, the chances of opposite-polarity flux cancellation within such pixels are higher, resulting in lower magnetic flux density measurements.

Secondly, the μ value of the observation influences the observed height: closer to the limb, the absorption line in which the measurements are taken forms higher in the atmosphere than close to the disc centre (see Schou et al. 2023, for a discussion). Whereas this change in observation height is part of what we aim to observe in the intensity, it is an undesired effect in the case of $B_{\rm LOS}$ measurements, which are different to those carried out closer to the disc centre, distorting any comparisons between the two.

Thirdly, the incident polarised radiation from the Sun also depends on the angle of the observation, owing to the properties of the Zeeman effect. Due to radiative transfer effects and the finite width and geometry of solar magnetic features, the Stokes V amplitude need not scale linearly with μ (see Solanki et al. 1998). These additional effects include, but are not limited to, the following: (1) changes in the width and strength (including potential saturation) of the spectral line as a consequence of the lower temperature and increased turbulent velocities sensed by the line towards the limb; (2) possible changes in the Zeeman saturation of the Stokes V profile due to changes in field strength as a consequence of a greater formation height of the line and the larger inclination of the field relative to the LOS; and (3) the passage of individual rays through both magnetised and unmagnetised gas, etc.

Fourthly, the identification and isolation of facular features is also more challenging close to the limb because the apparent extension of the magnetic canopy of sunspots increases towards the limb (Giovanelli & Jones 1982; Solanki et al. 1994). As the canopy contributes significantly to Stokes V, it can be mistaken for a facular contribution (see Yeo et al. 2013; Ball et al. 2012).

Because of these restrictions, studies of the contrast of bright magnetic features are typically curtailed near the solar limb. For example, Yeo et al. (2013) studied the facular intensity contrast as a function of distance from the disc centre (in terms of the cosine of the heliocentric angle, denoted as $\cos\theta = \mu$) and the measured magnetic flux density, normalised by μ ($B_{\rm LOS}/\mu$), using data from the Helioseismic and Magnetic Imager on board the Solar Dynamics Observatory (SDO/HMI, see Schou et al. 2012). (The normalisation by μ corrects for the geometrical effects to first order under the assumption that the field is vertical to the local solar surface). Due to the factors discussed above, weak network features ($B_{\rm LOS}/\mu < 50\,{\rm G}$) could not be identified in the magnetograms near the limb ($\mu \leq 0.4$), so that the centre-to-limb variation (CLV) of facular intensity contrast in this regime remains unclear.

These restrictions could be overcome (or at least their severity reduced) if, in addition to a magnetograph on the ground, or in Earth's orbit, a second such instrument observing the Sun from a different viewpoint were available. The Solar Orbiter mission (Müller et al. 2020) brings this new perspective to solar observations: it reaches a wide range of positions outside the Sun-Earth line and it carries the Solar Orbiter/Polarimetric and Helioseismic Imager (SO/PHI; Solanki et al. 2020), the first solar magnetograph to provide data with significant angular separations from Earth. A combined analysis of simultaneous observations by SO/PHI and on-ground or Earth orbiting instruments presents an opportunity to examine the Sun from two perspectives simultaneously. In particular, this allows the uncertain $B_{\rm LOS}$ measurements at the limb to be substituted with more certain ones, inferred from observations closer to the disc centre, hence improving on earlier studies of facular contrast.

In this study, we present such an effort. To highlight the potential of such multi-angle studies to better constrain the dependence of facular brightness on the measured magnetic flux density and the distance to the limb, we combined simultaneous observations from SO/PHI and SDO/HMI (Schou et al. 2012). We stress that we do not aim to provide final results. Instead, this study demonstrates that such a combination of viewpoints can indeed improve our knowledge of facular contrast, in particular close to the solar limb.

The paper is structured as follows. We present our method in Sects. 2 and 3 by first detailing the observations from SO/PHI and SDO/HMI and their processing, and then by describing how we combined the two vantage points. In Sect. 4, we explain how we derived the relationship of the facular contrast to μ and $B_{\rm LOS}/\mu$ from the combined data obtained by the two instruments, and from SO/PHI's perspective alone; we then provide a discussion. In Sect. 5 we summarise our findings and discuss how the obtained results can be improved and extended in the future.

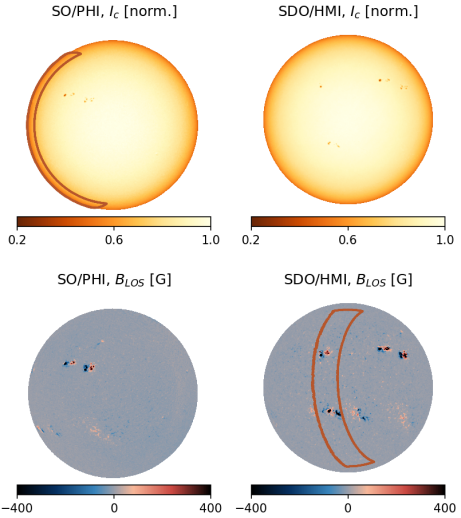

Fig. 1. Co-observations of the two instruments. We show I_c (upper row) and B_{LOS} (lower row) observed by SO/PHI full disc telescope (FDT, left column) and SDO/HMI (right column), on 6 September 2021. The two instruments observed the Sun with 59.45° angular separation. The brick-red outlines on the panels show the regions that we combined for the analysis: I_c from SO/PHI and B_{LOS} from SDO/HMI within the overlap region of the two instruments, with $0.1 < \mu_{SO/PHI} < 0.4$ and $\mu_{SDO/HMI} > 0.4$.

2. Data and their processing

2.1. Data

The SO/PHI (Solanki et al. 2020) is an imaging spectropolarimeter, sampling the photospheric Fe I 617.3 nm absorption line. It has two telescopes: the Full Disc Telescope (FDT) and the High Resolution Telescope (HRT, see Gandorfer et al. 2018). As their names suggest, the FDT covers the full solar disc at all phases of the spacecraft's orbit (with a pixel plate scale 3.75″), while the HRT only images a fraction of it (pixel plate scale 0.50″). The SO/PHI measures the full Stokes vector (I, Q, U and V) at six wavelength positions: five inside the spectral line, and one in the nearby continuum. From these, through the Zeeman and Doppler effects, the vector magnetic field ($\boldsymbol{B}$) and the LOS velocity (v_{LOS}) can be determined at the average formation height of the spectral line. In addition, the continuum intensity is also returned. In this study, we use data products obtained in the longitudinal mode of the SO/PHI instrument. This is a simplified mode, which is applied on board to reduce processing time and telemetry volume (see Albert et al. 2020). It provides the continuum intensity (I_c), and B_{LOS} (instead of $\boldsymbol{B}$), calculated with analytical formulae via the centre-of-gravity technique (Semel 1967; Rees & Semel 1979; Landi Degl'Innocenti & Landolfi 2004). These results are referred to as classical estimates. The measurement duration for a full data set is approximately 33 s.

The SDO/HMI observes the same absorption line, using the same principle. Some relevant differences between the instruments are the pixel plate scale (0.505″ for SDO/HMI), the sampling wavelengths of the line (SDO/HMI's six wavelength samples are uniformly spaced and centred over the line, sometimes resulting in the continuum not being directly sampled), and while it provides similar data products, it uses somewhat different techniques to derive them. Here we use the 720 s data products: the reconstruction of continuum intensity, and the LOS magnetogram (`hmi.M_720s`; calculated with the MDI-like algorithm, see Couvidat et al. 2016).

We use 10 pairs of SO/PHI–SDO/HMI observations, recorded during the cruise phase of SO, one from each day in the period 1 to 10 September 2021. The SO/PHI data used in the study is of the full solar disc, recorded with the FDT. During the observations, the angular separation of the two instruments changed from 67° to 52°, while SO's distance to the Sun varied from 0.58 AU to 0.60 AU. The SO/PHI-FDT at these distances observes the Sun with a radius of 440 to 453 pixels. The SO/PHI data have been fully reduced on board the spacecraft, including the calibration and the determination of B_{LOS} (for details of the onboard processing see Albert et al. 2020). Due to the early phase of the mission, and the novelty of the onboard data processing, the calibration data and processes applied during the reduction of these data sets are preliminary.

Since we are mainly interested in extending earlier studies of facular contrast to locations closer to the solar limb, we analyse areas that appear at $0.1 < \mu < 0.4$ in SO/PHI data, and at $\mu > 0.4$ in SDO/HMI data. As an example, Fig. 1 shows I_c and B_{LOS} from co-observations of SO/PHI and SDO/HMI on 6 September 2021. The regions that we analyse lie within the brick-red contours: the I_c at the limb from SO/PHI, and the corresponding area in the SDO/HMI B_{LOS} at large μ values. We remark that combining the data the other way around, that is taking I_c from SDO/HMI (from the limb), and complementing them with B_{LOS} from SO/PHI (closer to disc centre) would also be possible. However, such a combination is expected to be less accurate, as we have higher noise levels in the SO/PHI magnetograms (due to e.g. the lower amount of temporal averaging).

2.2. Attuning the observations

To prepare the SDO/HMI data products for combination with SO/PHI data, we convolve them with the point spread function (PSF) of the SO/PHI-FDT. As results of more accurate studies were not yet available, we used a theoretical PSF: the Airy disc of the telescope. This assumes a perfect telescope, only limited by the diffraction of light. To arrive at the effective PSF, we adjust this to the difference in distance to the Sun of the two instruments. Due to the large difference in aperture size (140 mm in SDO/HMI vs. 17.5 mm in SO/PHI-FDT) which is not nearly compensated by the difference in distance to the Sun (1 AU for SDO/HMI and 0.6 AU for SO/PHI), we consider the SDO/HMI PSF to be negligible relative to that of SO/PHI. More accurate PSF estimates, available now (see Bailén et al. 2023; Kahil et al. 2023), will be used in subsequent studies.

Next, we resample the SDO/HMI data to match the spatial sampling of the SO/PHI-FDT observations (i.e. we bin the SDO/HMI data by a non-integer factor). We achieve this in the Fourier domain. We crop the convolved data (conserving the lower frequency regions) to a dimension which after the inverse

transform will provide the same solar radius in pixels as we observe in the corresponding SO/PHI data set.

For our analysis, the $B_{\rm LOS}$ values come exclusively from SDO/HMI observations (degraded and resampled to mimic SO/PHI), while the intensity contrast values are exclusively from SO/PHI. Thus, in principle, we do not need to worry about the magnetic and continuum intensity cross-calibration of the two instruments. However, the cross-calibration might have an effect on the comparison of the results obtained from combining the two viewpoints with those obtained from SO/PHI only, and can therefore affect our results presented in Fig. 5 (see Sect. 4). We see a good continuity of the results, and therefore believe that for the scope of this pre-study we can use data that have not been cross-calibrated. Efforts to cross-calibrate SDO/HMI and SO/PHI-FDT data products are underway (Vacas 2022, priv. comm.), and should be used by future studies.

2.3. Identification of faculae

We identify faculae or network, sunspots or pores, and internetwork following the method described by Yeo et al. (2013; for a discussion on the effects of identification methods, see Centrone & Ermolli 2003). This is done for both instruments individually. In the case of SDO/HMI, we use the PSF-degraded and resampled data. Faculae or network are identified in the magnetograms by their elevated $B_{\rm LOS}$ levels, while sunspots or pores are identified in the $I_{\rm c}$ images by lower intensity levels. Finally, parts of the Sun that do not qualify to be either network, faculae, sunspot, or pore are counted as internetwork.

We first detect pixels with magnetic signals sufficiently above the noise level of the $B_{\rm LOS}$ maps:

$$B_{\rm LOS}(x,y) > 3\sigma_{B_{\rm LOS}}(x,y), \tag{1}$$

where x and y are detector plane coordinates, $B_{\rm LOS}$ is the measured LOS magnetic field, and $\sigma_{B_{\rm LOS}}$ is the standard deviation of $B_{\rm LOS}$, a measure of the noise in $B_{\rm LOS}$.

We determined $\sigma_{B_{\rm LOS}}$ following the method described by Ortiz et al. (2002) and Yeo et al. (2013). This method includes two steps: (1) a computation of the CLV of the noise, and (2) a computation of the deviations from the obtained noise CLV profile. Thus, we first calculated the standard deviation, σ, of the magnetogram signal over concentric rings of pixels at similar distances from the disc centre and removed outliers, outside 3σ, iteratively, until convergence. We also fitted a polynomial to the standard deviation versus distance profiles, thus establishing the CLV noise profiles. Afterwards, we used a moving window to determine any deviations from the CLV noise profile, and fitted a polynomial surface to the result. We note, that if a window contains mostly active region pixels, the standard deviation within it is higher than for a quiet Sun region. Therefore, our noise levels should rather be considered as an upper limit. We prefer this conservative approach, where we may miss some facular pixels, over the potential inclusion of some noise in the analysis.

When we apply this method to the 720 s SDO/HMI magnetograms at their original resolution, our approach returns the noise level 4 to 7 G. This is close to the values of 4.7 to 7.8 G reported by Liu et al. (2012). We note that the SDO/HMI team used more accurate methods to determine the noise level than we do. After changes in the processing of the 720 s magnetograms in 2016, these values are expected to be somewhat lower (Liu 2022, priv. comm.). Through analysing internetwork pixels, Korpi-Lagg et al. (2022) found ∼5.5 G noise levels prior to 2016, and ∼4.75 G afterwards.

For the resampled SDO/HMI magnetograms, we find the noise level in the range from 3.5 to 5.2 G. The downsampling of the data by nearly a factor of four, that is averaging over ∼16 pixels, does not reduce the noise level by a factor of four. This reduction would be expected if the photon noise were the only noise source, however, that is not the case for the 720 s HMI LOS magnetograms (see Liu et al. 2012). Moreover, at the resulting resolution, while quiet Sun weak magnetic fields are visible, they are wrongly classified as noise. This again leads to a conservative pixel classification, as we potentially exclude some pixels from the analysis which harbour network magnetic fields.

In the case of the SO/PHI magnetograms, the variation of the noise level over the field of view does not show a clear CLV. Instead, it is dominated by a large-scale gradient across the field of view, the origin of which is still under investigation. This indicates that also for SO/PHI, the noise level is not driven by photon noise only. In the absence of a clear CLV of the noise profile for the SO/PHI magnetograms, we calculate the noise directly with the moving window. This yields noise levels ranging from 7.1 G to 10.4 G, which is higher than what we find in the resampled SDO/HMI data.

Next, we identified the pixels that belong to sunspots or pores based on $I_{\rm c}$. To achieve this, we first calculated the CLV of the quiet Sun at the continuum wavelength following the method described by Neckel & Labs (1994). We then found the large-scale deviations of the quiet Sun $I_{\rm c}$ from the CLV, which we consider to be a residual of the flat field correction, following Yeo et al. (2013). The SO/PHI $I_{\rm c}$ observations are subject to a ghost image, which is a faint (∼0.5% of the intensity) duplicate image of the Sun overlaid on the solar disc with a small spatial offset. Therefore, we first mitigated the effect of this ghost image on the sensor, and then determined the residuals on the result.

We normalised $I_{\rm c}$ by its CLV and the flat field residuals:

$$I_{\rm c,norm}(x,y,t) = \frac{I_{\rm c}(x,y,t)}{{\rm CLV}_{I_{\rm c}}(x,y) R_{I_{\rm c}}(x,y)}, \tag{2}$$

where t is time (which refers to one of the 10 considered data sets), $I_{\rm c,norm}$ denotes the normalised $I_{\rm c}$, ${\rm CLV}_{I_{\rm c}}$ denotes the centre to limb variation of the quiet Sun intensity, and $R_{I_{\rm c}}$ marks residuals of the flat field correction, present in the $I_{\rm c}$ data.

To obtain an intensity threshold for identifying sunspots, we again followed Yeo et al. (2013). For the 10 data sets, we derived the quiet Sun $I_{\rm c,norm}$ standard deviation, which we denote $\sigma_{I_{\rm c},{\rm QS}}$. The threshold separating sunspots from the internetwork ($I_{\rm c,threshold}$) was set, conservatively, at the mean of the minimum value of $I_{\rm c,norm}(x,y,t) - 3\sigma_{I_{\rm c},{\rm QS}}(x,y,t)$ for each of the 10 days. The $I_{\rm c,threshold}$ is 0.965 in SO/PHI, and 0.975 in SDO/HMI. We consider all pixels below these values to belong to sunspots or pores.

As a final step in our pixel segmentation, we found all isolated pixels identified as faculae based on the previous criteria. We considered these to be false positives, and therefore treated them as internetwork fields.

Figure 2 shows the distribution of the pixels of interest derived from the magnetograms of both instruments. The top panels show $B_{\rm LOS}/\mu$ at various μ values, while the bottom panels show $I_{\rm c}$. The SO/PHI $I_{\rm c}$ (bottom left panel) shows a weak downward trend when approaching the limb, indicating a bias in the normalisation of $I_{\rm c}$. This is a result of imprecision in determining the radius of the Sun in the images, mainly due to two factors: low spatial resolution, and the as yet uncorrected distortion of the SO/PHI-FDT. In SO/PHI magnetograms, where the region was close to the limb, we find 853 facular pixels, which is

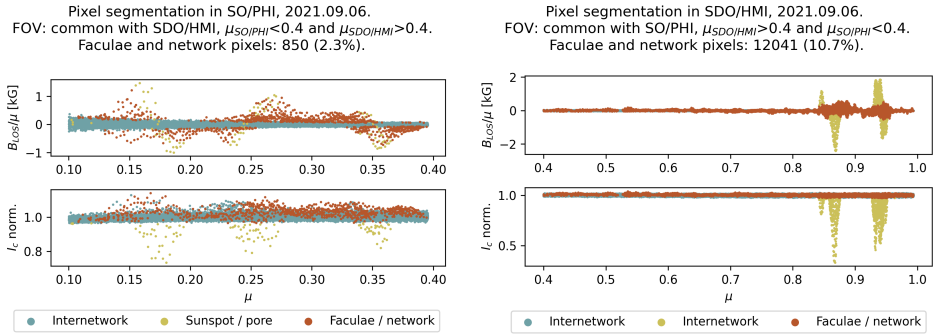

Fig. 2. Classification of pixels within the common area of interest in both instruments. We show pixels from the region $0.1 < \mu_{\mathrm{SO/PHI}} \leq 0.4$ and $\mu_{\mathrm{SDO/HMI}} > 0.4$, and their distribution with μ from images recorded on 6 September 2021. In this field of view, we identify 2.2% of the SO/PHI pixels (close to limb) and 6.2% of SDO/HMI pixels (closer to disc centre) as faculae.

2.2% of all pixels in this area. In the resampled SDO/HMI data, where the region appeared closer to the disc centre, we identify 12 041 pixels as faculae, that is 10.7% of all pixels in this area. The difference in the fraction of pixels identified as faculae is due to the combined effect of three factors. (1) The noise level in the SDO/HMI data is lower than that in SO/PHI. (2) The signal-to-noise ratio of the B_{LOS} measured close to the disc centre is higher than that measured closer to the limb. (3) Due to the foreshortening effect, pixels close to the limb represent a larger surface area on the Sun, which leads to more averaging and thus more potential cancellation of oppositely signed magnetic flux (in SO/PHI data) as compared to pixels recorded closer to the disc centre (HMI data).

The produced maps that mark the locations of the facular pixels were then used for our analysis (see Sect. 4).

2.4. Definition of the intensity contrast

Following Yeo et al. (2013), we calculate the continuum intensity contrast of the facular pixels. We define C_{I_c}, as:

$$C_{I_c}(x, y, t) = I_{\mathrm{c,norm}}(x, y, t) - 1, \tag{3}$$

where $I_{\mathrm{c,norm}}(x, y, t)$ is defined in Sect. 2.3.

3. Combining the two vantage points

Our goal here is to assign to each I_{c} pixel measured by SO/PHI at the limb the corresponding B_{LOS}/μ value measured by SDO/HMI closer to the disc centre. The close-to-centre SDO/HMI measurements are a 'super-sampled' version of what SO/PHI measured close to limb: due to foreshortening, several pixels at a large μ value combine into a single one at the limb (i.e. the spatial coverage of the pixels increases). Thus, to assign the SO/PHI limb pixels with the B_{LOS}/μ values measured by SDO/HMI, we first need to cross-match the pixels in the observations by the two instruments, that is, we have to find which B_{LOS}/μ pixels in SDO/HMI correspond to the I_{c} pixels measured by SO/PHI. To do this co-alignment, we re-projected the SDO/HMI B_{LOS}/μ data to the coordinate system of SO/PHI, using the SunPy (see SunPy Community 2020) implementation of the method described in DeForest (2004). This method uses a Hanning window to weigh the input pixels in the footprint of each output pixel, reducing aliasing effects, and producing values close to the mean. Thereby, the mean of B_{LOS}/μ over the input pixels is (roughly) preserved in the output pixel. We additionally correct for the time difference in the data acquisition of the two instruments and the difference in the light travel time, by considering the differential rotation of the Sun (method from Howard et al. 1990, also implemented in SunPy).

To improve data alignment and correct for any shift originating from small inaccuracies in our knowledge of the observing geometry (described in World Coordinate System, coordinates, see Thompson 2006), we derive and apply a preliminary distortion model to the re-projected data. This distortion model is based on the pixel to pixel local correlation of the B_{LOS}/μ by SO/PHI and the re-projected measurements of it by SDO/HMI in the overlapping area. From the cross-correlation values, we derive a map giving the correct position of each pixel. Such an empirical method is susceptible to errors due to noise. Therefore, to minimise these errors, we fitted a second order polynomial surface to the resulting map. We apply the derived distortion model to the SDO/HMI data after re-projecting it, instead of correcting the distortion in the SO/PHI measurements. This decision was taken here to preserve the intensity contrast observed at the limb, as methods readily available to correct the SO/PHI data, based on interpolations, lower it. To illustrate the quality of the data alignment, Fig. A.1 shows an example of a co-aligned SO/PHI and SDO/HMI region together with cross-sections of B_{LOS}/μ through the region.

We also re-project the facular map found in the SDO/HMI magnetogram close to the disc centre (see Sect. 2.3) with the method used for B_{LOS}/μ, to SO/PHI's coordinate system, and align the result with the distortion model described above. This re-projected SDO/HMI-based facular map consists of pixels that have varying amount of contribution from pixels identified as facular in the original SDO/HMI data (before re-projection). In order to make sure that we analyse pixels that behave as faculae (i.e. the facular contribution is not insignificant compared to the internetwork contribution), we set a threshold based on B_{LOS}/μ. We included in our analysis only those re-projected pixels that have the resulting B_{LOS}/μ above the 3σ noise level of the SO/PHI-FDT (in line with the identification process of faculae that we used earlier, see Eq. (1)). This is a conservative threshold, and we might miss some faculae that could be considered,

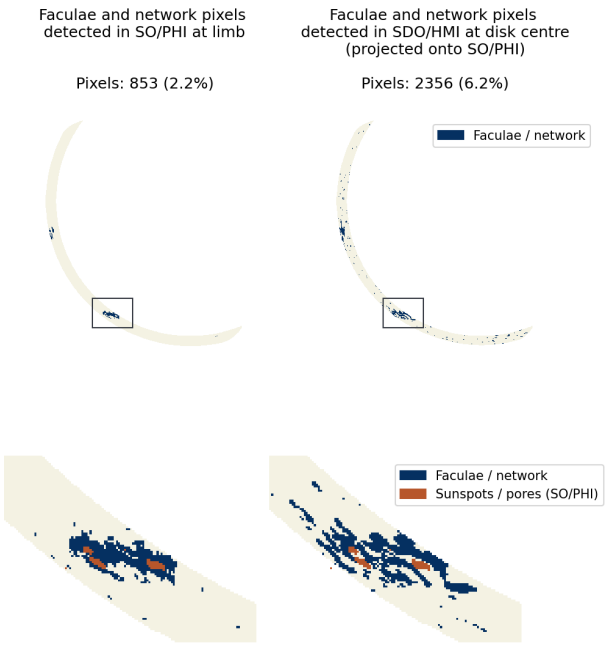

Fig. 3. Faculae map identified in SO/PHI (left) and in SDO/HMI, re-projected to the coordinate system of SO/PHI (right). The upper row shows the area analysed in the study, the lower row shows a magnification of the area marked by the black rectangle on the top. In the magnified view, we also show the area that was identified as sunspot in the SO/PHI observations. We indicate the number of pixels identified as faculae in each figure (853 in SO/PHI, and 2356 in SDO/HMI, representing 2.2% and 6.2% of the pixels in this area, respectively). The data shown here are from 6 September 2021.

however for this study we prioritise the avoidance of false positives over the inclusion of all facular pixels. At the same time, we can now consider even stand-alone pixels as correct identification, as they were observed in several SDO/HMI pixels close to the disc centre. Furthermore, we exclude any pixels that have contributions from sunspots or pores, as the measured intensity would be strongly affected by these features. The resulting facular map shows significantly more facular pixels near the limb than the SO/PHI-FDT magnetogram. Figure 3 compares the faculae maps obtained at the limb using SO/PHI data and at large μ from SDO/HMI data, projected in the figure onto SO/PHI's coordinates. The 12 041 facular pixels, identified close to the disc centre in the resampled SDO/HMI magnetograms (from Fig. 2), convert into 2356 pixels at the limb. The facular features at the limb, found through the re-projection of the SDO/HMI facular map, represent 6.2% of all the pixels in this region, compared to 2.2% for those obtained directly from the SO/PHI limb data. This increase in the percentage of pixels identified close to limb with the data from disc centre indicates that many faculae with small flux density have been systematically missed at the limb in previous studies. However, the re-projection of the SDO/HMI facular map shows fewer faculae in the close surroundings of sunspots. This has to do with the extended magnetic canopies of sunspots. In the near-limb SO/PHI observations, the magnetic canopy of the sunspot appears particularly extended (particularly in $B_{\rm LOS}$), leading to sunspots being surrounded by pixels displaying a high magnetic flux density. These pixels are falsely identified as faculae in the SO/PHI facular map, whereas in the SDO/HMI facular maps the same region is located at high μ, and the canopies produce at most a very weak $B_{\rm LOS}$ signal close to the sunspot, which is not mistaken for faculae.

By inferring the $B_{\rm LOS}$ at low μ values from the re-projection of the same areas measured at a higher μ, we reduce the uncertainty in the $B_{\rm LOS}$ values measured close to the limb. We circumvent the problems arising at the limb, including the diminishing LOS component, lower light levels, increasing pixel coverage, changes in the formation height of the line, the radiative transfer effects, and the apparently extended sunspot canopy affecting faculae identification.

Our analysis involves a number of assumptions and approximations. Firstly, in our re-projection, we approximated the solar surface as a plane, ignoring any obstructions that occur in our line of sight due to the undulated solar surface. This could lead to cases where we identify faculae close to the disc centre, which are, however, obstructed by solar granulation closer to the limb. Such possible pixels would exhibit the intensity (and magnetic field) of internetwork at the limb, and, therefore, could bias the analysis towards lower contrast levels. Secondly, we considered the studied flux tubes to be vertical with respect to the solar surface, and therefore assumed that a normalisation by μ accounts for the foreshortening. Thirdly, we assumed that the different wavelength sampling of the spectral line, the somewhat different data reduction codes used to retrieve the $B_{\rm LOS}$, and the different observation time (over 720 s for SDO/HMI, and 33 s for SO/PHI) provide equivalent results. All of these assumptions might have an effect on our results and should be considered further in future studies.

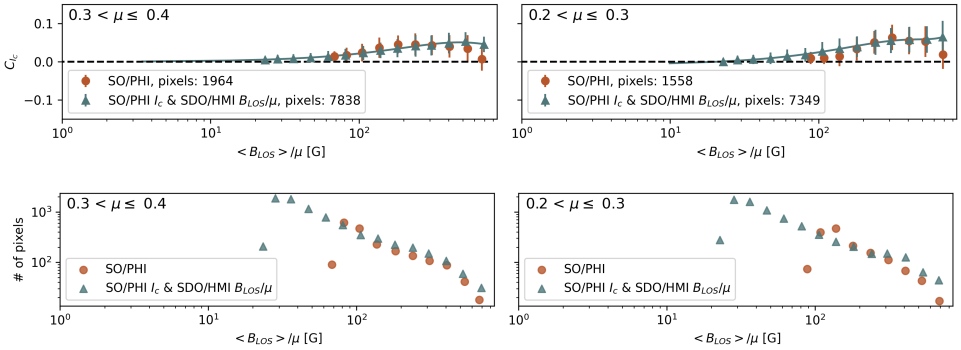

Fig. 4. Facular contrast as a function of $B_{\rm LOS}/\mu$, and the number of pixels in each bin. Top: we computed the contrast curves using the combined SO/PHI and SDO/HMI data as well as the SO/PHI data alone in two μ intervals ($0.1 < \mu \leq 0.3$, right column, and $0.3 < \mu \leq 0.4$, left column). We split the data into equal intervals of $\log(B_{\rm LOS}/\mu)$. The error bars represent the standard deviation of the pixels within each bin. We fitted a third order curve to the combined data points (continuous green line). Bottom: based on the number of pixels in each bin, we exclude from the plots SO/PHI-based data with $\mu < 0.2$.

4. Results and discussion

The intensity contrast depends on both the location of the feature on the disc and the magnetic field strength averaged over the pixel. To disentangle the dependence of C_{I_c} on each of these two factors, we consider individual μ and $B_{\rm LOS}/\mu$ intervals following Ortiz et al. (2002).

First, we consider the dependence on $B_{\rm LOS}/\mu$. We first split all data into two μ intervals ($0.1 < \mu \leq 0.3$ and $0.3 < \mu \leq 0.4$) and look at the dependence of the contrast on $B_{\rm LOS}/\mu$ in each of them. In each interval, we bin the data into 14 equal intervals of $\log(B_{\rm LOS}/\mu)$, and compute the bin-averaged C_{I_c} (see Fig. 4). The standard deviation within the bins is shown in the figure as error bars. The two curves show the intensity contrast derived exclusively from SO/PHI data (brick-red markers), and from the combined measurements (i.e. C_{I_c} from SO/PHI and $B_{\rm LOS}$ from SDO/HMI re-projected to the coordinate system of SO/PHI, as described in Sect. 3, shown in pine-green symbols). We show data with $\mu > 0.1$ for the combined measurements, and with $\mu > 0.2$ for SO/PHI-only data. The restriction to $\mu > 0.2$ for these data is due to the low signal-to-noise ratio in the SO/PHI magnetograms at $\mu \leq 0.2$. We plot the number of data points entering each $\langle B_{\rm LOS}\rangle$ bin, separately, in the bottom panels. When using the SO/PHI data alone, the weakest regions we could detect at $\mu < 0.4$ were those with roughly $B_{\rm LOS}/\mu \approx 80$–$90$ G. By using the combined data, we could extend our analysis to regions as weak as $B_{\rm LOS}/\mu \approx 20$ G.

Earlier studies found that, in regions not extremely near to the limb, the contrast of facular features initially increases with $B_{\rm LOS}/\mu$, then usually decreases again at yet higher $B_{\rm LOS}/\mu$ values (see e.g. Ortiz et al. 2002; Yeo et al. 2013). Although the error-bars are rather high, we see a similar tendency in the top-left panel of Fig. 4, too. At the same time, closer to the limb, the contrast of faculae keeps increasing with increasing magnetic flux density (see the top-right panel), also in agreement with previous studies. This behaviour is due to the fact that for larger facular features (or pores) produced by stronger magnetic fields, we see increasingly more of the darker central part of the flux tube when approaching the disc centre, similarly to sunspots. Near the limb, we see more of the hot walls, so that all features are bright.

Similarly, we then split all the data into six $B_{\rm LOS}/\mu$ intervals and derive the dependence of the contrast on μ within each of these individual ranges (see Fig. 5). Our results suggest that studies involving two vantage points (such as this one) have the largest impact on pertaining to faculae with lower flux density. Therefore, we choose smaller intervals for the lower $B_{\rm LOS}/\mu$ range, and group a larger range into one interval for the higher flux densities. Another driver of this choice are the few magnetograms used in this study, which mean that there are relatively few pixels showing large flux densities. Within each interval, we created bins that are $\Delta\mu = 0.05$ wide and calculate the mean intensity contrast in each (for reference, the widest pixel in the analysed area covers $0.02\,\mu$). Again, by combining data from two viewpoints (in pine-green), we significantly extend the μ range beyond what was possible with data from a single perspective (in brick-red), especially at low $B_{\rm LOS}/\mu$.

The determination of the distance from disc centre, where the facular contrast is highest ($\mu_{\rm max}$), has been a long-standing debate in facular studies (see Solanki 1993). To determine the $\mu_{\rm max}$ in our contrast curves, we fitted a third order polynomial to the bins calculated from the combined SO/PHI and SDO/HMI observations at $\mu \leq 0.4$, and from SO/PHI only data at $\mu > 0.4$ (see Fig. 5). We calculated $\mu_{\rm max}$ based on the obtained fit, and compare our values to those reported in earlier studies by Ortiz et al. (2002) and Yeo et al. (2013) in Table 1. We find the trends in $\mu_{\rm max}$ with changing $B_{\rm LOS}/\mu$ to be similar to what earlier studies observed, which is the increase of $\mu_{\rm max}$ with decreasing magnetic flux density. However, we do not observe the inversion of this trend for the weakest flux densities. Our $\mu_{\rm max}$ values are also on average somewhat lower than those found by Ortiz et al. (2002) and Yeo et al. (2013). We must consider, however, that the resolution of our data is lower than of that used in the compared studies. Another difference to these studies is the $B_{\rm LOS}/\mu$ intervals in which we derive $\mu_{\rm max}$. We note, however, that repeating the analysis for the intervals used by Yeo et al. (2013) and Ortiz et al. (2002), yielded no significant difference in the results.

Our extension of the observed μ range for low $B_{\rm LOS}/\mu$ values compared to the SO/PHI-only contrast curves indicates that combining two vantage points leads to more accurate $\mu_{\rm max}$ in

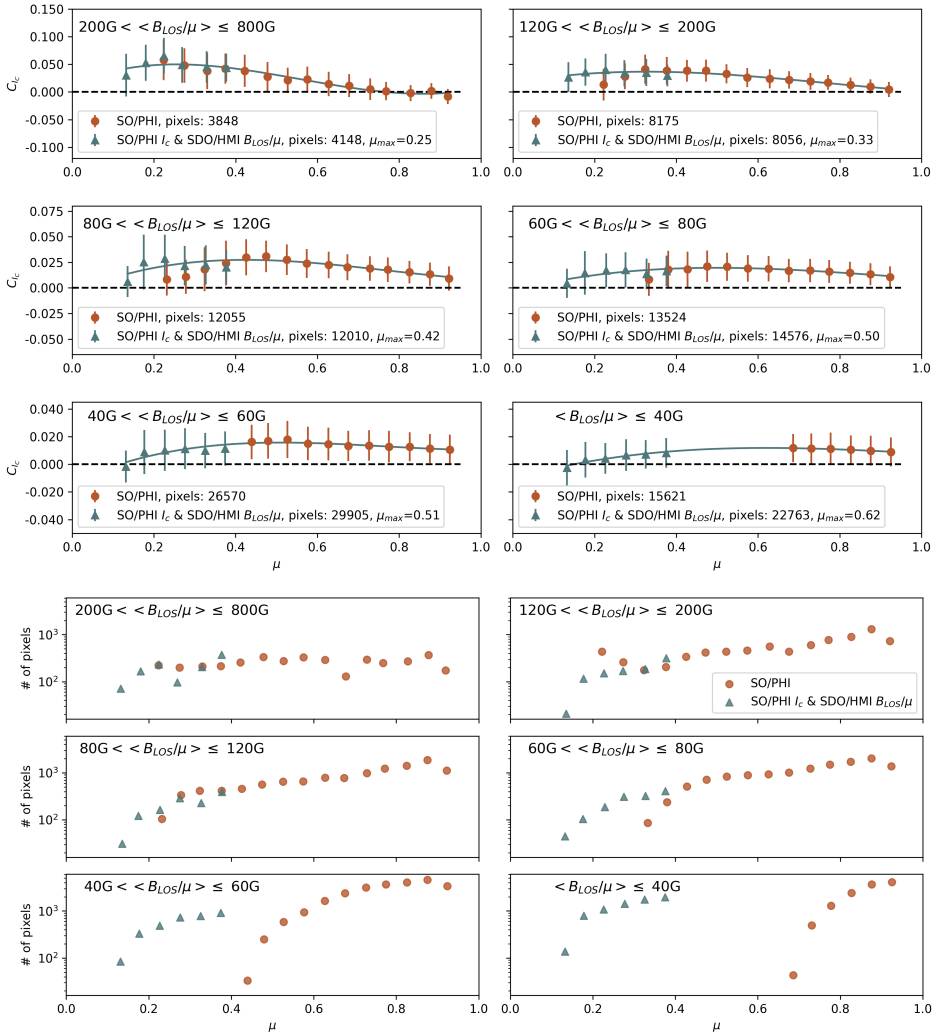

Fig. 5. Same as Fig. 4, but now showing facular contrast vs. μ. The data are displayed in six intervals of $B_{\rm LOS}/\mu$, and in bins of $\Delta\mu = 0.05$. The third order fit here is done through the combined points, extended with the points derived from SO/PHI only data where $\mu > 0.4$.

such regions than enabled by single viewpoint observations. To this end, however, more and higher spatial resolution data are needed to be analysed than what is considered in the present study. Due to the large error bars in our results, which are the consequence of the provisional nature of the data, their low resolution, the low statistics (only ten days of observations), and possible biases related to the normalisation of the I_c as a consequence of the low resolution and distortion, our results must be considered preliminary.

5. Conclusions and outlook

One of the unprecedented opportunities offered by Solar Orbiter is that by co-observing together with other spacecraft in Earth's orbit, we have the possibility to observe the properties of a given region on the solar surface from two different vantage points. In this work, we use co-observations of SDO/HMI and SO/PHI, with an approximately 60° angle between their LOS, to study the dependence of facular brightness on the magnetic field strength

Table 1. Values of μ_{max} calculated for various B_{LOS}/μ ranges in this work, compared to what Yeo et al. (2013) and Ortiz et al. (2002) find.

B_{LOS}/μ [G]	This study	Yeo et al. (2013)	Ortiz et al. (2002)
<40	0.62		
<50		0.38	0.50
40–60	0.51		
50–80			0.55
60–80	0.50		
50–100		0.45	
80–120	0.42		0.50
100–180		0.45	
120–200	0.33		0.49
180–280		0.40	
200–300			0.42
280–380		0.38	
300–400			0.42
380–500		0.36	
400–500			0.35
200–800	0.25		
500–600			0.22
500–640		0.33	
640–800		0.29	

and μ close to the solar limb. Earlier such studies faced the problem of strongly reduced magnetogram signals when measuring the LOS component of the magnetic field close to the limb. This is because of two main effects. Firstly, most of the field emerging in facular and network regions is roughly aligned with the solar surface normal, so that towards the limb its LOS component becomes increasingly weak, eventually falling below the instrumental noise level. Secondly, due to the reduced spatial resolution at the limb produced by foreshortening, the in-pixel averaging and cancellation effects of the measured flux density become more important. The combination of these effects, together with others (e.g. increased noise near the limb and the apparent extension of the magnetic canopy of sunspots), make it harder to detect faculae via their magnetic signature near the solar limb. Therefore, to measure the continuum intensity contrast in facular regions close to the limb, we combined SO/PHI continuum intensity measured close to the solar limb with the magnetic field co-observed by SDO/HMI closer to the disc centre. Based on these data, we derived curves that describe the intensity contrast of facular pixels in relation to their position on the solar disc (expressed in μ) and to their magnetic flux density (observed as B_{LOS}, and normalised to μ to counteract geometrical effects).

The preliminary results presented here highlight the potential of combining data from different angles. In particular, such a combined approach allows for more reliable B_{LOS}/μ measurements for areas with $0.1 < \mu \leq 0.4$. As a consequence, we could identify and analyse faculae near the limb with significantly lower B_{LOS}/μ values than what is possible from a single vantage point (e.g. that of SO/PHI), and thus extend the facular contrast curves to lower B_{LOS}/μ and μ values. This allowed us to include in our analysis the μ ranges where the maximum of the contrast curves occurs (μ_{max}, i.e. the position of the turning point of the curves, where the contrast changes its trend from increasing towards the limb to decreasing) even for low B_{LOS}/μ values.

Our results mostly confirm the trend of μ_{max} observed by Yeo et al. (2013) and Ortiz et al. (2002), in that, apart from the lowest flux densities, μ_{max} increases with decreasing B_{LOS}/μ. For these ranges we find that μ_{max} might lie closer to the limb than observations from a single point of view (e.g. that of SO/PHI, or of SDO/HMI, see Yeo et al. 2013; Ortiz et al. 2002) indicate. However, the same studies also observed an inversion of this trend around $B_{LOS}/\mu \approx 50$ G, which we cannot confirm.

Studies historically disagree on μ_{max} (see, e.g. Solanki 1993) due to several factors, including (but not limited to), the resolution of the observations, the method of identification of facular features (see Centrone & Ermolli 2003), and the systematic exclusion of features that could not be clearly identified as faculae (see Auffret & Muller 1991). The μ_{max} values computed by us still have significant uncertainties, as our study is preliminary and can be improved in multiple aspects listed below. However, the presented results suggest that analysing more and higher resolution data from two vantage points can lead to a more certain determination of μ_{max} than is possible from a single view point.

To consolidate the results presented here, different aspects of the present study need to be improved.

1. One obvious task is to extend the investigation using combined data also beyond $\mu = 0.4$, for example to close the gap in data points between $\mu = 0.4$ and 0.8 seen in Fig. 5 for $\langle B_{LOS}/\mu \rangle \leq 40$ G. This is straightforward with an increasing amount of available data, although it should be noted that the advantage of combining two vantage points decreases with increasing μ.
2. Also, improving the statistics by including more data from SO/PHI would make the results more robust. Fortunately, Solar Orbiter is still in a relatively early phase of its science mission, holding the promise of many more observation campaigns from various angles between the spacecraft, the Sun, and Earth. Therefore, we expect to significantly improve the statistics compared with the present paper.
3. SO/PHI data with higher resolution would be of great value to overcome the problem of the large pixels and the poor resolution of magnetic features (not just close to the limb). This can be achieved either by employing data acquired at smaller distances from the Sun with the SO/PHI-FDT (which also provides an opportunity for a direct study on the effect of changing the plate scale), or by using data from the SO/PHI-HRT, which will allow one to observe at an even higher resolution than SDO/HMI, especially when close to perihelion. Such data (from both SO/PHI telescopes) will be particularly valuable after deconvolution of the PSF (determined using phase diversity, see Kahil et al. 2023; Bailén et al. 2023). For the impact of PSF reconstruction on facular studies with SDO/HMI, readers can refer to Yeo et al. (2014) and Criscuoli et al. (2017).
4. The SO/PHI data employed here have been reduced on board preliminarily. The use of data reduced with improved methods is imperative. The data reduction methods of SO/PHI have already been refined beyond what was available at the time of the processing of the data for this study, and they are being continuously improved further.

These improvements will be implemented in future studies.

Acknowledgements. We thank the referee for their insightful comments, that helped us to improve the paper. We are grateful to Kok Leng Yeo for her strong support and contribution to the work presented here. We thank Yang Liu for his support in investigating the SDO/HMI data products. This work has been carried out in the framework of the International Max Planck Research School (IMPRS) for Solar System Science at the Technical University of Braunschweig. Solar Orbiter is a space mission of international collaboration between ESA and NASA, operated by ESA. We are grateful to the ESA SOC and MOC teams for their support. The German contribution to SO/PHI is funded by the BMWi through DLR and by MPG central funds.

The Spanish contribution is funded by AEI/MCIN/10.13039/501100011033/ and European Union "NextGenerationEU/PRTR" (RTI2018-096886-C5, PID2021-125325OB-C5, PCI2022-135009-2, PCI2022-135029-2) and ERDF "A way of making Europe"; "Center of Excellence Severo Ochoa" awards to IAA-CSIC (SEV-2017-0709, CEX2021-001131-S); and a Ramón y Cajal fellowship awarded to DOS. The French contribution is funded by CNES. The SDO/HMI data are courtesy of NASA/SDO and the HMI Science Team.

References

Albert, K., Hirzberger, J., Kolleck, M., et al. 2020, J. Astron. Telesc. Instrum. Syst., 6, 048004
Auffret, H., & Muller, R. 1991, A&A, 246, 264
Bailén, F., Orozco Suárez, D., Blanco Rodríguez, J., et al. 2023, A&A, submitted
Ball, W. T., Unruh, Y. C., Krivova, N. A., et al. 2012, A&A, 541, A27
Barthol, P., Gandorfer, A., Solanki, S. K., et al. 2011, Sol. Phys., 268, 1
Beeck, B., Schüssler, M., Cameron, R. H., & Reiners, A. 2015, A&A, 581, A42
Buehler, D., Lagg, A., Solanki, S. K., & van Noort, M. 2015, A&A, 576, A27
Buehler, D., Lagg, A., van Noort, M., & Solanki, S. K. 2019, A&A, 630, A86
Carlsson, M., Stein, R. F., Nordlund, Å., & Scharmer, G. B. 2004, ApJ, 610, L137
Centrone, M., & Ermolli, I. 2003, Mem. Soc. Astron. It., 74, 671
Couvidat, S., Schou, J., Hoeksema, J. T., et al. 2016, Sol. Phys., 291, 1887
Criscuoli, S., Norton, A., & Whitney, T. 2017, ApJ, 847, 93
DeForest, C. E. 2004, Sol. Phys., 219, 3
Foukal, P., Ortiz, A., & Schnerr, R. 2011, ApJ, 733, L38
Gandorfer, A., Grauf, B., Staub, J., et al. 2018, in Space Telescopes and Instrumentation 2018: Optical, Infrared, and Millimeter Wave, eds. M. Lystrup, H. A. MacEwen, G. G. Fazio, et al., SPIE Conf. Ser., 10698, 106984N
Giovanelli, R. G., & Jones, H. P. 1982, Sol. Phys., 79, 267
Howard, R. F., Harvey, J. W., & Forgach, S. 1990, Sol. Phys., 130, 295
Jafarzadeh, S., Solanki, S. K., Lagg, A., et al. 2014, A&A, 569, A105
Kahil, F., Riethmüller, T. L., & Solanki, S. K. 2019, A&A, 621, A78
Kahil, F., Gandorfer, A., Hirzberger, J., et al. 2023, A&A, 675, A61 (SO Nominal Mission Phase SI)
Keller, C. U., Schüssler, M., Vögler, A., & Zakharov, V. 2004, ApJ, 607, L59
Kobel, P., Solanki, S. K., & Borrero, J. M. 2011, A&A, 531, A112
Korpi-Lagg, M. J., Korpi-Lagg, A., Olspert, N., & Truong, H. L. 2022, A&A, 665, A141
Krivova, N. A., Solanki, S. K., Fligge, M., & Unruh, Y. C. 2003, A&A, 399, L1
Lagg, A., Solanki, S. K., Riethmüller, T. L., et al. 2010, ApJ, 723, L164
Landi Degl'Innocenti, E., & Landolfi, M. 2004, Polarization in Spectral Lines (Springer), 307
Liu, Y., Hoeksema, J. T., Scherrer, P. H., et al. 2012, Sol. Phys., 279, 295
Martínez Pillet, V., del Toro Iniesta, J. C., Álvarez-Herrero, A., et al. 2011, Sol. Phys., 268, 57
Müller, D., St. Cyr, O. C., Zouganelis, I., et al. 2020, A&A, 642, A1
Neckel, H., & Labs, D. 1994, Sol. Phys., 153, 91
Ortiz, A., Solanki, S. K., Domingo, V., Fligge, M., & Sanahuja, B. 2002, A&A, 388, 1036
Rees, D. E., & Semel, M. D. 1979, A&A, 74, 1
Schou, J., Scherrer, P. H., Bush, R. I., et al. 2012, Sol. Phys., 275, 229
Schou, J., Hirzberger, J., Orozco Suárez, D., et al. 2023, A&A, 673, A84 (SO Nominal Mission Phase SI)
Semel, M. 1967, Ann. Astrophys., 30, 513
Shapiro, A. I., Solanki, S. K., Krivova, N. A., et al. 2017, Nat. Astron., 1, 612
Solanki, S. K. 1993, Space Sci. Rev., 63, 1
Solanki, S. K., & Stenflo, J. O. 1984, A&A, 140, 185
Solanki, S. K., Montavon, C. A. P., & Livingston, W. 1994, A&A, 283, 221
Solanki, S. K., Steiner, O., Buente, M., Murphy, G., & Ploner, S. R. O. 1998, A&A, 333, 721
Solanki, S. K., Inhester, B., & Schüssler, M. 2006, Rep. Progr. Phys., 69, 563
Solanki, S. K., Barthol, P., Danilovic, S., et al. 2010, ApJ, 723, L127
Solanki, S. K., Krivova, N. A., & Haigh, J. D. 2013, ARA&A, 51, 311
Solanki, S. K., del Toro Iniesta, J. C., Woch, J., et al. 2020, A&A, 642, A11
Spruit, H. C. 1976, Sol. Phys., 50, 269
SunPy Community (Barnes, W. T., et al.) 2020, ApJ, 890, 68
Thompson, W. T. 2006, A&A, 449, 791
Yeo, K. L., Solanki, S. K., & Krivova, N. A. 2013, A&A, 550, A95
Yeo, K. L., Feller, A., Solanki, S. K., et al. 2014, A&A, 561, A22
Yeo, K. L., Solanki, S. K., Norris, C. M., et al. 2017, Phys. Rev. Lett., 119, 139902
Yeo, K. L., Solanki, S. K., Krivova, N. A., et al. 2020, Geophys. Res. Lett., 47, e2020GL090243

[1] Max-Planck-Institut für Sonnensystemforschung, Justus-von-Liebig-Weg 3, 37077 Göttingen, Germany
e-mail: albert@mps.mpg.de; solanki@mps.mpg.de
[2] Instituto de Astrofísica de Andalucía (IAA-CSIC), Apartado de Correos 3004, 18080 Granada, Spain
e-mail: jti@iaa.es
[3] Univ. Paris-Sud, Institut d'Astrophysique Spatiale, UMR 8617, CNRS, Bâtiment 121, 91405 Orsay Cedex, France
[4] Instituto Nacional de Técnica Aeroespacial, Carretera de Ajalvir, km 4, 28850 Torrejón de Ardoz, Spain
[5] Universitat de València, Catedrático José Beltrán 2, 46980 Paterna-Valencia, Spain
[6] Leibniz-Institut für Sonnenphysik, Schöneckstr. 6, 79104 Freiburg, Germany
[7] Institut für Datentechnik und Kommunikationsnetze der TU Braunschweig, Hans-Sommer-Str. 66, 38106 Braunschweig, Germany
[8] University of Barcelona, Department of Electronics, Carrer de Martí i Franquès, 1 – 11, 08028 Barcelona, Spain
[9] Instituto Universitario "Ignacio da Riva", Universidad Politécnica de Madrid, IDR/UPM, Plaza Cardenal Cisneros 3, 28040 Madrid, Spain
[10] Institut für Astrophysik, Georg-August-Universität Göttingen, Friedrich-Hund-Platz 1, 37077 Göttingen, Germany
[11] Fraunhofer Institute for High-Speed Dynamics, Ernst-Mach-Institut, EMI, Ernst-Zermelo-Str. 4, 79104 Freiburg, Germany

Appendix A: Re-projection of SDO/HMI data onto SO/PHI's coordinate system

Figure A.1 shows $B_{\rm LOS}/\mu$ over a selected part of the disc in both SO/PHI and SDO/HMI data, to illustrate the quality of the data alignment of magnetic features selected from the solar scene. The SDO/HMI data has been re-projected from the disc centre (where it was observed) to the coordinate system of SO/PHI, and aligned through local correlation of $B_{\rm LOS}/\mu$, as described in Sect. 3. In the right panels, we show $B_{\rm LOS}/\mu$ along cross-sections marked by the corresponding lines on the maps (panels on the left). We note, that verifying the alignment is not straightforward due to the difference in the observation angle, as well as the smaller pixel size and lower noise levels in the re-projected SDO/HMI observations.

Misalignment of the pixels would lead to assigning internetwork or sunspot/pore $I_{\rm c}$ pixels to facular $B_{\rm LOS}/\mu$ pixels. This would change the derived facular intensity contrast (by decreasing it and by shifting the curves in μ or $B_{\rm LOS}/\mu$), as well as increase the standard deviation of the bins, shown in Figs. 4 and 5. Based on inspection of different areas, as shown in Fig. A.1, we consider it unlikely that the misalignment of pixels is a major source of error in the contrast curves. However, a more robust distortion model allowing a more reliable alignment would certainly be of benefit for subsequent studies.

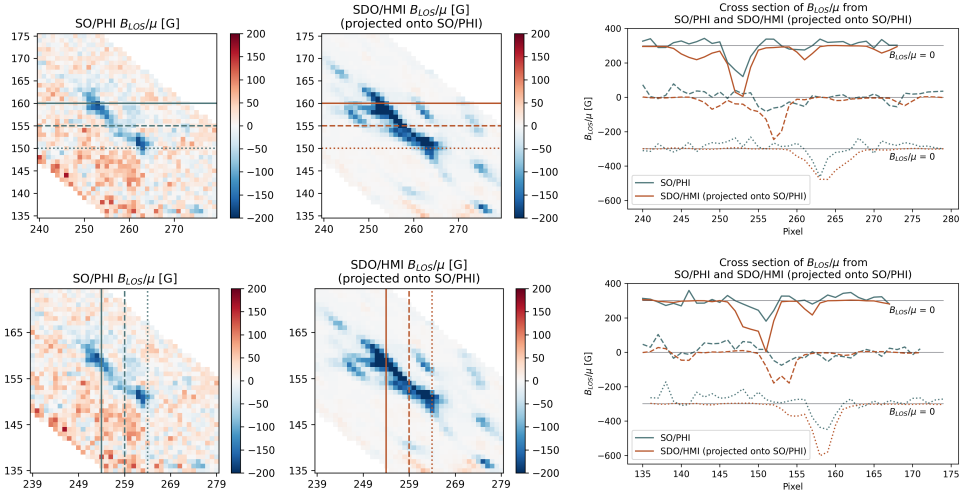

Fig. A.1. Detailed view (left column) of $B_{\rm LOS}/\mu$ for a selected area in SO/PHI data at the limb and in SDO/HMI close to disc centre, after re-projection to the limb. The right column shows examples of $B_{\rm LOS}/\mu$ along cross-sections marked by the lines in the maps on the left. In the right panels, the different curves are offset by 300 G in ordinate for better visibility (the respective 0 G is marked by the horizontal lines).

Research dissemination

List of publications

First authored

- **K. Albert**, N. A. Krivova, J. Hirzberger, S. K. Solanki, A. Moreno Vacas, D. Orozco Suárez, N. Albelo Jorge, T. Appourchaux, A. Alvarez-Herrero, J. Blanco Rodríguez, A. Gandorfer, P. Gutierrez-Marques, F. Kahil, M. Kolleck, R. Volkmer, J.C. del Toro Iniesta, J. Woch, B. Fiethe, I. Pérez-Grande, E. Sanchis Kilders, M. Balaguer Jiménez, L. R. Bellot Rubio, D. Calchetti, M. Carmona, A. Feller, G. Fernandez-Rico, A. Fernández-Medina, P. García Parejo , J.L. Gasent Blesa, L. Gizon, B. Grauf, K. Heerlein, A. Korpi-Lagg, T. Lange, A. López Jiménez, T. Maue, R. Meller, R. Müller, E. Nakai, W. Schmidt, J. Schou, J. Sinjan, J. Staub, H. Strecker, I. Torralbo, G. Valori. "Intensity contrast of solar network and faculae close to the solar limb, observed from two vantage points", *Astronomy and Astrophysics*, 678 (2023) A163; https://doi.org/10.1051/0004-6361/202346037;
- **K. Albert**, J. Hirzberger, J. S. Castellanos Durán, D. Orozco Suárez, J. Woch, H. Michalik, S. K. Solanki. "Accuracy Analysis of the Onboard Data Reduction Pipeline for the Polarimetric and Helioseismic Imager on the Solar Orbiter Mission", *Solar Physics*, 298, 58 (2023); https://doi.org/10.1007/s11207-023-02149-y;
- **K. Albert**, J. Hirzberger, M. Kolleck, N. Albelo Jorge, D. Busse, J. Blanco Rodríguez, J. P. Cobos Carrascosa, B. Fiethe, A. Gandorfer, D. Germerott, Y. Guan, L. Guerrero, P. Gutierrez-Marques, D. Hernández Expósito, T. Lange, H. Michalik, D. Orozco Suárez, J. Schou, S. K. Solanki, J. C. del Toro Iniesta, J. Woch. "Autonomous on-board data processing and instrument calibration software for the Polarimetric and Helioseismic Imager on-board the Solar Orbiter mission", I 6(4) 048004 (18 December 2020); https://doi.org/10.1117/1.JATIS.6.4.048004;
- **K. Albert**, J. Hirzberger, D. Busse, J. S. Castellanos Durán, M. Kolleck. "Metadata and Their Importance in SO/PHI's On–Board Data Processing", *Astronomical Society of the Pacific Conference Series*, 527, Astronomical Data Analysis Software and Systems XXIX, 2019;
- **K. Albert**, J. Hirzberger, D. Busse, J. Blanco Rodríguez, J. S. Castellanos Durán, J. P. Cobos Carrascosa, B. Fiethe, A. Gandorfer, Y. Guan, M.

Kolleck, A. Lagg, T. Lange, H. Michalik, S. K. Solanki, J. C. del Toro Iniesta, and J. Woch. "Performance analysis of the SO/PHI software framework for on-board data reduction", *Astronomical Society of the Pacific Conference Series*, 523, Astronomical Data Analysis Software and Systems XXVIII, 2018;

- **K. Albert**, J. Hirzberger, D. Busse, T. Lange, M. Kolleck, B. Fiethe, D. Orozco Suárez, J. Woch, J. Schou, J. Blanco Rodríguez, A. Gandorfer, Y. Guan, J. P. Cobos Carrascosa, D. Hernández Expósito, J. C. del Toro Iniesta, S. K. Solanki, H. Michalik. "Autonomous on-board data processing and instrument calibration software for the SO/PHI", *SPIE Conference Proceedings*, 10707, Software and Cyberinfrastructure for Astronomy V, 107070O (6 July 2018); https://doi.org/10.1117/12.2311718.

Co-authored

- J. Sinjan, D. Calchetti, J. Hirzberger, F. Kahil, G. Valori, S. K. Solanki, **K. Albert**, N. Albelo Jorge, A. Alvarez-Herrero, T. Appourchaux, L. R. Bellot Rubio, J. Blanco Rodríguez, A. Feller, A. Gandorfer, D. Germerott, L. Gizon, J. M. Gómez Cama, L. Guerrero, P. Gutierrez-Marques, M. Kolleck, A. Korpi-Lagg, H. Michalik, A. Moreno Vacas, D. Orozco Suárez, I. Pérez-Grande, E. Sanchis Kilders, M. Balaguer Jiménez, J. Schou, U. Schühle, J. Staub, H. Strecker, J. C. del Toro Iniesta, R. Volkmer and J. Woch. "Magnetic fields inferred by Solar Orbiter: A comparison between SO/PHI-HRT and SDO/HMI", *Astronomy and Astrophysics*, 673 (2023) A31; https://doi.org/10.1051/0004-6361/202245830;
- J. Schou, J. Hirzberger, D. Orozco Suárez, **K. Albert**, N. Albelo Jorge, T. Appourchaux, A. Alvarez-Herrero, J. Blanco Rodríguez, A. Gandorfer, D. Germerott, L. Guerrero, P. Gutierrez-Marques, F. Kahil, M. Kolleck, S. K. Solanki, J. C. del Toro Iniesta, R. Volkmer, J. Woch, B. Fiethe, I. Pérez-Grande, E. Sanchis Kilders, M. Balaguer Jiménez, L. R. Bellot Rubio, D. Calchetti, M. Carmona, W. Deutsch, A. Feller, G. Fernandez-Rico, A. Fernández-Medina, P. García Parejo, J. L. Gasent Blesa, L. Gizon, B. Grauf, K. Heerlein, A. Korpi-Lagg, A. López Jiménez, T. Maue, R. Meller, A. Moreno Vacas, R. Müller, E. Nakai, W. Schmidt, J. Sinjan, J. Staub, H. Strecker, I. Torralbo and G. Valori. "The ratio of horizontal to vertical displacement in solar oscillations estimated from combined SO/PHI and SDO/HMI observations", *Astronomy and Astrophysics*, 673 (2023) A84; https://doi.org/10.1051/0004-6361/202345946;
- S. L. Yardley, C. J. Owen, D. M. Long, D. Baker, D. H. Brooks, V. Polito, L. M. Green, S. Matthews, M. Owens, M. Lockwood, D. Stansby, A.

W. James, G. Valori, A. Giunta, M. Janvier, N. Ngampoopun, T. Mihailescu, A. S. H. To, L. van Driel-Gesztelyi, P. Démoulin, R. D'Amicis, R. J. French, G. H. H. Suen, A. P. Rouillard, R. F. Pinto, V. Réville, C. J. Watson, A. P. Walsh, A. De Groof, D. R. Williams, I. Zouganelis, D. Müller, D. Berghmans, F. Auchère, L. Harra, U. Schuehle, K. Barczynski, É. Buchlin, R. Aznar Cuadrado, E. Kraaikamp, S. Mandal, S. Parenti, H. Peter, L. Rodriguez, C. Schwanitz, P. Smith, L. Teriaca, C. Verbeeck, A. N. Zhukov, B. De Pontieu, T. Horbury, S. K. Solanki, J. C. del Toro Iniesta, J. Woch, A. Gandorfer, J. Hirzberger, D. Orozco Súarez, T. Appourchaux, D. Calchetti, J. Sinjan, F. Kahil, **K. Albert**, R. Volkmer, M. Carlsson, A. Fludra, D. Hassler, M. Caldwell, T. Fredvik, T. Grundy, S. Guest, M. Haberreiter, S. Leeks, G. Pelouze, J. Plowman, W. Schmutz, S. Sidher, W. T. Thompson, P. Louarn, A. Federov. "Slow Solar Wind Connection Science during Solar Orbiter's First Close Perihelion Passage", *The Astrophysical Journal Supplement*, 267 (2023) 11; https://doi.org/10.3847/1538-4365/acd24b;

- G. Valori, D. Calchetti, A. Moreno Vacas, É. Pariat, S. K. Solanki, P. Löschl, J. Hirzberger, S. Parenti, **K. Albert**, N. Albelo Jorge, A. Álvar Herrero, T. Appourchaux, L. R. Bellot Rubio, J. Blanco Rodríguez, A. Camp Jara, A. Feller, A. Gandorfer, P. García Parejo, D. Germerott, L. Gizon, J. M. Gómez Cama, L. Guerrero, P. Gutierrez Marques, F. Kahil, M. Kolleck, A. Korpi Lagg, D. Orozco Suárez, I. Pérez Grande, E. Sanchis Kilders, J. Schou, U. Schühle, J. Sinjan, J. Staub, H. Strecker, J. C. del Toro Iniesta, R. Volkmer, J. Woch. "Stereoscopic disambiguation of vector magnetograms: First applications to SO/PHI-HRT data", *Astronomy and Astrophysics*, 677 (2023) A25; https://doi.org/10.1051/0004-6361/202345859;
- M. Janvier, S. Mzerguat, P. R. Young, É. Buchlin, A. Manou, G. Pelouze, D M. Long, L. Green, A. Warmuth, F. Schuller, P. Démoulin, D. Calchetti, F. Kahil, L. R. Bellot Rubio, S. Parenti, S. Baccar, K. Barczynski, L. K. Harra, L. A. Hayes, W. T. Thompson, D. Müller, D. Baker, S. Yardley, D. Berghmans, C. Verbeeck, P. J. Smith, H. Peter, R. Aznar Cuadrado, S. Musset, D. H. Brooks, L. Rodriguez, F. Auchère, M. Carlsson, A. Fludra, D. Hassler, D. Williams, M. Caldwell, T. Fredvik, A. Giunta, T. Grundy, S. Guest, E. Kraaikamp, S. Leeks, J. Plowman, W. Schmutz, U. Schühle, S D. Sidher, L. Teriaca, S K. Solanki, J. C. del Toro Iniesta, J. Woch, A. Gandorfer, J. Hirzberger, D. Orozco Suarez, T. Appourchaux, G. Valori, J. Sinjan, **K. Albert**, R. Volkmer. "A multiple spacecraft detection of the 2 April 2022 M-class flare and filament eruption during the first close So-

lar Orbiter perihelion", *Astronomy and Astrophysics*, 677 (2023) A130; https://doi.org/10.1051/0004-6361/202346321;

- J. D. Nölke, S. K. Solanki, J. Hirzberger, H. Peter, L. P. Chitta, F. Kahil, G. Valori, T. Wiegelmann, D. Orozco Suárez, **K. Albert**, N. Albelo Jorge, T. Appourchaux, A. Alvarez-Herrero, J. Blanco Rodríguez, A. Gandorfer, D. Germerott, L. Guerrero, P. Gutierrez-Marques, M. Kolleck, J. C. del Toro Iniesta, R. Volkmer, J. Woch, B. Fiethe, J. M. Gómez Cama, I. Pérez-Grande, E. Sanchis Kilders, M. Balaguer Jiménez, L. R. Bellot Rubio, D. Calchetti, M. Carmona, W. Deutsch, A. Feller, G. Fernandez-Rico, A. Fernández-Medina, P. García Parejo, J. L. Gasent Blesa, L. Gizon, B. Grauf, K. Heerlein, A. Korpi-Lagg, T. Lange, A. López Jiménez, T. Maue, R. Meller, A. Moreno Vacas, R. Müller, E. Nakai, W. Schmidt, J. Schou, U. Schühle, J. Sinjan, J. Staub, H. Strecker, I. Torralbo, D. Berghmans, E. Kraaikamp, L. Rodriguez, C. Verbeeck, A. N. Zhukov, F. Auchere, E. Buchlin, S. Parenti, M. Janvier, K. Barczynski, L. Harra, C. Schwanitz, R. Aznar Cuadrado, S. Mandal, L. Teriaca, D. Long, P. Smith. "Coronal voids and their magnetic nature", *Astronomy and Astrophysics*, 678 (2023) A196; https://doi.org/10.1051/0004-6361/202346040;
- D. Calchetti, M. Stangalini, S. Jafarzadeh, G. Valori, **K. Albert**, N. Albelo Jorge, A. Alvarez-Herrero, T. Appourchaux, M. Balaguer Jiménez, L. R. Bellot Rubio, J. Blanco Rodríguez, A. Feller, A. Gandorfer, D. Germerott, L. Gizon, L. Guerrero, P. Gutierrez-Marques, J. Hirzberger, F. Kahil, M. Kolleck, A. Korpi-Lagg, A. Moreno Vacas, D. Orozco Suárez, I. Pérez-Grande, E. Sanchis Kilders, J. Schou, U. Schühle, J. Sinjan, S. K. Solanki, J. Staub, H. Strecker, J. C. del Toro Iniesta, R. Volkmer, J. Woch. "Spectropolarimetric investigation of magnetohydrodynamic wave modes in the photosphere: First results from PHI on board Solar Orbiter", *Astronomy and Astrophysics*, 674 (2023) A109; https://doi.org/10.1051/0004-6361/202245826;
- A. Moreno Vacas, D. Orozco Suárez, H. Strecker, J. C. del Toro Iniesta, J. M. Borrero, **K. Albert**, S. K. Solanki, F. J. Bailén, L. R. Bellot Rubio, J. Hirzberger, J. Sinjan, P. Santamarina Guerrero, G. Valori, N. Albelo Jorge, A. Alvarez-Herrero, T. Appourchaux, J. Blanco Rodríguez, D. Calchetti, A. Feller, B. Fiethe, A Gandorfer, D. Germerott, L. Gizon, J. M. Gómez Cama, L. Guerrero, P. Gutierrez-Marques, F. Kahil, M. Kolleck, A. Korpi-Lagg, H. Michalik, I. Pérez-Grande, E. Sanchis Kilders, J. Schou, U. Schühle, J. Staub, R. Volkmer, J. Woch. "Comparison of magnetic data products from Solar Orbiter SO/PHI-FDT and SDO/HMI", *Astronomy and Astrophysics*, 685 (2024) A28; https://doi.org/10.1051/0004-6361/202349096

- F. J. Bailén, D. Orozco Suárez, J. Blanco Rodríguez, J. C. del Toro Iniesta, H. Strecker, A. Moreno Vacas, P. Santamarina Guerrero, J. Hirzberger, **K. Albert**, N. Albelo Jorge, T. Appourchaux, A. Alvarez-Herrero, A. Gandorfer, D. Germerott, L. Guerrero, P. Gutierrez-Marques, F. Kahil, M. Kolleck, S. K. Solanki, R. Volkmer, J. Woch, B. Fiethe, J. M. Gómez Cama, I. Pérez-Grande, E. Sanchis Kilders, M. Balaguer Jiménez, L. R. Bellot Rubio, D. Calchetti, M. Carmona, W. Deutsch, A. Feller, G. Fernandez-Rico, A. Fernández-Medina, P. García Parejo, J. L. Gasent Blesa, L. Gizon, B. Grauf, K. Heerlein, A. Korpi-Lagg, T. Lange, A. López Jiménez, T. Maue, R. Meller, H. Michalik, R. Müller, E. Nakai, W. Schmidt, J. Schou, U. Schühle, J. Sinjan, J. Staub, I. Torralbo and G. Valori. "Determination of the SO/PHI-HRT wavefront degradation using multiple defocused images", *Astronomy and Astrophysics*, 681 (2024) A58; https://doi.org/10.1051/0004-6361/202346019;
- F. Kahil, A. Gandorfer, J. Hirzberger, D. Calchetti, J. Sinjan, G. Valori, S. K. Solanki, M. Van Noort, **K. Albert**, N. Albelo Jorge, A. Alvarez-Herrero, T. Appourchaux, L. R. Bellot Rubio, J. Blanco Rodríguez, A. Feller, B. Fiethe, D. Germerott, L. Gizon, L. Guerrero, P. Gutierrez-Marques, M. Kolleck, Korpi-A. Lagg, H. Michalik, Moreno A. Vacas, Orozco D. Suárez, I. Pérez-Grande, E. Sanchis Kilders, J. Schou, U. Schühle, J. Staub, H. Strecker, C. J. del Toro Iniesta, R. Volkmer, J. Woch. "Wavefront error of PHI/HRT on Solar Orbiter at various heliocentric distances", *Astronomy and Astrophysics*, 675 (2023) A61; https://doi.org/10.1051/0004-6361/202346033;
- P. Loeschl, G. Valori, J. Hirzberger, J. Schou, S. K. Solanki, D. Orozco Suárez, **K. Albert**, N. Albelo Jorge, T. Appourchaux, A. Alvarez-Herrero, J. Blanco Rodríguez, A. Gandorfer, D. Germerott, L. Guerrero, P. Gutierrez-Marques, F. Kahil, M. Kolleck, J. C. del Toro Iniesta, R. Volkmer, J. Woch, B. Fiethe, I. Pérez-Grande, E. Sanchis Kilders, M. Balaguer Jiménez, L. R. Bellot Rubio, D. Calchetti , M. Carmona, W. Deutsch, A. Feller, G. Fernandez-Rico, A. Fernández-Medina, P. García Parejo, J. L. Gasent Blesa, L. Gizon, B. Grauf, K. Heerlein, A. Korpi-Lagg, T. Lange, A. López Jiménez, T. Maue, R. Meller, A. Moreno Vacas, R. Müller, E. Nakai, W. Schmidt, U. Schühle, J. Sinjan, J. Staub, H. Strecker, and I. Torralbo. "A first rapid synoptic magnetic field map using SDO/HMI and SO/PHI data", *Astronomy and Astrophysics*, 681 (2024) A59; https://doi.org/10.1051/0004-6361/202346046;
- K. L. Yeo, N. A. Krivova, S. K. Solanki, J. Hirzberger, D. Orozco Suárez, **K. Albert**, N. Albelo Jorge, T. Appourchaux, A. Alvarez-Herrero, J.

Blanco Rodríguez, A. Gandorfer, P. Gutierrez-Marques, F. Kahil, M. Kolleck, J. C. del Toro Iniesta, R. Volkmer, J. Woch, B. Fiethe, I. Pérez-Grande, E. Sanchis Kilders, M. Balaguer Jiménez, L. R. Bellot Rubio, D. Calchetti, M. Carmona, A. Feller, G. Fernandez-Rico, A. Fernández-Medina, P. García Parejo, J. L. Gasent Blesa, L. Gizon, B. Grauf, K. Heerlein, A. Korpi-Lagg, T. Maue, R. Meller, A. Moreno Vacas, R. Müller, E. Nakai, W. Schmidt, J. Schou, J. Sinjan, J. Staub, H. Strecker, I. Torralbo and G. Valori. "Reconstruction of total solar irradiance variability as simultaneously apparent from Solar Orbiter and Solar Dynamics Observatory", *Astronomy and Astrophysics*, 679 (2023) A25; https://doi.org/10.1051/0004-6361/202345872;

- D. Yang, L. Gizon, H. Barucq, J. Hirzberger, D. Orozco Suárez, **K. Albert**, N. Albelo Jorge, T. Appourchaux, A. Alvarez-Herrero, J. Blanco Rodríguez, A. Gandorfer, D. Germerott, L. Guerrero, P. Gutierrez-Marques, F. Kahil, M. Kolleck, S. K. Solanki, J. C. del Toro Iniesta, R. Volkmer, J. Woch, I. Pérez-Grande, E. Sanchis Kilders, M. Balaguer Jiménez, L. R. Bellot Rubio, D. Calchetti, M. Carmona, W. Deutsch, A. Feller, G. Fernandez-Rico, A. Fernández-Medina, P. García Parejo, J. L. Gasent Blesa, B. Grauf, K. Heerlein, A. Korpi-Lagg, T. Lange, A. López Jiménez, T. Maue, R. Meller, A. Moreno Vacas, R. Müller, E. Nakai, W. Schmidt, J. Schou, U. Schühle, J. Sinjan, J. Staub, H. Strecker, I. Torralbo and G. Valori. "Direct assessment of SDO/HMI helioseismology of active regions on the Sun's far side using SO/PHI magnetograms", *Astronomy and Astrophysics*, 674 (2023) A183; https://doi.org/10.1051/0004-6361/202346030;
- F. Kahil, J. Hirzberger, S. K. Solanki, L. P. Chitta, H. Peter, F. Auchère, J. Sinjan, D. Orozco Suárez, **K. Albert**, N. Albelo Jorge, T. Appourchaux, A. Alvarez-Herrero, J. Blanco Rodríguez, A. Gandorfer, D. Germerott, L. Guerrero, P. Gutiérrez Márquez, M. Kolleck, J. C. del Toro Iniesta, R. Volkmer, J. Woch, B. Fiethe, J. M. Gómez Cama, I. Pérez-Grande, E. Sanchis Kilders, M. Balaguer Jiménez, L. R. Bellot Rubio, D. Calchetti, M. Carmona, W. Deutsch, G. Fernández-Rico, A. Fernández-Medina, P. García Parejo, J. L. Gasent-Blesa, L. Gizon, B. Grauf, K. Heerlein, A. Lagg, T. Lange, A. López Jiménez, T. Maue, R. Meller, H. Michalik, A. Moreno Vacas, R. Müller, E. Nakai, W. Schmidt, J. Schou, U. Schühle, J. Staub, H. Strecker, I. Torralbo, G. Valori, R. Aznar Cuadrado, L. Teriaca, D. Berghmans, C. Verbeeck, E. Kraaikamp and S. Gissot. "The magnetic drivers of campfires seen by the Polarimetric and Helioseismic Imager (PHI) on Solar Orbiter", *Astronomy and Astrophysics*, 660 (2022) A143; https://doi.org/10.1051/0004-6361/202142873;

- F. Kahil, A. Gandorfer, J. Hirzberger, D. Orozco Suárez, **K. Albert**, N. Albelo Jorge, T. Appourchaux, A. Álvarez-Herrero, J. Blanco Rodríguez, D. Germerott, L. Guerrero, P. Gutierrez Marquez, J. Sinjan, D. Calchetti, M. Kolleck, S. K. Solanki, J. C. del Toro Iniesta, R. Volkmer, J. Woch, B. Fiethe, J. M. Gómez Cama, I. Pérez-Grande, E. Sanchis Kilders, M. Balaguer Jiménez, L. R. Bellot Rubio, M. Carmona, W. Deutsch, G. Fernandez-Rico, A. Fernández-Medina, P. García Parejo, J. L. Gasent Blesa, L. Gizon, B. Grauf, K. Heerlein, A. Korpi-Lagg, T. Lange, A. López Jiménez, T. Maue, R. Meller, H. Michalik, A. Moreno Vacas, R. Müller, E. Nakai, W. Schmidt, J. Schou, U. Schühle, J. Staub, H. Strecker, I. Torralbo, G. Valori. "Image quality of data products of the high resolution telescope of the polarimetric and helioseismic imager", Proc. SPIE 12180, Space Telescopes and Instrumentation 2022: Optical, Infrared, and Millimeter Wave, 121803F (27 August 2022); https://doi.org/10.1117/12.2628942;
- J. Sinjan, D. Calchetti, J. Hirzberger, D. Orozco Suárez, **K. Albert**, N. Albelo Jorge, T. Appourchaux, A. Alvarez-Herrero, J. Blanco Rodríguez, A. Gandorfer, D. Germerott, L. Guerrero, P. Gutierrez Marquez, F. Kahil, M. Kolleck, S. K. Solanki, J. C. del Toro Iniesta, R. Volkmer, J. Woch, B. Fiethe, J. M. Gómez Cama, I. Pérez-Grande, E. Sanchis Kilders, M. Balaguer Jiménez, L. R. Bellot Rubio, M. Carmona, W. Deutsch, G. Fernandez-Rico, A. Fernández-Medina, P. García Parejo, J. L. Gasent Blesa, L. Gizon, B. Grauf, K. Heerlein, A. Korpi-Lagg, T. Lange, A. López Jiménez, T. Maue, R. Meller, H. Michalik, A. Moreno Vacas, R. Müller, E. Nakai, W. Schmidt, J. Schou, U. Schühle, J. Staub, H. Strecker, I. Torralbo, G. Valori. "The on-ground data reduction and calibration pipeline for SO/PHI-HRT", Proc. SPIE 12189, Software and Cyberinfrastructure for Astronomy VII, 121891J (29 August 2022); https://doi.org/10.1117/12.2629323;
- S. K. Solanki, J. C. del Toro Iniesta, J. Woch, A. Gandorfer, J. Hirzberger, A. Alvarez-Herrero, T. Appourchaux, V. Martínez Pillet, I. Pérez-Grande, E. Sanchis Kilders, W. Schmidt, J. M. Gómez Cama, H. Michalik, W. Deutsch, G. Fernandez-Rico, B. Grauf, L. Gizon, K. Heerlein, M. Kolleck, A. Lagg, R. Meller, R. Müller, U. Schühle, J. Staub, **K. Albert**, M. Alvarez Copano, U. Beckmann, J. Bischoff, D. Busse, R. Enge, S. Frahm, D. Germerott, L. Guerrero, B. Löptien, T. Meierdierks, D. Oberdorfer, I. Papagiannaki, S. Ramanath, J. Schou, S. Werner, D. Yang, A. Zerr, M. Bergmann, J. Bochmann, J. Heinrichs, S. Meyer, M. Monecke, M.-F. Müller, M. Sperling, D. Álvarez García, B. Aparicio, M. Balaguer Jiménez, L. R. Bellot Rubio, J. P. Cobos Carracosa, F.

Girela, D. Hernández Expósito, M. Herranz, P. Labrousse, A. López Jiménez, D. Orozco Suárez, J. L. Ramos, J. Barandiarán, L. Bastide, C. Campuzano, M. Cebollero, B. Dávila, A. Fernández-Medina, P. García Parejo, D. Garranzo-García, H. Laguna, J. A. Martín, R. Navarro, A. Núñez Peral, M. Royo, A. Sánchez, M. Silva-López, I. Vera, J. Villanueva, J.-J. Fourmond, C. Ruiz de Galarreta, M. Bouzit, V. Hervier, J. C. Le Clec'h, N. Szwec, M. Chaigneau, V. Buttice, C. Dominguez-Tagle, A. Philippon, P. Boumier, R. Le Cocguen, G. Baranjuk, A. Bell, Th. Berkefeld, J. Baumgartner, F. Heidecke, T. Maue, E. Nakai, T. Scheiffelen, M. Sigwarth, D. Soltau, R. Volkmer, J. Blanco Rodríguez, V. Domingo, A. Ferreres Sabater, J. L. Gasent Blesa, P. Rodríguez Martínez, D. Osorno Caudel, J. Bosch, A. Casas, M. Carmona, A. Herms, D. Roma, G. Alonso, A. Gómez-Sanjuan, J. Piqueras, I. Torralbo, B. Fiethe, Y. Guan, T. Lange, H. Michel, J. A. Bonet, S. Fahmy, D. Müller, and I. Zouganelis. "The Polarimetric and Helioseismic Imager on Solar Orbiter", Astronomy and Astrophysics, *Astronomy and Astrophysics* 642, A11 (2020); https://doi.org/10.1051/0004-6361/201935325;

- T. Lange, B. Fiethe, H. Michel, H. Michalik, **K. Albert**, J. Hirzberger. "On-board processing using reconfigurable hardware on the solar orbiter PHI instrument", 2017 NASA/ESA Conference on Adaptive Hardware and Systems (AHS). July 2017, pp. 186–191; https://doi.org/10.1109/AHS.2017.8046377;
- T. Lange, B. Fiethe, Y. Guan, H. Michalik, **K. Albert**, J. Hirzberger, D. O. Suárez, and M. Rodríguez-Valido. "A flexible and heterogeneous framework for scientific image data processing on-board the Solar Orbiter PHI instrument", Proc. SPIE 11155, Image and Signal Processing for Remote Sensing XXV, 1115506 (7 October 2019); https://doi.org/10.1117/12.2532102.

Conferences

Talks

- The 8th Solar Orbiter Workshop, Belfast (GB-NIR), 2022: **K. Albert**, K. L. Yeo, J. Hirzberger, A. Moreno Vacas, D. O. Suárez, N. Krivova, S. K. Solanki, J. C. del Toro Iniesta, J. Woch, A. Gandorfer, A. Alvarez-Herrero, T. Appourchaux, R. Volkmer, and the SO/PHI team. "A first multi-angle look at intensity contrast of solar network and faculae";
- AGU Fall meeting, Online, 2020: **K. Albert**, J. Hirzberger, M. Kolleck, N. Albelo Jorge, D. Busse, J. Blanco Rodríguez, J. P. Cobos Car-

rascosa, B. Fiethe, A. Gandorfer, D. Germerott, Y. Guan, L. Guerrero, P. Gutierrez-Marques, D. Hernández Expósitod, T. Lange, H. Michalik, D. Orozco Suárez, J. Schou, S. K. Solanki, J. C. del Toro Iniesta, J. Woch. "First results from SO/PHI's on-board data reduction";

- SPIE Astronomical Telescopes + Instrumentation, Austin (USA-TX), 2018: **K. Albert**, J. Hirzberger, D. Busse, T. Lange, M. Kolleck, B. Fiethe, D. Orozco Suárez, J. Woch, J. Schou, J. Blanco Rodríguez, A. Gandorfer, Y. Guan, J. P. Cobos Carrascosa, D. Hernández Expósito, J. C. del Toro Iniesta, S. K. Solanki, H. Michalik. "Autonomous on-board data processing and instrument calibration software for the SO/PHI";
- Annual Meeting of the German Astronomical Society, Göttingen (DE), 2017: **K. Albert**, J. Hirzberger, A. Gandorfer, J. Woch, S. K. Solanki, H. Michalik. "Autonomous data reduction for the space-borne spectropolarimeter PHI";
- Rocks and Stars II conference, Göttingen (DE), 2017: **K. Albert**, J. Hirzberger, A. Gandorfer, J. Woch, S. K. Solanki, H. Michalik. "Autonomous flat field acquisition and correction techniques for the space-borne spectropolarimeter PHI".

Posters

- The 9th Solar Polarization Workshop, Göttingen (DE), 2019: **K. Albert**, J. Hirzberger, N. Albelo Jorge, D. Busse, J. Blanco Rodrguez, J. S. Castellanos Duran, J. P. Cobos Carrascosa, B. Fiethe, A. Gandorfer, Y. Guan, L. Guerrero, P. Gutierrez-Marques, M. Kolleck, A. Lagg, T. Lange, H. Michalik, S. K. Solanki, J. C. del Toro Iniesta, and J. Woch. "On-board data reduction pipeline for SO/PHI";
- Astronomical Data Analysis Software and Systems XXIX, Groningen (NL), 2019: **K. Albert**, J. Hirzberger, D. Busse, J. S. Castellanos Durán, M. Kolleck. "Metadata and Their Importance in SO/PHI's On–Board Data Processing";
- Astronomical Data Analysis Software and Systems XXIX, Maryland (USA-MD) 2018: **K. Albert**, J. Hirzberger, D. Busse, J. Blanco Rodríguez, J. S. Castellanos Durán, J. P. Cobos Carrascosa, B. Fiethe, A. Gandorfer, Y. Guan, M. Kolleck, A. Lagg, T. Lange, H. Michalik, S. K. Solanki, J. C. del Toro Iniesta, and J. Woch. "Performance analysis of the SO/PHI software framework for on-board data reduction".

Others

- Master's thesis, K. Albert (2014). SvalPoint: A Multi-track Optical Pointing System (Dissertation); Retrieved from http://urn.kb.se/resolve?urn=urn:nbn:se:ltu:diva-59429.

Words of gratitude

Dear Johann, discovering solar physics with you was absolutely fantastic. Thank you for being always there for me, as teacher, as role model, as moral support. Thank you for answering my endless questions, for thinking together on difficult problems, and for always making time for discussions. Thank you for being there in the highs and in the lows, always giving just the right support. I could have never imagined a better, or kinder Doktorvater. As a matter of fact, for once, I am truly short of words to express all that I am grateful to you – this doesn't even begin to cover it. I am just absolutely overjoyed to be working with you.

Dear Sami, thank you for your guidance, your advocacy, your continued support, and constant encouragement – as well as for those late night paper revisions. I am truly humbled for being given the chance to learn from you.

Dear Natasha, I have learned so much from you in just the few years. Thank you for always taking the time to carefully look at my work, and for always showing me a new angle, that I didn't see before. Working with you is such a joy!

Dear Professor Michalik, thank you for being there along the long way, and supporting me in completing my thesis.

Dear Sonja, thank you for having all the answers to the many question, and kind words to every worry that turned up during the years.

You, dear SO/PHI team, thank you for the great cooperation. Thank you for challenging ideas, celebrating the successes, and pulling through the tough times together. Nestor, and Dennis, it is such a pleasure implementing this monster of a software with you, thank you for being there to figure this out together! Martin and Pablo, thank you for the many discussions, and for always bringing a new point of view. David, Julian, and Hanna, thank you for the great cooperation. It is so much fun analysing the tiniest and weirdest details, devising all the creative ideas and drafting grand plans together with you. I am just so happy to know you!

Dear Joachim, I am incredibly grateful for your support. Thank you for always advocating for me!

Dear Jesper, thank you for being a mentor, a friend, and delightful company on many of our travels. Thank you for your endless kindness, the fun meetings in motion, and that your door is always open.

All the friends that I made at MPS, thank you for making me feel at home! Sebas, you have always been the best office mate, a fierce but always kind and constructive critique: discussing science with you is always a lot of fun. Last but not least, thank you for the plots that you helped me out with for the thesis! Many thanks also to all those lovely people that made me feel welcome when I arrived, have been around for lunch, coffee, chilled afternoons and evenings, but also in the hard times, during the Corona lock-downs, in supporting each-other. Azaymi, Ricardo, Franziska, Philipp, Damien, Bianca, Alex, Wieland: you surely know that you are among these people. And all my friends outside MPS, thank you for cheering me along the way.

My dear family, thank you for being there. There are no words to express my gratitude – I am the person that I am today thanks to you. Dear Astrid and Arne, you fantastic sparks of joy, I am humbled to have you as my teachers in life. My dearest Patrik, you know well: "Ohne dich hätt' ich mich niemals getraut". "I love you too much".